Site C0019[1]

Expedition 343/343T Scientists[2]

Chapter contents

Introduction

The primary objective of drilling at Integrated Ocean Drilling Program (IODP) Site C0019 was to measure the fault zone physical properties, recover fault zone material, and directly record temperature from the fault zone responsible for a Mw 9.0 earthquake. The shallow distribution of large slip for the Tohoku-oki earthquake provides an unprecedented opportunity to directly access a fault that has recently moved tens of meters. The 2011 Tohoku-oki earthquake and tsunami originated from slip on the megathrust fault surface west of the Japan Trench where the Pacific plate subducts below Honshu Island. The subduction zone is characterized by a relatively rapid convergence rate of ~8 cm/y (e.g., Apel et al., 2006), a high level of seismic activity, and a deep trench.

Site C0019 science objectives, as summarized in the IODP Expedition 343 *Scientific Prospectus* (Mori et al., 2012), are closely aligned with the overall goals of IODP. In the IODP Initial Science Plan, research concerning solid earth cycles and geodynamics highlights the seismogenic zone initiative, which advocates subduction zone studies that include investigating the behavior of rocks and sediments to better understand the fault zone and integration with studies of earthquake mechanics. Furthermore, Expedition 343 Japan Trench Fast Drilling Project (JFAST) directly addresses Challenge 12 of the IODP *Science Plan for 2013–2023*: "What mechanisms control the occurrence of destructive earthquakes, landslides, and tsunami?" As outlined in the report from the International Continental Scientific Drilling Program (ICDP)/Southern California Earthquake Center (SCEC) international workshop on rapid response drilling (Brodsky et al., 2009), fundamental questions regarding stress, fault-related fluid flow, and the structural and mechanical characteristics of the earthquake rupture zone can be addressed uniquely through rapid response drilling at Site C0019:

1. What was the stress state on the fault that controlled rupture during the earthquake and was the stress completely released?
2. What is the temperature anomaly remaining from the frictional heat produced at the time of the earthquake (which can be used to infer the level of dynamic friction)?
3. How can we identify the fault zone in the core samples?

[1] Expedition 343/343T Scientists, 2013. Site C0019. *In* Chester, F.M., Mori, J., Eguchi, N., Toczko, S., and the Expedition 343/343T Scientists, *Proc. IODP,* 343/343T: Tokyo (Integrated Ocean Drilling Program Management International, Inc.). doi:10.2204/iodp.proc.343343T.103.2013
[2] **Expedition 343/343T Scientists' addresses.**

doi:10.2204/iodp.proc.343343T.103.2013

4. What will detailed analyses of textures and small-scale structures in the fault zone core samples imply about the role of fluids and pressurization during rupture?

Secondary science objectives include carrying out other geological, geochemical, and microbiological observations in accordance with the IODP measurements guidelines (**www.iodp.org/program-policies/**). As a specific example, there is some evidence that great amounts of hydrogen may be released at the time of large faulting (e.g., Kita et al., 1982). The massive amounts of hydrogen may greatly stimulate microbiological activity; thus, samples of the fault may contain records of biogeochemical and microbiological processes.

Operations

Expedition 343

Shimizu, Japan, port call

Loading for Expedition 343 began on 25 March 2012 at Shimizu, Japan. A "prespud" meeting was held aboard the D/V *Chikyu,* with representatives from the Center for Deep Earth Exploration (CDEX), Marine Works Japan, Mantle Quest Japan, and the Expedition 343 Science Party on 31 March 2012. The *Chikyu* departed Shimizu at 1630 h on 1 April en route to Site C0019 (proposed Site JFAST-3).

Transit to Site C0019

During transit to Site C0019, the *Chikyu* engaged in a series of system integration tests with the dual elevator system (DES) and began building up drill pipe stands and casing running tools for the 20 inch wellhead. The *Chikyu* arrived on site at 0800 h on 3 April 2012. However, extreme winds (30 m/s, maximum gusts near 40 m/s) necessitated putting the vessel into auto heading mode and entering wait on weather (WOW) while poor weather conditions persisted. The *Chikyu* continued to WOW until the morning of 5 April, when transponders were dropped for determining dynamic positioning. The underwater television (UWTV) cable was rigged up in the moonpool for a free-fall test on 6 April and required troubleshooting; winch and software issues affected deployment. While the UWTV troubleshooting was taking place, the jetting bottom-hole assembly (BHA) and running tool for the miniature temperature logger (MTL) observatory was being rigged up and tested. Testing for the UWTV continued for several days, working to resolve cable twisting and kinking issues. Eventually, it was necessary for the *Chikyu* to move to deeper water (7500 m) to fully unwind the weighted UWTV cable. Problem solving focused on eliminating unwanted rotation in the cable, which could result in wrapping and snapping the UWTV cable on the drill string while deployed near the seafloor. Finally, on 13 April, the *Chikyu* moved to the site location and prepared the guide horn and running tool for the 20 inch casing. All holes surveyed and drilled at Site C0019 were along a transect running along strike at ~10 m intervals (Fig. **F1**).

Hole C0019A

Initial operations began with running the 20 inch casing with a 30 inch outside diameter guide funnel into the water at 1800 h on 13 April 2012, reaching 2415 m drilling depth below rig floor (DRF) at 2400 h. Once the BHA reached 4074 m DRF, the DES was installed and tested in preparation for running deeper. However, several problems with the DES operation were discovered, delaying jetting in Hole C0019A. Preparations for running the UWTV were made but then postponed because of 14 h of WOW (waves exceeding operational criteria). After WOW, the UWTV was lowered to the wellhead housing at 4677 m DRF. While running to the seafloor, the DES and UWTV continued to experience problems during operation. A seabed survey started on 17 April at 1945 h, taking advantage of the weather and close proximity of the planned coring hole and the logging-while-drilling (LWD) hole. Once the survey was completed, the *Chikyu* returned to the LWD hole position to jet in the 20 inch casing. After troubleshooting the DES again, jetting in Hole C0019A (37°56.3367′N, 143°54.8100′E) (Table **T1**) began on 18 April at 0745 h. The jetting was successful to 28.0 meters below seafloor (mbsf), but the running tool would not release. Many attempts were made to release the running tool, but all were unsuccessful. It was decided to recover the running tool dart with the wireline winch, which eventually succeeded by 2030 h. Investigation showed no apparent issues with the dart, so the running tool dart was rerun with a new shear pin. The tool still refused to part from the wellhead, so attempts were made to jar down nine times. Attempts at raising pressure and repeating dart landings were equally unsuccessful, although continuous observation with the UWTV showed no apparent mechanical irregularities that might account for the stuck casing. Upon retrieval, the X Barrel Retrieving Tool showed no pin shear. Ultimately, the decision was made on 19 April to pull the casing and running tool out of the hole and return them to the rig floor for inspection. On 20 April, the running tool and wellhead were laid down for careful inspection and testing of the running tool. During this time, the *Chikyu* moved to drop a

new seafloor transponder to replace a malfunctioning one. Because the jet-in failed, it was decided to move on and begin LWD drilling at a new hole.

Hole C0019B

Preparations to assemble the LWD BHA to drill the logging hole began while the casing and casing running tool were inspected. On 21 April 2012, the LWD tools were made up and run in for a shallow-water test. Unfortunately, a first shallow communication and function test at the sea surface revealed that the proVISION tool was not functioning properly. After some unsuccessful attempts at repair, the tool was removed, and then the 8½ inch LWD BHA, including geoVISION, arcVISION, and measurement-while-drilling (MWD) (TeleScope) tools, was run. Subsequent shallow tests of the MWD pulse telemetry were conducted at water depths of 1988.7, 3872.4, and 5985.0 m. Spud in of Hole C0019B was achieved at 0000 h on 23 April, followed by jetting in with an initial surface pump rate of 150–500 gallons per minute (gpm). About 1 h later, the spud-in pumping rate was increased and the MWD mud-pulse transmission was confirmed. At ~0915 h the bit passed 7049.5 meters below sea level (mbsl). This is the deepest total drill pipe length from the sea level in the history of scientific ocean drilling. After continuous drilling and real-time monitoring to 576.0 mbsf, the drill string was pulled up because of WOW on 24 April. Drilling operations were resumed from 576.0 mbsf at 2400 h on 24 April. On the evening of 25 April, the largest changes in resistivity and natural gamma radiation (NGR) were observed at the interval of ~820–840 mbsf. The large changes in the logging parameters were interpreted as showing that the LWD had reached a hard chert layer, which was the designated target formation. At 2145 h on 25 April, the rate of penetration (ROP) had dropped to nearly zero and the decision was made to stop drilling. The borehole reached a final depth of 850.5 mbsf (7740 mbsl). This extends the world record for total length of drill pipe below sea level, which was set 2 days earlier. Repeat measurements at three designated 50 m intervals were conducted while pulling out of the borehole. By the end of the day of 25 April the LWD assembly was out of the borehole, all LWD tools were recovered on the rig floor by 1200 h on 27 April, and all memory data were successfully downloaded.

Hole C0019C

Preparations for the wellhead installation in Hole C0019C began on 28 April 2012 with the make-up and running of the 20 inch casing and running tool BHA. The wellhead and running tool BHA were run into the water from 0215 h and had reached 4084 m DRF by 1415 h. To prevent problems with the inner lining of the drill pipe from fouling the running dart landing, the pipe was flushed with 1000 gpm of seawater at 1000, 2000, 3000, and 4000 m. The UWTV was installed and run in the hole at 2000 h and underwent a function check at 180 m. Communication checks failed to contact the minibeacon attached to the UWTV, and a phase of troubleshooting began. The drill pipe continued to be run in, in conjunction with the UWTV, until the seafloor was tagged at 0815 h on 29 April. Jetting in the 20 inch casing began in Hole C0019C at 1500 h, confirming the seafloor depth at 6928.5 m DRF (Table T1), stopping only when the casing reached 29 mbsf. Upon starting to pick up the core barrel retrieving tool (CBRT), it was found that the core line winch counter was malfunctioning, so it was run with a calculated pay out. Circulation to clear out Hi-Vis mud began, and then the CBRT with dart was run to 6721 m DRF without pumping. Closing and pumping at 20, 40, and 60 strokes per minute began when the CBRT suddenly released the wellhead; recovery of the CBRT and dart showed that the dart broke in two within the drill pipe. The UWTV and drill pipe were pulled up to 4100 m DRF, and the minibeacon signal on the UWTV was checked every 1000 m with no response. The UWTV was recovered to the surface by 1415 h on 30 April, and the running tool BHA was recovered and laid down on 1 May.

The LWD assembly was made up in preparation for reentry into the wellhead of Hole C0019C on 1 May. Just as for Hole C0019B, the LWD tools included the geoVISION, arcVISION, and MWD (TeleScope) tools. Following the standard procedure, the tools were assembled and shallow communication and function tests were conducted on the surface and at water depths of 320, 2014, and 3917 m. On 2 May, because of bad weather the drill string was brought up to ~3000 m DRF and secured for riding out rough seas. Following 2 days of WOW, operations resumed, running the LWD assembly with UWTV on 5 May. Adjusting vessel position, the attempt to reenter the wellhead was successful at 0000 h on 5 May. The LWD assembly was continuously run into Hole C0019C; however, there was an engineering problem at 1400 h on 6 May with a loss of the BHA at ~120 mbsf. Analysis of LWD data showed that the disconnection of the BHA was not a result of any abnormal conditions of the borehole or the response of the formations being drilled. Once the pipe was returned to the ship on 7 May, the engineering staff determined it was a mechanical failure of one section of the drill

pipe. The loss of the BHA inside the wellhead necessitated abandoning this hole and starting preparation for jetting a new wellhead in Hole C0019D.

Hole C0019D

Preparation for jetting a new wellhead in Hole C0019D began at 1700 h on 7 May 2012 once the remaining sections of the LWD BHA had been recovered and examined on the rig floor. On 8 May, the jetting BHA and running tool were made up and run into the water, reaching 5030 m DRF by 1000 h. The seafloor was reached by 0500 h on 9 May, and Hole C0019D was tagged at 0630 h at 6929.5 m DRF (Table **T1**). Jetting-in operations began at 0945 h, when the seabed was noted as being 6926 m DRF, a 3.5 m difference! The wellhead was jetted in to 27.5 mbsf by 1245 h, when operations to release the running tool began. Several issues were encountered, particularly that the tool would not release, even after confirming landing of the dart several times. The drillers made multiple attempts over the next few hours, finally noting, by visual UWTV confirmation, that the tool had released at 2000 h. Preparations for drilling began with the UWTV recovery, when the video feed from the UWTV was lost. Attempts to recover visual communications failed, so the UWTV was recovered on deck to examine it more closely. Finally, at 1000 h on 10 May, the UWTV was recovered on the working cart above the moonpool so that troubleshooting could begin. Meanwhile, the jetting BHA was recovered on deck, laying down at 2130 h. The umbilical cable for the UWTV was found to have one more cut fiber-optic line and two short circuits in the power lines, all close to the spool connection. A quick consultation among the Co-Chief Scientists, Operations Superintendents (OSIs), Offshore Installation Managers (OIMs), and Expedition Project Managers (EPMs) concluded that since the problem could not be fixed rapidly, coring operations would begin immediately.

Hole C0019E

The decision was made on 10 May 2012 to proceed with a blind spud of Hole C0019E with the coring BHA without use of the UWTV. The location was selected with two considerations in mind: (1) it was close to Hole C0019B (10 m south of Hole C0019B), where the LWD data could guide and identify key target intervals, and (2) it was far enough away to minimize the possibility that the holes would intersect at depth. The rotary core barrel BHA was made up and run in the hole on the morning of 11 May, reaching 4000 m DRF by 1845 h. Sea conditions necessitated WOW, which continued until 0600 h on 12 May. There were several more short WOW periods during 12 May, mainly caused by maximum wave heights exceeding operational criteria. The seafloor was reached on 13 May, when the center bit was dropped for washing down and tagging the seafloor. The seafloor depth (6918 m DRF) was estimated from drilling parameters (Table **T1**). A test core was drilled from 176.5 to 86 mbsf and recovered on deck on 14 May at 0752 h. It was decided to drill ahead before recovering the next series of cores, which began on 16 May at 648 mbsf. Cores 343-C0019E-2R and 3R were recovered, and then we drilled ahead to 680 mbsf. From this point, we cored continuously until reaching 729 mbsf on 19 May, when a consultation among the OSIs, OIMs, Co-Chief Scientists, and EPMs decided that with the limited time left in the expedition, we would drill ahead to 770 mbsf before resuming coring. The drill ahead target was reached on 19 May, with the first core (343-C0019E-10R) of the second coring run on deck at 2359 h. It was decided to core ahead until the end of 22 May so that we would have the best chance of recovering the next identified presumed fault zone at 820 mbsf. Coring operations finished at 844.5 mbsf at 1640 h on 22 May, with the recovery of Core 343-C0019E-21R, a short chert section of 0.5 m, after a drilling advance of 8 m. A deplugger assembly containing three MTL sensors was dropped, and then pulling out of the hole operations commenced. The BHA was back on deck by 0400 h on 24 May, and the ship began moving 30 nmi west of Site C0019 to reach the helicopter rendezvous point at 0445 h.

Expedition 343 end

Expedition 343 ended at sea on 24 May 2012, with the helicopter transfer (in three flights) of the science party to Sendai, Japan, from the *Chikyu*.

Expedition 343T

This expedition was a continuation of JFAST from 5 to 19 July 2012, which sailed with a small science party (one EPM, two scientists, and one observer). The objective was to deploy the MTL observatory in Hole C0019D, which could not be completed during Expedition 343 in April and May. The first task was to unwind the cable for the UWTV so that repairs could be carried out on the portion of the cable close to the end attached to the drum. On 10 July, the wellhead that was placed during Expedition 343 was located and reentered by 2230 h with a mud motor BHA. During 11 and 12 July, a borehole was drilled to 854.8 mbsf. The use of a mud motor with a polycrystalline diamond compact bit enabled fast drilling, and total depth (TD) was reached after ~15 h of drilling. On 14 July, temperature sensors attached to the prepared rope were placed in 829.2 m of 4½ inch

steel tubing that was hanging from the rig floor (see **"Observatory and downhole measurements"** for details). Lowering the tubing with the observatory instruments to the seafloor began that evening. The bottom of the observatory tubing entered the wellhead at ~1045 h on 16 July and was lowered into place until the casing hanger met with the seafloor wellhead at ~1730 h. Detachment of the casing running tool was completed at ~1815 h on 16 July. Recovery of the casing running tool continued until 0600 h on 17 July, after which an unsuccessful attempt was made to recover the four working transponders.

In contrast to operations in April and May, observatory installation was completed without any major problems. Drilling was done quickly using a mud motor. The UWTV performed well, the two releases from the running tool occurred smoothly, and the 4½ inch tubing with the temperature sensors was quickly and smoothly placed in the borehole. Also, no time was lost because of bad weather and operations were completed ahead of schedule.

The observatory deployment, which could not be done in the ~40 days of operations in April and May, was completed in ~1 week in July. One reason for the successful installation during IODP Expedition 343T is the knowledge gained in April and May about drilling conditions and deepwater operations. Fixing the cable for the UWTV, engineered solutions to the running tool release problems, and experience in drilling previous boreholes at the same site all contributed to the success of Expedition 343T.

The *Chikyu* began transit to Hachinohe Port at 1245 h on 18 July, reaching the standby anchoring point at 0900 h on 19 July. The scientists disembarked via harbor boat, ending Expedition 343T at midnight on 19 July.

Logging while drilling

Data and log quality

Hole C0019B

Available data

Hole C0019B was drilled with LWD/MWD tools. Unfortunately, the proVISION tool was not deployed as planned because of a mechanical issue; therefore, nuclear magnetic resonance measurements were not obtained. MWD data were transmitted in real time with a limited set of LWD data (see Table **T2** in the "Methods" chapter [Expedition 343/343T Scientists, 2013]) through the drilling fluid telemetry system. When the LWD tools were recovered on the rig floor, memory data were successfully downloaded and processed according to the data flow described in **"Shipboard data flow and quality check"** and Figure **F5,** both in the "Methods" chapter (Expedition 343/343T Scientists, 2013). A list of available LWD data is given in Table **T2** in the "Methods" chapter (Expedition 343/343T Scientists, 2013).

Depth shift

The mudline (seafloor) was identified from the midpoint of the first break in the gamma ray and resistivity logs (Fig. **F2**). A mudline was picked at 6918 meters below rig floor (mbrf) in Hole C0019B. All LWD data were converted to LWD depth below seafloor (LSF). In this section, LSF is referred to as meters below seafloor, based on the mudline depth.

Logging data quality

Figure **F3** shows the overview of the log quality control (QC) logs. The logs indicate that the borehole was drilled smoothly and no significant vertical tool shocks were detected by the sensors in the tools. Minimal variations in downhole rotations per minute (rpm) indicate that the bit rotation was generally stable. Initial target ROP was <55, <45, and ~30 m/h for 0–200, 200–500, and 800 mbsf to TD, respectively. The actual ROP fluctuated throughout the hole and frequently exceeded the target ROP. Short depth intervals of missing resistivity-at-the-bit (RAB) electrical images resulted when the ROP exceeded 50 m/h. Although the overall quality of the image data is good, image data are missing in a total of 15.2% of the logged section; of this, 8.8% is in the uppermost 237 m of the borehole. Time-after-bit (TAB) logs for deep and shallow button resistivity measurements are shown in Figure **F3.** Most of the intervals were measured immediately after the borehole was drilled. However, owing to periods of long pipe connection operations, TAB values are exceptionally high over certain intervals: 416–419, 564–567, and 717–720 mbsf, where borehole breakouts are widened. Apparent abrupt temperature deviations also occur at two of the high TAB intervals. The geoVISION tool measured borehole azimuth and inclination. Hole deviation is ~2° to the north-northwest to ~400 mbsf, and then hole inclination increases steadily to 8° (toward the north). The annular pressure profile shows no indication of inflow from the formation into the borehole or obstruction of the borehole because of borehole wall collapse, which would have resulted in an increase in pressure. Also, there is no indication of pressure decreases associated with loss of circulation because of permeable formations or faults. Repeat measurements were taken in three areas of interest while pulling out of the hole. These intervals were between 335 and 377, 682 and 727, and 807 and 847 mbsf. The LWD resistivity data showed some offset

compared to the original downpass. This indicates some degradation and enlarging of the borehole over time. Inclination of the borehole also affected the quality of the repeat RAB electrical images, which exhibit an electrical artifact likely due to the tool being pressed against the borehole wall.

Hole C0019C

Available data

Hole C0019C was drilled with LWD/MWD tools. Unfortunately, because of an engineering problem the BHA, including LWD/MWD tools (geoVISION/arcVISION/TeleScope), was lost at ~120 mbsf. Therefore, only real-time data above 120 mbsf were obtained. MWD data and a limited set of LWD data (see Table T2 in the "Methods" chapter [Expedition 343/343T Scientists, 2013]) were transmitted in real time through the drilling fluid telemetry system right up until the moment of BHA disconnection. A list of available real-time data is given in Table T2 in the "Methods" chapter (Expedition 343/343T Scientists, 2013).

Depth shift

The mudline (seafloor) was determined from the drillers depth at 6928.5 mbrf in Hole C0019C. All data were converted to LWD depth below seafloor (LSF) (also referred to as mbsf) based on the mudline depth.

Logging data quality

Figure F4 shows the overview of the QC logs. The logs indicate that the borehole was drilled smoothly. Variations in downhole rotations per minute were small, indicating that the bit rotation was quite stable. The annular pressure profile shows no indication of inflow from the formation into the borehole or obstruction of the borehole because of borehole wall collapse. Also, there is no indication of pressure decreases associated with loss of circulation because of permeable formations or faults. Drilling parameters and MWD data show that the disconnection of the BHA was not a result of any abnormal conditions of the borehole or the response of the formations being drilled.

Log characterization and lithologic interpretation

Hole C0019B

Hole C0019B log units were characterized from visual inspection of gamma ray (primarily) and resistivity log responses (Fig. F5). Resistivity images were used to identify finer scale characteristics within the units. Four primary log units were defined from the variability of log responses (Figs. F5, F6, F7). Overall in the upper 820 m of the borehole, both gamma ray intensity and resistivity increase with depth. In the gamma ray log, this trend is broken by significant lows in the data (~20 gAPI lower) that occur at 168 and 535 mbsf. Resistivity in the upper 820 m of Hole C0019B ranges from 0.4 to 2.7 Ωm, and gamma ray values range from 17 to 71 gAPI.

Log Unit I (0–194.1 mbsf) is characterized by relatively low gamma ray values ranging from 17.2 to 59.6 gAPI (mean = 40.6 gAPI). This unit is also defined by a significant separation in the shallow and deep resistivity curves, with average values of 0.93 and 1.14 Ωm, respectively, which suggests that either the formation is more permeable and unconsolidated than the units beneath or the borehole is more washed out in this section. RAB images collected in this section are of lower quality because of high ROP. Therefore, because of the limited information, it is very difficult to assign an exact lithology to this unit. However, on the basis of previously drilled sites in the Japan Trench (Sacks, Suyehiro, Acton, et al., 2000), we suggest that this could relate to a less compacted siliceous (diatomaceous) mudstone (compared to the unit beneath).

Log Subunit IIa (194.1–537.2 mbsf) is defined as an interval of relatively consistent gamma ray intensity with values ranging from 31.5 to 66.5 gAPI (average = 48.7 gAPI). Resistivity values range from 0.40 to 2.32 Ωm (average = 1.36 Ωm). There appear to be two main intervals where resistivity increases with depth (an interval between the top of Subunit IIa and 363 mbsf, and an interval from ~370 to 443 mbsf), separated by a step function. Additionally, there are two negative excursions at ~340 and 370 mbsf that may relate to structural features. RAB images also show the main trends noted above as zones transitioning from darker, more conductive layers to lighter, more resistive bands. Borehole breakouts visible on RAB images disappear toward the base of this subunit (at ~470 mbsf) (see **"Structural geology and geomechanics"**).

Log Subunit IIb (537.2–820.6 mbsf) is defined at its top by an increase in gamma ray values and the reappearance of borehole breakouts in RAB images. Gamma ray values range from 21.9 to 71.1 gAPI (average = 51.6 gAPI). Overall, gamma ray intensity increases with depth in this subunit. Additionally, from 670 mbsf downhole, gamma ray values become much more varied and fluctuating (10–30 m scale fluctuations), stabilizing again at ~790 mbsf. In line with this is a steadily increasing trend in resistivity, with values ranging from 0.41 to 2.78 Ωm. Within

this subunit there is further evidence of cyclicity in the resistivity log response. Additionally, similar to Subunit IIa the occurrence of borehole breakouts becomes significantly less common near the base of this subunit (from 730 mbsf). There is also a significant conductive feature at ~720 mbsf, shown as a large negative excursion in the standard logs and a dark band in RAB images. A highly resistive band (2 m thick) at the base of this unit may correspond to another zone of interest with regard to structure and faulting (see **"Structural geology and geomechanics"**).

Comparing the gamma ray and resistivity log responses from Hole C0019B log Unit II to neighboring Ocean Drilling Program (ODP) Leg 186 Sites 1150 and 1151 ~300 km away (Sacks, Suyehiro, Acton, et al., 2000), similar values are seen in diatomaceous muds that were recovered and logged at these sites (and others including Deep Sea Drilling Project [DSDP] Leg 56 Sites 436 and 434; Shipboard Scientific Party, 1980); therefore, we may have similar lithologies in Hole C0019E over this interval. The overall pattern of increasing resistivity is in keeping with a conventional compaction trend; however, much smaller scale cycles are present in the resistivity data (see **"Physical properties and hydrogeology"**).

Log Unit III (820.6–835.9 mbsf) is defined by a significant increase in the gamma ray intensity (to ~90 gAPI). Gamma ray values remain high for 16 m before dropping sharply to ~20 gAPI. The high gamma ray values, ranging from 47.5 to 103.3 gAPI, define log Unit III (820–836 mbsf). Resistivity exhibits a decreasing trend over this unit. Such elevated gamma ray values would normally indicate a clay-rich unit (potentially a similar lithologic unit to the clay recovered from Site 436; Shipboard Scientific Party, 1980) at these depths in the borehole. RAB images also indicate a more conductive area compared to log Unit II.

Log Unit IV (835.9–850 mbsf) is characterized by a sharp decrease in gamma ray values and increase in resistivity log responses. Overall, this log unit is defined by low gamma ray values and high resistivity. Gamma ray values range from 14.6 to 45.3 gAPI (average = 25.8 gAPI) and resistivity ranges from 0.89 to 8.61 Ωm. RAB images primarily show a region of very high resistivity in layers and patches throughout this unit. A number of sharp peaks in resistivity reach a maximum of 8.61 Ωm below which resistivity decreases. With the exception of the very upper 10 m of this unit, gamma ray values are the lowest measured in the borehole. Such values (low gamma ray and high resistivity) are consistent with lithologies such as chert. The varying resistivity values shown in the log curves and RAB images may indicate some interbedding of chert and a more conductive material. Cherts were also observed below a brown clay at Site 436 (Shipboard Scientific Party, 1980).

In a cross-plot of gamma ray values and resistivity (Fig. **F6**) log Units I and II can be identified as the main grouping of points with low resistivity and low to intermediate gamma ray values. Very little difference between the two units can be seen in this plot. Log Units III and IV are easily distinguished from this main grouping. The high gamma ray values and low resistivity of log Unit III is visible on the right-hand side of the plot. Unit IV centers around 20 gAPI as resistivity increases. The log units are more easily differentiated by plotting gamma ray and resistivity data ranges on a box and whisker plot (Fig. **F7**). As previously stated, these units were primarily defined using the gamma ray data.

Hole C0019C

As noted above in **"Data and log quality,"** only real-time data were acquired in Hole C0019C. These data include total gamma radiation, annular pressure, annular temperature, ring resistivity, bit resistivity, and average shallow and deep button resistivity and were measured between ~51 and 120 mbsf. Gamma ray values range between 35 and 60 gAPI. The values show no particular trend over this short interval (Fig. **F8**); average gamma ray values slightly decrease from 70 mbsf to the base of the section. Resistivity values range from 0.4 to 1.5 Ωm with the exception of bit resistivity, which has values up to 22 Ωm; however, this exception relates to an anomalous peak in the data. Overall, the resistivity curves show very little significant variation downhole. However, two negative excursions occur at ~66 and ~77 mbsf (indicating more conductive zones), with the sharpest and largest being the latter (between 73 and 81 mbsf). Finally, annular temperature increases from 3° to 4°C at ~62.5 mbsf.

The data ranges for both gamma ray and resistivity are very similar to those encountered within log Unit I of Hole C0019B in the same depth range. However, the conductive signal observed at ~77 mbsf is not present at a similar shallow level in the resistivity data collected in the previously logged hole.

Physical properties and hydrogeology

Resistivity logs

Figure **F9** shows a comparison of the gamma ray log, five different resistivity measurements (ring; bit; and shallow, medium, and deep button resistivity), and the difference between the shallow and deep button

resistivity. Superposition of the deep, medium, and shallow button resistivity shows generally good agreement among the logs. The logs show overall increasing resistivity values from the seafloor to the base of log Unit II; smaller scale deviations from this trend will be discussed in this text. A sharp increase in resistivity at the base of log Unit II is followed by a gradual decrease through log Unit III. There is another sharp increase in resistivity at the top of log Unit IV, which then follows a series of resistivity peaks and decreasing resistivity trends to the bottom of the hole.

Systematic comparisons of the resistivity logs were made using cross-correlations. Figure **F10** shows cross-plots of shallow and deep button resistivity as well as bit and ring resistivity. Ring resistivity is generally greater than bit resistivity, and this is most evident in log Unit IV. The difference between the two measurements is ~0–5.6 Ωm for all resistivity values. Comparison of shallow and deep button measurements indicates that deep resistivity is generally higher than shallow resistivity. Zones where deep resistivity is significantly higher than shallow resistivity tend to correlate with zones of lower gamma ray values.

In log Unit I, the overall resistivity values increase from ~0.6 to 1.3 Ωm with noticeable ~100 m cycles of an increasing trend followed by a decreasing trend (arrows in Fig. **F9**). The increasing trends probably correspond to the increased compaction of sediments, whereas the decreasing trends may correspond to gradual changes in lithology. In log Unit I, the deep resistivity button values are significantly higher than those for the shallow button, possibly indicating washouts or invasion of the formation by drilling fluid. The latter case could indicate more permeable sediments. The difference between shallow and deep resistivity decreases at the log Unit I/II boundary. In log Unit I, the average difference between the two measurements is 0.22 Ωm, whereas the average difference in log Unit II is 0.16 Ωm.

In log Unit II, resistivity continues to gradually increase from ~1.3 to 1.6 Ωm, but with the presence of ~10 to ~100 m cycles of increasing trends, which are generally followed by more rapid decreasing trends (stepped/sawtooth trends). Most of the increasing trends are bounded by conductive features, commonly accompanied by upward increasing resistive intervals several meters above them. The tops of these packages, represented by a conductive peak and higher resistivity interval, are found at the top of the unit at 194–210, 260–270, 362–371, 443–457, and 523–532 mbsf. Between 640 and 720 mbsf resistivity decreases from ~1.6 to ~1.3 Ωm. Between 688 and 701 mbsf a series of lower resistivity peaks are observed. At 720 mbsf a low resistivity peak of 0.88 Ωm is observed, followed by an increasing trend of resistivity to the base of the unit. Smaller scale features can be found at other depths within log Unit II. The patterns described above could imply sediment packages of different lithologies, an overall homogeneous sediment unit cut by thrust faults (producing repeated sediment packages), or a combination of these. At its base, log Unit II includes an interval of higher resistivity (~2.14 Ωm) from 818 to 820 mbsf.

At the top of log Unit III is a 1 m wide interval of low resistivity before a higher resistivity value interval from ~821 to ~827 mbsf. Gamma radiation increases sharply at the top of this interval, followed by a gradual decrease in resistivity from 2.4 to 1.1 Ωm over the ~827 to ~836 mbsf interval (Figs. **F9, F11**).

The top of log Unit IV is marked by a sharp increase in resistivity to 4.8 Ωm, and then a decrease to 0.9 Ωm (Figs. **F9, F11**). Resistivity jumps to 7.9 Ωm at 840.3 mbsf before following a gradual decreasing trend to the base of the hole. Resistivity peaks that are a few meters thick probably correspond to chert layers (see **"Log characterization and lithologic interpretation"**). The shallow, medium, and deep button resistivities become very noisy through log Units III and IV, and the deep and shallow signals are significantly different.

Estimation of porosity from ring resistivity measurements

We calculated seawater electrical resistivity using an estimated temperature profile and used it to evaluate the formation factor from the ring resistivity (see **"Logging while drilling"** in the "Methods" chapter [Expedition 343/343T Scientists, 2013]). We estimated a temperature profile in the formation using a surface heat flow of 45 mW/m^2 and constant thermal conductivity. We assume a 1.3°C bottom water temperature and a steady-state conductive temperature profile. The estimated temperature at the bottom of the hole is 36°C (Fig. **F12**). Formation factors were then converted to estimated porosity values using Archie's law (Archie, 1942). Archie's law parameters (a = 1; m = 2.7) were constrained after core was recovered by cross-plotting discrete resistivity and porosity measurements.

Estimated porosity decreases gradually from ~70% at the top of the hole to ~43% at the top of log Unit II (Fig. **F12**). Log Unit II is marked by cyclic trends of decreasing and increasing porosity. If we assume that porosity decreases exponentially with depth because of vertical compaction (e.g., Athy, 1930), the observed cyclic trends imply the appearance of different compaction trends. These different patterns may

reflect packages of sediments with different chemical composition; alternatively, they may reflect true porosity differences related to variations in stress history, local changes in lithology, and/or the presence of fractures or faults.

At the top of log Unit III (820–823 mbsf), estimated porosity stays around 41% whereas the gamma ray values increase, possibly indicating higher clay content. Porosity sharply increases to 44% at 827 mbsf and then gradually increases to 47% at the base of the unit. The estimated porosity of the resistive layers in log Unit IV is ~20%–30%. At the base of this unit porosity is ~36%.

The estimated density log mirrors the porosity log, with values ranging from 1.55 to 1.98 g/cm^3 in the layers (probably chert) of Unit IV (Fig. **F12**).

Structural geology and geomechanics

Structural geology

Orientations of bedding and fractures

We made a major effort to interpret bedding (Fig. **F13**) and fractures accurately from borehole resistivity images. We utilized three simultaneous observers. Each pick was critically examined by this team, with classification as bed or fracture by consensus.

In the upper 275 mbsf, bedding orientations of the Hole C0019B resistivity images tend to be shallow, averaging 27° (Fig. **F14**). In the section from 275 to 820 mbsf, bedding dips average 57°. Finally, the section below 820 mbsf showed an average dip of 22°. Fractures are rare in the upper 300 mbsf and common from 300 mbsf to deeper than 800 mbsf. A zone of enhanced fracturing occurs at ~720 mbsf.

Three structural domains are defined on the basis of bedding orientation (dip) distributions: Domain 1 (upper frontal wedge, 0–275 mbsf), Domain 2 (frontal wedge core, 276–820 mbsf), and Domain 3 (frontal wedge base, 820 mbsf to base of hole). Note that Domain 1 shows sparse fractures/faults, whereas fractures/faults are more numerous in Domains 2 and 3 (Fig. **F14**). Domains 1 and 2 have logging signatures similar to the siliceous mudstone that is widespread along the Japan Trench slope (see **"Log characterization and lithologic interpretation"**). Conversely, the sediments of Domain 3 show large variations in gamma ray values and resistivity and could be interpreted as a clay-chert sequence, going downsection.

On a stereographic projection, the poles to bedding define a girdle that trends 300° (Fig. **F15A**). This girdle of bedding suggests cylindrical folding with a mean axial trend of 030°, which is ~20° northeast of a line parallel to the regional trench slope. This mean axial direction is nearly normal to the convergence direction of 292° at 93 mm/y (Argus et al., 2011). The stereographic projection of the poles to fractures shows a broader girdle; however, the trend is still to the northwest (Fig. **F15B**).

Probable major faults

Because the principal goal of Expedition 343 was to instrument the fault that caused the 2011 Tohoku-oki earthquake, there was considerable interest in finding this fault in the drilled section. Numerous fractures (and also some potential faults) were observed in the logged section. However, two zones appear to be the most probable major fault zones:

- Probable fault at 720 mbsf: at 720 mbsf, a high-conductivity zone ~1 m thick is associated with a dip transition from shallow to more steeply dipping beds and an interval of concentrated fracturing (Figs. **F16, F17A**).
- Probable fault at 820 mbsf: at 820 mbsf, a transition from steep bedding dips to dominantly shallow dips occurs just above the top of a zone of high gamma ray values (Figs. **F14, F18**). High gamma ray values below 820 mbsf are interpreted as a clay layer characteristic of the incoming oceanic plate of the North Pacific Ocean (Shipboard Scientific Party, 1980). The structural transition resembles that of a décollement and lies in the zone of layered reflectors above the basaltic oceanic crust (Fig. **F19**). The high gamma ray values decrease downsection, transitioning to a section interpreted as chert (see **"Log characterization and lithologic interpretation"**).

Geomechanics: borehole breakout analysis

Breakouts occurred over a wide depth range in Hole C0019B (e.g., Figs. **F20, F21**) and were observed in log Units I and II but were not found in log Units III (clay) or IV (chert). We counted a total of 221 breakouts. The cumulative length of all breakouts reached ~96 m, corresponding to ~11% of penetrated borehole total depth. No drilling-induced tensile fractures were observed in this borehole.

Interestingly, the breakout azimuth distribution appears different in the shallow portion of the hole compared to the deeper part (corresponding to approximately 50–537 and 537–820 mbsf, respectively) (Fig. **F21**). In the shallower portion, the breakout azimuths systematically change orientation from 060° at 70 mbsf to 180° at 140 mbsf and then change back to 135° from 140 to 200 mbsf. From 200 to 530 mbsf, breakouts are rather sporadic and their azimuths are variable. In the deeper portions of the borehole, breakouts display a strong preferred orientation of 045°.

The mean azimuth of breakouts in the deeper portion of the hole is 49° (or 229°) and the standard deviation is 23°. The mean azimuth was not calculated for the shallow portion of the hole because of the apparent progressive change in orientation. Because the borehole breakouts occur at the same azimuth as the minimum horizontal stress (S_{hmin}) but perpendicular with the maximum horizontal stress (S_{Hmax}) (see the "Methods" chapter [Expedition 343/343T Scientists, 2013]), the S_{Hmax} orientation can be interpreted as 139° ± 23° (or 319° ± 23°) in the deeper part of Hole C0019B. The stress orientation in the shallower portion is not constant. We observe a progressive change in the breakout azimuth orientation to 140 mbsf, here, where this trend terminates there is likely a discontinuity, maybe a fault. This is supported by a conductive peak in the resistivity logs. Changes in bedding dips are also consistent with the presence of a discontinuity at this depth. Breakout width ranged between ~30° and 130° over the entire hole with a mean value of ~67°.

Lithology

Seven lithologic units were recognized during examination of cores from Site C0019 (Fig. F22; Table T2). The units were differentiated on the basis of color, composition (siliciclastic, volcaniclastic, or siliceous microfossil components), grain size, and presence of minor lithologies. We also used X-ray computed tomography (CT) images to identify characteristic bioturbation and structural styles where possible for each unit. Unit boundaries were only sampled for the contacts between Units 5 and 6 and 6 and 7 because of the operational constraints and incomplete recovery. In addition, Units 1 and 2 were restricted to one and two cores respectively.

Unit 1 (slope facies or wedge sediments)

Interval: sampled from Sections 343-C0019E-1R-1 to 1R-CC, 25 cm
Depth: 176.5–185.2 mbsf
Age: undetermined

The dominant lithology of Unit 1 is medium olive-gray siliceous mudstone (Figs. F23, F24), which extends from 176.5 to 185.2 mbsf. A secondary lithology is defined by isolated, few-millimeter to 2 cm thick layers of yellowish gray ash with gradational contacts. The siliceous mudstone is dominated by abundant siliceous microfossils (diatoms, sponge spicules, and radiolarians), abundant clay- to silt-sized siliciclastic material, and includes common ash shards. Biogenic silica, terrigenous silt grains, and angular ash/glass fragments are generally 10–100 µm in size. Unit 1 also contains decimeter-spaced, millimeter to centimeter thick, dark gray to black laminae that are locally laterally discontinuous. Smear slide observations indicate that the composition is 22%–70% biogenic silica, 0%–45% siliciclastic mineral grains, and 10%–33% volcanic ash.

Light yellowish gray to light olive-gray ash with 60%–97% volcaniclastic grains is a secondary lithology within Unit 1 (Figs. F23, F24). Ash occurs in several centimeter-thick wavy layers or discontinuous elongate patches up to a few centimeters long with interfingering and gradational boundaries with surrounding siliceous mud. The edges of ash-rich layers are mixed with the adjacent siliceous mudstone and contain many burrows, suggesting they have been preferentially bioturbated. Ash layers typically appear brighter in X-ray CT images than the surrounding siliceous mudstone. The mudstone adjacent to ash layers is generally darker gray than surrounding mudstone.

Three bulk mudstone samples (177, 183, and 185 mbsf) were analyzed with X-ray diffraction (XRD), and qualitative mineral mode by weight was estimated (see "Lithology" in the "Methods" chapter [Expedition 343/343T Scientists, 2013]). The three samples gave nearly identical results: ~¾ total clay, <¼ quartz, <¼ plagioclase, and negligible calcite. This analysis is approximate due to the limitations of the method and does not include estimation of other phases, including amorphous volcanic ash, opaline silica, and accessory minerals. Mineral grains may be part of the siliciclastic fraction, but volcanic ash is also a potential contributor, so these estimates are not directly comparable to the grain component estimates from smear slide observations.

Subrounded pumice clasts (<<1%) up to 4 mm in diameter are sporadically distributed throughout Unit 1 (Fig. F23). These clasts are white-gray and very friable (easily crushed and smeared when the core was split with a wire). Pumice fragments occur in isolation, concentrated (locally up to 5%) in short intervals, or in pod-shaped clusters (probably relict fragments from the in situ weathering of larger clasts) with a mantle of darker gray mudstone.

No obvious burrows were observed on the split core surface, but subtle mottling and patches of different color ranging from olive-brown to dark gray are common. The mottled areas commonly obliterate the primary layering and correspond to areas where discontinuous tubular structures on a range of scales, interpreted as burrows, are identified in X-ray CT images. Burrows are subhorizontal to vertical and filled with material either slightly brighter or slightly darker in the X-ray CT image than the surrounding siliceous mudstone. Cross sections of the burrows observed in the X-ray CT image are round to ellipti-

cal. Smaller burrows that are very bright in the X-ray CT image are common throughout Unit 1. These 0.5–1 mm wide traces follow circuitous, random paths through the mud and concentrate within the traces of the larger burrows. They also form useful one-dimensional offset markers for identifying shear surfaces (see **"Structural geology"**).

The origin of Unit 1 material is difficult to determine because siliceous mudstone is widespread along the Japan Trench slope, both seaward and landward of the trench (see DSDP Leg 56/57 [Scientific Party, 1980]), and we did not observe the nature of the boundaries of this unit. This unit is therefore interpreted as representing either the upper part of wedge sediments or as slightly compacted and deformed forearc slope deposits.

The abundant volcaniclastic material probably originates from the volcanic arc associated with the Japan Trench subduction system, but any further interpretation of its significance will require dating of the volcaniclastic component (by geochemical correlation to ash stratigraphy already established throughout Japan).

Only one core has been sampled from this unit, therefore its upper and lower boundaries cannot be established. It has been differentiated from Unit 2 on the basis of contrasting color, grain size, siliceous material content, and other macroscopic features.

Unit 2 (brown and bluish gray mudstone)

Interval: sampled from Sections 343-C0019E-2R-1 through 3R-CC
Depth: 648.0–659.7 mbsf
Age: undetermined

Unit 2 comprises bluish gray and grayish brown ashy mudstone and extends throughout 648.0–659.7 mbsf (equivalent to Cores 343-C0019E-2R and 3R). This interval is characterized by good recovery but pervasive drilling- or recovery-induced brecciation. As a result, the two lithologies within Unit 2 are represented primarily by a few 5–20 cm clasts and biscuits with rounded ends (Fig. **F25**). The relative proportion of the two main lithologies was not measured because they were represented by so little intact core. The remainder of the recovered material was in ~1 cm to sand-sized cuttings. In Core 2R, the drilling breccia was sorted with the coarsest particles in the center axis of the core liner, gradually fining to the outside. In Core 3R, the different sizes of cuttings were well-mixed with no sorting trends noted. No sorting is apparent between lithologies, with roughly equal proportions of each throughout the cores.

The bluish gray ashy mudstone contains abundant siliciclastic grains (50%–55%) with common to abundant volcaniclastic (30%–35%) and common biogenic components (10%). Overall, this ashy mudstone has a speckled gray/black appearance at the grain scale. Paler areas where the dark grains are absent define mottled patches. Rare elliptical, pale gray patches correspond to worm burrows. Thin (1–2 mm), black, discontinuous laminations are interbedded in the mudstone. Semiquantitative analysis of bulk powder XRD spectra showed the bluish gray ashy mudstone contains ~¾ clay, <¼ quartz, <¼ plagioclase, and negligible calcite.

The grayish brown ashy mudstone is fossiliferous and contains dominant siliciclastic grains (60%–70%, with silt slightly more abundant than clay) and common volcaniclastic grains (~25%–30%) with biogenic fragments present and occasionally common (2%–10%). All components are fine grained (<63 µm). Semiquantitative XRD interpretation suggests the grayish brown ashy mudstone is composed of ~¾ clay, <¼ quartz, <¼ plagioclase, and negligible calcite. Bedding is poorly defined and both calcite-cemented burrows and mud-filled burrows indicate extensive bioturbation. Macrofossils are mostly disaggregated fragments (undifferentiated), but two whole gastropod shells were observed. Calcite cement occurs in irregular patches that may correspond to brighter X-ray CT areas compared to noncemented areas. In the X-ray CT images, the calcite cement patches are weakly aligned.

Cuttings are predominantly composed of the two main lithologies. The reddish brown ashy mudstone cuttings are angular to subangular, and the bluish gray cuttings are subangular to subrounded. Possible sublithologies identified from isolated fragments within the cuttings only included carbonate veins and a medium-pale gray ashy mudstone.

The mixing of gray and brown mudstone throughout the recovered drilling breccia in Cores 343-C0019E-2R and 3R may indicate that Unit 2 is composed of repetitive interbeds of the two lithologies. The overall scarcity of biogenic components in the two lithologies differentiates Unit 2 from Unit 1 (in which biogenic microfossils are abundant). Silt in Unit 2 indicates a relatively proximal sediment source. Macrofossils suggest a shallow depositional environment compared to the trench axis.

Unit 3 (gray mudstone)

Interval: sampled from Section 343-C0019E-4R-1 through Core 16R
Depth: 688.5–820.1 mbsf
Age: undetermined

Unit 3 consists of four dominant lithologies (Fig. F26):

1. Olive-brown-gray ashy mudstone,
2. Dark gray mudstone with black interlayers,
3. Clay-rich mudstone, and
4. Dark gray mudstone with abundant pyrite.

These units are interbedded on the meter scale with occasional centimeter-scale interlayers and intermittent centimeter-scale secondary clay and silt beds. All lithologies are dominated by siliciclastic material and contain trace or present siliceous microfossils and fossil fragments, with rare horizons containing up to 15% siliceous fragments. Ash is abundant in the ashy mudstone, but otherwise ash layers are rare, and ash content decreases significantly downhole below the ashy mudstone. XRD data show the overall quartz, feldspar, and clay content of Unit 3 is generally consistent throughout the section, except for discrete clay and silt beds. Unit 3 has a much higher component of siliciclastic material and a lesser component of volcanic and siliceous grains than Unit 1. Unit 3 contains none of the red to red-brown and bluish gray mudstone of Unit 2.

The dominant lithology in Unit 3 consists of a dark gray to black fine-grained mudstone with bedding defined by thin interlayers of black, very fine grained clay-rich laminations (Figs. F26A, F27A). Siliclastic material (>70%) is dominant, with common volcaniclastic (≤30%) and common or present siliceous material (≤15%). Dark gray to black laminations are common, are often wavy, and have laterally variable thickness. Discontinuous beds and clay lenses indicate soft-sediment deformation. The mudstone is commonly strongly mottled, with mixing of gray and black materials. Ash-rich layers are rare, and isolated pumice clasts are present.

The ashy mudstone is greenish gray to black, ultrafine-grained, and laminated and contains dominant siliciclastic (≤70%), abundant volcaniclastic (10%–45%), and common siliceous components (Figs. F26B, F27B). Grain size is characterized by approximately equal clay-sized (50%–60%) and silt-sized (40%–50%) fractions, with silt occurring as black and colorless grains. Bedding is defined by medium gray to black compositional bands consisting of dominant siliclastic (70%) and volcaniclastic (30%) grains, with trace siliceous microfossil grains. Laminations range from submillimeter to several millimeters thickness and locally contain discontinuous lenses of pyrite. These layers frequently occur as streaky or wavy laminae. Thin, planar, coherent, laminated beds are present but less common. Mottled areas, rare elliptical black smudgy patches, and submillimeter gray mottling are common. Ashy mudstone includes light greenish gray claystone (>90% clay) and occasional sandy horizons, trace pumice fragments, and occasional pyrite in burrows.

Pyrite-rich mudstone has a similar composition to the dominant mudstone but with abundant black, elliptical, occasionally pyrite-bearing dark spots and numerous pyritized burrows and pyritized laminations (Fig. F26C). The elliptical spots have aligned long axes parallel to bedding where bedding is represented by laminations and define the layering where laminations are absent.

Clay-rich mudstone is the least common of the lithologies, occurring predominantly in Cores 343-C0019E-7R and 8R (Fig. F26D). Clay-rich mudstone is very similar to the dark mudstone (described above), with >70% siliciclastic material, <30% volcaniclastic material, and a minor siliceous component. Of the siliciclastic material, >90% is clay.

Unit 3 reflects a more terrigenous environment of accumulation than Units 1 and 2. Unit 3 accumulated at a time of lesser siliceous microfossils accumulation and increased distance from, or lesser activity of, volcanic sources.

Unit 4 (sheared clay)

Interval: sampled from Core 343-C0019E-17R
Depth: 821.5–822.5 mbsf
Age: undetermined

Unit 4 was sampled only in one 97 cm long core (Section 343-C0019E-17R-1) and mostly consists of strongly deformed clays (Figs. F28, F29). The clay is pervasively sheared, forming sharp, strongly aligned phacoids with polished, striated surfaces, defining a scaly fabric (see **"Structural geology"** for a description). From visual inspection and smear slide analysis we can recognize two main components: (1) red-brown clay and (2) dark brown to black clay. At the top of the core, 0.5–4 cm bands of the two clays are intercalated. A clast of gray mudstone (length = 13 cm) is enclosed inside the clay. Downhole from the mudstone interval, dark brown to black clay is dominant.

Smear slide analysis suggests that the red-brown clay is composed predominantly of clay minerals, with rare coarser grains and vitric grains, whereas the dark clay is composed mainly of dark brown clay minerals mixed with dark grains (probably Fe or Mn oxides/hydroxides). The specific clay phases in either clay were not identified by shipboard XRD analysis. However, the composite clay peak (at 19.4°–20.4°2θ) shape changes in Core 343-C0019E-17R compared to the surrounding mudrock, suggesting the clay composition in this layer is distinct (Fig. F30). This is supported by X-ray fluorescence (XRF) major element analyses that show Core 17R is relatively rich

in aluminum, potassium, and manganese but relatively depleted in calcium and sodium (Fig. F29).

The black clay and red-brown clay are intermixed in the predominantly black clay regions. Red-brown clay boundaries in these regions are sharp but do not correspond to phacoid boundaries. Red clay patches vary from submillimeter to centimeter size. Smearing of the red-brown component along the shearing scaly fabric surfaces is common. In one place, a clast of dark material surrounded by a thin rim (<1 mm) of red-brown material was observed, suggesting a diagenetic origin. The contrast in X-ray CT images between clasts of red-brown and black clay is negligible. In the split core we observed phacoids of fractured black material with a metallic luster just above the interval of high magnetic susceptibility identified by the whole-round multisensor core logger (MSCL-W).

The 13 cm long mudstone clast is composed predominantly of siliceous minerals; volcaniclastic grains and biogenic grains are also present. The boundaries between the clay and the mudstone clasts have probably been reworked during drilling, so it is not possible to directly observe the bounding surface; however, no evidence was found of a sedimentary transition to the surrounding clay.

Unit 5 (brown mudstone)

Interval: sampled from Sections 343-C0019E-18R-1 through 20R-2
Depth: 824–832.9 mbsf
Age: undetermined

Unit 5 is a yellowish to grayish brown mudstone composed of dominant (>85%) siliciclastic grains, minor (5%–10%) volcaniclastic grains, and trace (0%–5%) siliceous microfossils (radiolarians) (Fig. F31). The siliciclastic component of the rock is predominantly clayey in the upper part of the unit (Sections 343-C0019E-18R-1, 18R-CC, and 19R-1; >60% clay and <40% silt) and becomes siltier in the lower part (Sections 343-C0019E-19R-1 and 19R-2; <60% clay and >40% silt) with trace sand (≤3%). Elongate lenses of various colors of mudstone characterize Unit 5. Grayish brown, dark gray-brown, yellowish brown, and red-brown lenses occur in a discontinuous matrix of pale brown mudstone with abundant black silt grains that are likely manganese minerals. Bedding is commonly indistinct but is loosely defined by the alignment of the long axes of the elliptical lenses of all colors. Dark silty beds are commonly concentrated in laterally discontinuous horizons. In addition, centimeter-scale clay interbeds are present in which clay is dominant. Decimeter-scale fining-upward sequences from a basal, silty, manganese-rich mudstone to a more homogeneous clay-rich mudstone occur frequently in the lower 5 m of Unit 5. Irregular, white, sugary-textured patches of ash ≤1 cm thick are present throughout the unit. Burrows and mottling from bioturbation are common throughout the unit. Biogenic material is rare, and discrete ash layers and pumice fragments are common. The overall nature of the unit indicates a significant influx of siliciclastic and terrigenous material to the section, dominating over the biogenic source.

The contact with Unit 6 at the base of Unit 5 is most likely stratigraphic. As Units 6 and 7 represent the incoming plate sediments (see "Discussion"), Unit 5 also likely represents the underthrust incoming plate.

Unit 6 (pelagic clay)

Interval: sampled from Cores 343-C0019E-20R and 21R
Depth: 832.9–833.5 mbsf
Age: undetermined

The lower 60 cm of Core 343-C0019E-20R (interval 20R-2, 53–114 cm) consists of centimeter-scale laminar, dark brown, yellow, pink, and green clays, with occasional white laminae (Fig. F28A). Unit 6 consists of >90% siliclastic grains, with trace volcaniclastic grains and siliceous microfossils. Diatoms are not observed in this interval; however, radiolarians are present. More than 75% of the material falls in the clay-size fraction. Some grain boundaries show evidence of siliceous mineralization. The clay contains minor amounts of pyrite and/or manganese oxides and possible zeolites. The unit is poorly lithified and was muddy when the core was split. The bottom section consists of green to light green clays and gradationally transforms into chert (Unit 7). Radiolarian molds are present in the basal section of Unit 6.

Unit 6 is interpreted as pelagic clay accumulated on the incoming Pacific plate. Similarity in color and lamination to that observed in the underlying cherts and the intermixing of clay and chert observed in Cores 343-C0019E-20R and 21R suggest that the underlying chert is formed by silicification of the clay. The transition from pelagic clays in Unit 6 to chert in Unit 7 is indicated by the presence of chert nodules and intercalated chert layers within Unit 6, suggesting the transition is a diagenetic front.

Unit 7 (chert)

Interval: Cores 343-C0019E-20R and 21R
Depth: 833.5–836.8 mbsf
Age: undetermined

Yellow-brown and chocolate-brown laminar chert was recovered as fragments at the base of Core 343-

C0019E-20R and in Core 21R, corresponding to 833–847 mbsf (Fig. F28B). Yellow-brown chert consists of millimeter- to submillimeter-scale laminae of light yellow-brown (5Y 7/2) and dark yellow-brown (5Y 6/3) chert with occasional translucent subcentimeter-scale bands of amber (10YR 5/6) chert.

The chert fragments in Core 20R occur in the lowermost 3 cm of Section 20R-2 (interval 115–118 cm) as well as in the 8 cm recovered in the core catcher. The fragments in Section 20R-2 occur directly below a predominantly intact interval (20R-2, 103–105 cm, see Fig. F28A) of layered grayish yellow to greenish yellow clay. The chert fragments in Core 21R occur in the lowermost 8 cm of Section 21R-1 (interval 22–30 cm) as well as the 17 cm recovered in the core catcher. The uppermost 22 cm of Section 21R-1 is composed of brown and dark gray to black mudstone fragments, which are interpreted to be fragments of Units 2 and 3 that fell to the bottom of the borehole and were recovered in our last core.

The chert found in Cores 20R and 21R is interpreted to represent a silicification of the laminated pelagic clays recovered in Core 20R. This unit is correlated to the chert recovered in the incoming Pacific plate by DSDP Leg 56 Site 436 (Shipboard Scientific Party, 1980). Similar to Leg 56, the fine-scale laminations within in the chert represent the only primary sedimentary structures, implying minimal transport and reworking of the clays prior to silicification.

Discussion

Correlation of lithologic units to Site 436

Site 436 is located off Northern Honshu and represents the most proximal drilling site that can be used as a reference for the section cored at Site C0019 (Shipboard Scientific Party, 1980). Site 436 consists of three lithologic units: Unit 1, vitric diatomaceous silty clay and claystone; Unit 2, radiolarian diatomaceous claystone; and Unit 3, pelagic clay with chert and porcellanite.

Site 436 Units 1 and 2 are lithologically similar to Site C0019 Units 1–3, which comprise mudstone, siliceous mudstone, and locally ashy mudstone. This lithologic description is very general and does not necessarily imply a direct correlation between the units in Hole C0019E and the incoming plate strata. Site C0019 Units 4, 5, 6, and 7 correlate to Site 436 Unit 3, with direct matches between the brown clay at Site 436 and the multicolored clays and the chert at Site C0019. For example, chert in Site C0019 Units 6 and 7 closely resembles descriptions of chert at 378.5–397.5 mbsf at Site 436, in which scarce Albian–Cenomanian radiolarians indicate a Cretaceous depositional age (Shipboard Scientific Party, 1980). However, an equivalent of Site C0019 Unit 5 (brown mudstone) was not identified in Site 436 Unit 3. At Site C0019, the significant silt component, bioturbation, and volcaniclastic content of Unit 5 suggest a proximal terrigenous source compared to Unit 6. The lithology of Site C0019 Unit 5 could represent a stratigraphic variation between the two holes or could be structurally emplaced from the upper plate at Site C0019. The former interpretation is favored because of the absence of a sheared basal contact of Unit 5 at Site C0019.

Structural geology

Several diverse structures were recognized in the cores. This section leads off with a general description of the different structures. More specific details of those structures relevant to specific units are summarized below. Bedding was identified based on distinct changes (mostly centimeter scale) in lithology in the core or as coherent packages of layered bright and dark bands in X-ray CT images. Structures were classified as faults, normal faults, shear fractures, dark seams, dark bands, fissility, and sediment-filled veins. Faults are planar to curviplanar features that truncate and offset bedding or burrows. Dark seams are planar to curviplanar surfaces <1 mm thick marked by the presence of dark material, which is commonly bright in X-ray CT images relative to the host rock. Dark bands are tabular or curviplanar to irregular in thickness, are thicker than dark seams, and range up to 2–3 mm along their length. Drilling-induced damage is common throughout the core, manifesting as breccias, fractures, and biscuits.

Unit 1 (slope sediments)

Interval: sampled from Sections 343-C0019E-1R-1 to 1R-CC, 25 cm
Depth: 176.5–185.2 mbsf
Age: undetermined

Structures in lithologic Unit 1 were identified in both halves of the core and X-ray CT images where possible, though many features apparent in X-ray CT images could not be identified in the core.

Bedding orientations in Unit 1 were measured from two locations in the core and two additional locations using X-ray CT images. Average bedding dip is 30° ± 3° (Fig. F32). Appropriate paleomagnetic data to correct bedding strike to true azimuths were not obtained.

Some faults are visible in both the core and X-ray CT images (Fig. F33), but more commonly they are only observed in X-ray CT images. In the core, faults are narrow (few millimeters thick) zones of deformed

sediment with similar composition to the adjacent rock. In X-ray CT images, faults appear as tabular zones of bright material several millimeters thick. Recognized fault surfaces are polished and display slickenlines defined by aligned clay particles, which are correlated to bright surfaces in X-ray CT images. Of 10 mapped faults in this unit, all are dip-slip. Three are normal faults, and the shear sense of the others was not determined. Fault dip averages 69° ± 8°, ranging from 55° to 81°. Measured offsets are on the order of 1 cm, but several faults have offsets greater than the diameter of the core.

Sediment-filled veins clustered in isolated intervals and were also identified from X-ray CT images. They form closely spaced, 0.5–1 mm thick bands that appear brighter in X-ray CT images than the surrounding siliceous mudstone. In this unit some of these fractures offset bedding and worm burrows by up to a few millimeters.

Drilling-induced open fractures exploited existing faults, bedding planes, or other planes of material contrast within the core, and also occurred at random orientations. Biscuits were identified at places where the core was broken in a horizontal plane (perpendicular to core axis), minor breccia or soft (presumably remobilized) mud was observed within the break, and the bedding dip direction changed across the interval.

Unit 2 (wedge sediments)

Interval: sampled from Sections 343-C0019E-2R-1 through 3R-CC
Depth: 648.0–659.7 mbsf
Age: undetermined

Cores 343-C0019E-2R and 3R are completely made up of drilling-induced breccia (Fig. **F34**); therefore, in Unit 2 we only have measured bedding and structural features on three small pieces of intact rock, representing two different lithologies.

Structures in Unit 2 were identified in both halves of the core and in X-ray CT images where possible. The single probable bedding orientation measured (dip = 3°) is marked by a dark band that gradually darkens toward the top of the core. Additionally, five dip-slip faults were identified. Some were recognized in X-ray CT images as bright surfaces cutting burrows and were then located and measured in the core. Of these, faults cutting the grayish brown mudstone in Core 2R are coated by thin veins (<1 mm) of calcite. We identified a normal sense of shear on one fault on the basis of stepped striae. Two dark seams cut one of the calcite-veined faults with <1 mm displacement and truncate a burrow; they have been tentatively interpreted as possible pressure-solution seams, but might accommodate small shear displacement. Thin en echelon bands of dark material are interpreted as sediment-filled veins.

Unit 3 (wedge sediments)

Interval: sampled from Section 343-C0019E-4R-1 through Core 16R
Depth: 688.5–820.1 mbsf
Age: undetermined

The upper surface of Unit 3 was not observed. Unit 3 terminates at its base against the highly sheared clays of Unit 4, although the contact was not present in the core. The contact surface must lie within the 1.5 m interval that was not recovered between Cores 343-C0019E-16R and 17R.

Structures in Unit 3 were identified in the cores and X-ray CT images. The main structural features in Unit 3 are inclined bedding and fissility, dark seams, dark bands, fractures, brecciated zones, and faults/fault zones.

Bedding and fissility

Bedding is defined by parallel pale or dark laminations and compositional layering in the mudstone (Fig. **F34A**). Bedding may manifest as changes in brightness or may not be distinct in X-ray CT images (Fig. **F34B**). Bedding dips vary between 3° and 86° (Fig. **F32**). Locally, fissility is observed parallel to bedding, possibly opened because of drilling or unloading.

Although bedding dip is highly variable, some patterns are found in particular intervals (Fig. **F32**). In the interval between ~690 and ~725 mbsf, dips average 37° ± 20° and are variable through the entire interval. From ~770 to 790 mbsf, steeper dips dominate, including some potentially overturned intervals with very steep dips (average = 65° ± 15°). From ~800 mbsf to the base of the unit at ~820 mbsf, moderate dips dominate (average = 40° ± 12°).

Dark seams and dark bands

Some dark seams in this unit are anastomosing (Fig. **F35**). When arranged in sufficient density, these networks may form dark bands. On X-ray CT images, many dark seams and dark bands are marked by bright seams and bright bands, respectively, but a few dark bands do not display contrast in X-ray CT images. Dark seams and dark bands show offsets commonly less than a few millimeters and might truncate burrows, mottled textural features, sedimentary layering in the mudstone, and other dark seams and bands. Drilling-induced fractures forming striated surfaces exploit many of the dark bands and seams. In some X-ray CT images, the brightness of

the host rock changes across bright seams or bright bands, suggesting a lithologic contrast caused by displacement along seams or bands. In the middle part of this unit (Cores 343-C0019E-9R and 10R), dark bands locally contain visible (>100 µm) ellipsoidal to elongate pyrite aggregates, whereas toward the base of the unit, pyrite occurs within burrow-fill (see **"Unit 3 (gray mudstone)"** for more detail).

Truncation/offset relationships and X-ray CT brightness properties of dark seams in this unit suggest they are likely solution surfaces and/or very thin shear surfaces. Dark bands are typically shear surfaces, but may also rarely be bedding or bedding-parallel shear surfaces. In most cases, shear-related surfaces can be distinguished from bedding laminae because sheared bedding or dark bands have sharper, more planar boundaries, offset burrows observed in X-ray CT images, and are not parallel to bedding features.

Bright band near the H_2 concentration maximum

At 697.2 mbsf, the X-ray CT image displays an ~2–7 mm thick bright band that dips 10° with respect to a horizontal plane (Fig. **F36**). The CT numbers of the bright band range from 1406 to 1875, whereas those of surrounding material range between ~1200 and ~1300. These high X-ray CT numbers indicate relatively high bulk density (i.e., more compacted material) or relatively high concentration of elements of high atomic number in the bright band (e.g., concentration of Fe-rich minerals). The section above the bright band shows an inclined fissility in homogeneous sediment, whereas fissility is absent in the section below, which is distinctively mottled. During Expedition 343, the bright band was only described using the X-ray CT image because the interval including this band was taken as a structure whole-round sample for postcruise research.

The interval including the bright band is close to the location of an H_2 anomaly at 697.9 mbsf that may have been generated by recent faulting (see **"Geochemistry"**). Although it is possible that the bright band is similar to dark bands commonly seen in Unit 3, apparent changes in lithology and orientation across the bright band lead us to the other interpretation that the bright band is a localized slip zone.

Fault zone

Over a 27 cm depth interval centered around 719.85 mbsf, beds are truncated and crosscut by a 15 cm wide, 60° dipping zone of deformed rock. Narrow (<15 mm), anastomosing strands are located at the upper and lower edges of the zone. The rock in between these strands is darker in X-ray CT images, contains multiple narrow shear surfaces, and lacks coherent bedding, indicating the entire interval is deformed.

From 719 to 725 mbsf, the mudstone is broken into angular fragments, ranging from 1 to 10 cm in diameter, along sets of inclined fractures that may be parallel to, or exploit, dark seams (Fig. **F37**). The fractures are commonly polished and slickenlined and sharply cut burrows, mottled texture, and compositional layering in the mudstone. Downdip plunging, stepped slickensides on slip surfaces indicate a reverse sense of motion with respect to the horizontal plane. Bedding dips abruptly increase in the fault zone. This pattern of dip changes, if attributed to drag along the fault, also is consistent with a reverse shear sense. From 721.5 to 725 mbsf, brecciated zones with millimeter-scale clasts are common in the fractured mudstone. The intervals dominated by brecciated material are 10–30 cm thick and show heterogeneous distribution.

On the basis of the above features, we identify the fractured and brecciated interval between 719 and 725 mbsf as a fault zone. The location of this fault zone is well correlated with the interval of low resistivity identified from LWD (see **"Logging while drilling"**). No H_2 anomaly was reported from gas chemistry analysis in this interval (**"Geochemistry"**). As cores were not recovered below 725 mbsf, the base of this fault zone cannot be identified.

Sediment-filled veins

Core 343-C0019R-13R contains arrays of submillimeter-thick sediment-filled veins with lengths of 1–2 cm, in en echelon arrangement. These arrays are generally perpendicular to sedimentary layering (Fig. **F38**).

Younging indicators

Evidence of younging could not be identified within most of the sedimentary sequence composing Unit 3. But Cores 343-C0019E-13R and 14R have sedimentary contacts between fine- and coarse-grained, <5 cm thick beds that are either sharp or gradational. If the beds are normally graded, these beds young downcore in Core 13R, whereas they young upcore in Core 14R. In this case, younging reversals suggest the presence of an overturned syncline or rotated beds associated with faulting or slumping.

Tectonic fractures reactivated during drilling

The entire suite of cores making up this unit is variably dissected by open fractures that divide the rock into angular fragments. The open surfaces are com-

monly decorated by millimeter-scale striations. It is common for these striations to trend approximately downdip. In rare cases, evidence indicates that these fractures have opened along tectonic discontinuities. For example, in interval 343-C0019E-13R-1, 26–30 cm, an open fracture offsets bedding by 2 mm in a reverse sense. The fracture surface appears to have both 0.5 cm wavelength and amplitude ridges plunging downdip and millimeter-scale striations. It is inferred the former are tectonic, whereas the latter were developed during drilling. Open fractures that display millimeter-scale offsets commonly gently undulate, with wavelength >5 cm and amplitude ~0.5 mm.

Unit 4 (sheared clay)

Interval: sampled from Core 343-C0019E-17R
Depth: 821.5–822.5 mbsf
Age: undetermined

Unit 4 is equivalent to Core 343-C0019E-17R (Fig. F39). Structures in Unit 4 were identified by observation of the whole-round and X-ray CT images. Most of the core is composed of clay with a variably intense scaly fabric. The scaly fabric is defined by polished lustrous surfaces, commonly striated, enclosing narrow, variably shaped and sized lenses of less fissile material, termed phacoids. There is also an interval of cohesive mudstone with sheared boundaries, between 22 and 35 cm below the top of the section. Several 0.5–4 cm thick bands of red-brown and dark brown to black clay alternate at the top of the core. Downhole from the mudstone interval, dark brown and black clay are dominant (Fig. F39). The red-brown material includes patches of the dark brown material, and vice versa. Within each of these materials, patches have sharp edges, sometimes corresponding with the shear surfaces defining phacoids.

The long axes of the phacoids define the dominant pervasive foliation. In any observation section (e.g., axial, coronal, or sagittal) the phacoids appear to be bounded by two predominant orientations of surfaces, but locally in the coronal section one orientation predominates. In the uppermost 22 cm of the core, phacoids viewed in the sagittal section locally have asymmetric geometry, suggesting reverse shear sense (Fig. F40). Phacoid boundaries cannot be discerned in the X-ray CT image because the polished surfaces are too thin compared to the resolution of the X-ray CT image (~0.188 mm). The orientation of phacoid long axes is consistent at all scales, but smaller phacoids have a lower aspect ratio.

In general, the fabric gradually becomes less intense downcore and phacoids become larger, with one relatively abrupt increase in phacoid size. However, more intense fabric is present in some discrete intervals also at the bottom of the core. The scaly fabric is generally slightly more intense in the red-brown clay than in the dark brown and black clay.

The most intense scaly fabric is observed between 0 and 20 cm inside the red-brown clay where aligned platy (short axis <1 mm) phacoids define the foliation. Within this interval, a sharp curviplanar contact separates the predominantly red-brown from predominantly dark brown to black intervals. This contact is slightly wavy at the centimeter scale (amplitude <1 mm) and has no thickness; the foliation on either side is continuous up to the contact and is truncated against the contact, without deflecting. Just above the contact, the foliation forms ~2–3 cm asymmetric folds that are cut by the contact.

On either side of the mudstone interval (20–22 and 35–40 cm), intermediate grayish brown material is observed close to the mudstone. Above and below the mudstone, the foliation orientation in the intermediate material is different to that in the adjacent rock and changes orientation across a nonplanar contact. Twisting of the clay fabric is observed along the boundaries of the relatively competent mudstone. This is likely related to reworking of the fabric during drilling.

The mudstone interval includes three major sets of intersecting dark seams, some of which offset each other by a few millimeters. The major dark seams are subparallel to the bounding surfaces of lozenges in the mudstone clasts (most obvious in split working half, as illustrated in the structure tracing; Fig. F40).

Below 49 cm, the scaly fabric intensity decreases markedly across a transition zone of ~1 cm. Above this contact, the long axis of the phacoids averages ~8 mm long. Below the contact, less deformed lenses (5–30 mm long) of dark brown clay containing a weak foliation are present. More intensely deformed bands of black clay containing smaller phacoids surround these lenses.

Interpretation

Unlike the other units in Hole C0019E, in Unit 4 the primary bedding has been completely destroyed by the shear deformation that formed the scaly fabric. Black and red-brown clays are complexly intermixed and displaced along sets of shear surfaces. Structures formed during at least two stages of deformation have been observed, with the scaly fabric (Stage 1) being locally crenulated and cut by shear surfaces (Stage 2). Less intense scaly fabric has also been observed in discrete intervals at the top of Unit 5 (maximum thickness = 10 cm). Therefore, Unit 4 has been interpreted as the most deformed within the cored

interval. The section has not been oriented, but dominance of one orientation of phacoid-bounding surfaces in the coronal section (defining a less asymmetric fabric than that observed in other sections) suggests this section may be perpendicular to the dominant shear direction in the rock. The asymmetry of the fabric is consistent with reverse shear sense.

The fabric of three sets of intersecting dark bands in the mudstone interval is similar to that observed within Unit 3 in Core 343-C0019E-15R, whereas the fracture sets appear similar to that opened during drilling in the top of Unit 5 (Cores 18R and 19R). It is not clear which of these two units is a better candidate for correlation. The structures within the mudstone interval may have developed during shearing of the whole unit. Alternatively, since similar structures are observed in Units 3 and 5, they could predate the incorporation of the clast inside the shear zone as a tectonic lens.

Bedding dips change abruptly across the interval of scaly clay in Unit 4; the sediments above show moderate dips whereas those below are subhorizontal (Fig. **F32**), consistent with the abrupt change in bedding dips identified by LWD borehole image analysis (see **"Logging while drilling"**). We interpret that the sheared clay interval at 821.5–822.5 mbsf represents the plate boundary décollement zone. Recovery of Core 17R was not sufficient to identify the upper and lower boundaries of the décollement zone. If intervals not recovered during drilling from Cores 16R through 18R comprised sheared clay, the maximum thickness of the décollement zone could be 4.86 m. The décollement zone beneath the toe of the frontal prism at Site C0019 is localized in pelagic clay and is remarkably thinner than the few tens of meters thick décollement zones in other subduction zones such as Nankai and Barbados (Maltman et al., 1997; Moore et al., 2001).

Unit 5 (underthrust sediments)

Interval: sampled from Sections 343-C0019E-18R-1 through 20R-2
Depth: 824–832.9 mbsf
Age: undetermined

The rock type of this unit is brown silty clayey mudstone (see **"Lithology"**). Bedding is poorly defined, except by rare patches of discontinuous, dark mudstone. The unit is extensively bioturbated on the millimeter to centimeter scale. In places, discrete burrows can be recognized, but elsewhere there has been complete disruption of bedding.

Overall, the unit is mostly homogeneous, although it has been traversed by shear fractures and, locally, dark bands are present. These brittle deformation features are observed in the core face as well as in X-ray CT images.

Bedding

Compositional layering in brown silty clayey mudstone with dark elongated patches of dark particles (tentatively identified as Mn oxide nodules) identifies the bedding. However, the orientation is not clear in the core face. Evidence of burrows in the X-ray CT image suggests extensive bioturbation may be responsible for destruction of bedding. However, the sedimentary contact at the base of this unit dips 7°, similar to the few observed stratigraphic contacts within the unit (bottom of Fig. **F41**). Locally, burrows observed on the cut core face are apparently sheared (parallel elongation and increase of aspect ratio; see **"Shear surfaces"** below).

Weak scaly fabric

Within the unit we observed discrete zones with particularly high density of fractures. Weak, poorly defined scaly fabrics are suggested by intersecting fracture networks toward the top of this unit. The maximum thickness of any individual zone containing these incipient scaly fabrics is <10 cm.

Dark seams

Dark seams in this unit are planar and appear bright on the X-ray CT images. In some locations, dark seams cut burrows in the mudstone at a low angle. X-ray CT images show subtle changes in brightness across the bright bands, indicating lithologic contrasts across the bands. Therefore, we tentatively identify the dark seams as localized shear zones, deformation bands, or healed faults.

Shear surfaces

Shear surfaces are planar discontinuities oriented oblique to the bedding plane. They are not uniformly distributed. Visual observations on the core face indicate that shear surfaces are concentrated in distinct zones from 827.2 to 827.5 mbsf. Such zones are more dominant toward the lower part of this unit, where the bands form anastomosing networks around elliptical pods, which may be primary sedimentary structures or burrows (top of Fig. **F41**). These dip between 31° and 62°, averaging ~45°.

Units 6 and 7 (underthrust sediments)

Interval: sampled from Cores 343-C0019E-20R and 21R
Depth: 832.9–836.8 mbsf
Age: undetermined

Unit 6 consists of variably colored beds of soft clay. Unit 7 is chert, represented only by a few broken clasts stuck in the clay at the end of Section 343-C0019E-20R-2 and in Sections 21R-1 and 21R-CC. This relationship is attributed to drilling damage. The primary structural measurements in these units were of bedding surfaces in the clays (average dip = 6° ± 2°). Paleomagnetic data are not available for these intervals, so bedding strikes have not been corrected to geographic orientations. Only three tectonic faults were identified (dipping 14°, 55°, and 78°). These structures offset beds but not core margins and were not associated with regions of incoherent clay that we interpret to have developed during the drilling process (Fig. **F42**). It is significant that drilling-induced damage included fluidization of specific clay beds, resulting in extrusion of the clay and faulting in the adjacent layers to accommodate the extrusion. Other apparent faults probably result from drilling-induced damage because they are bounded by significant amounts of soft, structureless, intruded clay. Overall, intact lamination in Unit 6 indicates that very little structural deformation and no bioturbation affected these units of the underthrust sediments.

Biostratigraphy

Sampling for biostratigraphy

Table **T3** shows the list of samples that were examined for identification of microfossils. These analyses will be used to help date the sediments (I. Motoyama et al., unpubl. data).

Paleomagnetism

Because of the unavailability of the *Chikyu's* cryogenic magnetometer (see **"Paleomagnetism"** in the "Methods" chapter [Expedition 343/343T Scientists, 2013]), regular whole-core pass-through magnetic measurements of core sections could not be carried out during Expedition 343. Thus, shipboard paleomagnetic studies for Site C0019 consisted of measurements for natural remanent magnetization (NRM) and progressive demagnetization of discrete samples only with the ship's spinner magnetometer and alternating field (AF) demagnetizer. We stepwise AF demagnetized 56 paleomagnetic cubes or minicores to evaluate the directional stability and coercivity spectrum of each sample. We analyzed the results in Zijderveld diagrams (Zijderveld, 1967) and calculated the characteristic remanent magnetization (ChRM) direction using principal component analysis (Kirschvink, 1980). Anisotropy of magnetic susceptibility (AMS) of these discrete samples was measured with the Kappabridge KLY 3S. The Königsberger ratio, which is defined as the ratio of remanent magnetization to the induced magnetization in Earth's magnetic field, was also determined for the measured samples.

NRM, magnetic susceptibility, and Königsberger ratio

The most significant variations in NRM intensity and susceptibility for discrete samples from Site C0019 are well correlated with lithology (Fig. **F43**). The brown clayey mudstone in lithologic Units 5 and 6 have a mean NRM intensity of 4.33×10^{-2} A/m, which is the highest mean value among all the samples. Within lithologic Unit 3, NRM intensities average ~3.94×10^{-2} A/m except for a few discrete peaks of higher NRM intensities in some depth intervals (e.g., around 697.85, 770.44, and 801.04 mbsf). The siliceous/ash mud(stone) in lithologic Unit 1 has the lowest mean NRM intensity of 2.03×10^{-2} A/m.

Variations in magnetic susceptibility generally parallel the variations in NRM intensity in lithologic Unit 1 (Fig. **F43**), where the magnetic susceptibility values are generally ~1.0×10^{-3} SI. The high magnetic susceptibility in lithologic Unit 2 could be related to the presence of ashy mudstone (see **"Lithology"**). Magnetic susceptibility values tend to increase from the upper portion of lithologic Unit 3 and peak in the lower portion of Unit 3, and in Units 5 and 6, where magnetic susceptibility reaches ~4.5×10^{-3} SI. The variation in susceptibility is most likely caused by variations in the magnetic mineral type or magnetic mineral content and needs more detailed shore-based rock magnetic measurements.

The Königsberger (Q) ratio is defined as the ratio of remanent magnetization to the induced magnetization in Earth's magnetic field. In general, the Q ratio is used as a measure of stability to indicate a rock's capability of maintaining a stable remanence relative to the induced magnetization. The current total field value of the International Geomagnetic Reference Field in Hole C0019E (46,498 nT = 37.0 A/m), was used to calculate the Königsberger ratio for rock samples at Site C0019:

$$Q = J_{nrm}/(K_m \times H),$$

where

H = local geomagnetic field (A/m),
K_m = bulk susceptibility (SI), and
J_{nrm} = NRM intensity (A/m).

In general, Q ratios in a majority of samples in lithologic Units 1, 2, 5, and 6 are less than unity, suggesting that the total magnetization of samples contains

dominantly induced magnetization. In contrast, *Q* ratios in a majority of samples in lithologic Unit 3 are higher than unity, with a mean value of 1.48, except for two *Q* ratio peaks at 697.85 and 787.08 mbsf. This may suggest that the magnetic minerals in the mudstone are insusceptible to an external magnetic field.

Anisotropy of magnetic susceptibility

Figure **F44** shows the AMS parameters measured for discrete samples in Hole C0019E. In lithologic Unit 1, minimum susceptibility (K_{min}) inclinations ranges from 41° to 80°. Steeper K_{min} inclinations possibly represent the preservation of the primary fabric of the sediments. The low anisotropy degree parameter (P') reveals that the three principal axes of magnetic ellipsoids have small variations. Negative shape parameters (T) indicate that magnetic ellipsoids have a prolate component. In general, P' values increase gradually with depth in lithologic Unit 3, indicating an increasing degree of deformation or progressive compaction with depth. In lithologic Units 5 and 6, the anisotropy degree seems to gradually decrease, the positive shape parameter represents an oblate shape of the ellipsoid, and some K_{min} inclinations are steeper than 60°, possibly preserving the sedimentary or compaction fabric. Further shore-based study is required to better clarify these observations.

Paleomagnetic direction of discrete samples

Remanent magnetization of discrete samples was investigated using stepwise AF demagnetization techniques to extract the primary component of magnetizations acquired at the time of deposition. Figure **F45** illustrates the magnetic stability behavior of representative samples. Typically, two remanent magnetization components were isolated during AF demagnetization. The first- and second-removed components are here referred to as a low-coercivity component and a high-coercivity component, respectively. The low-coercivity component has generally steep inclination and demagnetized below 10–20 mT. Low-coercivity components with steep inclinations are found in numerous DSDP, ODP, and IODP paleomagnetic studies and are likely to be induced during drilling (Richter et al., 2007). The high-coercivity component is demagnetized above 10–20 mT and univectorially decays toward the origin of the vector plots. Some samples show curved trajectories rather than acute angles between two components because of overlapping coercivity, but most samples have a linear segment in an interval of high demagnetization levels. Three samples show no linear segments in the demagnetization diagram, so we omitted these samples from further paleomagnetic analyses. We regarded the high-coercivity component as the ChRM and calculated its direction using principal component analysis (Kirschvink, 1980).

Figure **F46** shows the ChRM direction for the downhole profile. Except for the lower part of lithologic Unit 3 (770–820.01 mbsf), ChRM inclination of most samples ranges between ±20° and 60°, which is somewhat shallower than the expected inclination (±57.3°) for the latitude of Hole C0019E (37°56′N). Samples from the lower part of Unit 3 (770–820.01 mbsf) show ChRM inclination shallower than ±57.3°. Steep tilt of beds (see **"Structural geology"**) after the acquisition of remanent magnetization is a possible explanation for the shallow inclination observed in the lower part of Unit 3. It is notable that all discrete samples within the upper part of Unit 3 (688.5–725.165 mbsf) except for the uppermost sample have positive ChRM inclination.

ChRM declination of Hole C0019E is generally not consistent even within each section of the cores, possibly because of severe biscuiting of the core (see **"Lithology"**). ChRM declination can be utilized for reorientation of beddings and deformation structures observed within coherent pieces with paleomagnetic samples (see **"Structural geology"**).

Paleomagnetic direction of archive halves

Remanent magnetization of archive halves of the core samples collected during Expedition 343 were measured at 2 cm intervals using the 2G long core superconducting rock magnetometer during Expedition 343T. Routine paleomagnetic measurements are typically performed with AF demagnetization at 5, 10, 15, and 20 mT. However, paleomagnetic results of the discrete samples showed that AF demagnetization below 15 mT is insufficient for removing the low-coercivity component of the core samples obtained during this expedition, which is likely to be induced during drilling. Therefore, we adopted AF demagnetization levels of 15 and 20 mT. We adopted AF demagnetization at 5, 10, 15, and 20 mT for Core 343-C0019E-17R, where no paleomagnetic discrete samples were measured. We omitted paleomagnetic measurements of Cores 2R and 3R because these cores are made up of drilling breccia (see **"Structural geology"**).

We adopted a sampling interval of 2 cm, which is less than the typical interval for pass-through paleomagnetic measurement of 5 cm. The dense sampling interval was adopted in order to determine paleomagnetic directions of as many coherent biscuits of the core samples as possible.

The NRM directions and remanent magnetization directions after AF demagnetization at 20 mT are shown in Figure F46 with the ChRM directions of discrete samples. The ChRM directions of discrete samples are fairly consistent with remanent magnetization directions after demagnetization at 20 mT for the corresponding depths of the archive halves.

Within lithologic Unit 1 and the upper part of lithologic Unit 3 (178.50–185.23 and 688.50–725.115 mbsf), distribution of inclinations after demagnetization at 20 mT centers at ±40°, which is shallower than the expected inclination (±57.3°). Positive inclination dominates at intervals between 184.2 and 184.8, 689.7 and 690.4, and 696.9 and 722.7 mbsf, whereas negative inclination dominates at intervals between 180.8 and 184.1, 689.0 and 689.4, and 696.1 and 696.6 mbsf. It is likely that these intervals belong to certain normal and reversed chronozones, respectively. However, identification of the specific chronozone for the intervals is quite difficult because of lack of shipboard biostratigraphy data. Shallow inclinations dominate in the lower part of the lithologic Unit 3 (770.00–820.01 mbsf), which is possibly due to steep tilt of beds (see "Structural geology") within the interval. Positive inclinations were obtained from the sheared clay of lithologic Unit 4 (822.10–822.36 mbsf). Inclination fluctuates between shallow and steep values within lithologic Units 5 and 6 (824.00–833.47 mbsf) and polarity zones are difficult to identify within these lithologic units.

Physical properties

In Hole C0019E, physical properties measurements were made to obtain basic information regarding lithology, porosity, strength, and deformation and for correlation with downhole logging data. After capturing X-ray CT images and letting the core reach thermal equilibrium with the ambient temperature of ~20°C, gamma ray attenuation (GRA) density, magnetic susceptibility, NGR, *P*-wave velocity (PWV), and noncontact electrical resistivity were measured using an MSCL-W. Cores were then split parallel to the core axis. One half was reserved for archiving and one half was for sampling and analysis (working half). A photo image logger (MSCL-I) and a color spectroscopy logger (MSCL-C) were used to collect images of the archive-half split surfaces. Thermal conductivity was measured using a half-space line source method on split working halves. Discrete samples were obtained from the working halves in order to measure moisture and density (MAD). Additional discrete cylindrical samples from working halves were taken to measure unconfined compressional strength (UCS). Electrical resistivity and *P*-wave velocity measurements for discrete samples (PWVD) were made on 2 cm × 2 cm × 2 cm samples cut from working halves. Some of these cube samples were further tested for *P*-wave and *S*-wave measurements under high pressure. Grain size analysis was restricted to Core 343-C0019E-1R, as all other cores were too lithified for the particle size analysis to be useful.

MSCL-W

Gamma ray attenuation density

Bulk density determined by GRA is observed to increase gradually downhole. Maximum values are ~1.3 g/cm^3 starting at 176.5 mbsf and increase throughout lithologic Unit 1 to ~1.7 g/cm^3 at 184.8 mbsf (Fig. F47). The upper range of GRA density values continues to increase through lithologic Unit 2 and the top of lithologic Unit 3, reaching ~1.9 g/cm^3 by 772 mbsf (Fig. F48). Between 785 and 812 mbsf, GRA density decreases slightly before reaching values of ~2.0 g/cm^3 from the bottom of Unit 3 through Unit 4. This overall trend of increasing bulk density is consistent with depth-dependent consolidation and porosity loss in sediment. Overall, GRA density varies widely and many measurements are unreliable because of the presence of air and/or water between the core and liner during measurement. However, because the maximum values we observe are in strong agreement with bulk density values obtained from MAD measurements on discrete samples (see "Moisture and density" below), we consider the upper range of these values to be valid.

Magnetic susceptibility

Magnetic susceptibility within Unit 1 appears to increase downhole and reaches peak values of 221.7 × 10^{-5} SI (Fig. F47). In Unit 2 magnetic susceptibility is generally >100 × 10^{-5} SI, whereas it is <100 × 10^{-5} SI in Unit 3. Within both Units 2 and 3, magnetic susceptibility also increases downhole relative to other values in the same unit (Fig. F48). Near the bottom of Unit 3, magnetic susceptibility values spike to values as large as ~330 × 10^{-5} SI at ~817.6 mbsf, which is considerably larger than maximum values elsewhere within the unit. In Unit 4, consisting of Core 343-C0019E-17R and a major shear zone interpreted to be the plate boundary décollement zone (see "Structural geology"), magnetic susceptibility increases within a ~40 cm interval centered around a peak value of 162 × 10^{-5} SI at ~822.2 mbsf. Background values elsewhere within the Unit 4 are <75 ×10^{-5} SI even where density measurements indicate that low values are not a result of insufficient core volume

filling the core liner (Fig. F49). Within Unit 5, magnetic susceptibility appears to slightly decrease downhole except for some local high values occurring within 827.1–828.2 mbsf. Magnetic susceptibility within Units 6 and 7 decreases with depth to ~2 × 10^{-5} SI at ~833.5 mbsf, with the exception of some high values of up to ~187 × 10^{-5} SI at ~833 mbsf and some values of ~50 × 10^{-5} SI within Unit 7. Magnetic susceptibility measured with the MSCL-W is generally consistent with bulk magnetic susceptibility of paleomagnetic discrete samples (see "Paleomagnetism").

P-wave velocity

PWV data recorded by the MSCL-W show significant scatter ranging between 800 and 2000 m/s (Figs. F47, F48). MSCL-W velocity measurements are lower than velocities calculated using the LWD logs (see "Logging while drilling"). This discrepancy is likely due to gaps between the core and core liner and core liner partially filled with air resulting in velocities lower than that of seawater (~1500 m/s). At any particular depth, upper values range between ~1500 and 1900 m/s; these values are generally consistent with values obtained from discrete measurements. However, an expected trend of increasing PWV with depth is difficult to identify.

Electrical resistivity

The electrical resistivity generally increases with depth to ~820 mbsf (Figs. F47, F48), with local variations probably caused by small-scale lithologic changes or variations in degree of compaction. These variations are in general agreement with LWD data from Hole C0019B (see "Physical properties and hydrogeology"). Lower than expected resistivity values in Unit 2 (~630–660 mbsf) are probably due to poor core quality. Lower values observed in Core 343-C0019E-16R (~818 mbsf), just above a major fault, are inconsistent with resistivity values obtained from discrete measurements and logging data. The values may be related to high amounts of drilling-induced fractures filled with drilling fluid. High-resistivity values in the upper portions of Core 343-C0019E-17R, consisting of the interpreted basal décollement zone (see "Structural geology"), may result from large amounts of air between the core material and liner, as suggested by correspondingly low densities (Fig. F49). Between ~821.9 and ~822.5 mbsf within Core 343-C0019E-17R, electrical resistivity values are consistently less than ~10 Ωm with no apparent change where there is a marked increase in magnetic susceptibility (Fig. F49). Below the fault, resistivity values should be taken with caution because they are lower than measurements from LWD and discrete samples. High-resistivity values in the last core, Core 343-C0019E-21R covering depths >836.55 mbsf, are also due to incompletely filled core liners.

Natural gamma radiation

NGR data from the MSCL-W were used to help correlate Hole C0019B with Hole C0019E (see "Logging while drilling" and "Core-log-seismic integration") and identify lithologic units (see "Lithology"). NGR ranges between ~5 and 20 counts per second (cps) in Unit 1, with the exception of higher values at ~179 mbsf (up to 50 cps). Average NGR increases in Units 2 and 3, averaging 24.7 and 27.5 cps, respectively. Values as high as ~40 cps were observed locally. Significantly higher NGR values (up to 58 cps, averaging nearly 40 cps) were observed within Unit 4. Compared to the overlying unit, this suggests an abrupt change in lithology consistent with structural and lithologic descriptions identifying this unit as the plate boundary décollement zone (see "Lithology" and "Structural geology"). Between ~821.9 and ~822.5 mbsf within Core 343-C0019E-17R and Unit 4, values show a marked decrease to 43.97 cps over a ~20 cm interval centered at 822.2 mbsf, corresponding to the location of a peak in magnetic susceptibility (Fig. F49). Elevated NGR values were also found at the top of Unit 5 before decreasing to levels similar to those observed in Units 2 and 3 (~25–30 cps) at ~826 mbsf. Average NGR drops to below 14 cps in Unit 6, signaling a switch to a lithology lacking in clays.

Moisture and density

MAD measurements provide characterization of grain density, bulk density, porosity, void ratio, and water content in Hole C0019E, despite incomplete core recovery. All MAD data are provided in Table T4. Below, we summarize the most important parameters, which are bulk density, grain density, and porosity. Downhole variations are graphically shown in Figure F50.

Bulk and grain density

In the spot core (343-C0019E-1R) taken below 176.5 mbsf (lithologic Unit 1/log Unit I), bulk densities in the siliceous mudstones vary between 1.53 g/cm^3 and 1.69 g/cm^3. Grain densities range from 2.45 to 2.57 g/cm^3.

In the next continuously cored interval (Cores 2R and 3R; lithologic Unit 2/log Subunit IIb) to 659.7 mbsf, sediment bulk density ranges from 1.72 to 1.88 g/cm^3, and grain density ranges from 2.39 to 2.67 g/cm^3. Some of the low grain density values in this depth interval may be related to inadequate

sampling of rock chips, which were the only available material.

In Cores 343-C0019E-4R–16R, which correspond to lithologic Unit 3 and form part of log Subunit IIb, bulk density values gradually increase downhole. Core 4R shows the lowest bulk density (1.75 g/cm³), whereas values higher than 1.9 g/cm³ are restricted to Core 8R or deeper (deeper than ~720 mbsf). This increase in bulk density probably reflects a higher degree of compaction in the sediment with burial. Grain density in Unit 3 ranges from 2.47 to 2.76 g/cm³, which is a characteristic range for pelagic and hemipelagic silicate minerals.

A single discrete sample taken from the plate boundary fault zone at 822 mbsf (Core 17R; lithologic Unit 4/uppermost log Unit III) before core splitting has a bulk density of 1.98 g/cm³ and grain density of 2.86 g/cm³. Beneath the fault zone, Core 18R through Section 20R-2, 53 cm, which form lithologic Unit 5 and the lower part of log Unit III, have bulk density values ranging from 1.76 to 2.03 g/cm³ and grain density values ranging from 2.58 to 2.74 g/cm³. In Core 21R a single discrete sample of chert representative of lithologic Unit 7 and log Unit IV has a bulk density of 2.01 g/cm³ and grain density of 2.54 g/cm³. No discrete MAD measurements were made for lithologic Unit 6, which showed evidence of invasion by drilling fluid.

Porosity

Porosity and void ratio values show a general downhole decrease in Hole C0019E cores. Samples from the spot core (343-C0019E-1R) encompassing Unit 1 show porosities between 55.3% and 68.7% and corresponding void ratios ranging from 1.24 to 2.05. The cored interval through Unit 2 between 648 and 660 mbsf has porosity values that vary between ~40.5% and 52.5%. This variability is unlikely to reflect petrographic differences between samples but may be related to water uptake in rock chips during core recovery. In contrast, samples from the third cored interval (688.5–729.0 mbsf), containing the upper portion of Unit 3, show a regular downhole decrease in porosity from values slightly >50% to ~45%. The lowest values were found in the fault zone between 719 and 725 mbsf (Cores 8R and 9R) (see **"Structural geology"**). This may suggest that these sediments have experienced shear-enhanced compaction, resulting in reduced porosity in the sheared lithologies.

Further downhole in the interval between 770 and 818.6 mbsf (Cores 10R through 16R) covering the lower part of lithologic Unit 3, porosity values scatter between 41.9% and 52.7%. In the sample taken from the décollement zone (Core 17R) at 822.49 mbsf, porosity is 48.2%. The underthrust brown mudstones beneath the décollement (Cores 18R through 20R) have porosity values between 35.9% and 52.5%. A chert sample from Core 21R has a porosity of 35.0%.

Unconfined compressive strength

We tested the UCS of nine minicores sampled from the split core working halves. Results are shown in Figure **F51** and listed in Table **T5.** The number of measurements was limited because pervasive fracturing induced by drilling resulted in a lack of adequately sized intact rock pieces suitable for sampling and measurement. UCS values are generally low in the upper portion of Unit 3, with two samples exhibiting strengths of 3.4 and 3.8 MPa and one low value of 1.3 MPa. The low-strength sample was recovered from within a fault zone at 720 mbsf (see **"Structural geology"**). In the lower portion of Unit 3 (below 800 mbsf), UCS increases significantly to 6.4–7.6 MPa. Within Unit 5, two tested samples show lower strengths of 3.4 and 4.7 MPa. These samples are located 5–10 m below the décollement zone, suggesting that their low strength relative to above the décollement may be related to either a different lithology or near-fault damage. A chert sample from Unit 7 was the strongest tested, with a minimum UCS of 65.3 MPa. This value should be considered a lower boundary estimate because the sample was tested several times due to failure of supporting material surrounding the sample, and therefore likely experienced fatigue. In general, the UCS data show a trend of increasing strength downhole, with low strength values exhibited by samples from near or within fault zones.

P-wave velocity

PWVD ranges from 1400 to 3300 m/s over the cored interval, with a clear trend of increasing velocity with depth (Fig. **F50;** Table **T6**). Discrete *P*-wave samples were only obtained from lithologic Units 2, 3, 5, and 7, with the majority coming from Unit 3. Measured velocity decreases in samples from Cores 343-C0019E-19R and 20R (Unit 5), which are from the footwall of the décollement zone at ~820 mbsf. Velocity reaches a maximum of ~3272 m/s in the cherts of Unit 7.

PWVD has an inverse relationship with porosity (Fig. **F52**). The majority of the samples follow an approximately linear trend except for the chert sample from Unit 7, which has a much higher velocity. Vertical anisotropy was calculated from resistivity measurements in the *x*-, *y*-, and *z*-directions. Horizontal an-

isotropy was not calculated because of orientation ambiguity in the *x*-*y* plane. Calculated vertical anisotropy in PWVD is small, ranging from ~0% to 6% (Fig. **F53**). In general, PWVD is nearly isotropic below 810 mbsf, where values are mostly ~2% or lower.

Elastic wave velocity measurements under high pressure

Elastic wave velocity was measured during Expedition 343 on five cubic samples. The sample taken from Core 343-C0019E-4R (688.57 mbsf) within Unit 3 was measured under confining pressures up to 90 MPa and used to estimate how the measured velocity changes temporally at a constant pressure. We found that stable values were reached after 2 h at confining pressures ≥70 MPa. Considering the limited available time for shipboard measurements, the measurements for other samples were conducted using stepwise increases of confining pressure. Pressure steps were 0, 5, 10, 15, 20, 30, and 50 MPa. We also measured velocity while depressurizing at 30, 10, and 0 MPa. Figure **F54** shows the results for each sample. Velocity generally increases with increasing pressure. Samples from Unit 3 (Cores 4R, 5R, and 7R) showed a similar range in velocity: 1.5–2.5 km/s for *P*-wave velocity and 0.8–1.5 km/s for *S*-wave velocity in the pressure range of 0–50 MPa. A sample from Core 19R in Unit 5 showed similar *S*-wave velocity to samples from Unit 3, but *P*-wave values were significantly higher. *P*-wave velocity also rapidly increased as a function of confining pressure. In contrast, velocities from Core 21R (Fig. **F54E**) were representative of the cherts within Unit 7 and were remarkably different from other cores. Measured velocity values did not change significantly within the range of confining pressures applied in this experiment, indicating extremely low compressibility. Although we attempted to conduct nine measurements for each sample within the whole applied range of confining pressures, we not always receive complete recordings (e.g., SXz of Core 7R). This was likely due to problems with signal communication, insufficient coverage of the silicon coating on the samples, or coupling of the sensor to the sample surface.

Electrical resistivity

In soft sediments from Core 343-C0019E-1R, resistivity was measured along the *y*- and *z*-axis with a four-pin, 2 kHz Wenner array (Fig. **F50;** Table **T7**). Resistivity in these samples increases with depth, with an average value of 0.72 Ωm. This value is lower than the deep-resistivity measurements from LWD. This difference may be caused by desiccation and cracking of the core samples during the ~24 h between core splitting and measurement. However, this likely has a greater effect on the soft sediment recovered from the shallow core (Core 343-C0019E-1R).

Below 688 mbsf (Core 4R), the rocks were indurated enough to measure resistivity on cube samples, although the number of samples was limited by core quality (Fig. **F50;** Table **T8**). In Units 1 and 3 (170–786 mbsf), resistivity increases with depth, with lower resistivity values in Core 7R (~714 mbsf) possibly related to the presence of ash layers. Resistivity then decreases to 810 mbsf, and then increases again in Core 15R (817 mbsf). Resistivity variations are in good agreement with variations in porosity from MAD measurements. In lithologic Units 5 and 7 (from 826 to 836 mbsf) below the major fault zone, resistivity decreases with depth and then increases in the Unit 7 cherts.

No clear trend in vertical anisotropy is observed downhole, although the magnitude of anisotropy can be large (–31% to 13% through Unit 5) compared to anisotropy in *P*-wave velocity (Fig. **F53**). The cherts in Unit 7 have very large values of anisotropy (98% vertical, 69% horizontal); however, similar anisotropy is absent in the *P*-wave velocity data.

The relationship between porosity and resistivity is illustrated in Figure **F55.** The trends in the data set provide a first approximation of Archie's law parameters (see **"Logging while drilling"**) in the different lithologic units. The logarithm of resistivity for Units 1, 3, and 5 broadly exhibits a linear relationship with porosity that does not include the chert from Unit 7.

Thermal conductivity

Thermal conductivity was measured on the working half of core sections from Hole C0019E at 45 discrete locations (Fig. **F50**). The mean of all measurements is 1.139 W/(m·K) (standard deviation = 0.118 W/[m·K]; n = 45). Unit 1, interpreted to be slope sediments, has the lowest values (mean = 0.874 W/[m·K]; standard deviation = 0.0141 W/[m·K]; n = 2). These low values are likely related to relatively higher porosity and possible desiccation of the samples (Fig. **F50**) compared with the deeper mudstones of Units 2–5, which have a mean value of 1.143 W/(m·K) (standard deviation = 0.074 W/[m·K]; n = 34). The clays of Unit 6 exhibit thermal conductivity that is slightly lower, yet comparable to the overlying mudstones, with a mean of 1.086 W/(m·K) (standard deviation = 0.0870 W/[m·K]; n = 3). A very high value of 1.622 W/(m·K) is observed in the chert from within Unit 7, which is expected because of its high density and silica content. Although two measurements were recorded in the depth interval for Unit 7, the lower value was measured in a cobble that was later inter-

preted as material that was displaced after drilling and fell downhole, possibly from Unit 3.

Particle size analysis

Grain size distribution was measured on seven sediment samples from Unit 1, ranging in depth from 177.5 to 184.7 mbsf in the shallow spot core in Hole C0019E (Fig. F56; Table T9). Below this depth, measurements were impossible because the grains in consolidated sediments could not be dispersed with a dilute alkaline solution of sodium polyphosphates ($[NaPO_3]_6$). The mean grain size of the measured sediments ranges from 24.6 to 69.5 µm, except for the sediments from Sections 343-C0019E-1R-5 and 1R-6. The mean grain size range is consistent with the lithologic description of the sediments, which indicate that they are composed of abundant clay- to silt-sized siliciclastic material. However, bimodal size distributions were measured in three samples (Sections 1R-3, 1R-6, and 1R-7; Fig. F56), indicating that grains >0.5 mm exist in the measured samples. After analysis, we confirmed that these large grains were aggregates of clayey siliciclastic materials, indicating dispersion of the sediment using both chemical and mechanical means was incomplete. Thus, the measured grain size may be overestimated.

The effect of H_2O_2 solution treatment on grain size distribution was evaluated using the sample from Section 1R-1, which contained little organic material. The mean grain size increased slightly from 24.6 to 32.5 µm and kurtosis decreased after H_2O_2 solution treatment (Table T9).

Color spectrometry

Color reflectance results of split core sections are shown in Figure F57. The L* value represents lightness, from black (L* = 0) to white (L* = 100). The a* value represents color changing from pure green (a* = –127) to pure red (a* = 127), and the b* value represents color changing from pure yellow (b* = –127) to pure blue (b* = 127).

For lithologic Unit 1, L* values range from ~25 to 48, a* values range from –2 to 1, and b* values range from 0 to 7. For Unit 2, the mixed brown and gray mudstone has L* values ranging from ~25 to 50, a* values ranging from –2 to 5, and b* values ranging from 0 to 10. For Unit 3, varying gray mudstone has L* values ranging from ~22 to 45, a* values ranging from –2 to 1, and b* values ranging from –2 to 5.

Below the 822 mbsf fault zone (Unit 4), L*, a*, and b* values all abruptly increase. The brown clay layer (Unit 5) has L* values ranging from 37 to 52, a* values ranging from 2 to 6, and b* values ranging from 5 to 16. Unit 6 has the widest ranges of all values, which can be judged qualitatively by its colorful appearance. L* values range from 32 to 65, a* values range from –1 to 10, and b* value range from 0 to 22. Variations in color spectrometry values are closely related to lithologic changes.

Geochemistry

Interstitial water geochemistry

Twelve whole-round core samples from 178.89 to 831.45 mbsf were collected for interstitial water analysis (Table T10). A single spot core (343-C0019E-1R) taken at the top of this interval is ~465 m shallower than the other cores and will not be presented in the figures. The remaining 11 cores were recovered from 689.44 to 831.45 mbsf, spanning the two major fault zones identified in LWD data and reaching into mudstone 1.2 m above lithologic Unit 6. Core sections processed for interstitial water were 15.5 to 31 cm long, and the volumes of interstitial water obtained were 4.2–23 mL except for the volume from Core 1R (63 mL). The interstitial water whole round from Core 19R was taken from two intervals on either side of a whole-round sample selected for anelastic strain recovery measurement. The whole-round sections with good condition for interstitial water sampling were limited, and the lengths of the whole rounds were generally shorter than ideal. Only three samples had sufficient water to measure alkalinity and pH (Table T10).

Possible contamination by drilling fluids

The 11 deepest interstitial water samples contained detectable dissolved sulfate at depths that should be below the sulfate–methane transition (SMT) zone. Sulfate concentrations ranged from 3.41 to 20.24 mM (Fig. F58; Table T10), compared to a seawater value of 28.9 mM. Generally, the presence of sulfate here would be taken as evidence for contamination of the whole rounds by drilling fluids. However, the observed interstitial water sulfate concentrations, if derived from contamination by drilling fluids, would suggest contamination of 12%–70%. The largest sulfate concentration was measured in a whole-round sample (Core 343-C0019E-20R) that was thoroughly cleaned by scraping, and only intact unfractured pieces were used for interstitial water extraction, so contamination is considered unlikely. Results from experiments using the perfluorocarbon (PFC) tracer (see "Microbiology") indicate minimum contamination by drilling fluids. Further evidence against contamination is that a correction for drilling fluid using the sulfate proxy would result in negative magnesium and potassium concentrations in some cases. Finally, cross-plots of strontium-sulfate and cesium-

lithium (Fig. F59) provide evidence for multiple fluid reservoirs and indicate interstitial water samples with high sulfate concentrations represent waters with in situ dissolved sulfate. For the data plotted here, no sulfate correction is applied, and the presence of dissolved sulfate is interpreted as evidence for a sulfate-bearing fluid reservoir at depth.

Sulfate, alkalinity, pH, phosphate, and ammonium

Because of the deep coring plan with incomplete core recovery through the hole, the sulfate profile to the SMT zone could not be established. Sulfate concentrations (SO_4^{2-}) from 689 to 816 mbsf generally vary in a range of <10 mM (Fig. F58; Table T10). Sulfate concentrations trend to lower values from 787 to 816 mbsf, the latter sample being the last taken from lithologic Unit 3 above the faulted horizon in Core 343-C0019E-17R. A large sulfate concentration is observed in each of the two interstitial water samples below Core 17R in Units 5 and 6 and above the chert horizon in Unit 7. These last two samples were obtained as relatively intact pieces from the whole round and it is unlikely that sulfate found in the interstitial water is due to drilling contamination, which suggests a deep source of sulfate-bearing fluids. Such high sulfate concentrations at these depths are rarely observed in accretionary prisms, although there is evidence at one of the Nankai reference section sites for dissolved sulfate entering the base of the sedimentary section, perhaps through oceanic basement (Expedition 322 Scientists, 2011).

Because alkalinity and pH could be measured in only two deep interstitial water samples (Fig. F58), no useful trends can be discerned. Measured alkalinity of the sample from 720.42 mbsf is relatively high (35 mM) compared to that of the deeper sample (7.9 mM). Given the low calcium concentrations and lack of carbonate found in the cores, it is unlikely that alkalinity values are substantially affected by carbonate precipitation. Measured pH is also relatively high in the sample from 720.42 mbsf (7.91) compared to the deeper sample (7.64). However, both alkalinity and pH from 720.42 mbsf are comparable to values measured on the sample from 178.89 mbsf.

The highest phosphate (PO_4) concentration of 96 µM is observed at 179 mbsf in Unit 1. Deeper values are substantially lower and generally decrease with depth (Fig. F58), possibly related to removal by oxide phases. Ammonium (NH_4) concentrations decrease systematically in the deeper core intervals (>688 mbsf). Phosphate and ammonium concentrations are likely related to production of these metabolites during degradation at shallower depths.

Salinity, chlorinity, and bromide

Salinity values are similar to seawater within most of Unit 3 (688.50–820.01 mbsf). However, salinity decreases to low values of 33.5 parts per thousand (ppt) at 810.53 mbsf and 33.6 ppt at 816.50 mbsf (Fig. F58). The low salinity values suggest either an exotic fluid source or possibly advanced dehydration of hydrous minerals at the base of Unit 3, immediately above the zone of highly sheared sediment. Below Unit 4, the plate boundary décollement zone (see "Structural geology"), salinity returns to near-seawater values in Cores 343-C0019E-19R and 20R.

Chlorinity (Cl) is similar to seawater concentrations at the upper target horizon, has slightly higher than seawater values at 787 and 802 mbsf, and then monotonically decreases toward the bottom of the hole (Fig. F58). The decrease suggests a reservoir of low-chlorinity fluids deeper than the maximum depth reached by drilling. A slight minimum at 699 and 706 mbsf in Unit 3 might reflect a similar low-chlorinity fluid source. The minimum is also located at the horizon with the highest hydrogen concentration (see below). The general similarity of Cl to seawater concentrations in much of the hole is consistent with the low amounts of observed volcanic matter in the dominant dark gray mudstone of Unit 3. Alteration of ash to clay minerals would have resulted in increases in Cl concentrations. Br concentrations are higher than seawater throughout the section, but show a general decrease with depth (Fig. F58). The lowest concentrations are observed in the bottom two samples of Hole C0019E. Elevated Br concentrations might reflect release from organic matter.

Major cations (Na, K, Mg, and Ca)

Major cations are lower than seawater values throughout most of the hole and show little variation in concentration in Unit 3 (Fig. F60). The very low calcium concentrations in Units 2 and 3 are consistent with the generally low abundances of observed carbonate minerals in visual core description. The lack of cation variation in these units likely reflects minimal alteration of sparse volcanic matter to clay minerals. Near the bottom of the hole (below 820 mbsf) in Units 5 and 6, calcium markedly increases and both potassium and magnesium decrease. The observed profiles below 780 mbsf are consistent with the formation of clay minerals (illite, chlorite, or mixed-layer clays) associated with fluid-rock interactions. The narrow depth range suggests

this process is only important in the deepest part of the hole. The increase in calcium concentrations might be expected to promote carbonate formation, but little carbonate was observed in the deep sediment horizons. Sodium concentrations, calculated from charge balance, decrease from Units 3 to 5 and could reflect minor alteration of volcanic matter to Na-bearing clays (smectite).

Minor and trace elements

The depth dependence of rubidium and cesium is consistent with that of other alkali metals, sodium and potassium, and decreases from Units 3 to 5 (Fig. F61). The decrease of cesium in the lowest part of the hole is remarkable. These observations are consistent with the involvement of fluids associated with Na-K–rich clay mineral formation. Silica concentrations are high throughout the hole, possibly related to the high abundance of siliceous microfossils (Fig. F60). There is a minimum in silica at 713 mbsf. Deeper than 780 mbsf, silica values increase with depth, negatively correlated with the values of sodium, potassium, magnesium, rubidium, and cesium. This suggests a supply of silica associated with mineral reactions such as clay mineral formation. Lithium and boron correspond with silica and are likely controlled by a similar mechanism to that which governs silica concentrations (Fig. F60). Manganese concentrations increase abruptly below the inferred décollement. Manganese values that are well correlated with calcium values are also likely to result from such mineral reactions.

Barium shows a complicated depth profile but is negatively correlated with sulfate values (Fig. F60). This strongly suggests the control of barium concentration by sulfate species in fluids and rocks. In contrast to barium, strontium shows relatively constant concentrations with a slight increase at the bottom of the hole, which is rather consistent with variations in silica, boron, and lithium (Figs. F60, F61). Decoupling of these alkali-earth metals indicates the formation of a barium-specific phase, possibly barite, in the deeper part of the hole.

Depth profiles for some of the trace metals such as zinc, copper, iron, molybdenum, lead, and uranium show a strong positive peak at ~700 mbsf near the upper fault horizon (Fig. F61). Zinc and molybdenum are also enriched in the lowermost part of the hole. Although the cause of trace metal enrichment at ~700 mbsf is unknown, it is possible that these anomalies result from fluid transfer associated with a seismic or postseismic event as suggested by hydrogen data.

Control of pore fluid compositions by mixing

The variations in pore fluid chemistry described above suggest the involvement of fluid-mineral interactions at various depths. Such fluid-mineral interactions may have produced two or more end-component fluids that mixed to form the observed pore fluid compositions. The relationship between sulfate and strontium concentrations and lithium and cesium concentrations for seawater and high-density drilling mud fluid (Table T11) are shown in Figure F59. The lack of clear correlation in these diagrams indicates that at least three end-components are controlling the pore fluid compositions, one of which is a seawater-like fluid. The data from fluids collected at depths shallower than 730 mbsf exhibit clear linear trends in the mixing diagrams, indicating mixing of seawater-like fluid and fluid characterized by low sulfate–high strontium and high lithium–high cesium concentrations. Some of the pore fluids collected from depths greater than 780 mbsf exhibit a different mixing trend, for which the contribution of the seawater-like component largely disappears, and another end-component fluid likely characterized by high sulfate–high strontium and high lithium–low cesium is involved. It should be noted that the seawater-like end-member component requires sulfate concentrations distinctly lower than seawater. Thus, this end-member component is not seawater itself and might represent deeper fluids of modified seawater composition. Although the drilling mud fluid apparently fits the end-component with high sulfate and low strontium, this scenario fails to explain the observed low lithium and cesium. Therefore, neither pure seawater nor drilling mud fluid can be end-component fluids, excluding the probability of pore fluid contamination by drilling. Therefore, two unidentified end-member fluids control the composition of deep pore fluids.

Carbon, nitrogen, and sulfur concentrations

The total carbon (TC), total nitrogen (TN), and total sulfur (TS) data are summarized in Table T12 and Figure F62. Calcium carbonate ($CaCO_3$) values range from 0.05 to 32.1 wt%. The highest values are at 688.82 and 689.41 mbsf. The average calcium carbonate value is 2.3 wt% and most samples have values <1 wt%. Total organic carbon (TOC) values remain low throughout the section, averaging 0.38 wt%. Some of the lowest TOC values are in Units 5 and 6 of the lower plate sedimentary section. Like TC, TN is relatively uniform in sediments of Unit 3 above the décollement. The TOC/TN average ratio of

5.47 is on the low end of that expected for marine origin, but most samples from Unit 3 (mean TOC/TN = 6.85) fall within the range of 6–9 expected for marine organic matter. TS content is mostly low, ranging from 0.01 to 3.12 wt%, with an average of 0.30 wt%. There are two local sulfur maxima at 705.83 and 810.50 mbsf. Excluding the two highest values, the mean sulfur content is 0.17 wt%.

Gas chemistry

Dissolved gas components in the sediments, such as H_2, CO, CH_4, and C_2H_6 were measured at the bottom of each section of the recovered core in Hole C0019E (Table **T13**), and the depth profile of concentration of each gas component is shown in Figure **F63.** It should be noted that the gas component concentrations in Cores 343-C0019E-2R and 3R are likely reduced from potential in situ concentrations because of heavy fragmentation and mixing of the core material during recovery (see **"Lithology"**). Thus, the following description and discussion based on the abundance of gas components excludes data from Cores 2R and 3R (Table **T13**).

A large and spatially restricted increase in H_2 concentration was found in the bottom of Section 343-C0019E-5R-1 (Fig. **F63**) at 697.4 mbsf. This sharp spike of H_2 includes neighboring sampling points in Sections 4R-CC and 5R-2 (Table **T13**). H_2 concentrations in this maximum were significantly higher than the other representative background levels of dissolved H_2 concentrations in Hole C0019E sediments, or so-called "drill bit–induced" H_2 concentrations.

Based on field observations and laboratory experiments, mechanochemical H_2 is expected to be produced with the creation of new surface area in rocks during friction work, and thus large amounts of H_2 is likely generated on major faults during earthquakes in natural environments (e.g., Wakita et al., 1980; Wiersberg and Erzinger, 2008; Hirose et al., 2011). Because many geophysical observations suggest that the Tohoku-oki earthquake induced a large amount of slip along one or more faults at depth beneath Site C0019 (Fujiwara et al., 2011), we predicted that a possible earthquake-induced H_2 concentration anomaly was generated and may still be observable in the sediments of Site C0019 14 months after the Tohoku-oki earthquake. The maximum H_2 concentration at ~700 mbsf may represent a signature of this predicted earthquake-induced H_2. A similar anomaly (minimum value) was also observed in the depth profile of the methane/H_2 ratio (CH_4/H_2) (Fig. **F63**). This value reveals a more standardized index of relative H_2 abundance in the subseafloor sediments and may constrain the duration of anomalous H_2 concentrations after the time of generation. In the LWD measurements, significant low gamma ray and resistivity signals were found at ~700 mbsf (see **"Logging while drilling"**). In addition, low chlorinity values were detected in the interstitial water obtained from the closest section of Core 5R (Section 5R-2) (Fig. **F58**). Together with the structural characterization of Section 343-C0019E-5R-1 (see **"Structural geology"**), these measurements suggest the existence of a major fault and may be associated with fault activity during a large earthquake. Due to incomplete core recovery from ~700 to ~705 mbsf, a detailed H_2 concentration anomaly profile from this section was not obtained. However, the H_2 anomaly is the first potential example of earthquake-induced H_2 production discovered in deep subseafloor sediments. Future isotopic and chemical-microbiological analyses will provide important insights into the earthquake-induced environmental impacts and the postearthquake biogeochemical and microbiological processes in the deep subseafloor environments of subduction zones.

The CO concentration depth profile is generally similar to the H_2 concentration profile but the pattern is less clear (Fig. **F63**). The stable C_1/C_2 ratio with depth indicates that the methane and ethane profiles are quite similar (Fig. **F63**). Methane concentrations are high (>1000 µM), except in a few samples, and exhibit some scatter (Table **T13**). Unusually low methane concentrations were found in Core 343-C0019E-20R. With increasing depth in Core 20R, methane concentration decreases to 9.6 µM (Fig. **F63**). The lowest methane concentration, at Section 20R-2 (833.5 mbsf), is two to three orders of magnitude lower than at other sampling points in Hole C0019E. This steep depletion might result from two processes: (1) very little in situ production of methane and/or (2) rapid diffusion of methane at this depth range in Core 20R. In particular, the rapid diffusion of methane points to the possible occurrence of relatively high fluid flow beneath Core 20R, likely within the oceanic basement basalt. The deep depletion of methane concentration is consistent with the observed decrease of chlorinity. These results strongly suggest the presence of another fluid end-member that is chemically distinct from seawater or possible faulting-enhanced fluid flow. Future compositional and chemical analyses and microbiological charac-

terizations will clarify the detailed chemical properties of and the origin of potential deep-sourced fluids.

Microbiology

Whole-round sampling

Whole-round samples were collected and analyzed from 12 of the 21 cores recovered from Hole C0019E (Table T14). Following the procedures described in "Microbiology" in the "Methods" chapter (Expedition 343/343T Scientists, 2013), the whole-round samples were subsequently subsampled for each analysis.

Contamination tests

PFC tracer was added to the drilling mud tank every time a new batch of drilling mud was prepared with surface seawater. After preparations were complete, a 50 cm^3 sample was collected to measure PFC concentration so that the drilling fluid contamination of core samples could be assessed. PFC concentrations in the drilling mud were variable, ranging from 1.66 to 989 $\mu g/cm^3$ (Table T14). These variations could be explained by the insufficient mixing of highly viscous drilling mud and PFC solution in the drilling mud tank. Two mud samples showed very high concentrations of PFC (Samples 343-C0019E-Mud-5/19–20 and Mud-5/20 in Table T14), which could represent insufficient mixing of the PFC solution. The other values (1.65–1.88 $\mu g/cm^3$) represent average PFC concentrations in drilling mud sufficiently mixed with PFC.

PFC concentrations in the microbiological whole-round samples were generally much lower than those measured in drilling mud. Predictably, the exterior portions of whole-round samples always have higher PFC contaminations than the interior (Table T14); therefore, microbiological subsamples were only collected from the interior. Among all samples collected, the interiors of Cores 343-C0019E-4R, 12R, and 19R were found to be completely free from any drilling mud contamination. This implies that these subsamples escaped contamination from not only the drilling mud, but also from ambient seawater during core recovery. Similarly, the interior parts of Cores 343-C0019E-5R, 7R, 8R, 15R, and 20R show relatively less drilling mud and seawater contamination (Table T14). However, both the exterior and interior of Cores 343-C0019E-6R and 13R exhibited high concentrations of PFC. Thus, the microbiological data and even interstitial water chemistry data from these samples should be carefully examined for the potential of drilling mud and seawater contamination.

Observatory and downhole measurements

MTL observatory

Installation and data recovery plans

The MTL observatory was installed beneath the seafloor in Hole C0019D on 16 July 2012 during Expedition 343T. Sensors were installed into the tubing on the rig floor on 14 July and the lowering of the observatory to the seafloor began that evening. The bottom of the observatory tubing entered the wellhead at ~1045 h on 16 July and was lowered into place until the casing hanger met with the seafloor wellhead at ~1645 h. Detachment of the casing running tool was completed at ~1815 h on 16 July. The final overall observatory length from the top of the casing hanger to the bottom shoe below the float collar is 829.20 m with the top of the casing hanger rising 4.42 m above the seafloor. The final calculated depths of the sensors are reported in Table T9 in the "Methods" chapter (Expedition 343/343T Scientists, 2013).

Dives by the remotely operated vehicle (ROV) *Kaiko* 7000II to Hole C0019D are scheduled for October 2012 and February 2013 to retrieve the temperature data. In October, the wellhead will be precisely located and checked so that retrieval of the MTL string can be done quickly in February. Two dives by ROV *Kaiko* are scheduled for each of the October and February visits.

Free-fall MTL string

The free-fall MTL string consisting of 1–3 MTLs inside of an internal core barrel was deployed for three separate runs in Hole C0019E. Run 1 was entirely within the water column, whereas Runs 2 and 3 recorded in the water column and subseafloor. The respective measurements from the sensors were consistent and nearly identical to each other throughout the course of the deployments. For simplicity, the figures within this section show only the results from the lowermost sensor. The absolute recorded depths converted internally from pressure measurements are slightly larger than reported from the drill floor and likely need correction. The subseafloor temperatures recorded were highly disturbed by the drilling process and changed steadily when continuously monitored at a given depth. Estimates of undisturbed formation temperature from the data will require further analysis and modeling. Pressure/

depth data are high enough resolution to clearly record oscillations consistent in period with heave motion recorded on board the *Chikyu*. The magnitude of these vertical oscillations appears to increase with accelerations of the core line winch upon extraction or following a drill stand being added or removed.

Run 1: 12 May 2012

During WOW on 12 May 2012, the free-fall MTL string was deployed with one sensor (serial number 023949) at ~1630 h Japan Standard Time (JST). After reaching the bottom of the drill string, it was retrieved by the core line winch and exited the water at ~1915 h. The bottom of the drill string was in the water column for the duration of the run and never below seafloor. Figure **F64** shows the recorded temperatures and depth as a function of time, whereas Figure **F65** shows the temperature data as a function of depth. Differences in temperature at a given depth from when the instrument was going up and going down likely reflect the effects of the instrument response time to changes in temperature and the fast speed at which the instrument changed depth during free fall and retrieval.

Run 2: 16 May 2012

During WOW on 16 May 2012, the free-fall MTL string was deployed with three MTLs (from bottom to top, serial numbers 023950, 023949, and 023947) at ~0700 h. It was recovered by core line winch and exited the water at ~1530 h for a total deployment duration of ~8.5 h. Figure **F66** shows the recorded temperatures and depth as a function of time, whereas Figure **F67** shows the temperature data as a function of depth. Figure **F67B** is zoomed in to show results while below seafloor and is annotated to describe how temperature changed in conjunction with other operations.

Run 3: 22–24 May 2012

After reaching TD in Hole C0019E and following the circulation of kill mud on 22 May 2012, the free-fall MTL string was deployed at ~1830 h with three MTLs in the same arrangement as Run 2. The free-fall MTL string was left within the drill string; it was not recovered by core line winch but was rather recovered by shortening the drill string stand by stand to the rig floor. The entire deployment lasted ~33 h, ending at ~0400 h on 24 May. Figure **F68** shows the recorded temperatures and depth as a function of time. Figure **F69** shows the temperature data as a function of depth. Figure **F69B** is zoomed in to show results while below seafloor. There was no circulation during the deployment. Interpretation of the temperature profile for the period during extraction will require further analysis and comparison with measured rig floor parameters. A sharp decrease in temperature at ~7900 m water depth likely results from an unplugging of the deplugger nozzle or drill bit and a resultant surge of water from the drill string.

Core-log-seismic integration

Comparison of continuous LWD data and physical properties measurements from core

The MSCL-W NGR and noncontact resistivity (NCR) and discrete sample resistivity measurements made on cores recovered from Hole C0019E were compared to the LWD measurements from Hole C0019B. The distance between the tops of the two holes is thought to be ~5 m from the *Chikyu* sea surface coordinates. NGR and LWD gamma ray values cannot be quantitatively compared because they are recorded in different units (counts per second and gAPI, respectively). NGR values were overlain on the LWD values with a scale that allowed for comparison of trends in the data (Fig. **F22**). Because of the limited time available for processing core data, a unit conversion was not performed on the gamma ray data; also, NCR core measurements were not corrected for temperature variations downhole.

NGR values in Core 343-C0019E-1R (~176.5–185 mbsf) have more scatter than the LWD values and show a slight increase with depth that is not apparent in the LWD data (Fig. **F22**). The NCR values are overlain on the average deep, medium, and shallow button resistivity LWD curves in Figure **F22.** The reliable NCR values are generally lower than the LWD resistivity with the difference between the two measurements decreasing toward the base of Core 1R. Note, however, that within the NCR data, scatter toward higher values is a result of air in gaps and fractures in the measured whole-round core sections. The discrete resistivity measurements have a similar relationship to LWD resistivity; values taken on the core are generally lower and the difference between the two measurements decreases toward the bottom of the core.

Recovery of material in Cores 343-C0019E-2R and 3R (~648–660 mbsf) was highly fragmented and sorted, therefore MCSL-W values are likely not representative of intact formation; however, we compare them here. NGR values are more variable than LWD gamma ray measurements; they also show a stepwise decrease at the boundary between the cores (~650 mbsf), whereas in the gamma ray log an increase with depth trend is observed. NCR resistivity values of Cores 2R and 3R do not match LWD resistivity;

they are lower by ~0.4 Ωm. There were no discrete resistivity measurements made on Cores 2R and 3R to compare to the LWD data.

Cores 343-C0019E-4R through 9R were recovered from ~688.5 to 725 mbsf. NGR measurements on the core are scattered but have a relatively consistent value range. The LWD gamma ray curve exhibits lows at 700 and 720 mbsf that are not observed in the NGR. The NCR correlates fairly well with the LWD resistivity from 688.5 to 720 mbsf with some scatter into higher values. From 720 to 725 mbsf, NCR values are still scattered and slightly higher than LWD resistivity. The discrete resistivity measurements in this zone agree well with the LWD data.

Cores 343-C0019E-10R through 21R were recovered from ~770 to 837 mbsf. Within this zone, NGR values match LWD gamma ray values well with some scatter. The zone of increased gamma ray values on the LWD logs corresponding to log Unit III (~820–835 mbsf) is seen in the NGR measurements but is ~3 m shallower. NCR values are scattered but match LWD data well except from ~818 to 826 mbsf. Within this zone NCR measurements show larger variation than LWD resistivity. The discrete resistivity measurements match the LWD data well. The spike in LWD resistivity (~836 mbsf) marking the top of log Unit IV was also observed on Core 343-C0019E-21R. Recovery was poor in this core, and consisted of pebbles. Therefore, no conclusions can be drawn regarding a depth shift between the holes.

Overall, the data from LWD and core measurements are in general agreement. Comparison of the two gamma ray data sets indicates the cored hole may be ~3 m shallower. The shift is observed in the lower section, where log Unit III is characterized by increased gamma radiation. In the shallower section, a lack of significant gamma ray excursions makes it difficult to correlate the data sets. The comparison of resistivity data sets does not clearly indicate any shift between holes; this may be partly due to the relatively low quality of NCR measurements and limited number of discrete sample measurements.

Seismic integration with LWD data

Seismic characteristics on the regional scale

Interpretations of regional seismic imaging generally identify three major seismic units in the lower trench slope where Site C0019 was drilled (Fig. **F19;** e.g., Tsuru et al., 2002). The uppermost unit (seismic Unit A) is wedge shaped with an acoustically chaotic character, without continuous reflectors, and corresponds to the frontal prism. The second unit (seismic Unit B) consists of continuous/semicontinuous subhorizontal reflectors interpreted as underthrust bedded layers or décollement surfaces. The lowermost unit (seismic Unit C) is the acoustic basement, probably corresponding to oceanic igneous crust.

Synthetic seismogram and time-depth calibration

To aid integration of LWD and seismic data, a synthetic seismic trace was created for Hole C0019B. The density and velocity logs used to determine the reflectivity series were calculated from resistivity-based porosity (see **"Logging while drilling"** in the "Methods" chapter [Expedition 343/343T Scientists, 2013]) and a wavelet extracted from Line HD33B. The wavelet and seismic data are Society of Exploration Geophysicists (SEG) reverse polarity (increases in acoustic impedance are troughs) and have a peak frequency of 48–50 Hz. The synthetic trace shows five possible significant reflectors at the seafloor and 70, 269, 368, and 839 mbsf.

An initial time-depth relationship was calculated at the LWD sampling interval (0.1524 m) for the borehole using the velocity log calculated from resistivity. The water column velocity was calculated from mudline depth on logs and the two-way traveltime of the seafloor reflector from seismic data. To preserve the character of the seafloor reflection, the calculated velocity log was spliced in at 3 m above the seafloor. The spliced log was used to determine Δt at the log sample interval, which was then integrated to get one-way traveltimes for each depth.

In the initial comparison of the synthetic seismic trace with the seismic data, the timing of the seafloor lined up well but the deeper section appeared slightly shifted. The three reflectors on the synthetic trace at 70, 269, and 358 mbsf were located within seismic Unit A. Observed coherent reflectors are rare in seismic Unit A and, where present, are often overprinted by steeply dipping noise, so confident correlations within the unit are difficult. The lower strong reflector on the synthetic trace was located within seismic Unit B but did not correlate with a specific observed seismic reflector using the initial time-depth relationship. To aid in better correlating the lower section, cross-correlation of the seismic and the lower 87 m of the synthetic was computed. The result indicates the synthetic reflector at 839 mbsf correlates best with the first strong reflector of bedded unit (9994 ms). To facilitate the fit of the synthetic and observed seismic traces, the rock velocities calculated from resistivity were increased uniformly by 2.5% and the time-depth relationship was recal-

culated. The fit of the synthetic seismic trace for Hole C0019B to the observed seismic data using the final time-depth relationship is shown in Figure F70.

Comparison of log and seismic units

The seismic section calibrated with the final time-depth relationship and the synthetic seismogram is compared to the four log units (Fig. F71; see "Log characterization and lithologic interpretation"). Log Unit I and most of log Unit II correspond to seismic Unit A. At the log Unit I/II boundary the reflection coefficient does not peak but reflectivity generally decreases across the boundary. Within log Units I and II, the reflectivity variations are coincident with resistivity excursions and likely represent structural or bedding features within the units.

The base of log Unit II and log Units III and IV are located within seismic Unit B. The top of log Unit III is coincident with a negative reflection coefficient, but because of the limited bandwidth of the synthetic and seismic data, it does not align with a peak on the seismic data at the location of Hole C0019B. The top of log Unit IV is coincident with a spike in resistivity and a strong positive-negative reflection coefficient pair. At 5 m below the top of the unit is a stepwise increase in resistivity and a strong positive reflection coefficient. The result in the synthetic seismogram is a tuned waveform with an apparent strong reflection just below the top of log Unit IV that matches well with the seismic section.

The seismic Unit A/B boundary is a continuous but relatively weak reflector on the seismic section. The boundary coincides with a slight stepwise increase in LWD resistivity and a small positive reflection coefficient at 785 mbsf. On the synthetic seismogram the boundary is represented by a relatively weak reflector consistent with the seismic character.

Geology and geophysics of Site C0019

Core, log, and seismic data are integrated, and the identified log units and structural domains, seismic units, lithologic units, and major structural features are compared in order to develop a unified interpretation of the geology and geophysics of the drill site. The log units are based on LWD gamma ray and resistivity responses and compare favorably with lithologic units identified through core analysis, particularly at the base of the borehole where contrasts in lithology and geophysical response are most dramatic (Fig. F72). The log Unit II/III, structural Domain 2/3, and lithologic Unit 3/4 boundaries correlate exactly. The changes observed across this boundary, specifically the abrupt change in bedding dip seen in RAB image logs and core, the increase in clay content of core samples as reflected by the concomitant increase in gamma radiation, K_2O, Al_2O, and MnO, and the presence of the scaly clay fault-rock that make up lithologic Unit 4, point to this boundary as a significant fault contact. The similarity of the lithologic units seen in core below the boundary with strata deposited on the Pacific plate at DSDP Site 436 (Shipboard Scientific Party, 1980) suggests this boundary is the plate interface (i.e., the décollement). Furthermore, the fact that observations of both the core samples and RAB image logs indicate that the entire sediment section above the boundary (structural Domains 1 and 2 and lithologic Units 1–3) is variable, often steeply dipping and fractured, which means it is consistent with a section comprising a shortened and accreted sequence of strata making up the frontal prism.

Above the plate boundary décollement and within the frontal prism, the log unit boundaries, structural domain boundaries, and lithologic boundaries do not correlate well. Boundaries demarcated on the basis of changes in stress indicated by borehole breakout patterns also do not correlate. Moreover, the entire prism (seismic Unit A) at Site C0019 lacks coherent or continuous reflectors and appears relatively transparent in seismic profiles. This likely reflects both the presence of inclined and faulted bedding and the relatively uniform properties of the sediment. Although the spot cores taken at 176.5–186.0 and 648.0–660.5 mbsf are considered to represent different lithologic units, both of these sections, as well as core from deeper intervals in the prism (688.5–729.0 and 770–821.5 mbsf), are mudstones composed predominantly of terrigenous silt and clay with varying amounts of vitric ash and biogenic silica. The subtle cyclicity in gamma ray and resistivity log response with depth in the prism may result from stacked and folded packages of sediment by reverse faulting. The apparent gradual decrease in porosity with depth from progressive consolidation interrupted by stepwise increases in porosity is consistent with such a structural interpretation. Given the variable but dominantly steep eastward dip of the sediment throughout most of the prism, even relatively small displacement on contractional faults would lead to significant repetition of strata as seen in a vertical borehole.

Although log, structural, and lithologic boundaries do not correlate well in the prism, correlations are noted between abrupt changes or discontinuities in different signals at several different locations in the prism. For example, at ~140 mbsf, an abrupt reversal in the progressive change in borehole breakout orientation correlates with a sharp change in bedding from moderate dips to very shallow dips, which

likely reflects a fault contact. Another marked change in borehole breakout distribution occurs at ~550 mbsf, and this appears to correlate with a local low gamma ray response. The fault and bounding fractured zone identified on the basis of RAB image logs and resistivity curves around 720 mbsf correlates with the fault zone at 719–725 mbsf and the geochemical anomaly at 700 mbsf identified in core samples. In addition, this fault coincides with an abrupt change in bedding dip documented in both logs and core.

The final time-depth relationship determined from the synthetic seismic trace and log-based density and seismic velocity model, allows the identification of the plate boundary décollement in the seismic profile. The lowermost strong reflector in the synthetic seismic trace falls within the bedded seismic Unit B. After cross-correlation–based alignment, this strong synthetic reflector at 839 mbsf correlates best with the first strong seismic reflector of the bedded unit at 9994 ms two-way traveltime. In the borehole, the plate boundary décollement occurs at ~820 mbsf, ~20 m shallower than the prominent reflector. Because the first strong reflector is fairly continuous in the seismic profile, one can infer the position of the décollement both landward and seaward in the seismic profile. As shown by the in-line seismic profile that passes through the drill site, this reflector can be traced from the site ~1.2 km to the east-southeast and several kilometers to the west-northwest above the horst. The cross-line seismic profile that passes through the drill site indicates the reflectors are continuous several kilometers parallel to the trench as well. Approximately 1.2 km in-line to the east-southeast, the basement is down-dropped along a normal fault to form a prominent sediment-filled graben that spans the axis of the trench. A distinct reflector continues from the top of the horst to the east and into the sediment fill of the graben (Fig. **F19**). The seismic character along this reflector is consistent with the general seismic structure of the décollement documented at the drill site (i.e., a hanging wall characterized as chaotic and seismically transparent [seismic Unit A] and a footwall consisting of subhorizontal seismic reflectors representing the bedded sediments [seismic Unit B] conformable with the underlying igneous basement of the subducting plate [seismic Unit C]). Thus, the reflector that continues from the horst into the graben and cuts some sediment layers in the footwall defines the décollement at the base of the displaced and thickened prism. The seismic data support the simple interpretation that the prism extends some 5 km east from the drill site to the axis of the trench (also see Kodaira et al., 2012). A first-order palinspastic reconstruction of the prism, assuming constant area balancing, implies the displacement on the décollement at the drill site is on the order of 3 km. Although the deformation associated with the décollement is much more localized than that seen at other subduction décollements (e.g., Nankai, Barbados), the structure and fabric of the décollement at the drill site is compatible with displacements of this magnitude. Thus it is expected that the décollement at the drill site is likely continuous with the deeper portions of the plate boundary interface tens of kilometers downdip. A plate boundary décollement of this size and position is hypothesized as the locus of tectonic displacement of the subducting plate in the geologic past, as well as during the recent rupture that propagated to the trench during the Tohoku-oki event.

References

Apel, E.V., Bürgmann, R., Steblov, G., Vasilenko, N., King, R., and Prytkov, A., 2006. Independent active microplate tectonics of northeast Asia from GPS velocities and block modeling. *Geophys. Res. Lett.,* 33(11):L11303. **doi:10.1029/2006GL026077**

Archie, G.E., 1942. The electrical resistivity log as an aid in determining some reservoir characteristics. *Trans. Am. Inst. Min., Metall. Pet. Eng.,* 146:54–62.

Argus, D.F., Gordon, R.G., and DeMets, C., 2011. Geologically current motion of 56 plates relative to the no-net-rotation reference frame. *Geochem., Geophys., Geosyst.,* 12(11):Q11001. **doi:10.1029/2011GC003751**

Athy, L.F., 1930. Density, porosity, and compaction of sedimentary rocks. *AAPG Bull.,* 14(1):1–24.

Brodsky, E.E., Ma, K.-F., Mori, J., Saffer, D.M., and the participants of the ICDP/SCEC International Workshop, 2009. Rapid response fault drilling: past, present, and future. *Sci. Drill.,* 8:66–74. **doi:10.2204/iodp.sd.8.11.2009**

Expedition 322 Scientists, 2010. Site C0012. *In* Saito, S., Underwood, M.B., Kubo, Y., and the Expedition 322 Scientists, *Proc. IODP,* 322: Tokyo (Integrated Ocean Drilling Program Management International, Inc.). **doi:10.2204/iodp.proc.322.104.2010**

Expedition 343/343T Scientists, 2013. Methods. *In* Chester, F.M., Mori, J., Eguchi, N., Toczko, S., and the Expedition 343/343T Scientists, *Proc. IODP,* 343/343T: Tokyo (Integrated Ocean Drilling Program Management International, Inc.). **doi:10.2204/iodp.proc.343343T.102.2013**

Fujiwara, T., Kodaira, S., No, T., Kaiho, Y., Takahashi, N., and Kaneda, Y., 2011. The 2011 Tohoku-oki earthquake: displacement reaching the trench axis. *Science,* 334(6060):1240. **doi:10.1126/science.1211554**

Hirose, T., Kawagucci, S., and Suzuki, K., 2011. Mechanoradical H_2 generation during simulated faulting: implications for an earthquake-driven subsurface biosphere. *Geophys. Res. Lett.,* 38(17):L17303. **doi:10.1029/2011GL048850**

Kirschvink, J.L., 1980. The least-squares line and plane and the analysis of palaeomagnetic data. *Geophys. J. R. Astron. Soc.,* 62(3):699–718. **doi:10.1111/j.1365-246X.1980.tb02601.x**

Kita, I., Matsuo, S., and Wakita, H., 1982. H_2 generation by reaction between H_2O and crushed rock: an experimental study on H_2 degassing from the active fault zone. *J. Geophys. Res., [Solid Earth],* 87(B13):10789–10795. **doi:10.1029/JB087iB13p10789**

Kodaira, S., No, T., Nakamura, Y., Fujiwara, T., Kaiho, Y., Miura, S., Takahashi, N., Kaneda, Y., and Taira, A., 2012. Coseismic fault rupture at the trench axis during the 2011 Tohoku-oki earthquake. *Nat. Geosci.,* 5(9):646–650. **doi:10.1038/ngeo1547**

Maltman, A., Labaume, P., and Housen, B., 1997. Structural geology of the décollement at the toe of the Barbados accretionary prism. *In* Shipley, T.H., Ogawa, Y., Blum, P., and Bahr, J.M. (Eds.), *Proc. ODP, Sci. Results,* 156: College Station, TX (Ocean Drilling Program), 279–292. **doi:10.2973/odp.proc.sr.156.037.1997**

Moore, G.F., Taira, A., Klaus, A., Becker, L., Boeckel, B., Cragg, B.A., Dean, A., Fergusson, C.L., Henry, P., Hirano, S., Hisamitsu, T., Hunze, S., Kastner, M., Maltman, A.J., Morgan, J.K., Murakami, Y., Saffer, D.M., Sánchez-Gómez, M., Screaton, E.J., Smith, D.C., Spivack, A.J., Steurer, J., Tobin, H.J., Ujiie, K., Underwood, M.B., and Wilson, M., 2001. New insights into deformation and fluid flow processes in the Nankai Trough accretionary prism: results of Ocean Drilling Program Leg 190. *Geochem., Geophys., Geosyst.,* 2(10):1058. **doi:10.1029/2001GC000166**

Mori, J., Chester, F.M., Eguchi, N., and Toczko, S., 2012. Japan Trench Fast Earthquake Drilling Project (JFAST). *IODP Sci. Prosp.,* 343. **doi:10.2204/iodp.sp.343.2012**

Richter, C., Acton, G., Endris, C., and Radsted, M., 2007. Handbook for shipboard paleomagnetists. *ODP Tech. Note,* 34. **doi:10.2973/odp.tn.34.2007**

Sacks, I.S., Suyehiro, K., Acton, G.D., et al., 2000. *Proc. ODP, Init. Repts.,* 186: College Station, TX (Ocean Drilling Program). **doi:10.2973/odp.proc.ir.186.2000**

Scientific Party, 1980. *Init. Repts. DSDP,* 56, 57: Washington, DC (U.S. Govt. Printing Office). **doi:10.2973/dsdp.proc.5657.1980**

Shipboard Scientific Party, 1980. Site 436: Japan Trench outer rise, Leg 56. *In* Scientific Party, *Init. Repts. DSDP,* 56, 57 (Pt. 1): Washington, DC (U.S. Govt. Printing Office), 399–446. **doi:10.2973/dsdp.proc.5657.107.1980**

Tsuru, T., Park, J.-O., Miura, S., Kodaira, S., Kido, Y., and Hayashi, T., 2002. Along-arc structural variation of the plate boundary at the Japan Trench margin: implication of interplate coupling. *J. Geophys. Res., [Solid Earth],* 107(B12):2357. **doi:10.1029/2001JB001664**

Wakita, H., Nakamura, Y., Kita, I., Fujii, N., and Notsu, K., 1980. Hydrogen release: new indicator of fault activity. *Science,* 210(4466):188–190. **doi:10.1126/science.210.4466.188**

Wiersberg, T., and Erzinger, J., 2008. Origin and spatial distribution of gas at seismogenic depths of the San Andreas Fault from drill-mud gas analysis. *Appl. Geochem.,* 23(6):1675–1690. **doi:10.1016/j.apgeochem.2008.01.012**

Zijderveld, J.D.A., 1967. AC demagnetization of rocks: analysis of results. *In* Collinson, D.W., Creer, K.M., and Runcorn, S.K. (Eds.), *Methods in Palaeomagnetism:* Amsterdam (Elsevier), 254–286.

Publication: 19 July 2013
MS 343343T-103

Figure F1. JFAST site map, showing the location of Holes C0019A–C0019E on a contoured bathymetry base map (contours are meters below sea level).

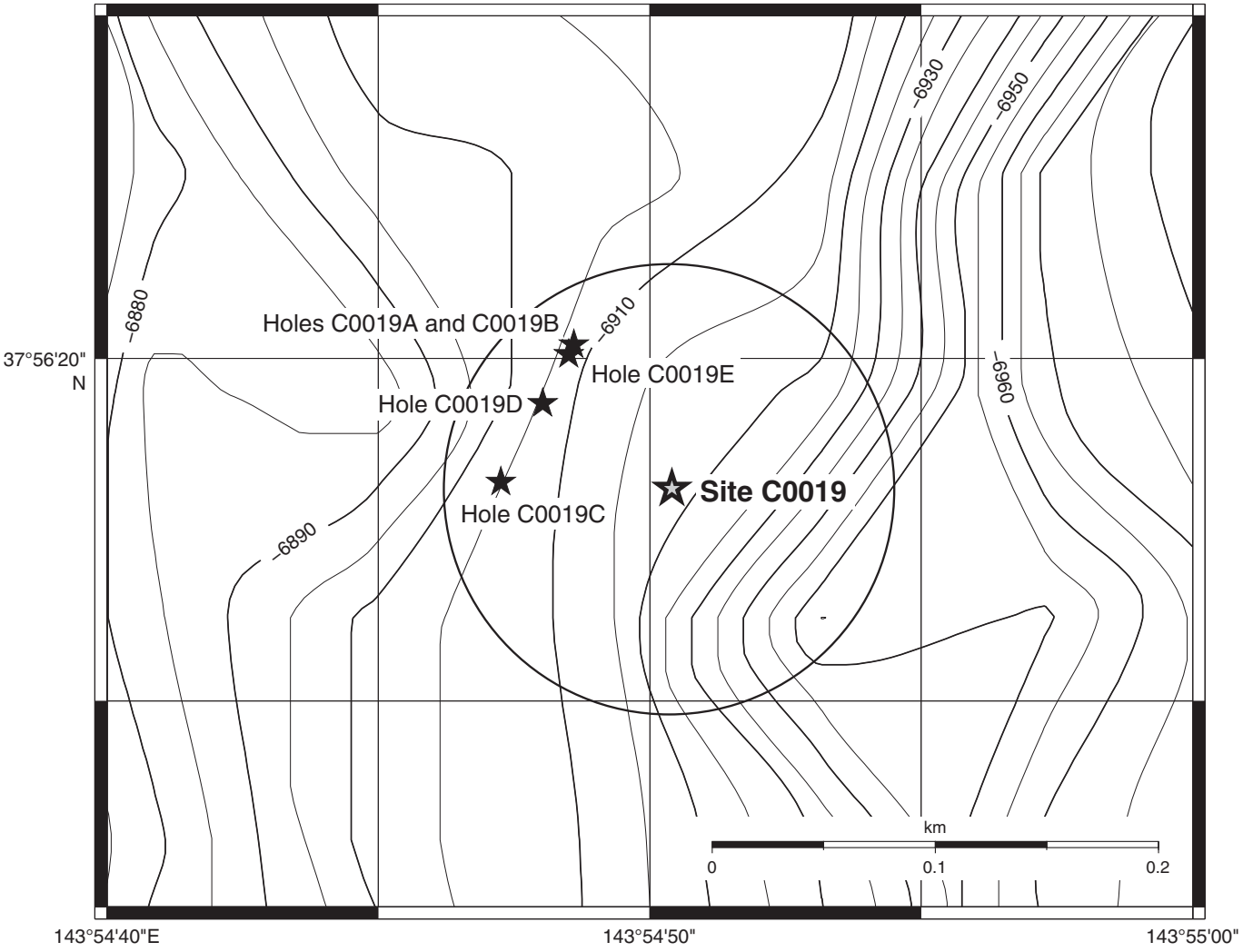

Figure F2. Mudline (seafloor) identification in Hole C0019B using gamma ray and resistivity logs from the geoVISION resistivity (GVR) tool (memory data). The seafloor was identified by a kick in the gamma ray and resistivity logs at 6918 m LWD depth below rig floor (LRF).

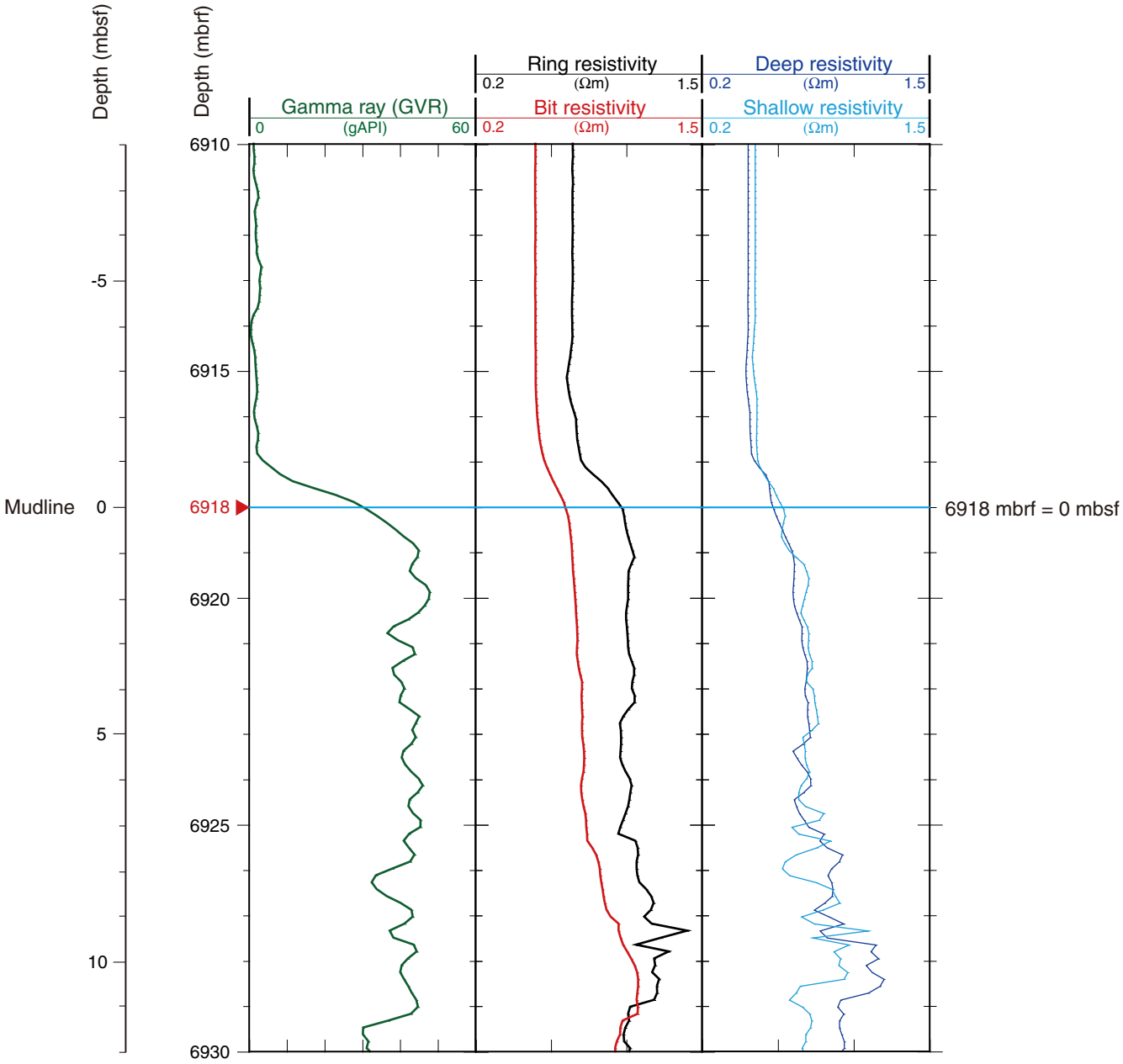

Figure F3. Overview of the log quality control logs, Hole C0019B. ROP = rate of penetration, BD = deep button, BS = shallow button.

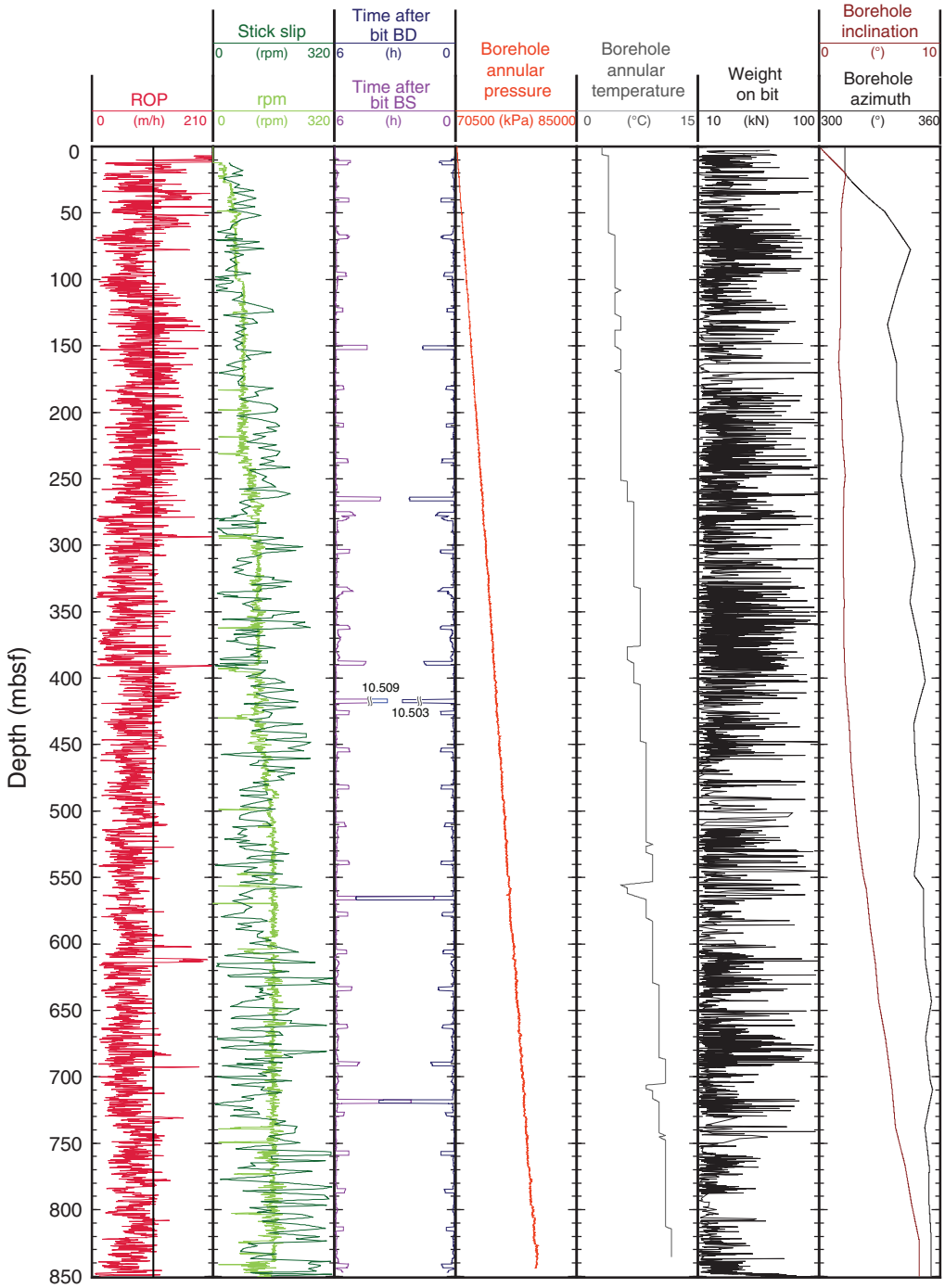

Figure F4. Overview of the log quality control logs, Hole C0019C, showing rate of penetration (ROP), collar rotations per minute (CRPM), weight on bit (WOB), and annular pressure and temperature.

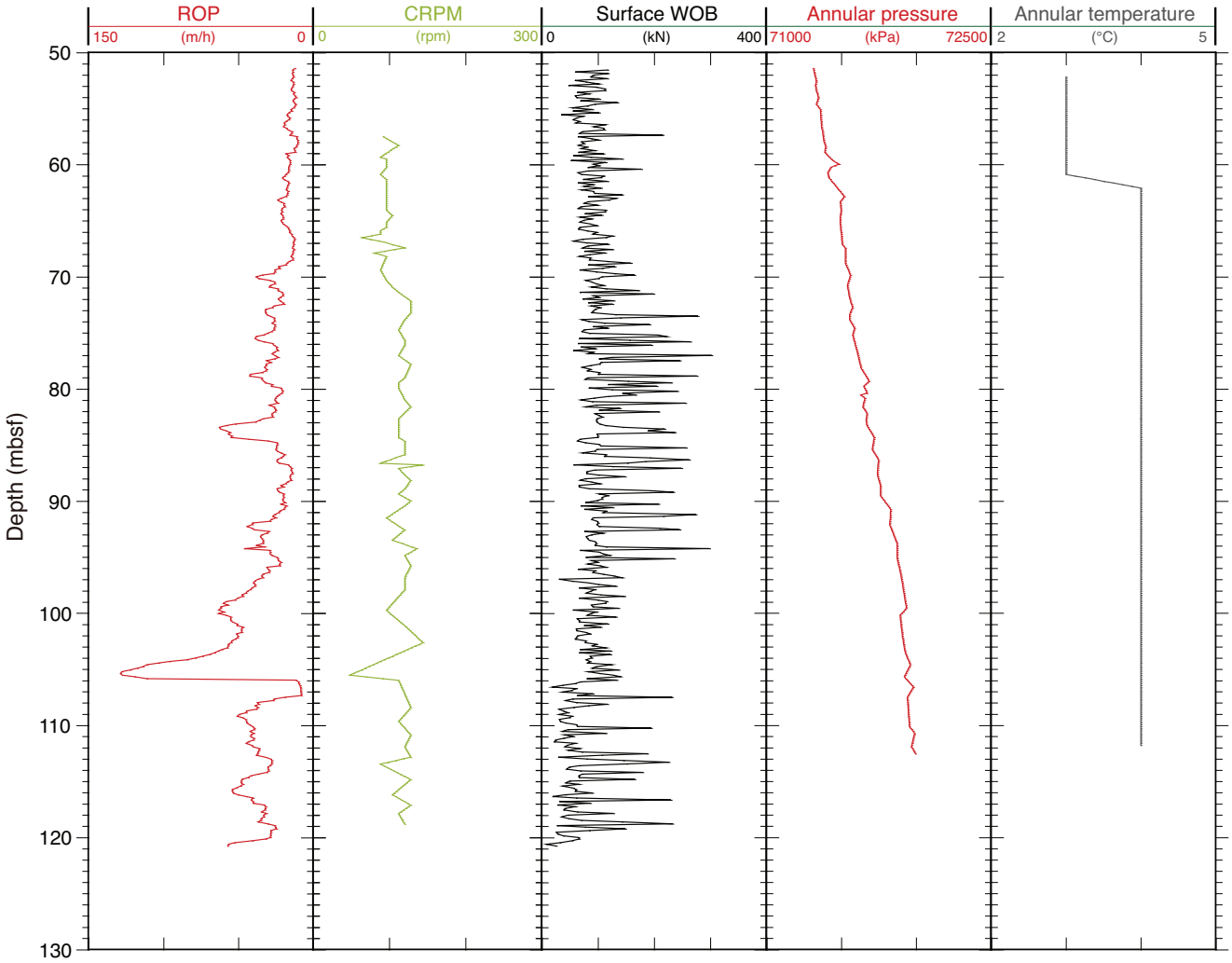

Figure F5. Overview of LWD log data collected in Hole C0019B, showing log units (defined from gamma ray and resistivity); electrical caliper (ECAL) (black line = bit size); gamma ray; bit and ring resistivity; average deep, medium, and shallow resistivity; and resistivity-at-the-bit (RAB) electrical image.

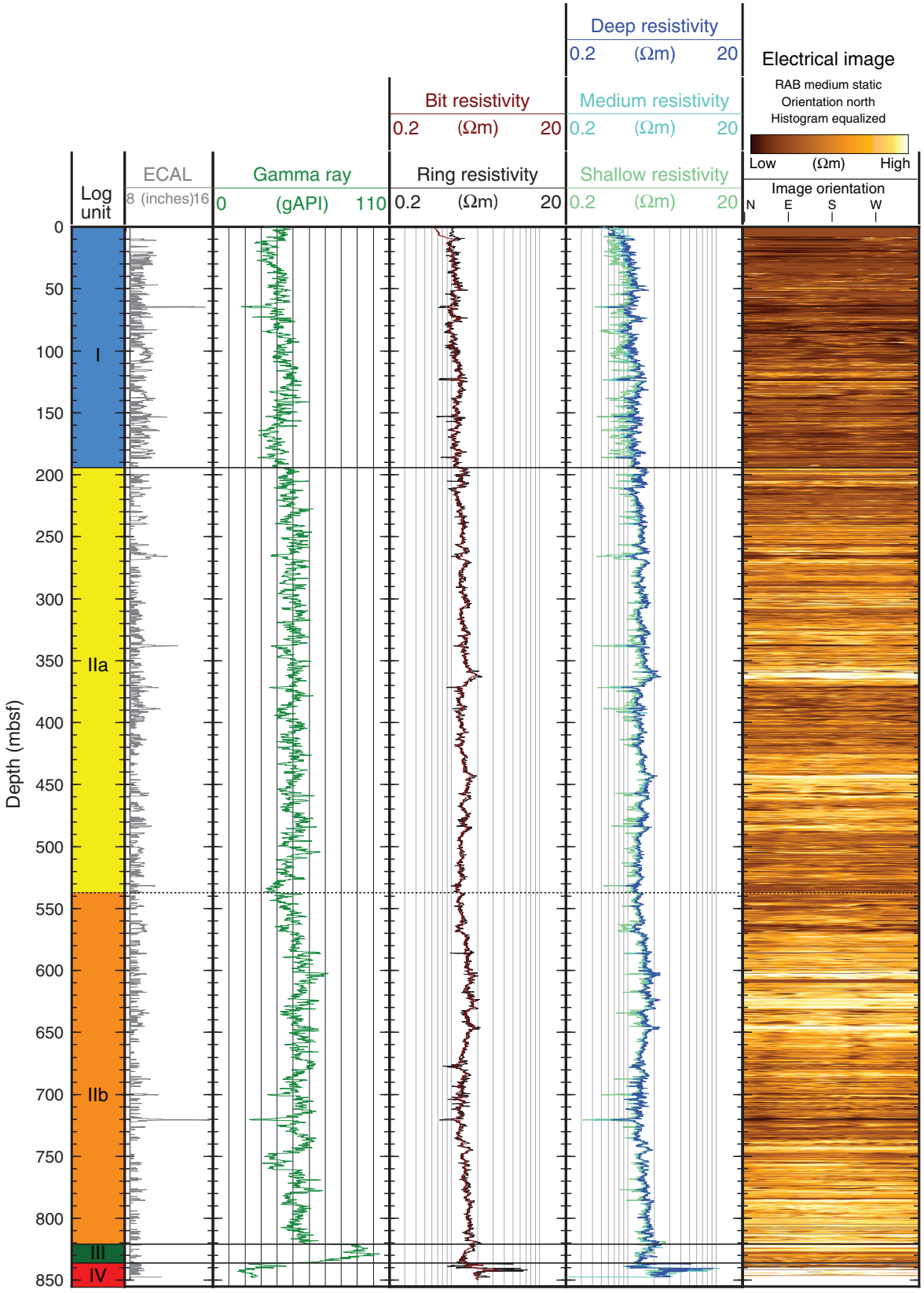

Figure F6. Cross-plot of deep button resistivity and gamma ray showing the distribution of each of the defined log units, Hole C0019B.

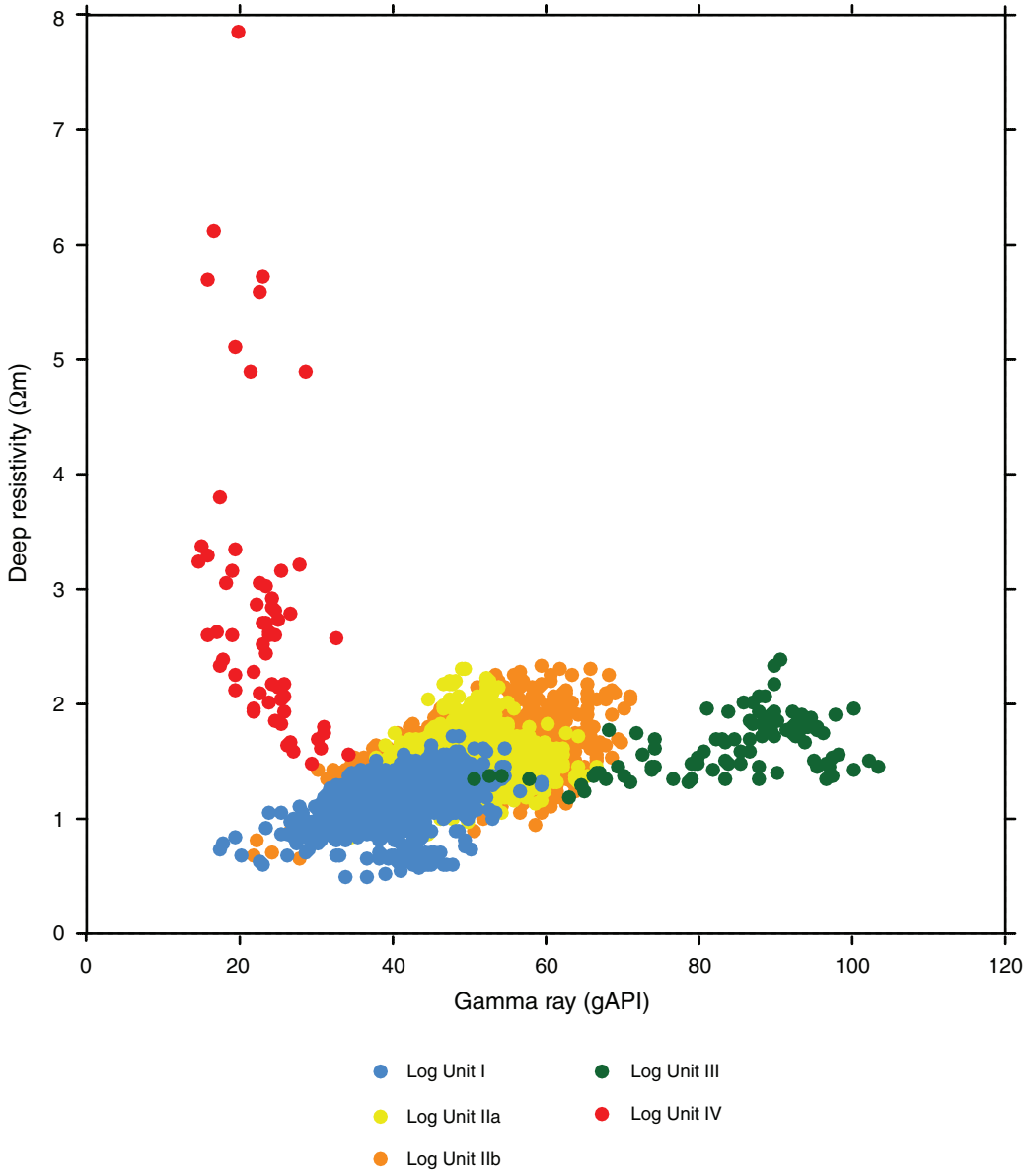

Figure F7. Box and whisker plots showing the (**A**) gamma ray and (**B**) deep resistivity value ranges for each of the defined log units, Hole C0019B. Box and whisker plots comprise the minimum, 25 percentile, median, 75 percentile, and maximum values.

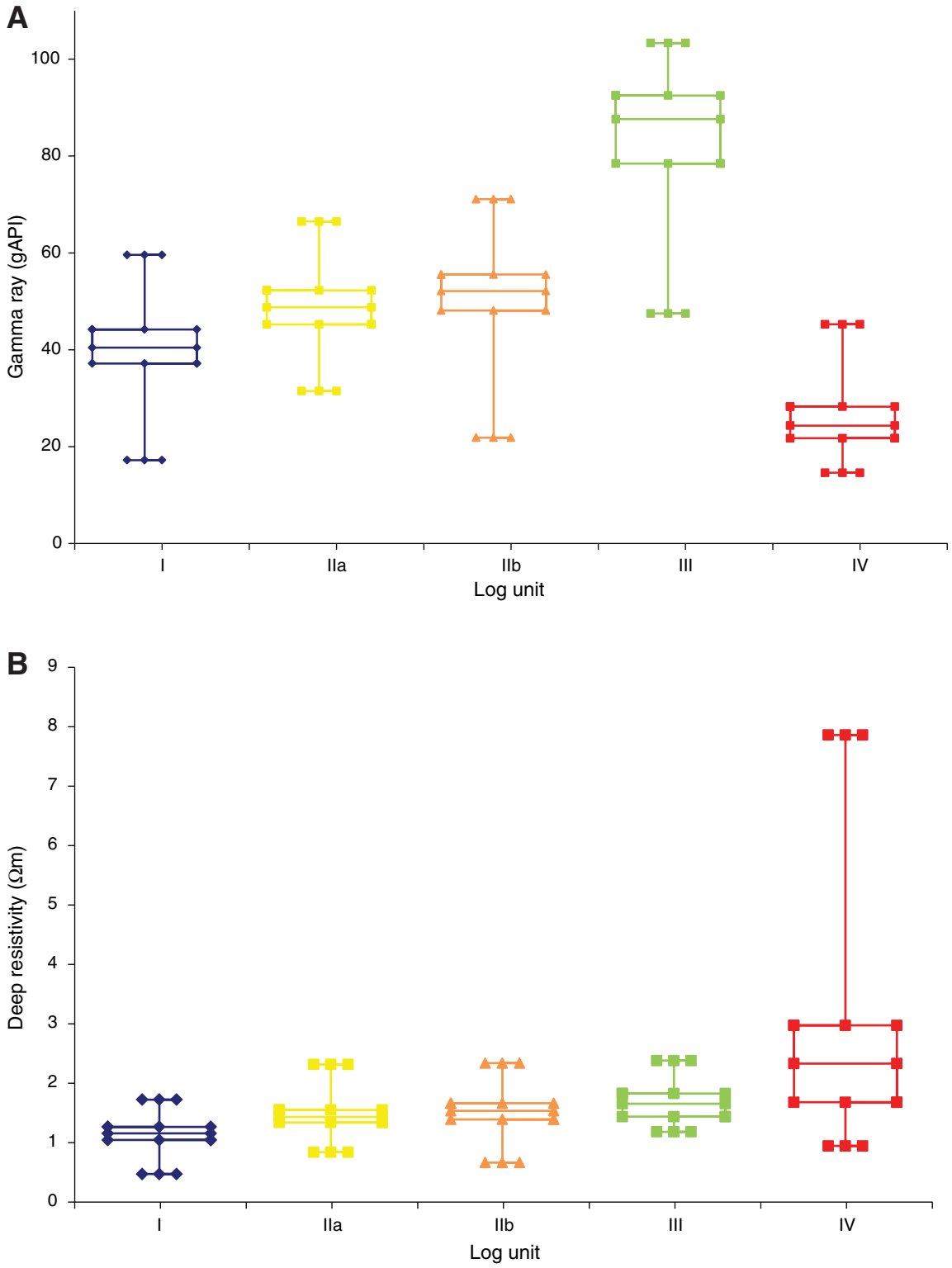

Figure F8. Overview of real-time data collected in Hole C0019C, showing total gamma ray, ring resistivity, bit resistivity, average shallow button resistivity, average deep button resistivity, and annular temperature.

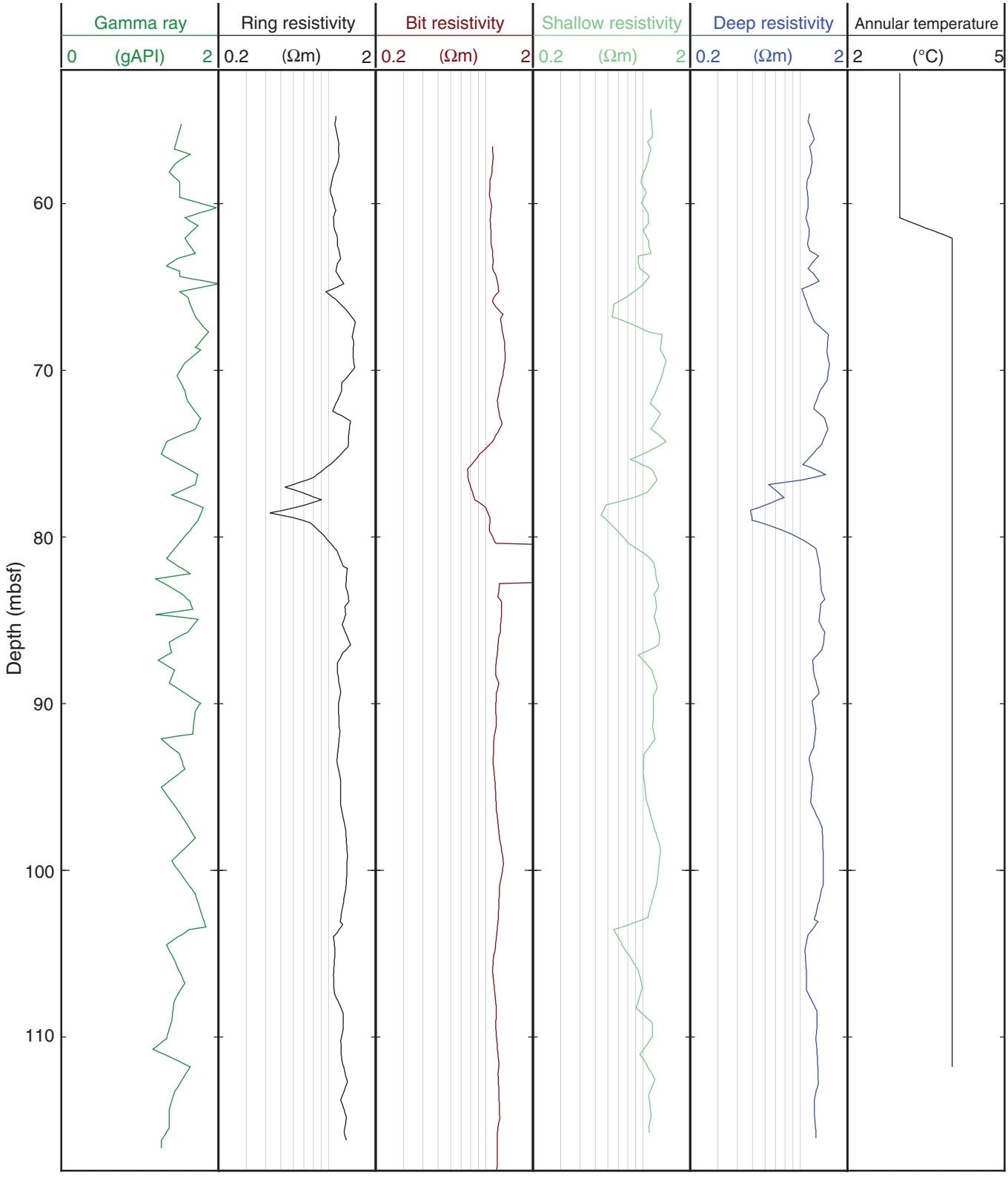

Figure F9. Plot of gamma ray, five resistivity logs, and the difference between deep and shallow resistivity illustrating variation in log response between the different log units, Site C0019.

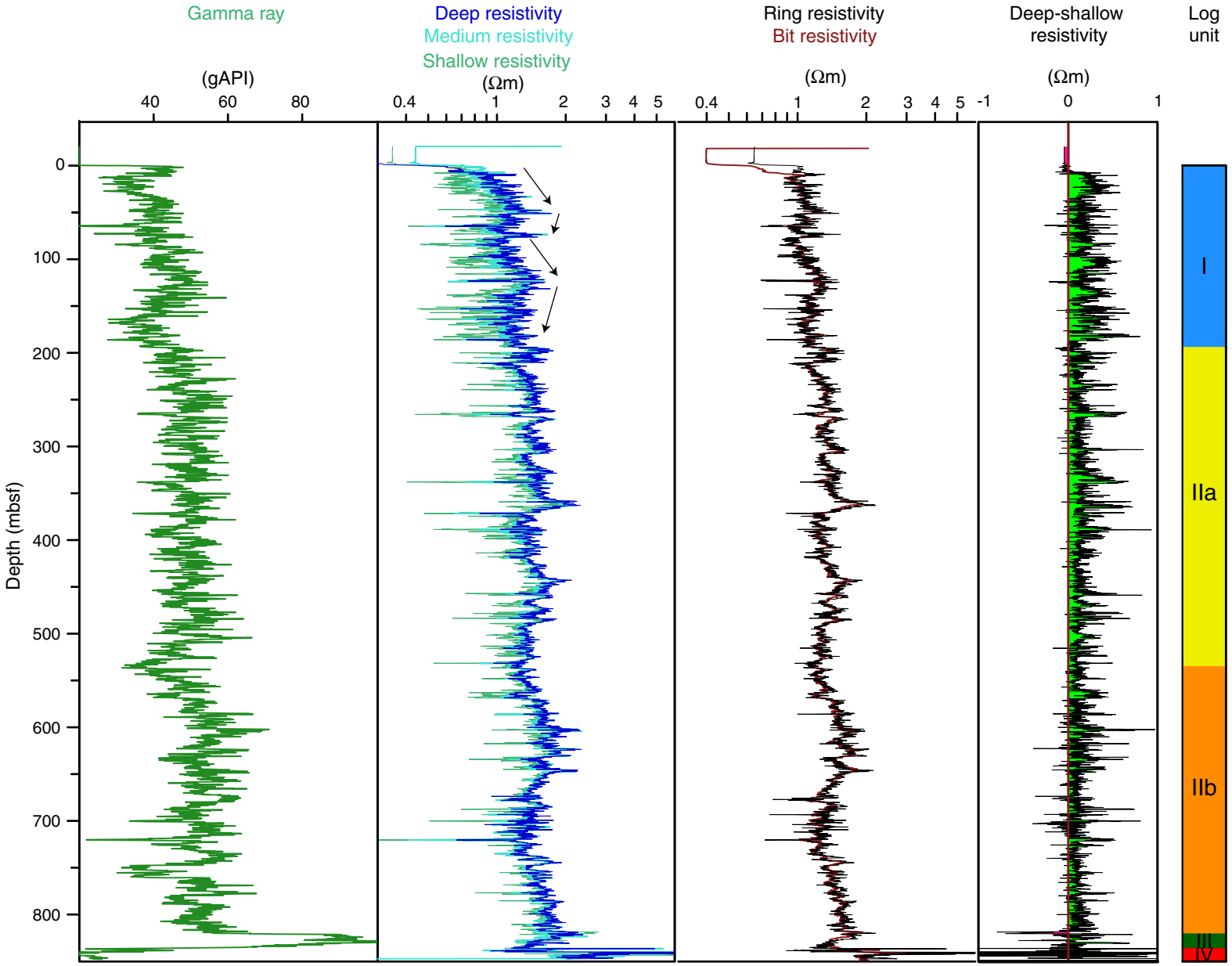

Figure F10. Correlation diagrams of (**A**) deep vs. shallow resistivity and (**B**) bit vs. ring resistivity, Hole C0019B.

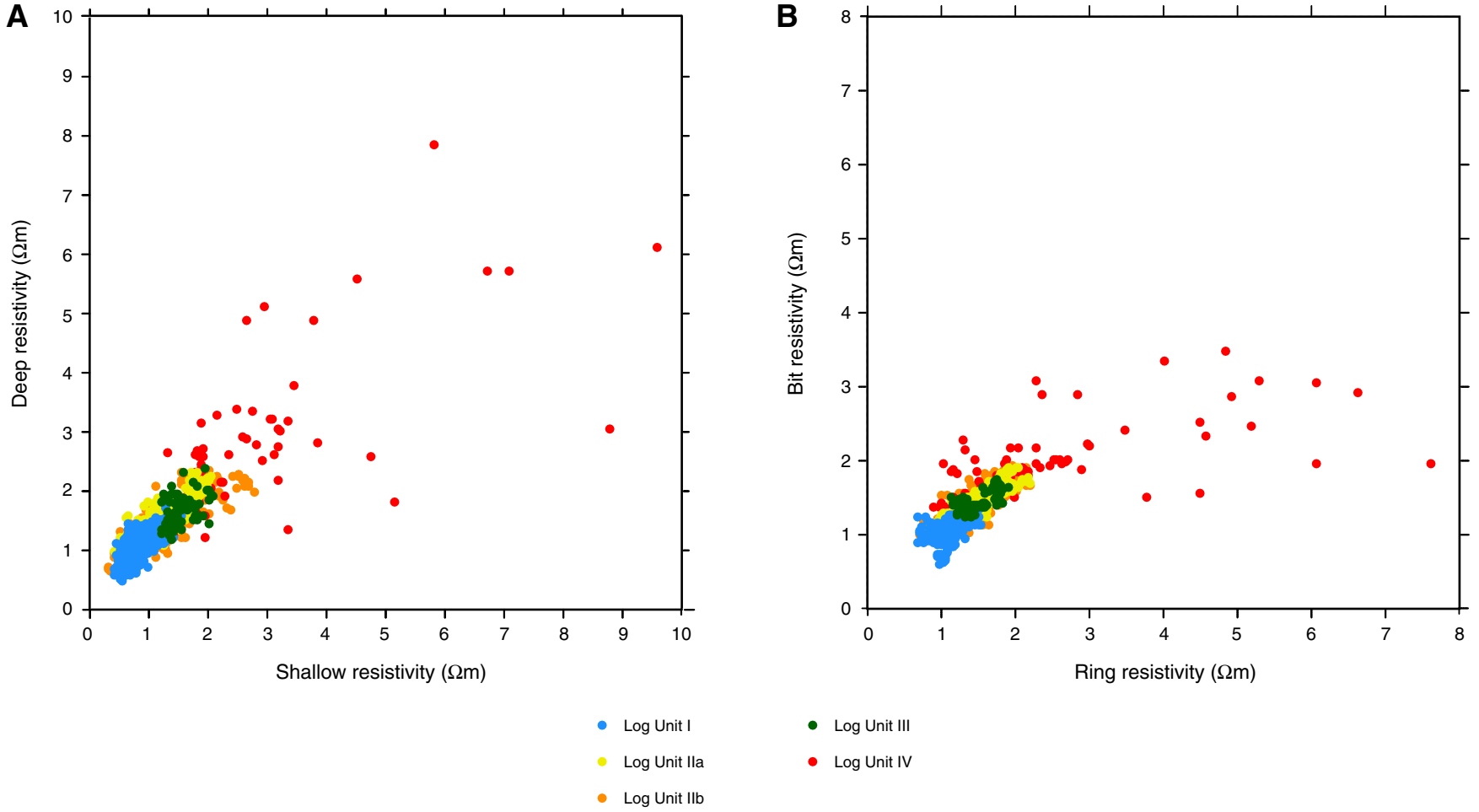

Figure F11. Plot of gamma ray, five resistivity logs, and the difference between deep and shallow resistivity illustrating variation in log response between log Units III and IV, Hole C0019B.

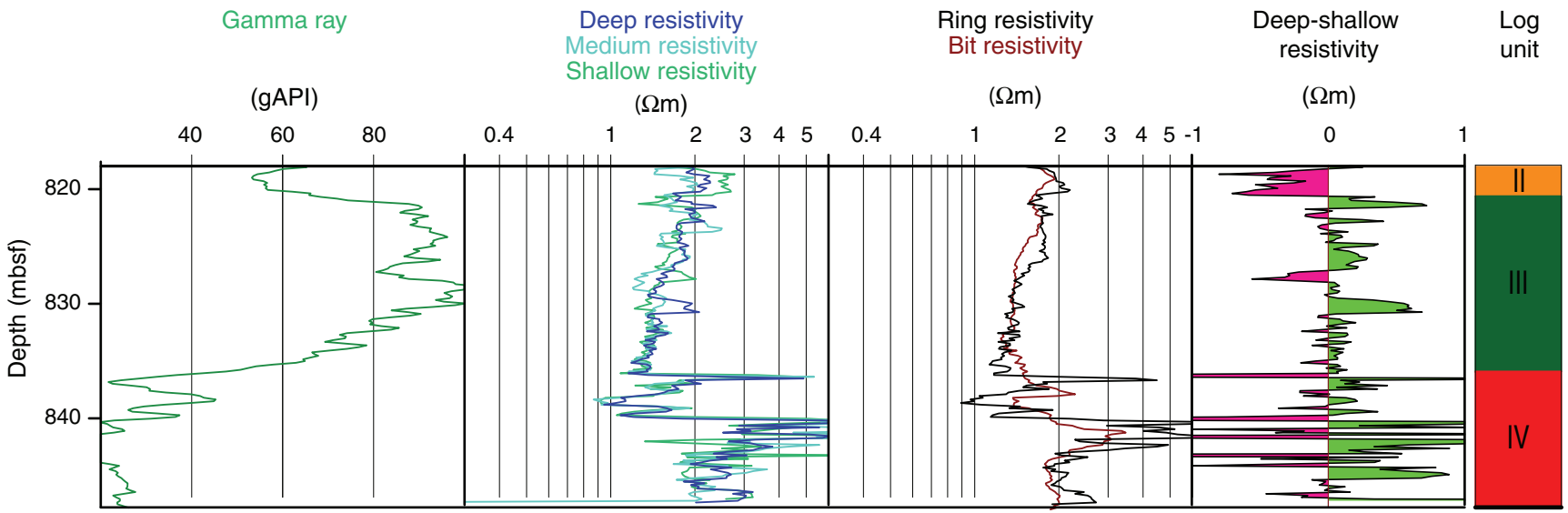

Figure F12. Plot of calculated temperature, porosity, and density for Hole C0019B.

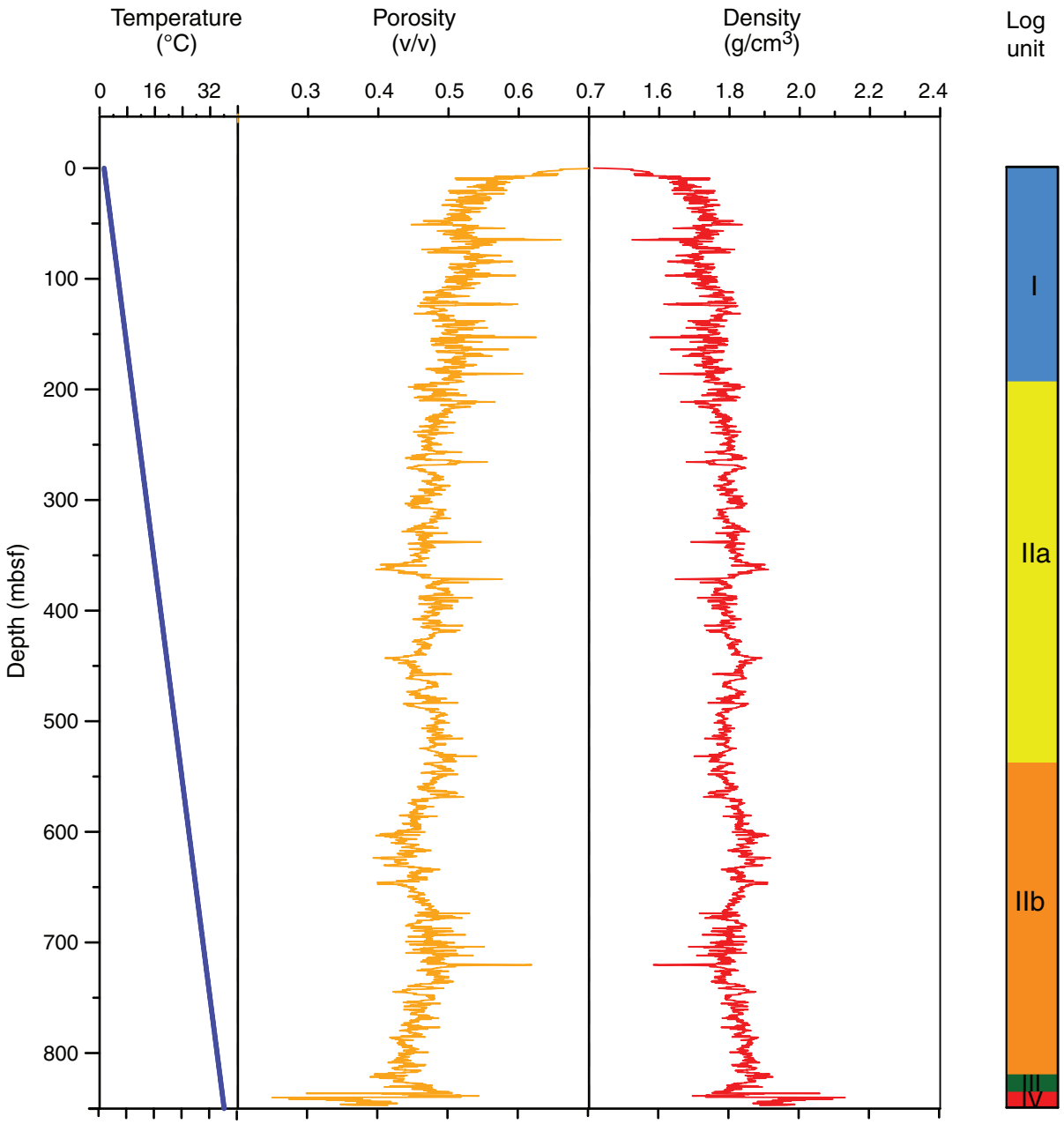

Figure F13. A. Examples of repeated picks on bedding surfaces, Hole C0019B. A number of sinusoids show similarly dipping planar surfaces that are interpreted as bedding. In contrast, fractures tend to be isolated planar surfaces. Four panels represent shallow, medium, and deep images with static normalization and a final medium image with dynamic normalization. Note the variation in images depending on the depth of investigation and normalization. **B.** Examples of high-resistivity layers at base of the hole. The layers are higher resistivity than any other feature observed elsewhere in the borehole and are interpreted as chert layers.

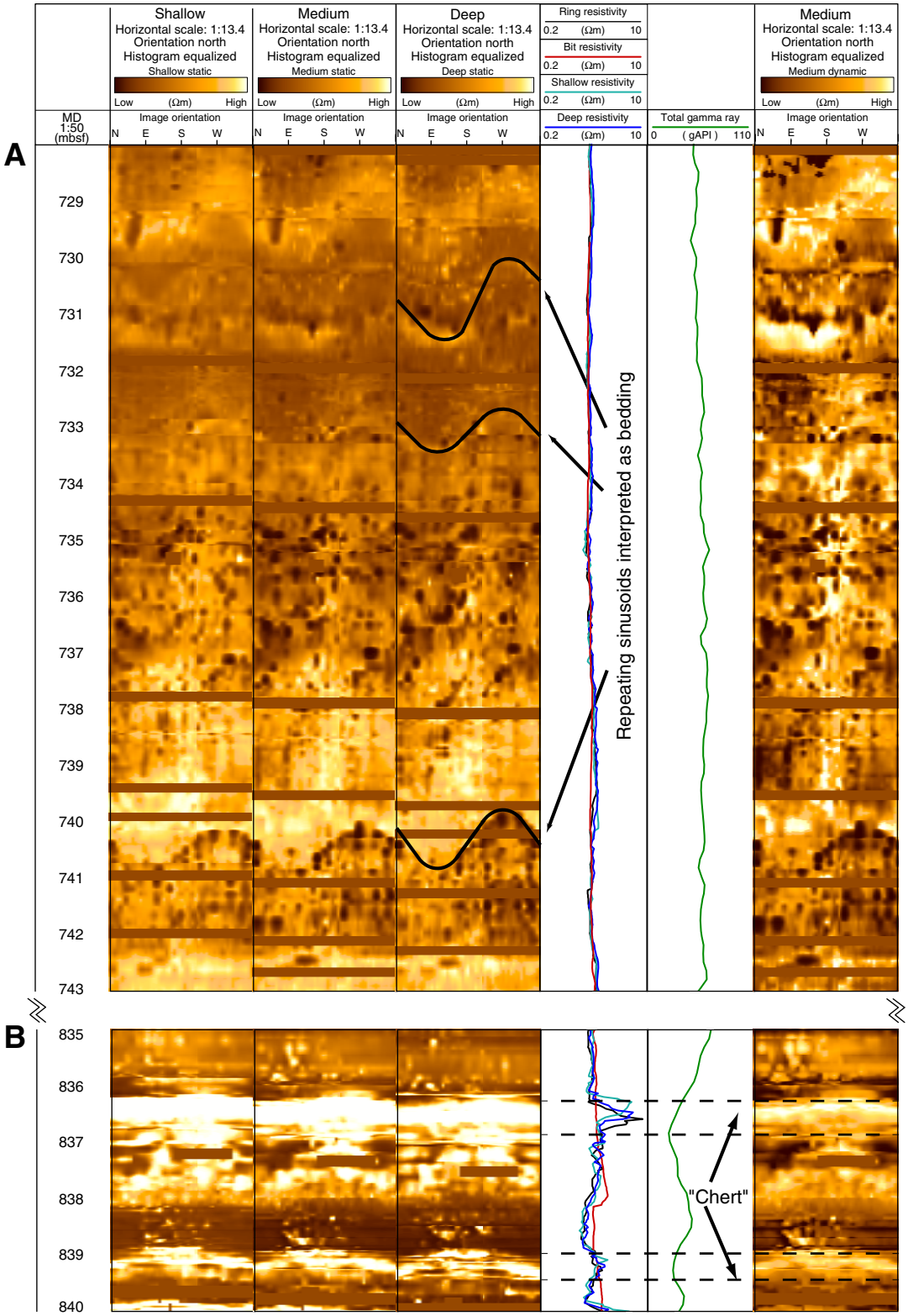

Figure F14. Distribution of bedding dips and faults/fractures with depth, Hole C0019B. Note that bedding dips are shallower in structural Domains 1 and 3 and steeper in Domain 2. Structural domain f = fracture zone (correlates with depth of probable fault at 720 mbsf) and is located based on LWD data only.

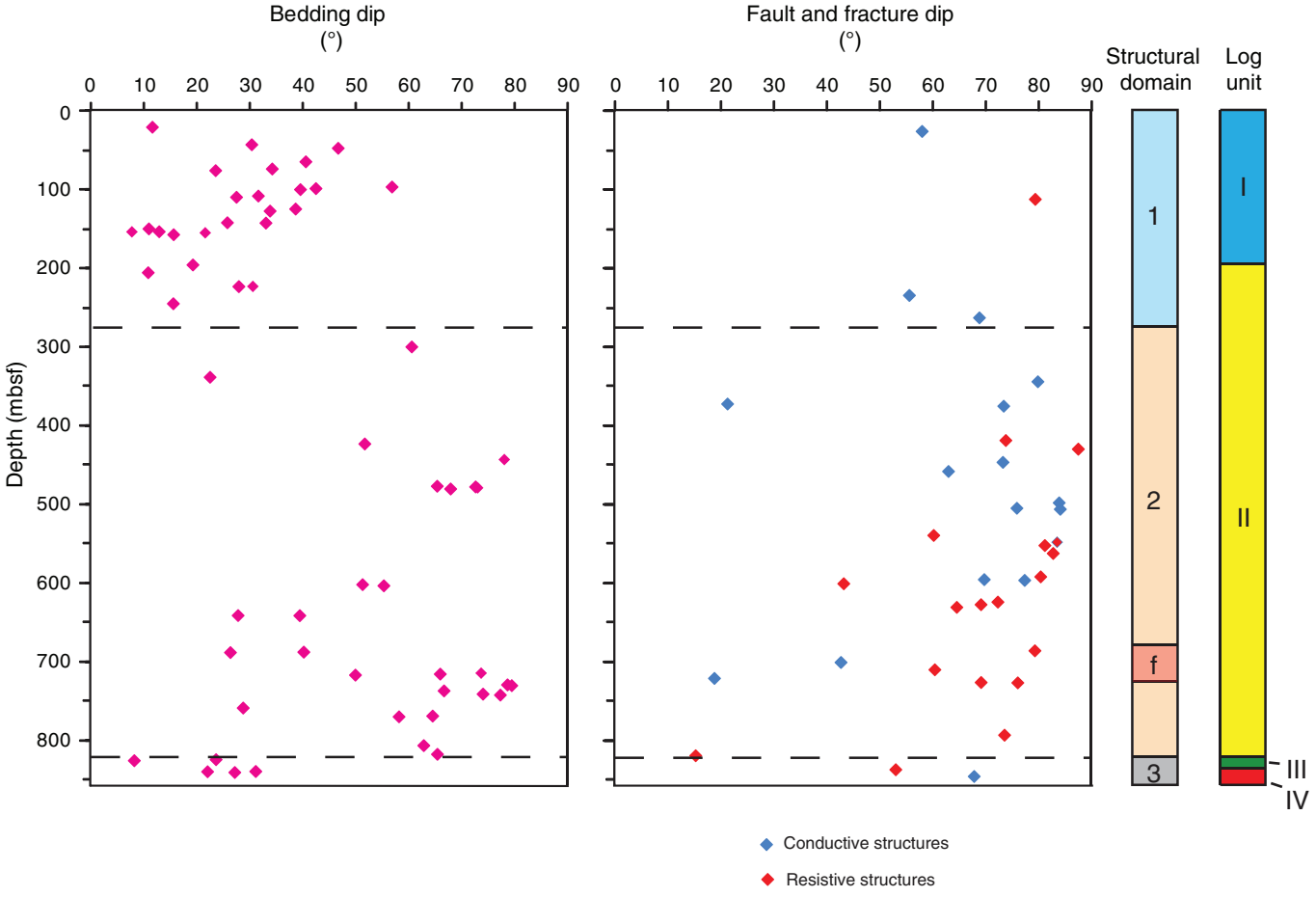

Figure F15. Stereographic projections, Site C0019. **A.** Bedding. Note girdle trending 300°, suggesting a fold trend of 030°, subparallel to the trench slope. **B.** Fractures/Faults. Note broader girdle, albeit still trending to the northwest.

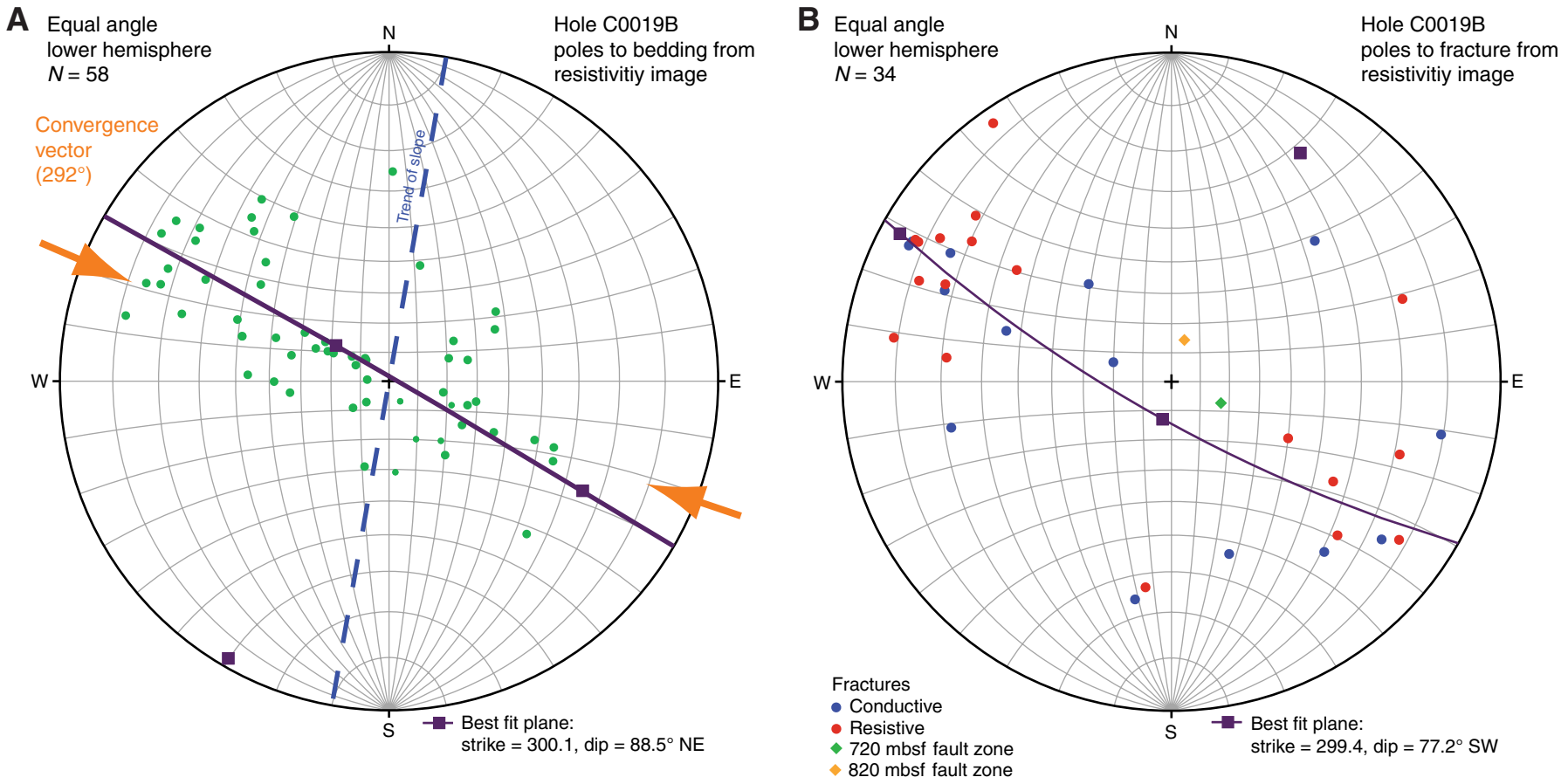

Figure F16. Fault at 720 mbsf identified as a zone of high conductivity at 720–721 mbsf, Site C0019. Note variations in imaging of feature across the four panels. The high-conductivity zone appears wider on static images relative to the single dynamic image. However, the range of low resistivity values in curve data provides convincing evidence of a 1 m thickness.

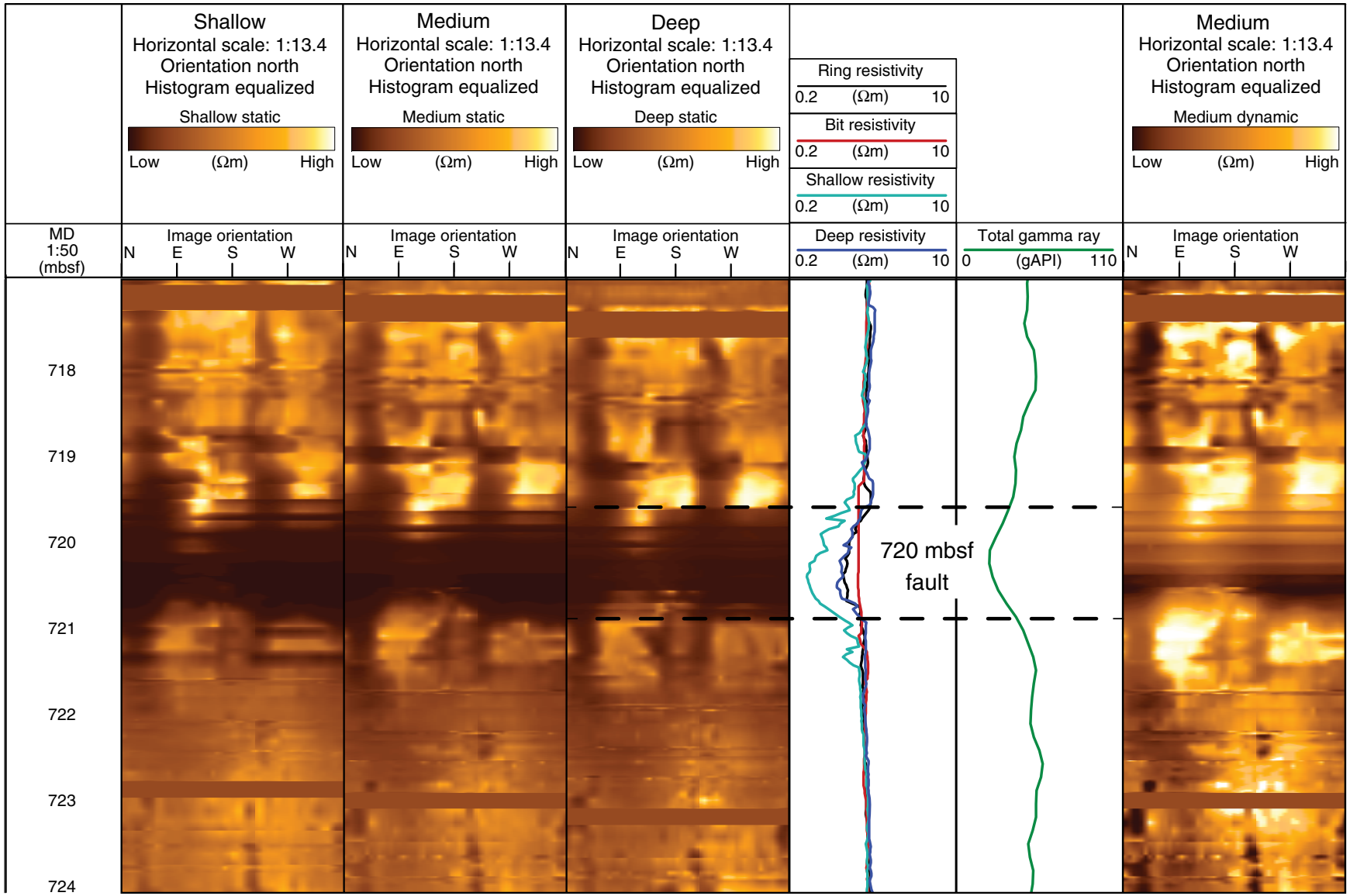

Figure F17. A. Projection of bedding attitudes onto plane trending 300°, the mean plane of the girdle of bedding dips, Site C0019. Bedding attitudes are projected from inclined orientation of the well along an average azimuth also projected into the plane oriented at 300°. **B.** Structural interpretation of bedding dips based on data in A. Interpretation accommodates shallow bedding dips of structural Domain 1 and steeper bedding dips of structural Domain 2, including a sequence of sheared-out folds around the probable fault at 720 mbsf. The relatively shallow dips of structural Domain 3 occur below the probable fault at 820 mbsf and lie in a zone of shallowly dipping reflectors just above the oceanic basement. This structural interpretation accommodates the bedding dip information as well as possible but is only one of many possible interpretations that could fit the available data. Dashed red lines = fault locations.

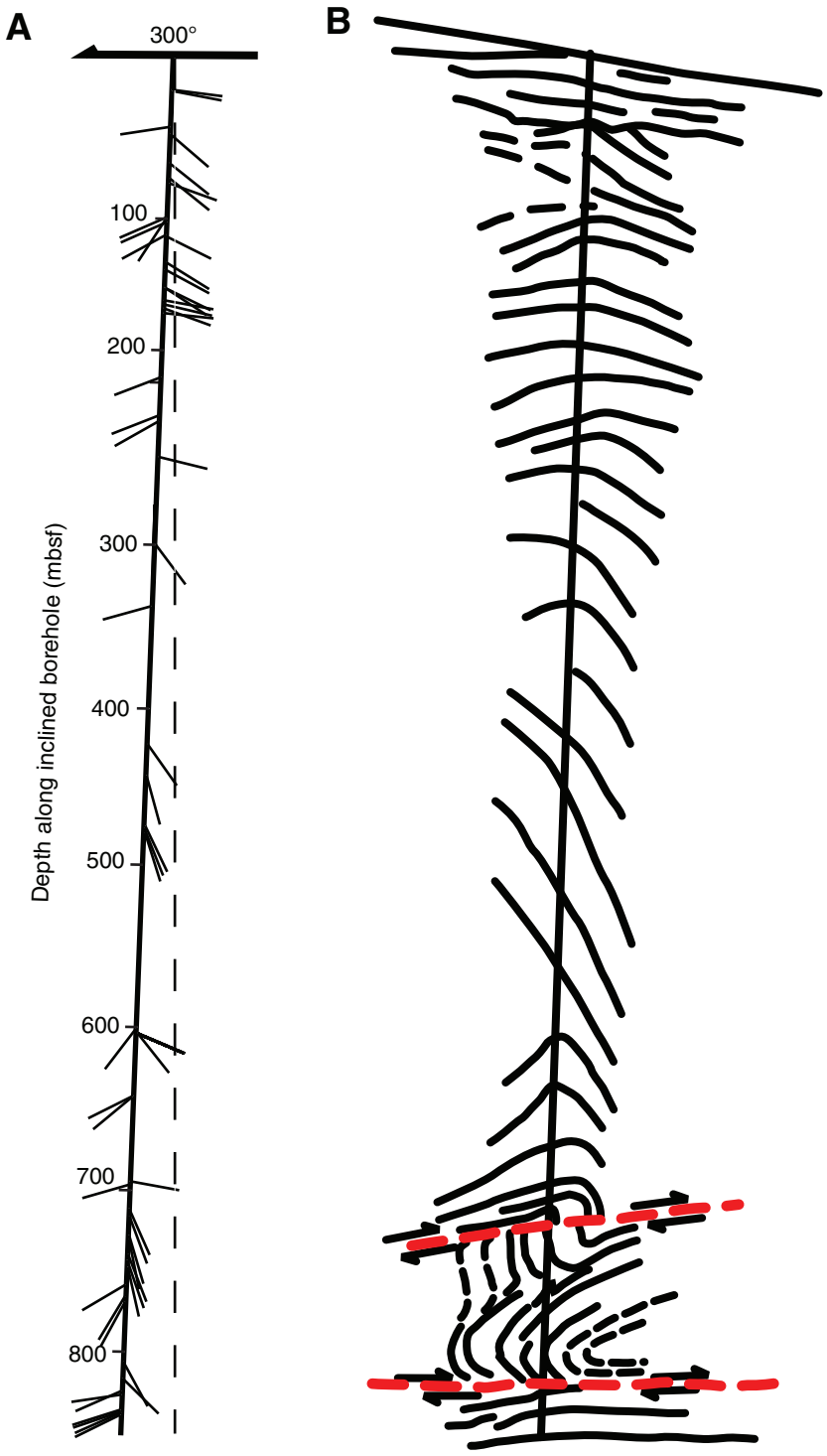

Figure F18. Fault zone at 820 mbsf, Site C0019. Interval extending from ~814 to 846 mbsf shows elevated resistivity and separates the high bedding dips of structural Domain 2 from low bedding dips of structural Domain 3. The 820 fault lies within layered reflectors at the sedimentary section base and may represent a true décollement surface separating the more deformed overlying structural Domain 2 from the lesser deformed underthrust brown clay-chert of structural Domain 3.

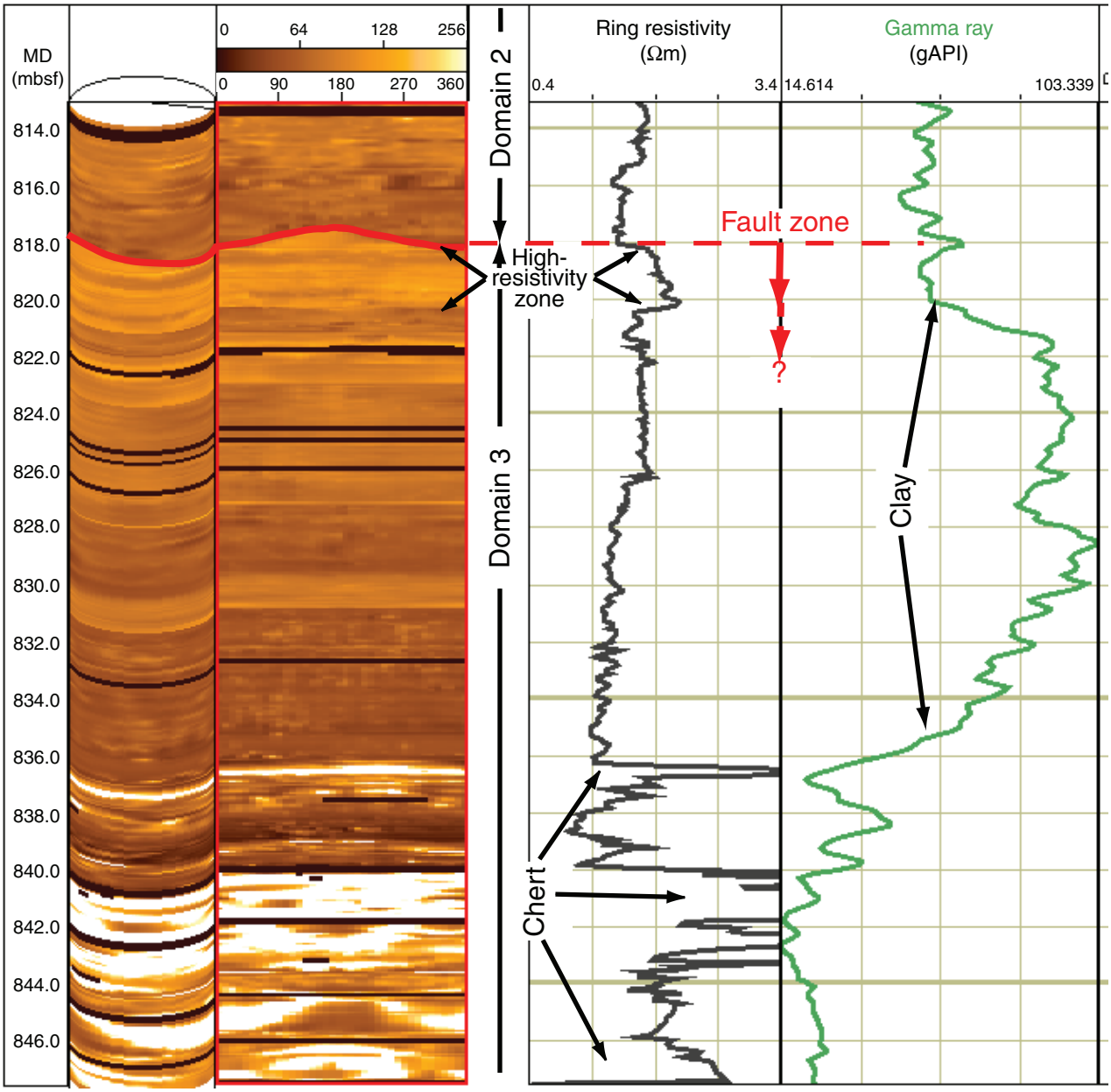

Figure F19. Depth converted seismic section of Line HD33B, Site C0019. Depth conversion is based on the original velocity model (see the "Methods" chapter [Expedition 343/343T Scientists, 2013]). Three seismic units are shown with transparent color: brown = seismic Unit A, yellow = seismic Unit B, green = seismic Unit C. CMP = common midpoint. VE = vertical exaggeration.

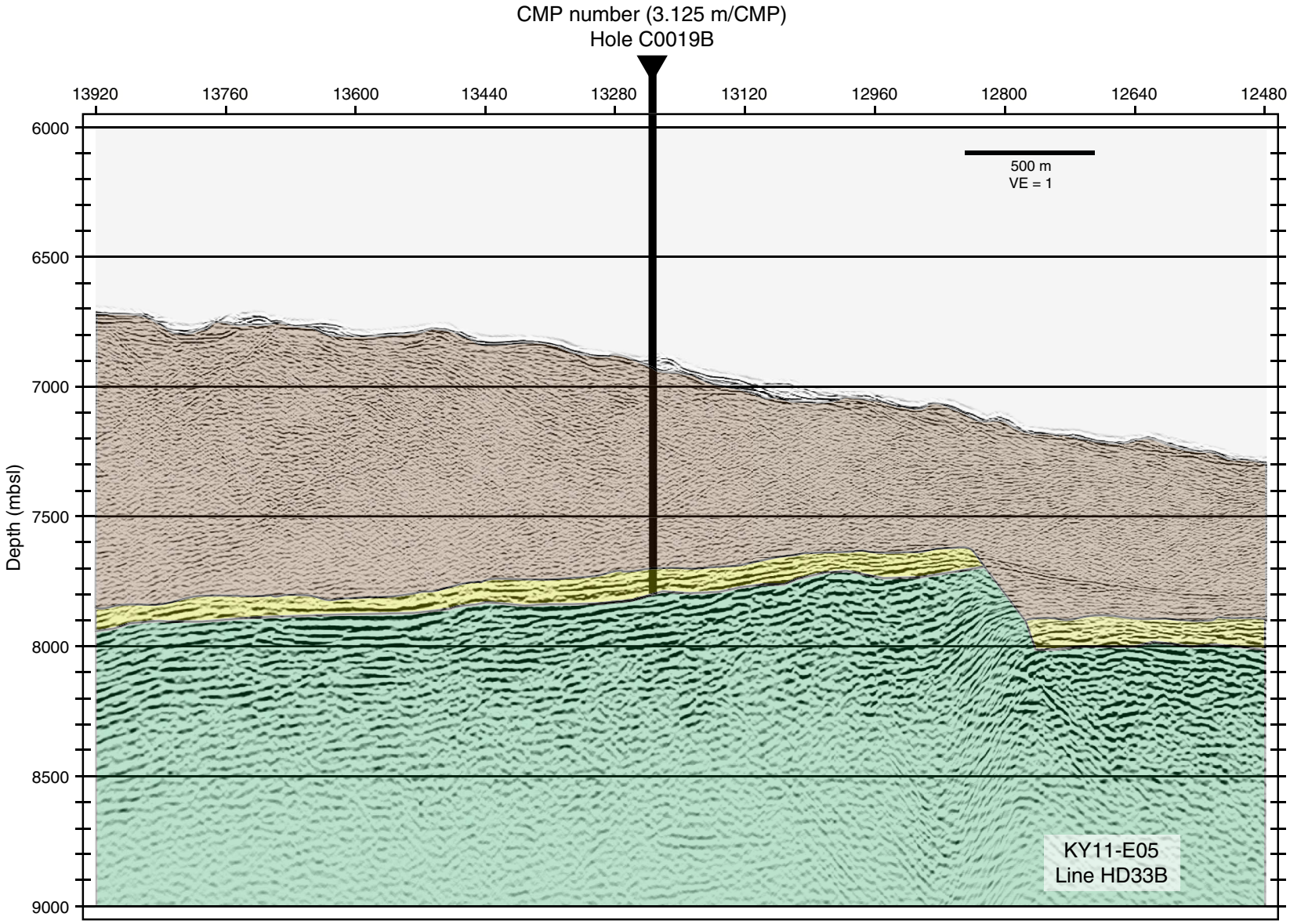

Figure F20. Unwrapped and 3-D borehole wall RAB electrical images (dynamically normalized shallow images) of Hole C0019B showing the presence of borehole breakouts, which occur on the borehole wall and appear on the electrical image as a pair of vertical black bands (conductive bands) ~180° apart.

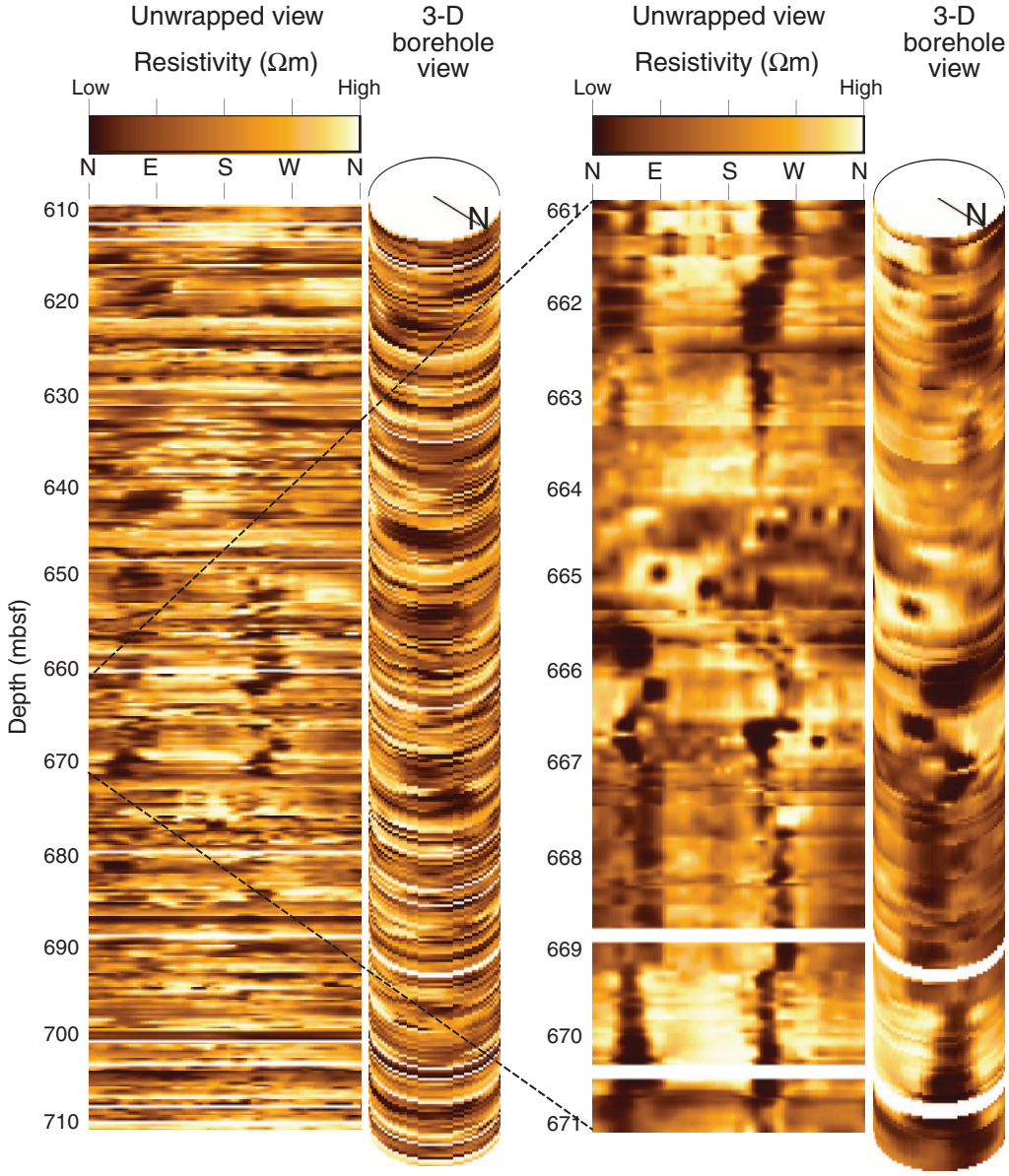

Figure F21. Variation of borehole breakout azimuth observed in Hole C0019B with depth. The azimuth appears to be highly variable in the shallow depth range but appears to have a preferred direction in the deeper part of the hole. Blue broken lines = mean azimuth in the deeper part. RAB = resistivity at the bit.

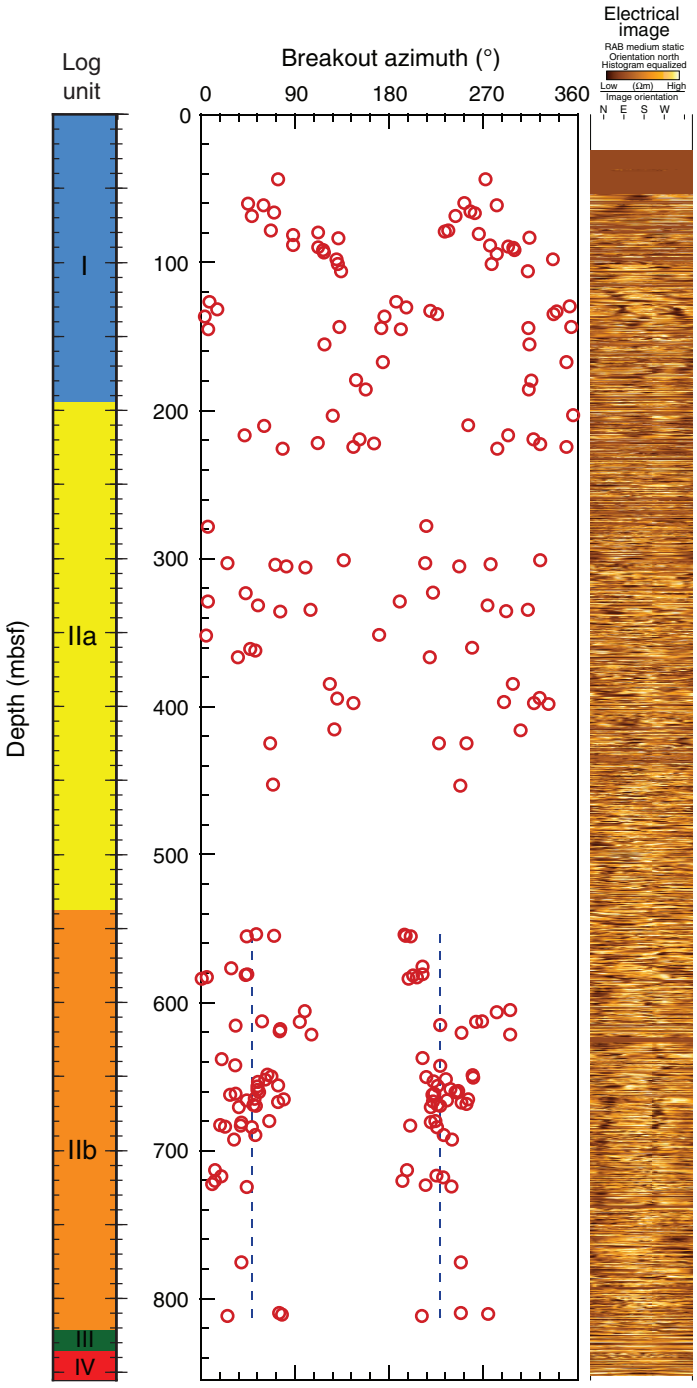

Figure F22. Core-log-seismic integration summary diagram, Site C0019. Lithologic units are defined from visual core description. Gamma ray: green line = logging while drilling (LWD) gamma ray (GR), green circles = MSCL-W natural gamma radiation (NGR). Resistivity: dark blue = deep button, turquoise = medium button, light green = shallow button, purple circles = MSCL-W noncontact resistivity (NCR), light blue circles = discrete resistivity. Density: dark blue = calculated log from LWD, light blue = MSCL-W GRA, circles = moisture and density (MAD). Magnetic susceptibility is from MSCL-W. Porosity: orange = calculated log from LWD, yellow circles = MAD. Compressional velocity: maroon = calculated log from LWD, pink = multisensor core logger (MSCL), red circles = discrete. RAB = resistivity at the bit.

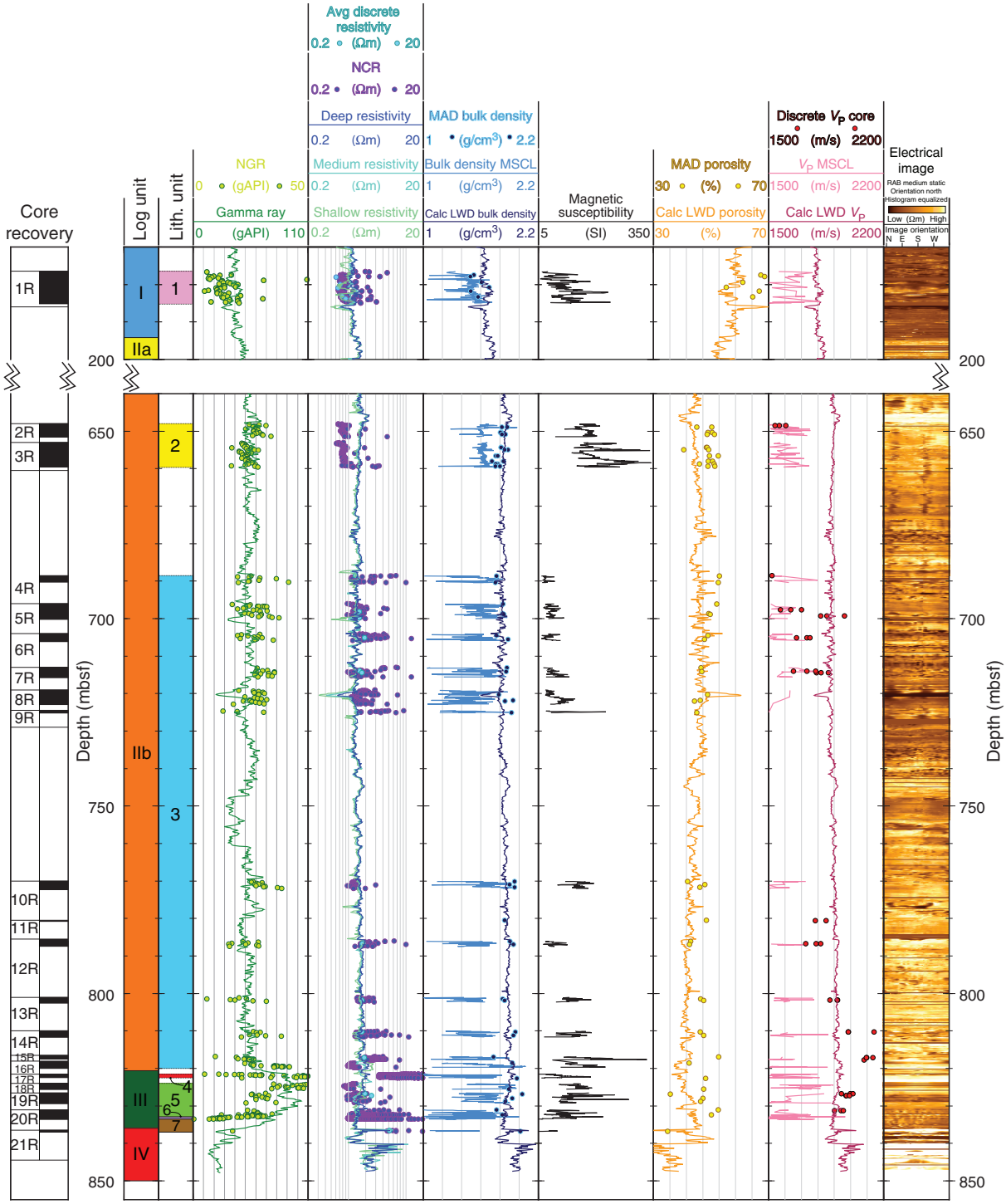

Figure F23. Photograph of Unit 1 siliceous mud showing an ash bed at 16–19 cm (Sample 343-C0019E-1R-CC, 9–24 cm). Color banding subparallel to bedding is visible. Pumice fragments are clustered within a horizon at 23–24 cm.

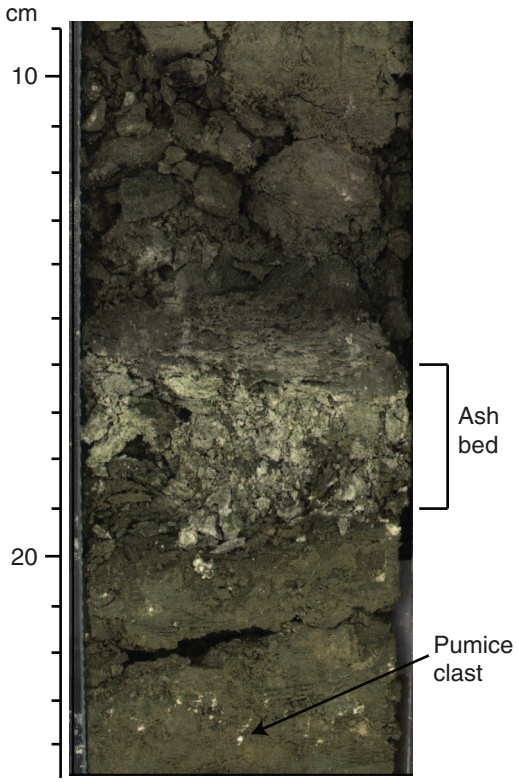

Figure F24. Smear slide images showing mixtures of siliceous microfossils, mud, and vitric volcanic ash. Sediment compositions fall mostly into the siliceous mudstone compositional field (see **"Lithology"** in the "Methods" chapter [Expedition 343/343T Scientists, 2013]). **A.** Siliceous microfossils. The microfossils are commonly broken and may be coated with clay (Sample 343-C0019E-1R-4, 78 cm). **B.** Siliciclastic minerals. The siliciclastic component was most recognizable as dark clumps of clay minerals; additionally, clay minerals lie dispersed in the background of the smear slide. Rare singular quartz and feldspar grains occur in the smear slides (Sample 343-C0019E-1R-CC, 17 cm). (Continued on next page.)

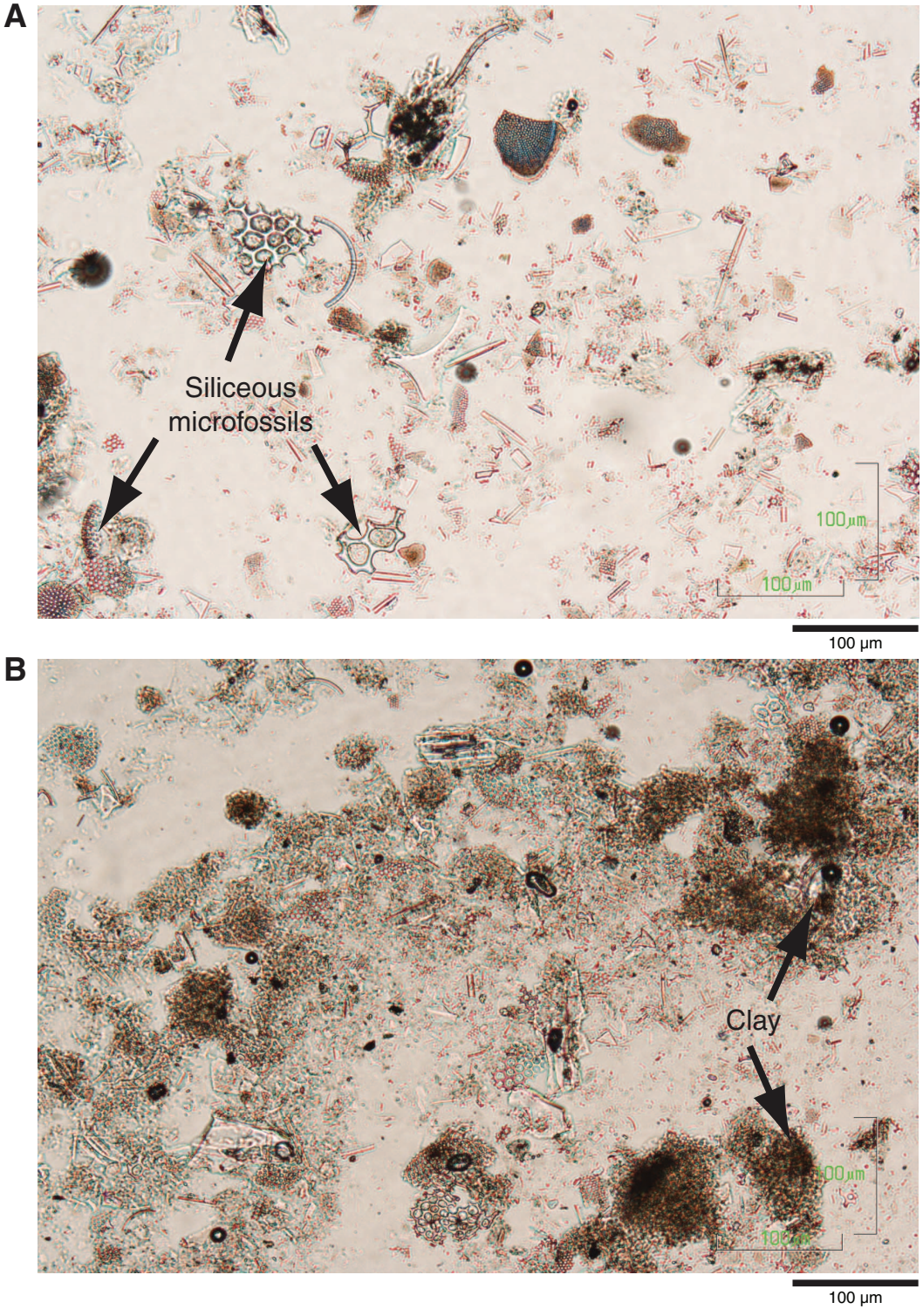

Figure F24 (continued). C. Volcaniclastic component. Although the volcaniclastic component is mostly glassy or vitric, inclusions of feldspar occur in the glass and some glassy fragments include unidentified dark mafic minerals or oxides (Sample 343-C0019E-1R-1, 14 cm).

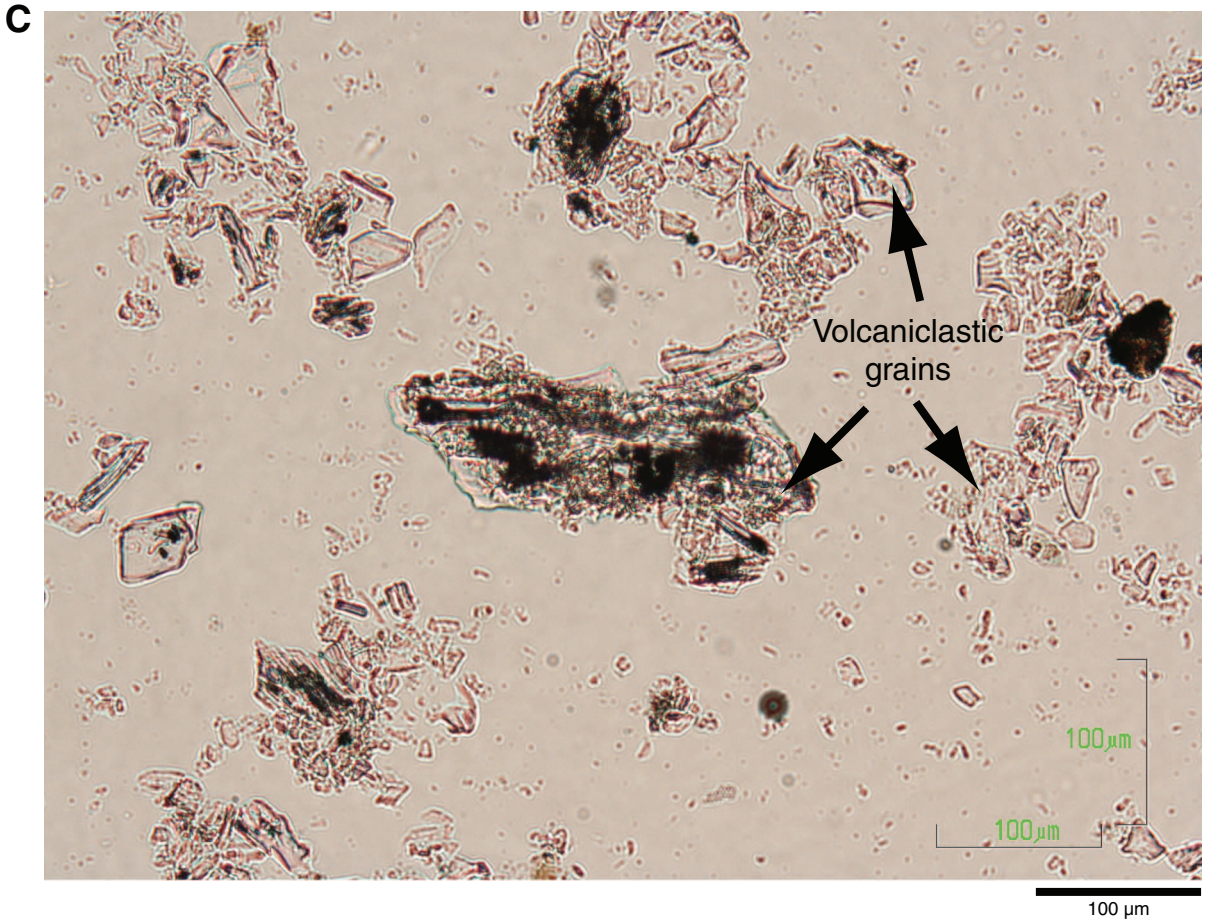

Figure F25. MSCL-I images of the two largest pieces of Unit 2 representing the two lithologies found throughout the cuttings, which comprised Cores 343-C0019E-2R and 3R. **A.** Bluish gray mudstone with mottled texture. **B.** Grayish brown mudstone with calcite-cemented and mud-filled burrows, shell fragments, and mottling.

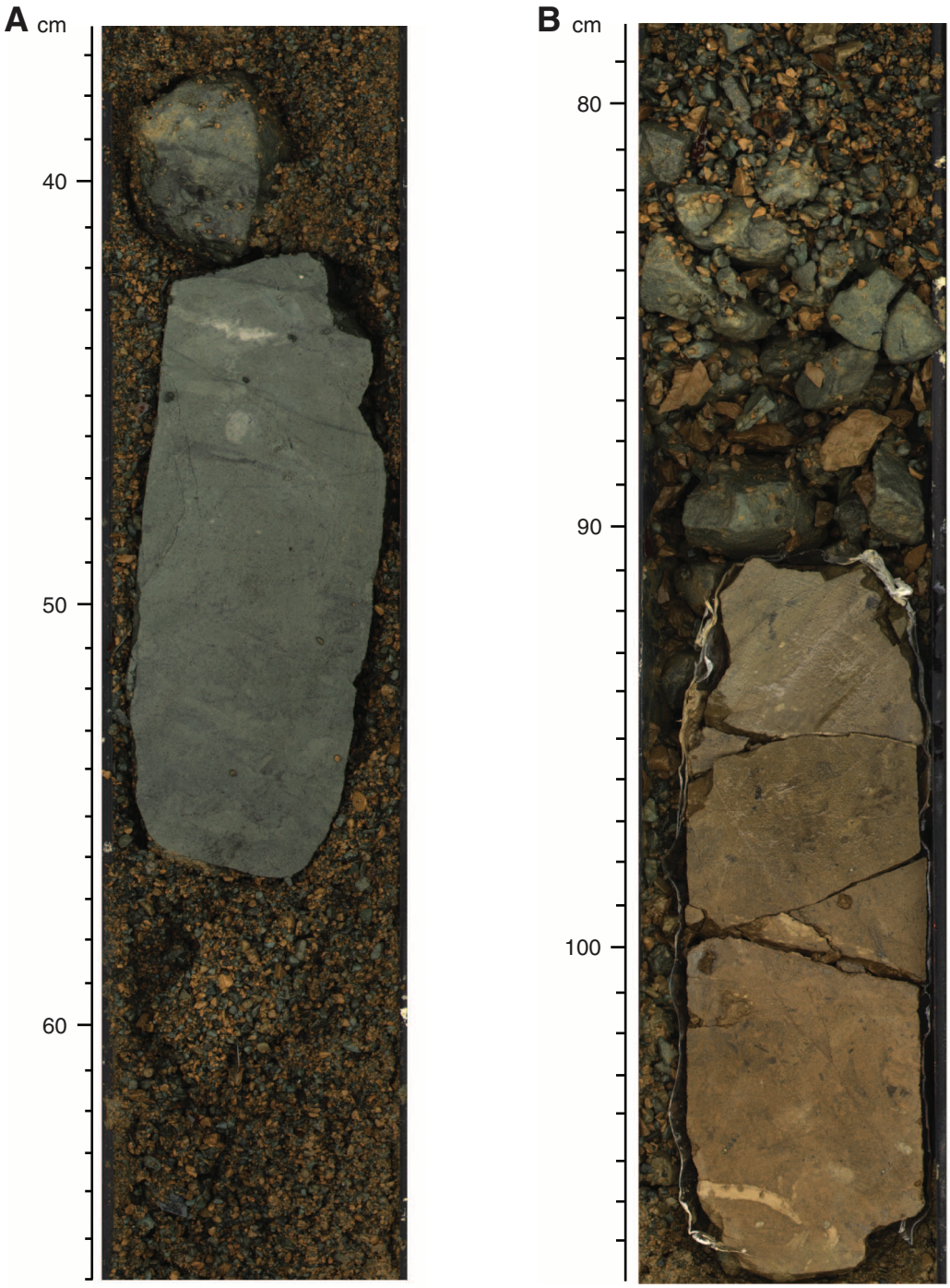

Figure F26. MSCL-I images of representative Unit 3 lithologies. **A.** Dark gray to black mudstone (interval 343-C0019E-10R-1, 19–44 cm). **B.** Ashy olive-brown-gray mudstone with minor color laminations (interval 343-C0019E-4R-1, 60–85 cm). **C.** Pyrite-rich mudstone with aligned elliptical dark spots defining bedding (interval 343-C0019E-13R-1, 22–41 cm). **D.** Clay-rich mudstone (interval 343-C0019E-4R-1, 1–21 cm).

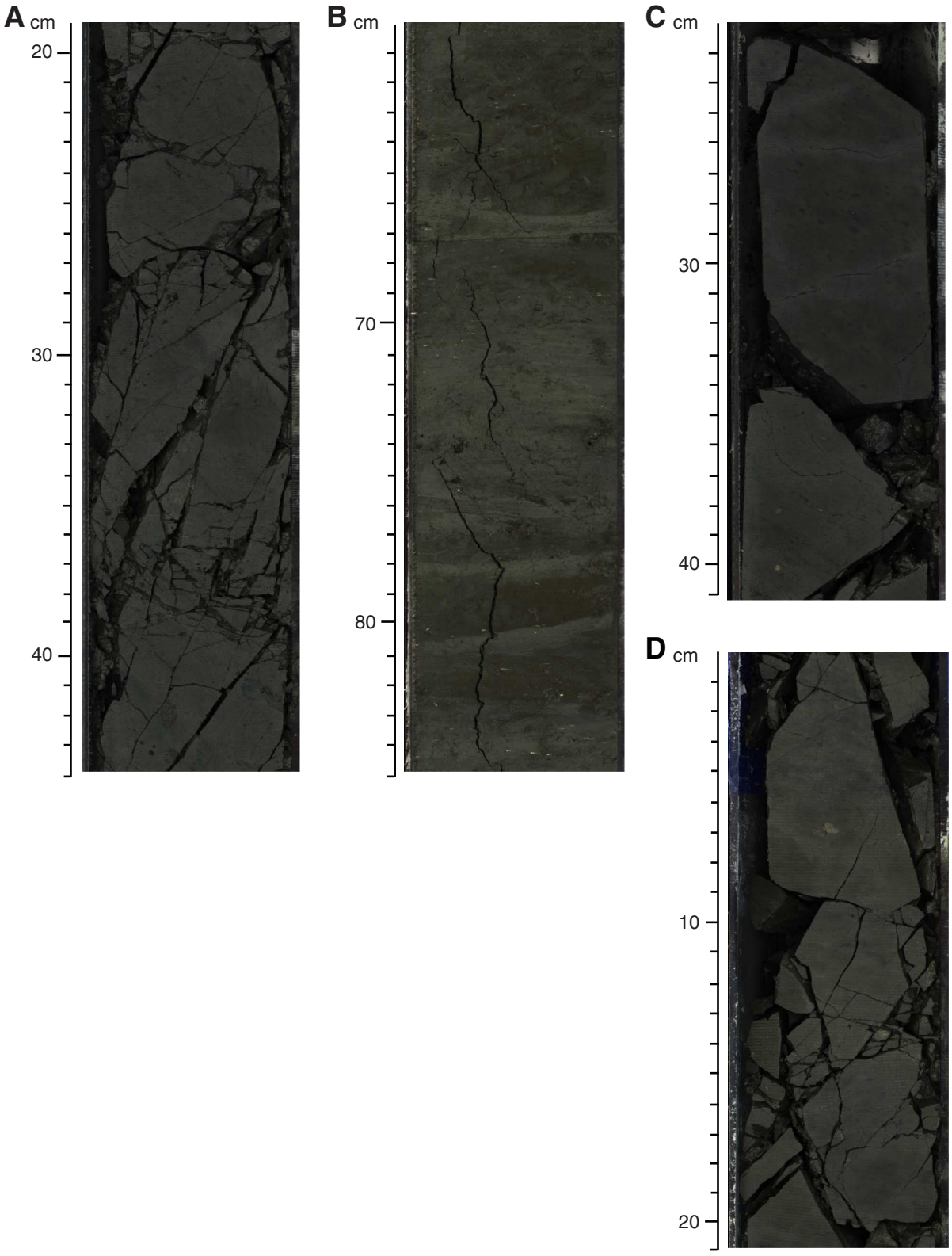

Figure F27. Representative smear slide photomicrographs of (**A**) dark mudstone and (**B**) ashy mudstone in Unit 3, Site C0019.

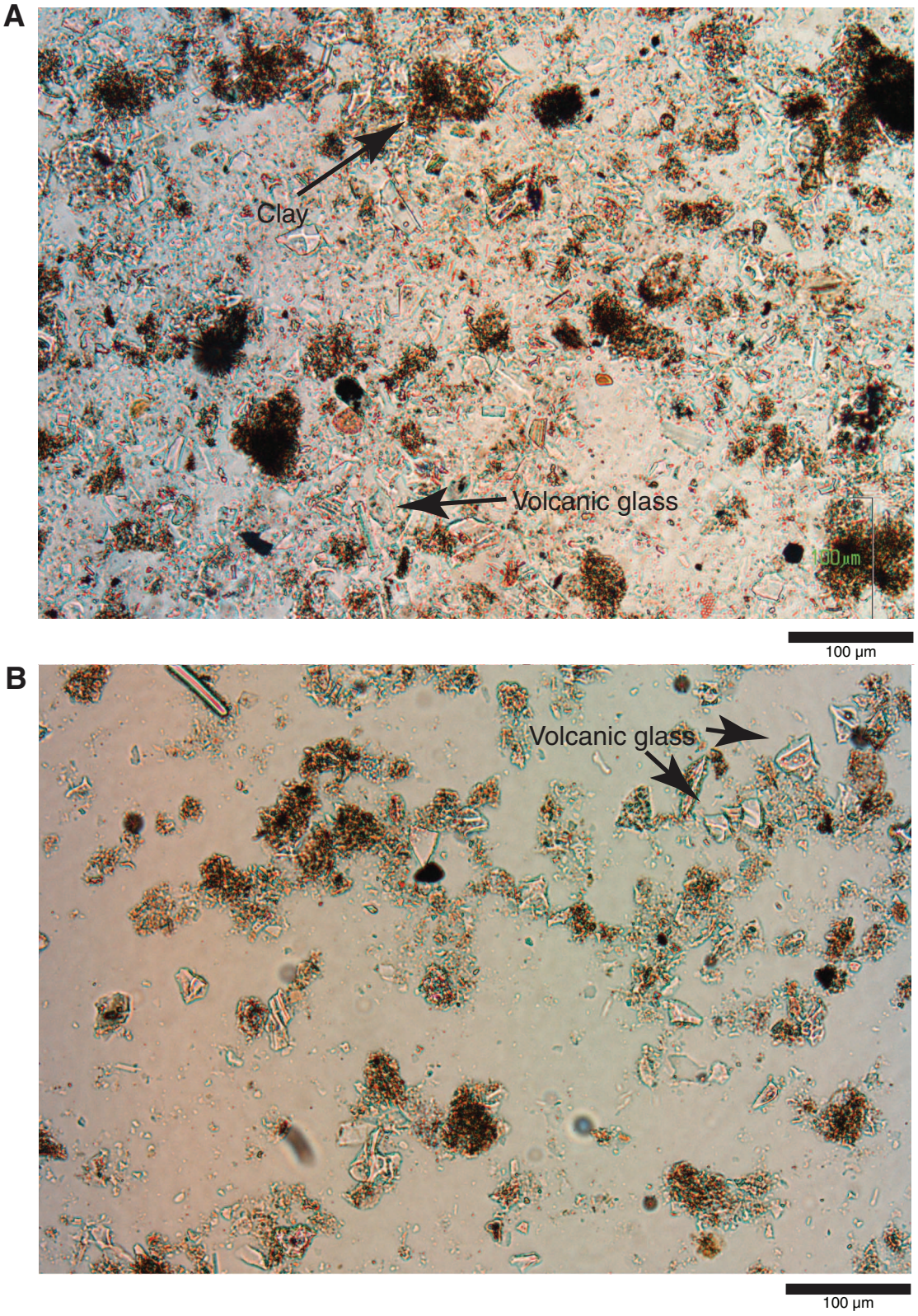

Figure F28. Core photographs of representative lithologies in Units 6 and 7. **A.** Unit 6 claystone (interval 343-C0019E-20R-2, 70–106 cm). Note the predominantly intact interval of chert at 103–105 cm. **B.** Unit 7 yellow-brown and dark brown chert (interval 343-C0019E-21R-CC, 0–14 cm).

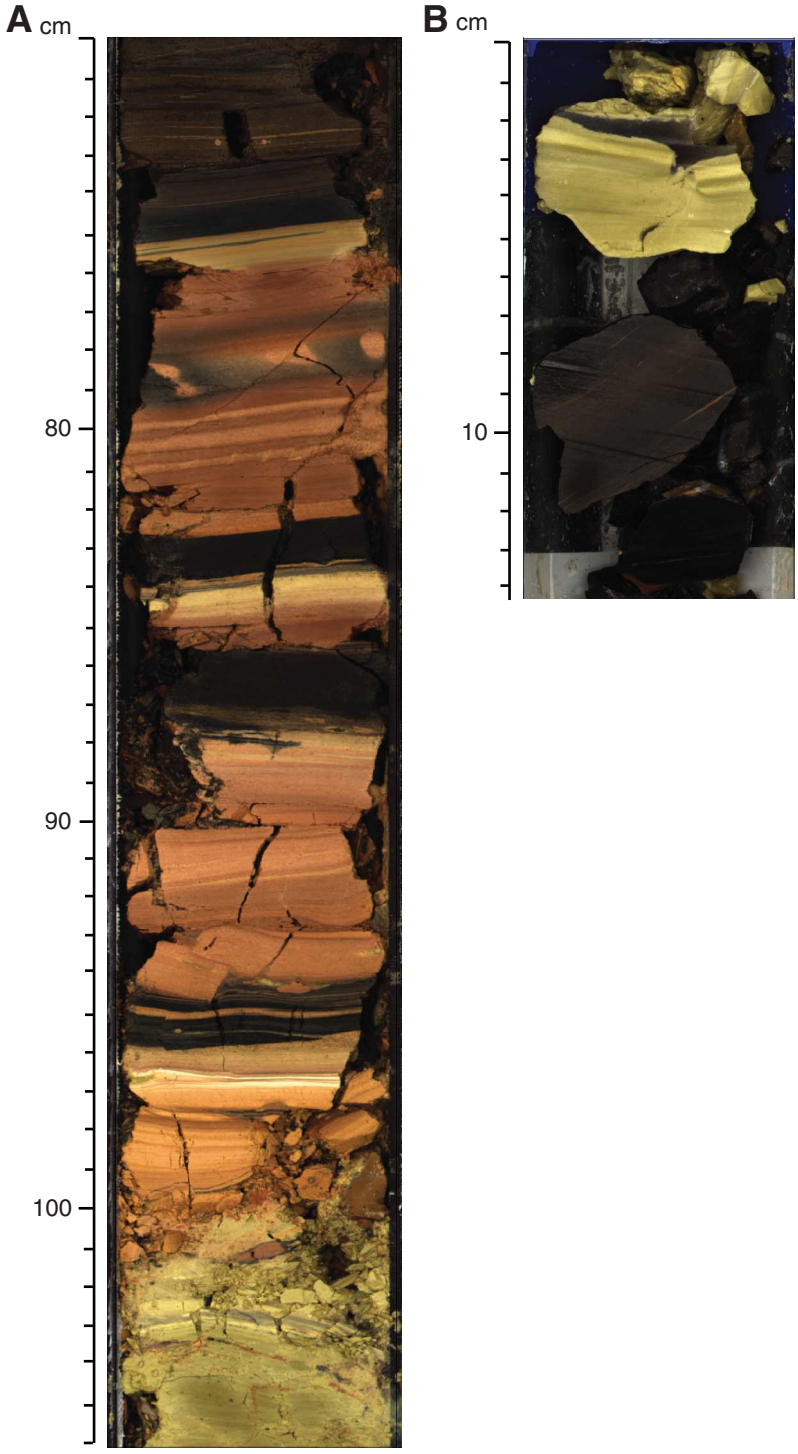

Figure F29. Major element abundances in the lower portion of Hole C0019E measured by XRF. Potassium, aluminum and manganese are relatively enriched in Unit 4, whereas calcium and sodium are depleted. Zones of core recovery are highlighted in gray. The position of significant faults identified in the core are shown (see "Structural geology" for a discussion). LOI = loss on ignition.

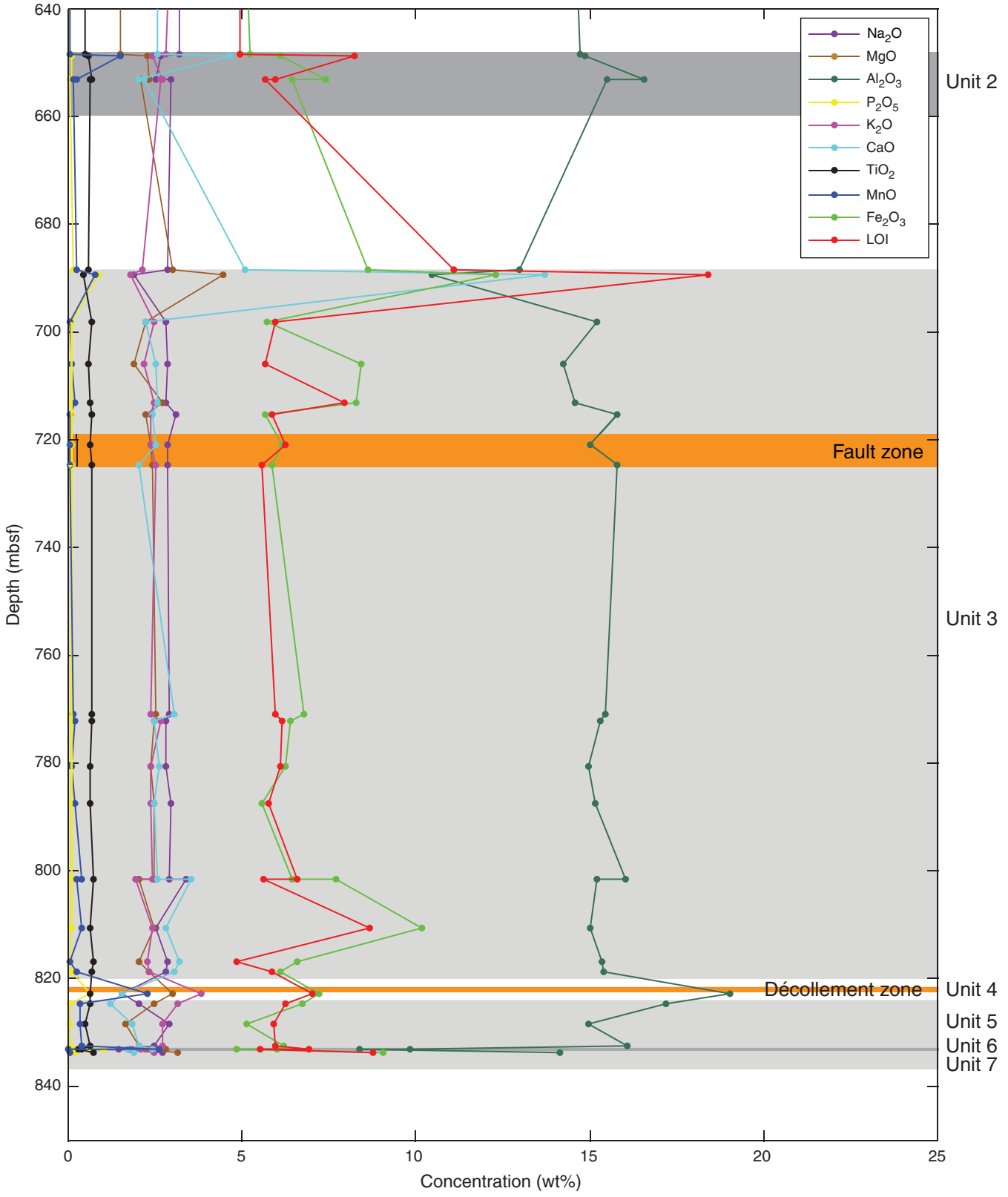

Figure F30. Whole-rock XRD patterns for samples from Unit 3 (Core 343-C0019E-14R) and Unit 4 (Core 17R). Sm = smectite, I = illite, K = kaolinite, C = chlorite, Cc = composite clay, Q = quartz, Pl = plagioclase.

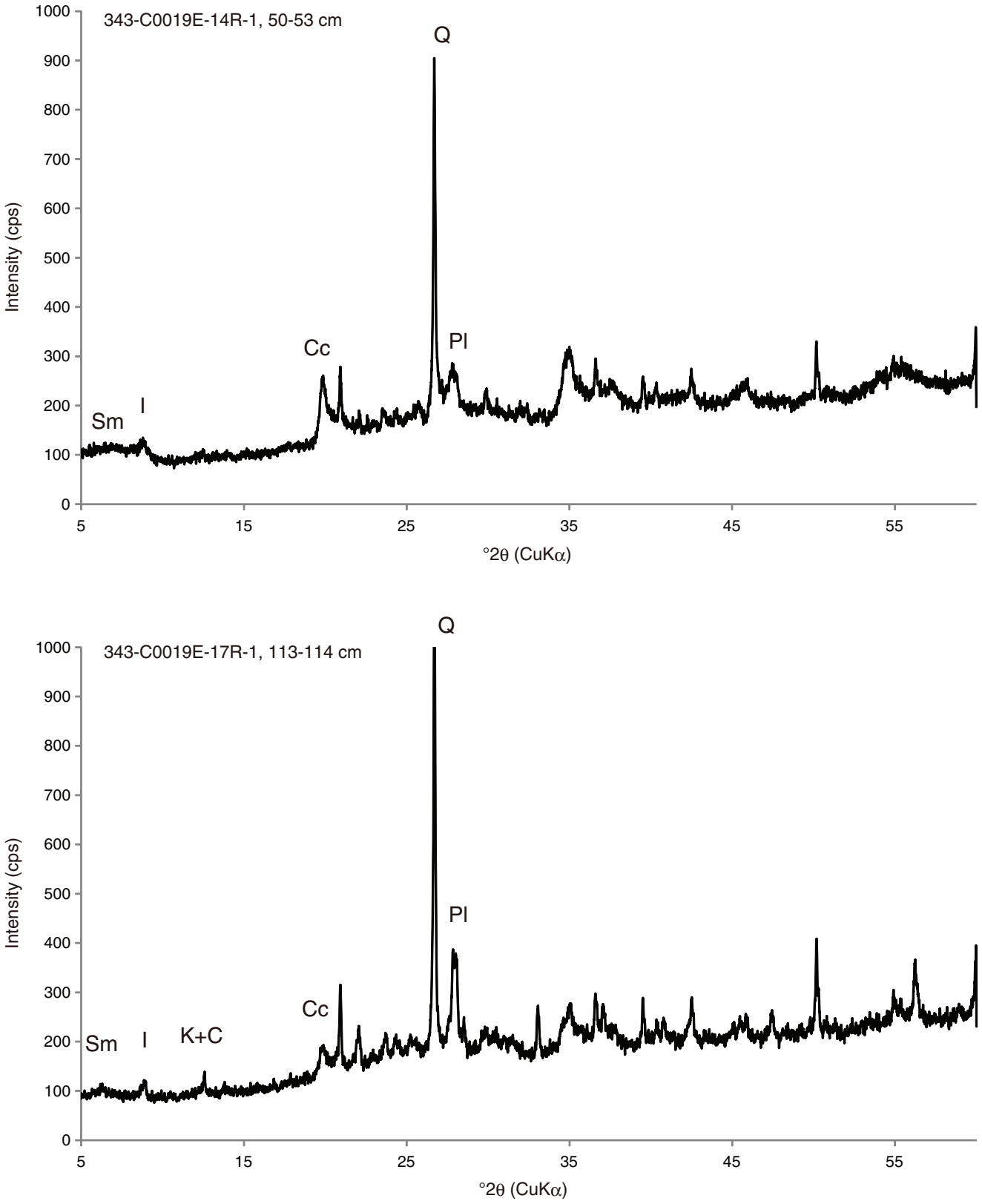

Figure F31. Representative core photograph of Unit 5 brown mudstone (interval 343-C0019E-1R-1, 54–85 cm).

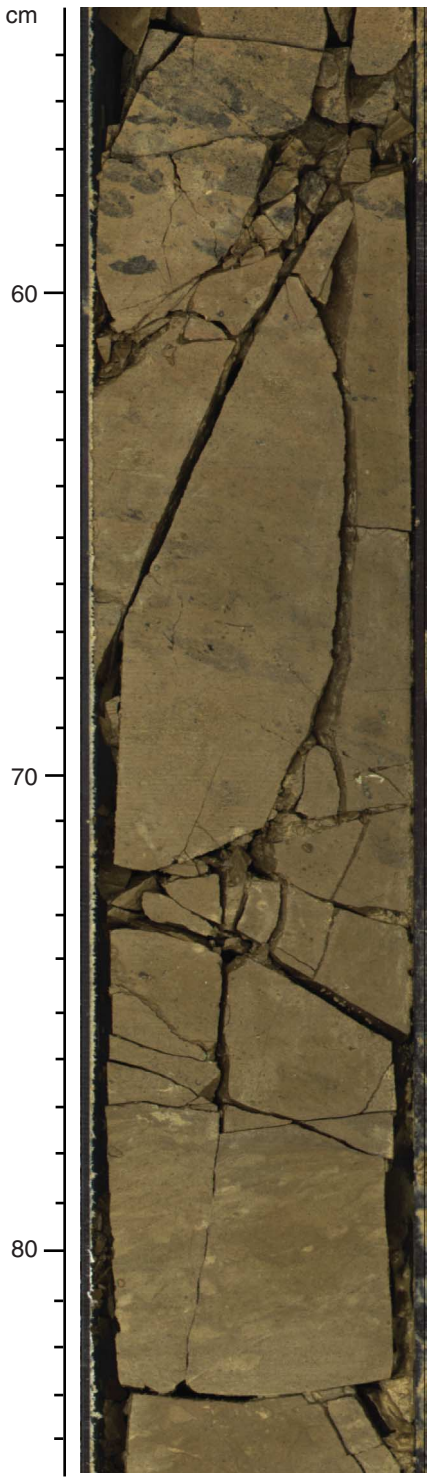

Figure F32. Dip vs. depth plots of bedding and deformation structures, Site C0019. Lithologic/structural units are also shown.

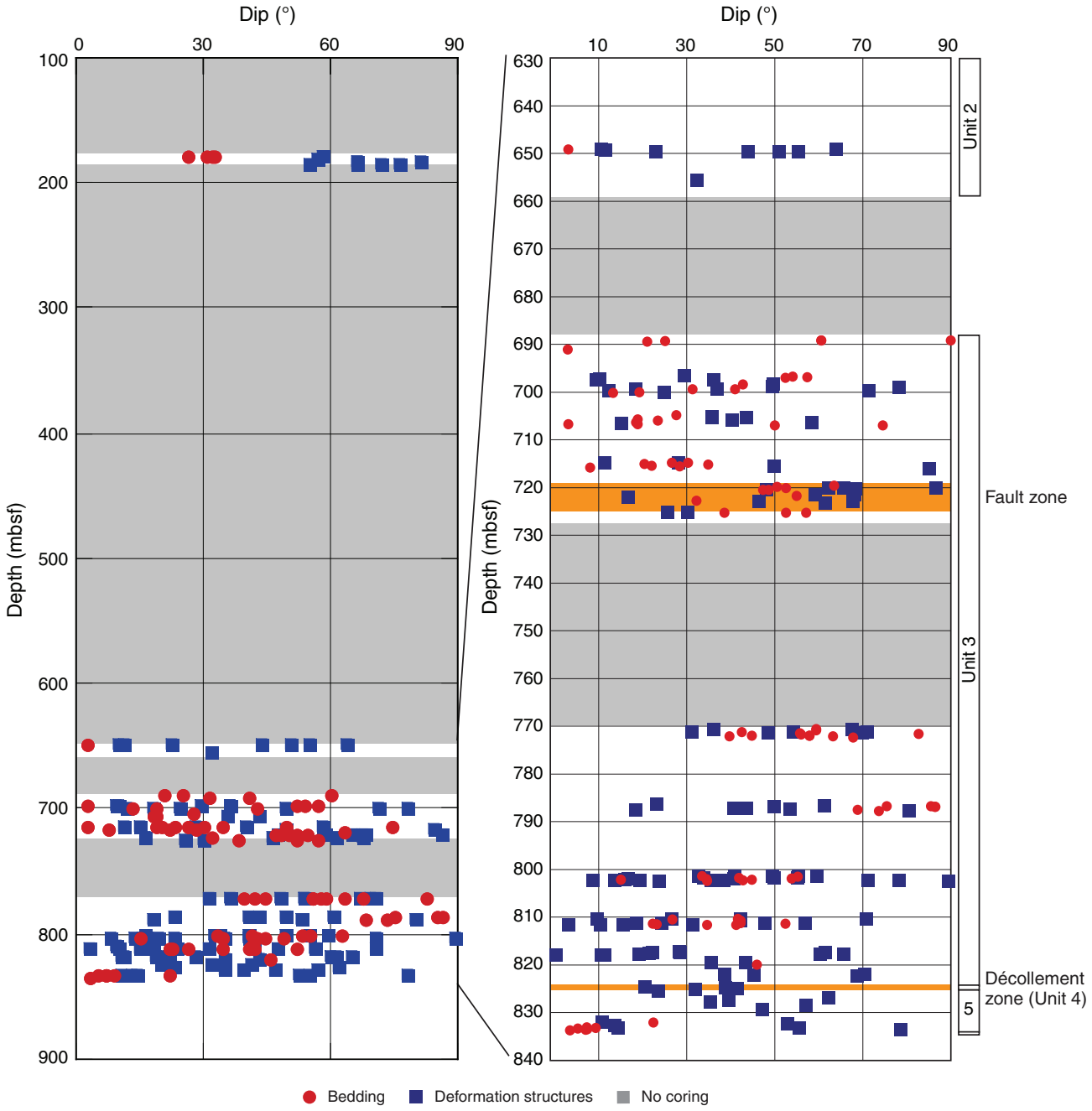

Figure F33. Core and X-ray CT images of a fault cutting mudstones in Unit 1 (interval 343-C0019E-1R-5, 62–76 cm). Fault surface is visible in core (left) as a planar polished surface with slickenlines that indicate normal slip. The fault is also visible in the X-ray CT image (right) as a bright band overprinted by a fracture (black void parallel to fault) that is likely a result of the coring process. Also visible in the core and X-ray CT image are open fractures at other orientations.

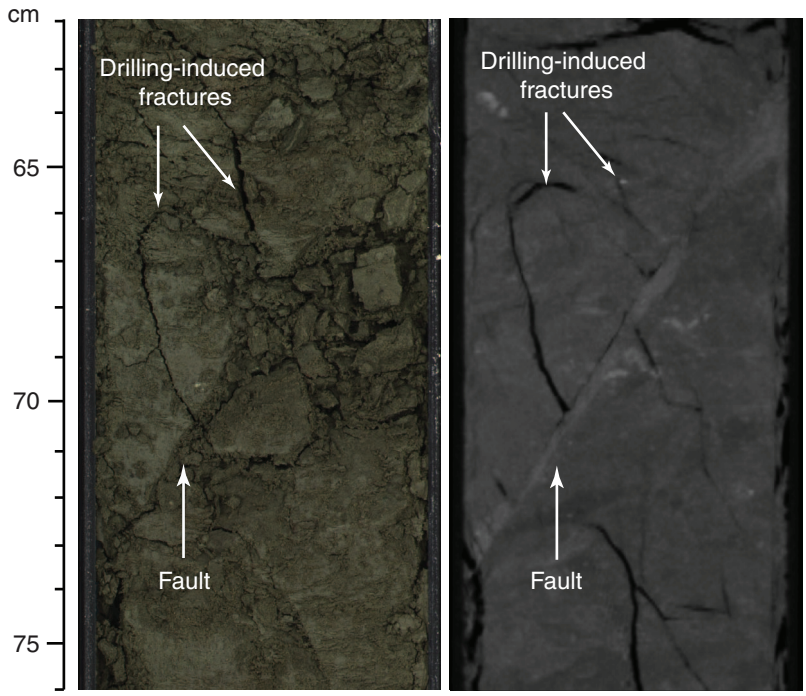

Figure F34. X-ray CT and core images of bedding in (**A**) Section 343-C0019E-7R-2 centered 13 cm below the top of the section, illustrating bright pyrite confined to the mudstone but no particular X-ray CT contrast between the mudstone and sandstone, and (**B**) Section 10R-2 centered 7 cm below the top of the section, illustrating bright layers, inferred to be bedding, that are not particularly apparent in the corresponding MSCL-I image (although they are faintly visible within the core itself).

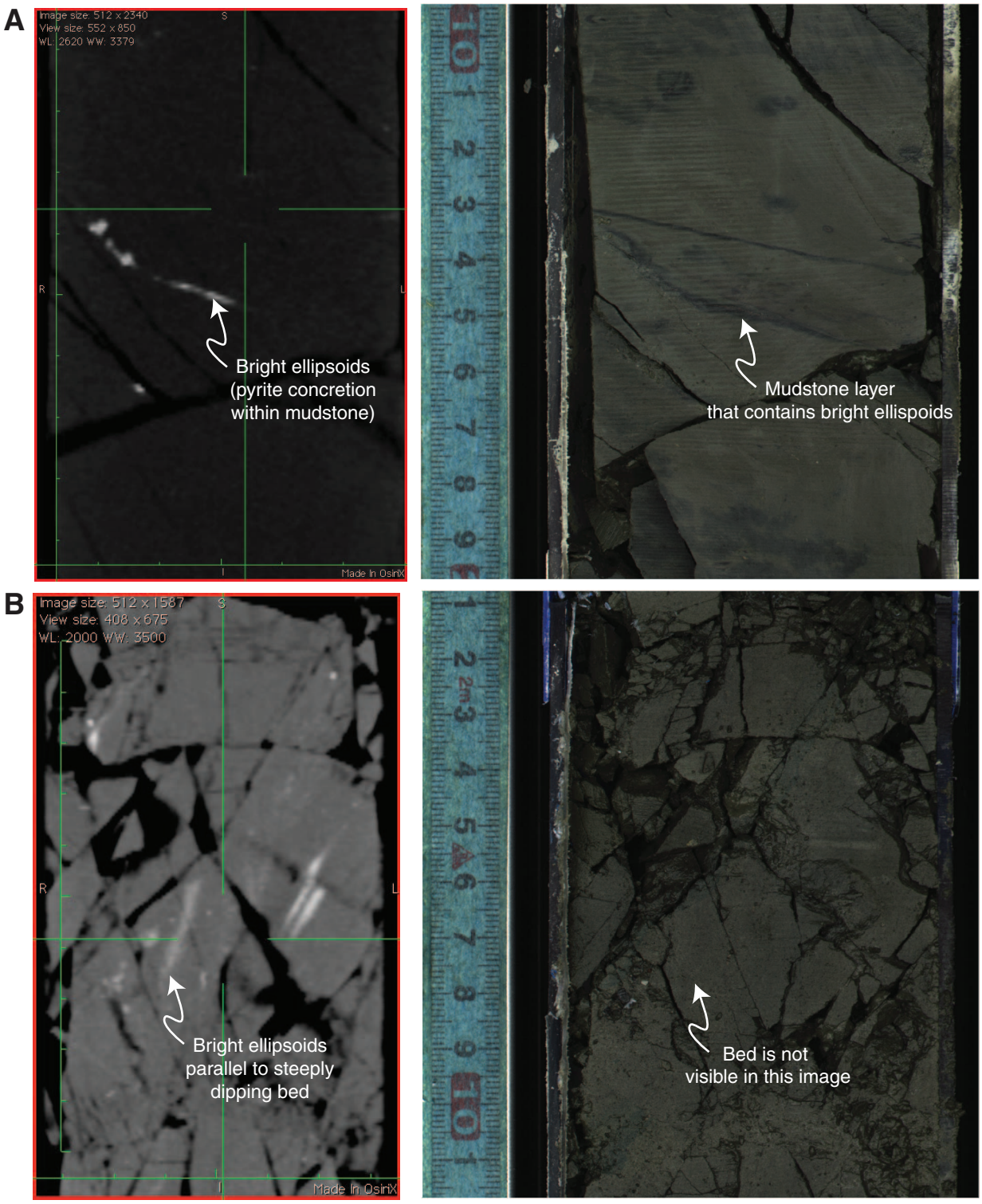

Figure F35. X-ray CT and core images of anastomosing dark seams and a horizontal dark band in Section 343-C0019E-14R-1, centered ~43.5 cm below the top of the section. Bedding is also evident in the MSCL-I image but is more subtle in the X-ray CT image.

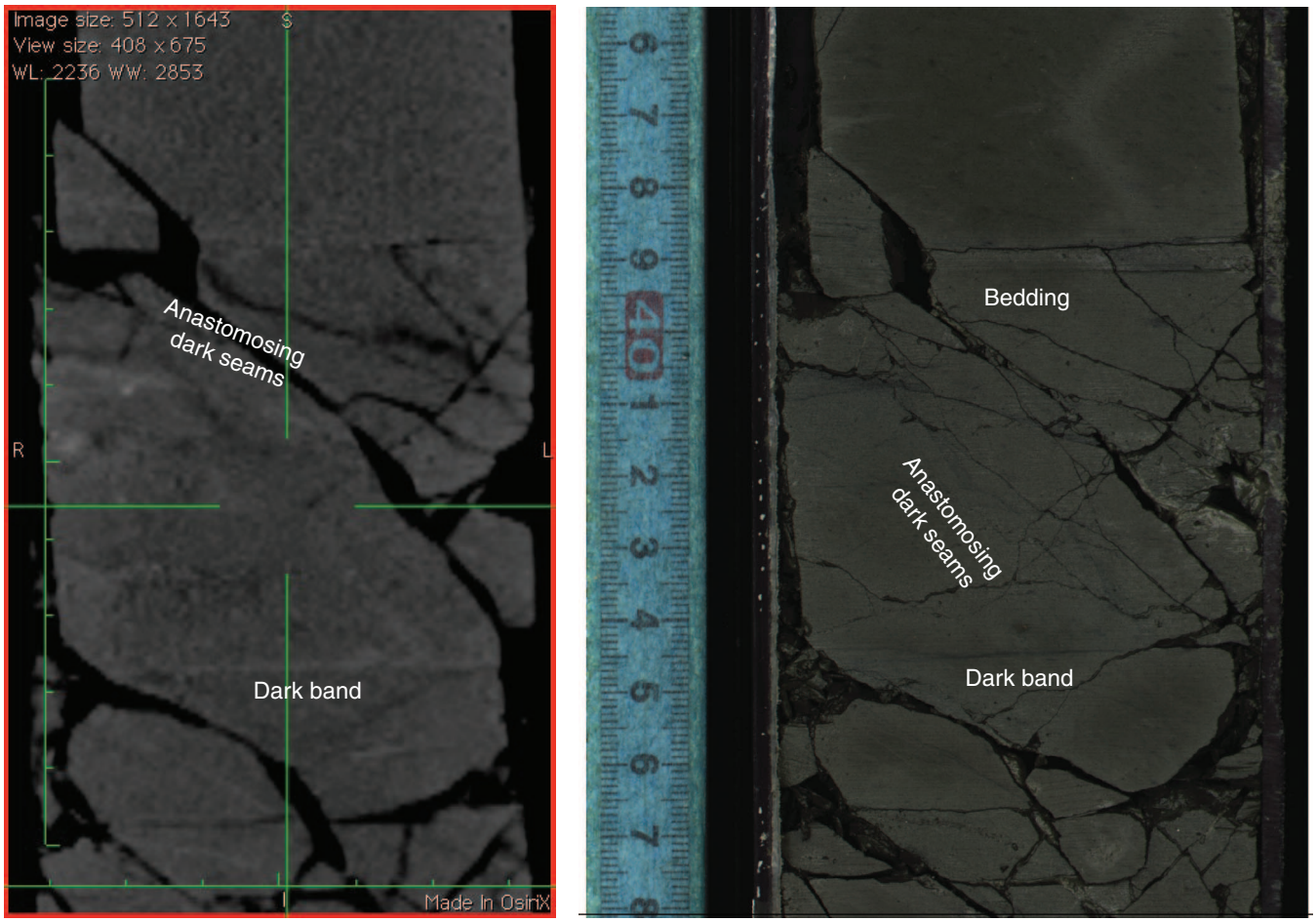

Figure F36. The bright band in X-ray CT image in Section 343-C0019E-5R-1, close to the location of pore water and H_2 gas anomalies at 698 mbsf.

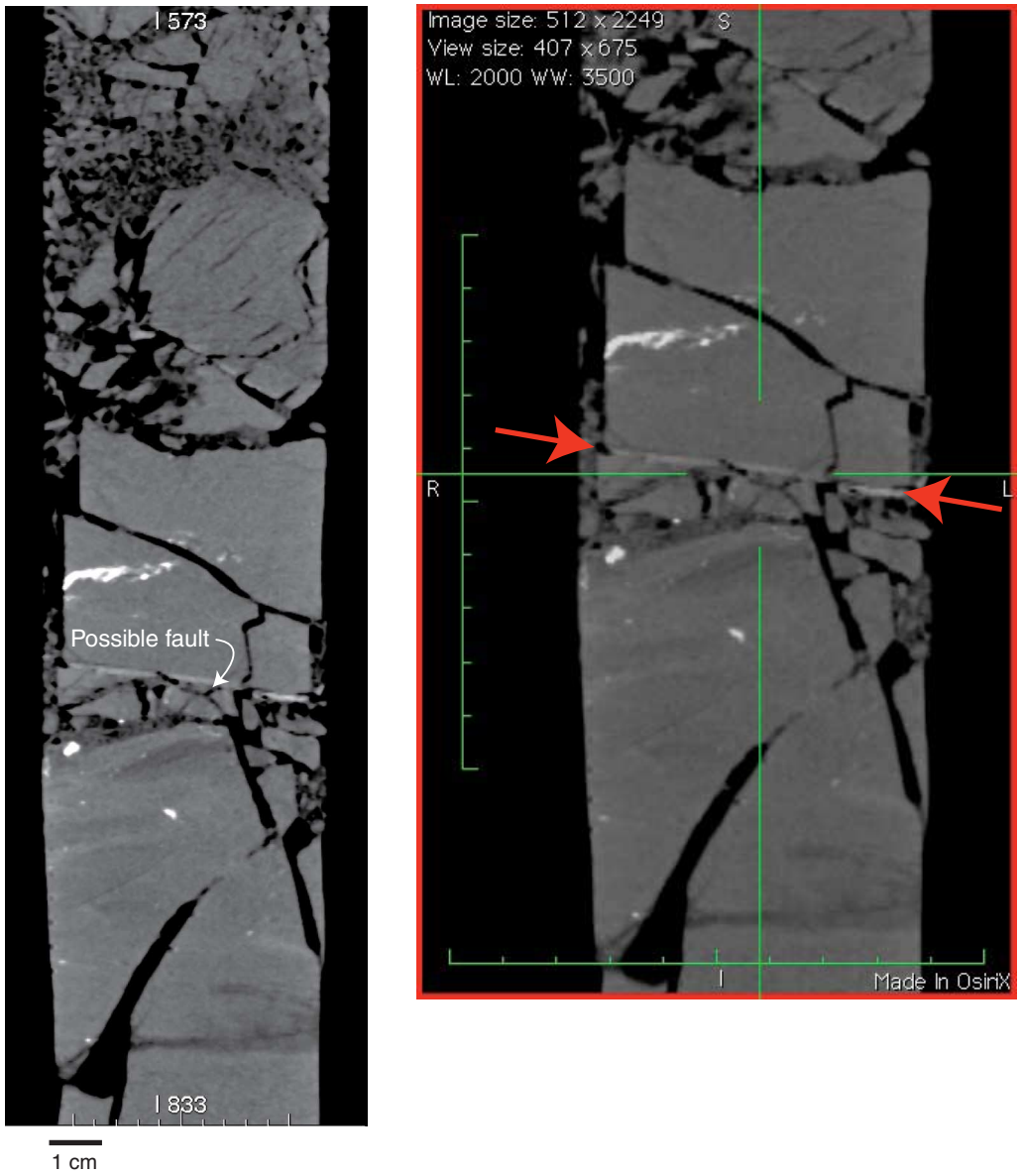

Figure F37. X-ray CT and core images of a 60°-dipping, 15 cm thick zone of anastomosing shear surfaces and deformed rock across which bedding dip changes (located 60–95 cm from the top of Section 343-C0019E-8R-1). **A.** Structure tracing scan. Red lines = bedding, blue lines = fractures, black lines = drilling induced damage. **B.** MSCL-I image. **C.** X-ray CT image of coronal section. Note the darker band dipping ~60° to the left in the image in the interval 60–95 cm from the section top.

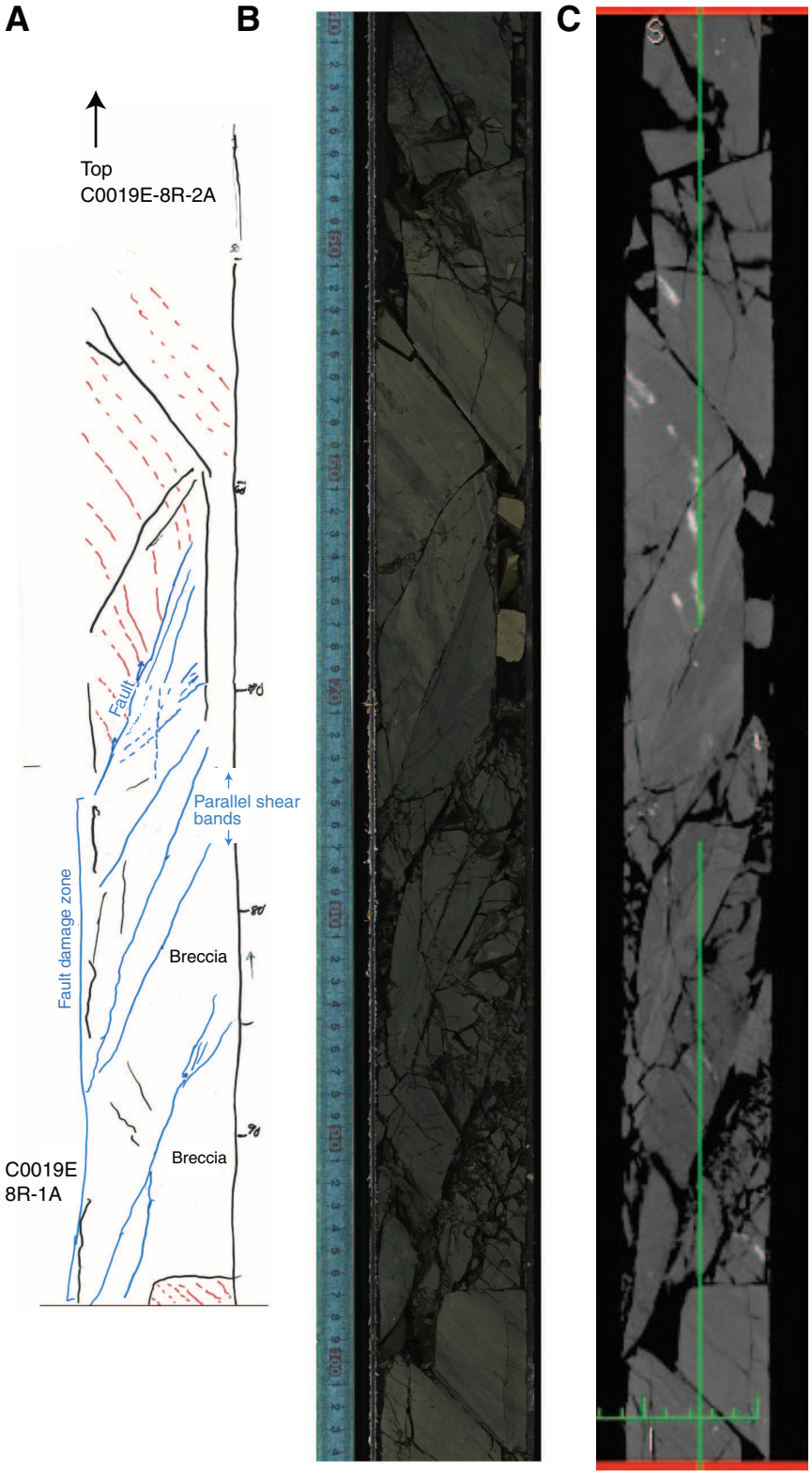

Figure F38. Core image of sediment-filled veins with local pyrite in Section 343-C0019E-13R-2, from 29 to 37.5 cm below the top of the core.

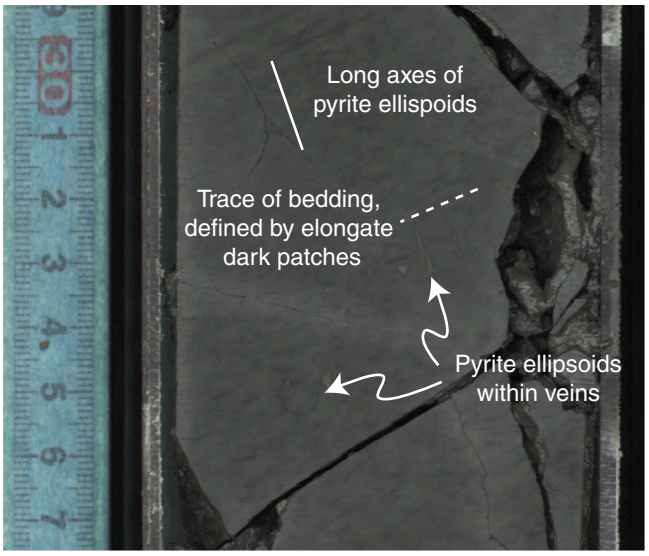

Figure F39. Core images of the Core 343-C119E-17R whole round in its entirety. Note intense scaly fabric, and a mudstone interval with sheared boundaries between 22 and 35 cm below the top of the section.

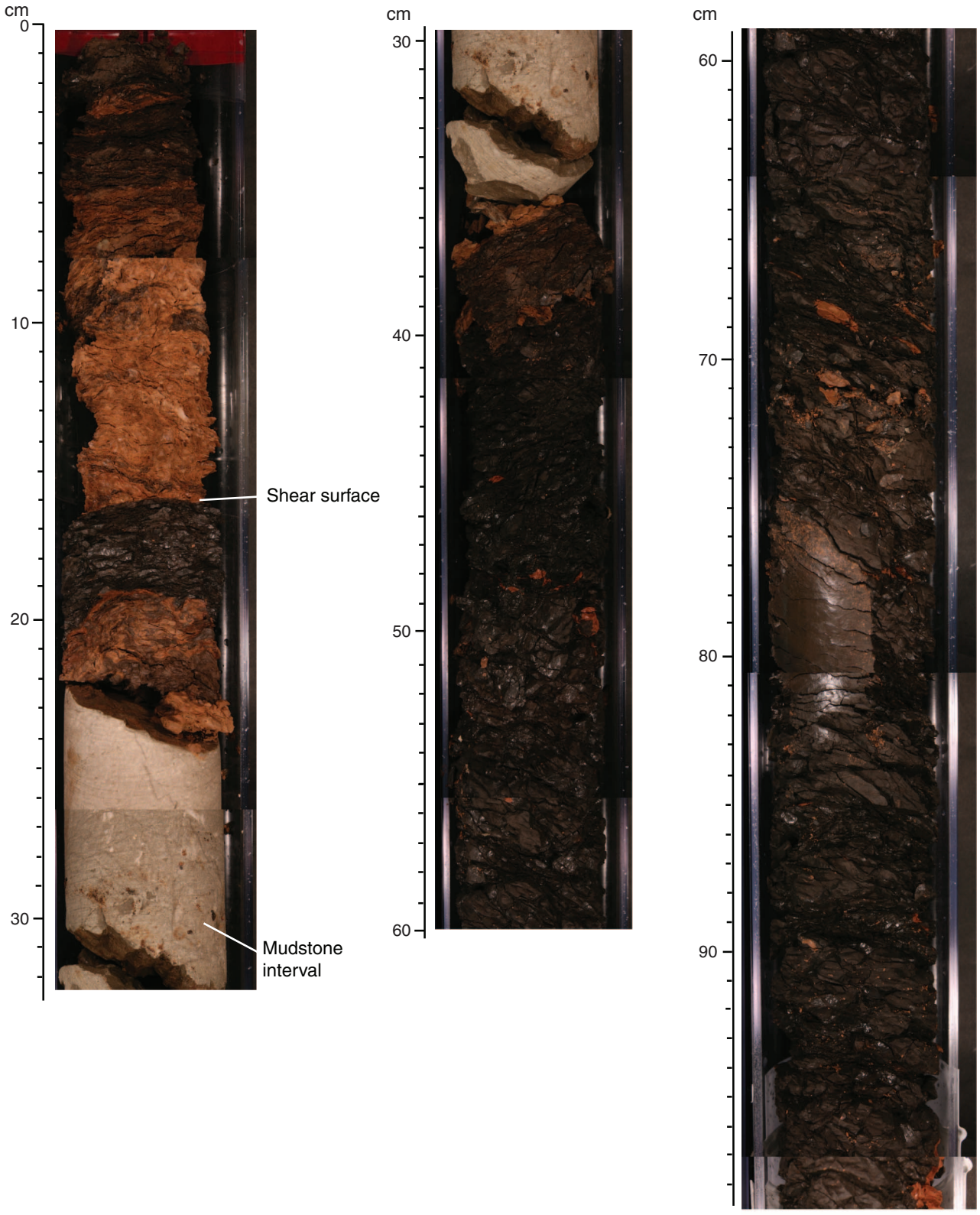

Figure F40. A. Photograph of the uppermost ~30 cm of Core 343-C119E-17R prior to splitting. **B.** Structure tracing demonstrating phacoid asymmetry (left and right edges). Note that the tracing of the core was produced on the core liner; in this image, the tracing has been "unwrapped" resulting in a flat image with apparent distortion along the edges compared to the core photograph.

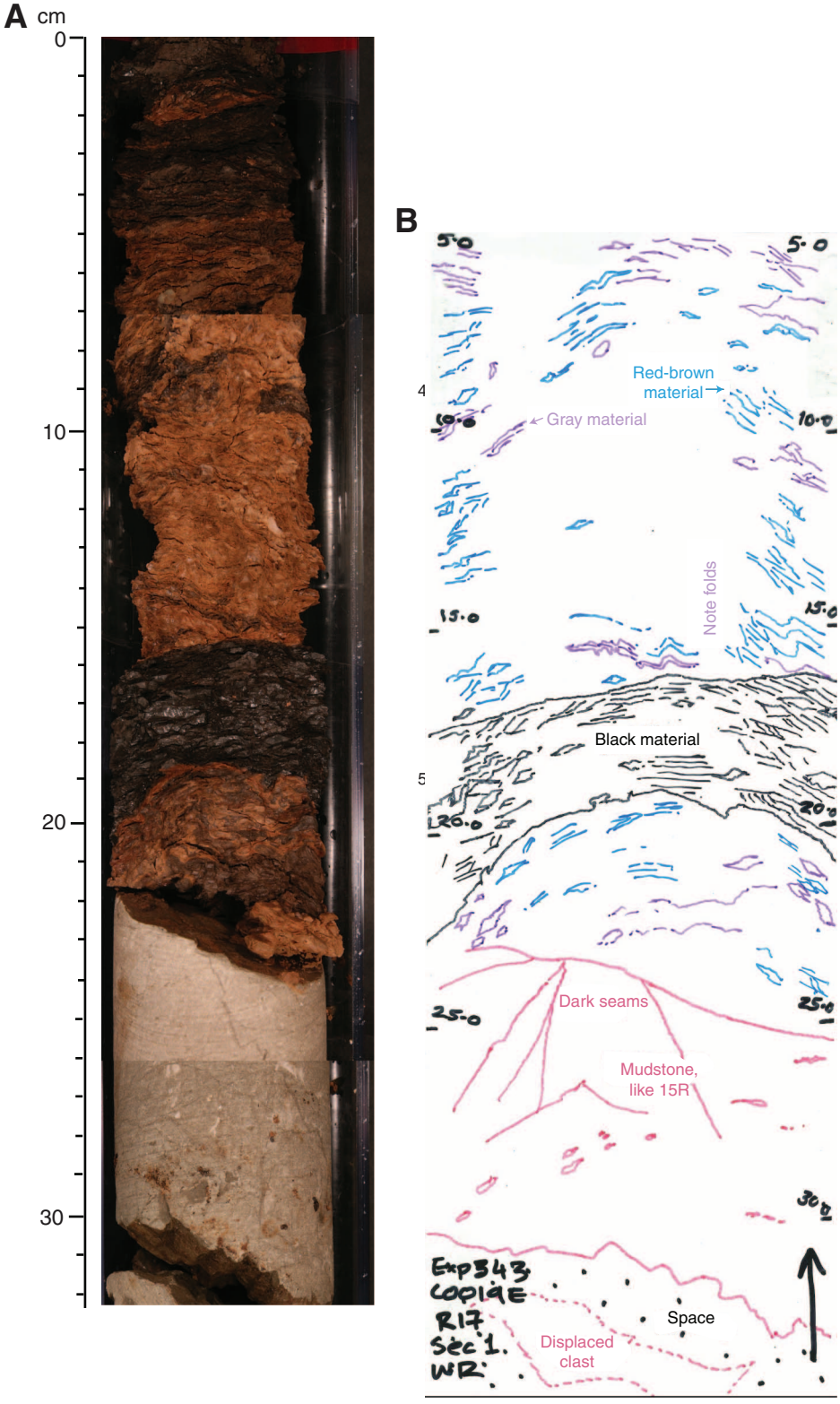

Figure F41. Image of lithologic Unit 5 in the split core showing the zone of shear surfaces (Core 343-C0019E-19R). Note the trace of bedding interface in the lower part of the figure, which is oblique to the trend of shear surfaces.

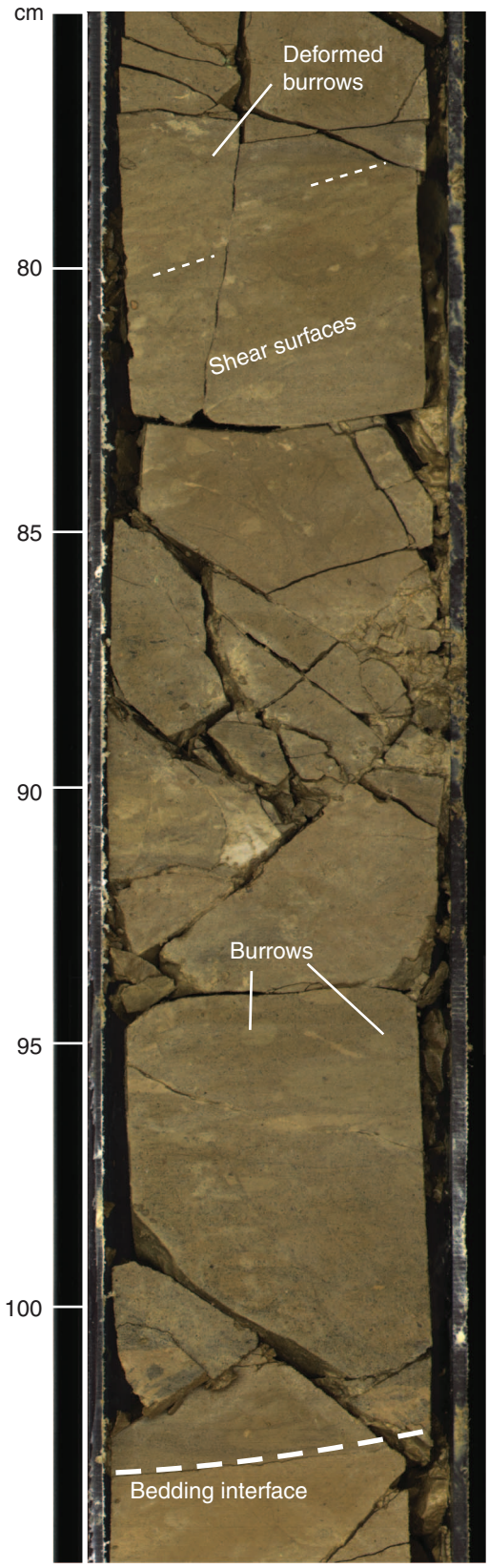

Figure F42. Core image of Core 343-C0019E-20R showing contact between lithologic Units 5 and 6 and both drilling-induced and natural deformation features in Unit 6.

Figure F43. Downhole plot of results of paleomagnetic measurements on discrete samples vs. depth, Hole C0019E. NRM = natural remanent magnetization.

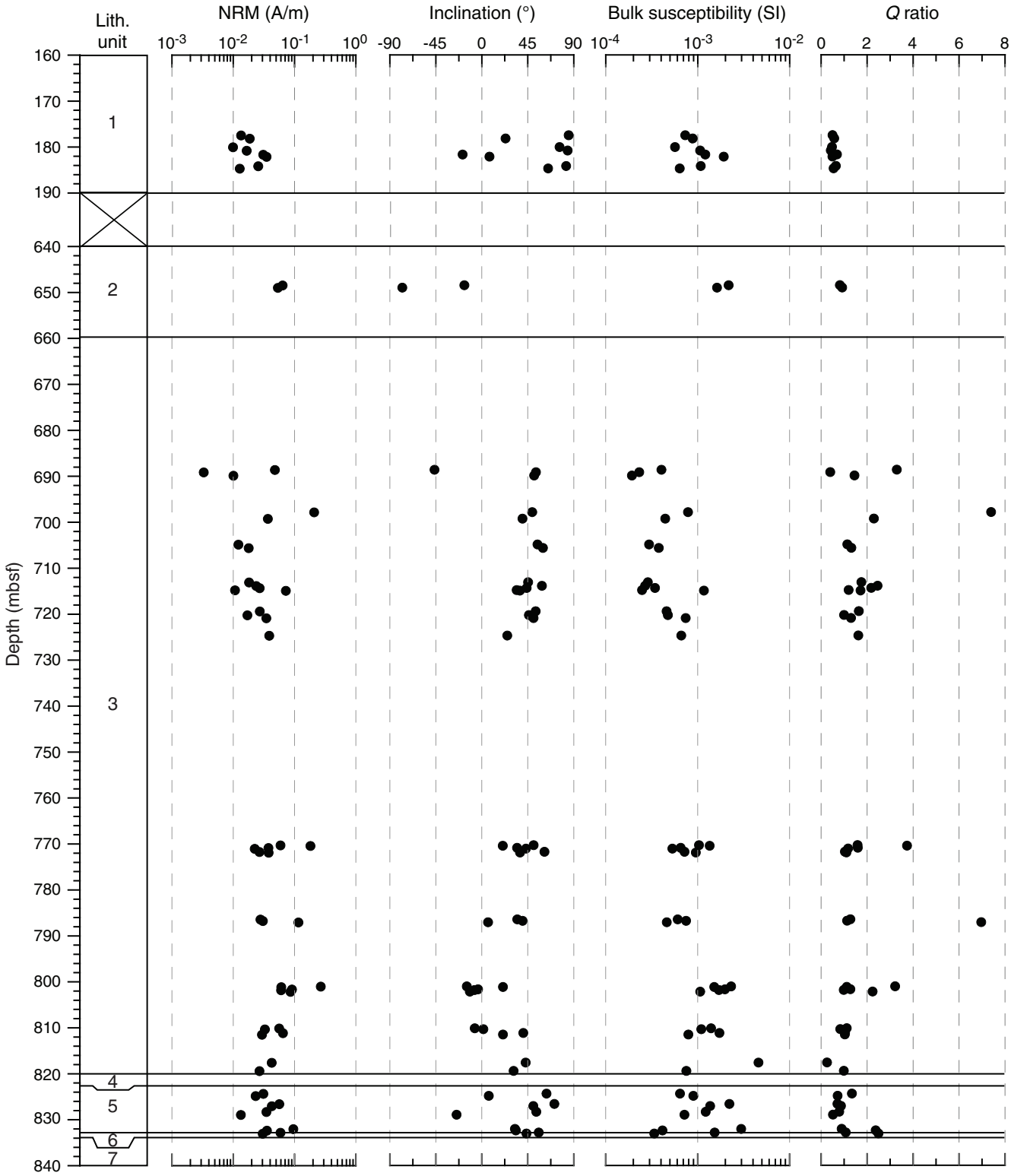

Figure F44. Downhole plot of parameters for AMS showing mean magnetic susceptibility (K_{mean}), minimum susceptibility (K_{min}) inclination, anisotropy degree parameter (P'), and shape parameter (T), Hole C0019E.

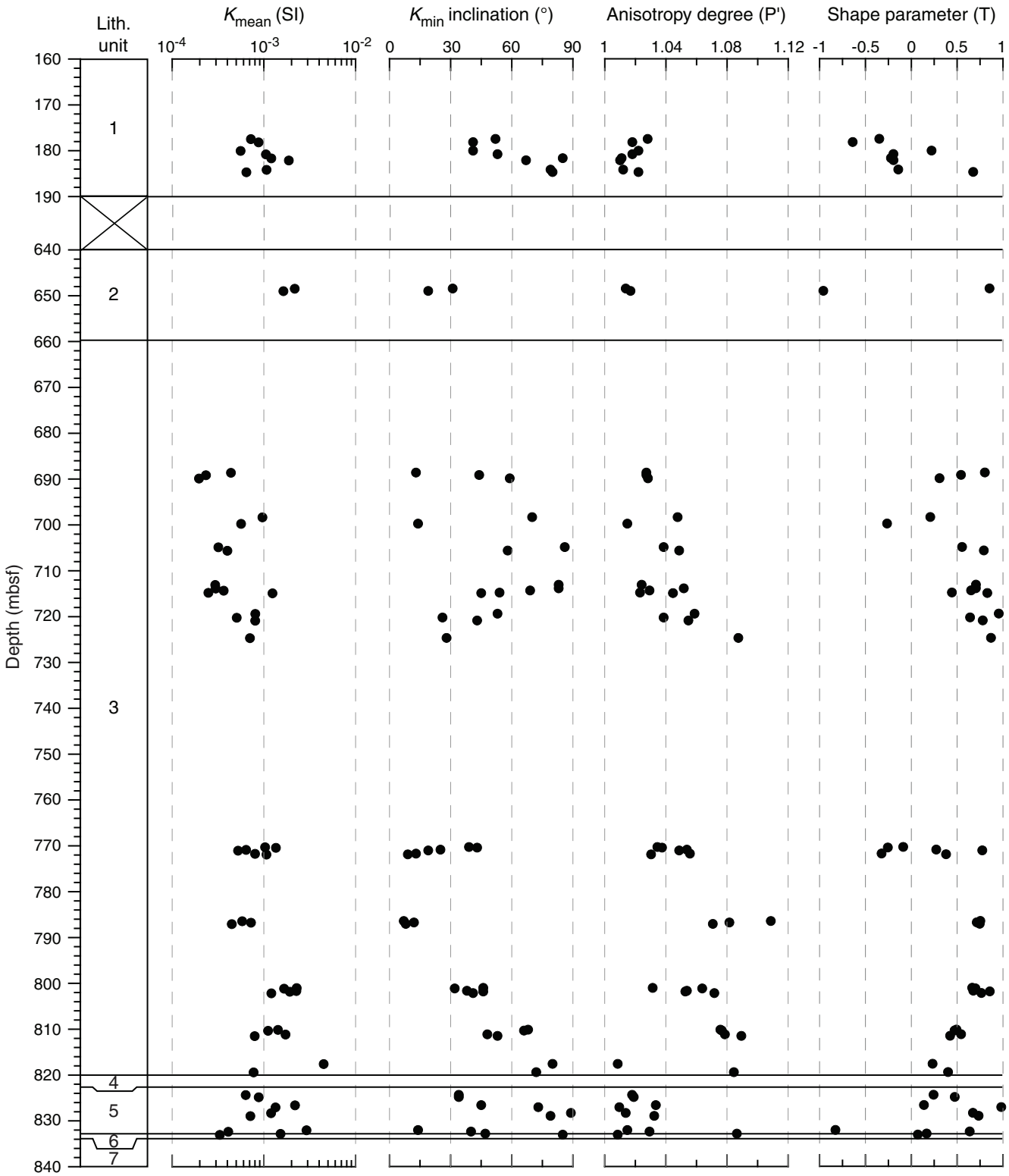

Figure F45. Representative vector endpoint diagrams of magnetization directions through stepwise AF demagnetization. Open circles = projection of magnetization vector endpoints onto the vertical plane, solid circles = projection of magnetization vector endpoints onto the horizontal plane. NRM = natural remanent magnetization. **A.** Sample 343-C0019E-1R-5, 34–36 cm. **B.** Sample 343-C0019E-10R-2, 4–6 cm.

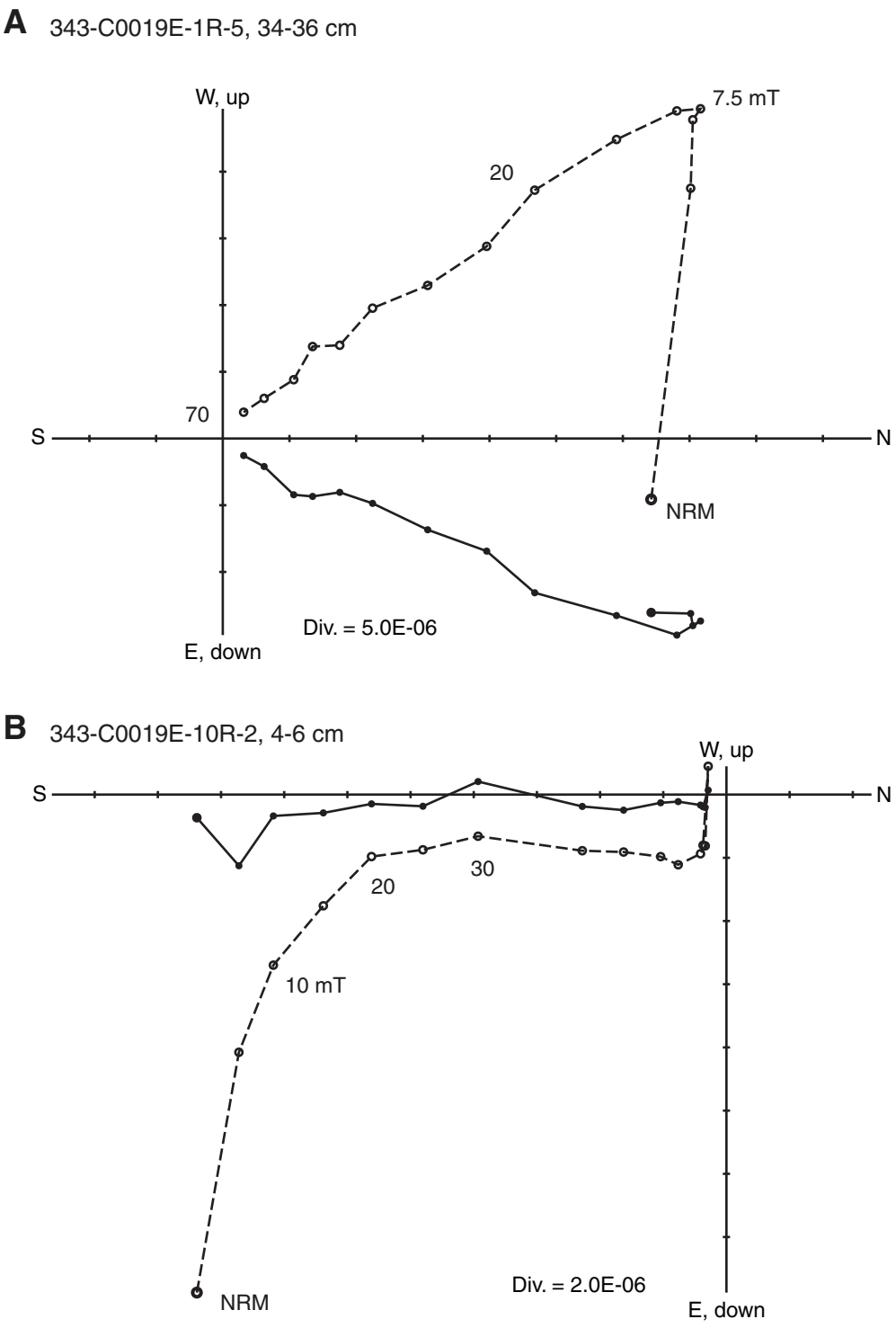

Figure F46. Profile of paleomagnetic declinations and inclinations for discrete paleomagnetic samples and archive halves, Hole C0019E. Black = paleomagnetic directions of discrete samples obtained using principal component analysis (PCA), blue = natural remanent magnetization (NRM) directions before demagnetization of archive halves, red = directions after AF demagnetization at 20 mT.

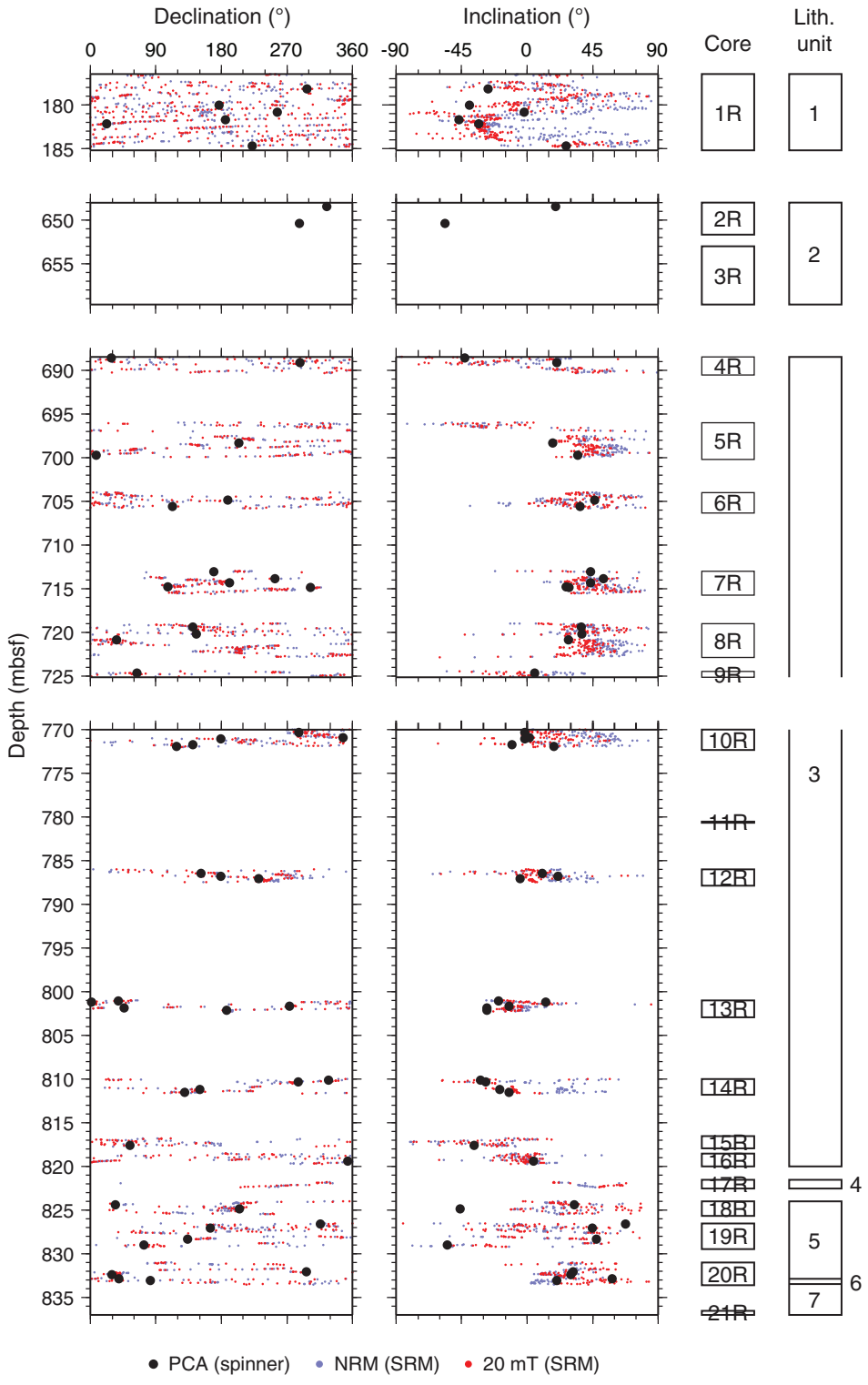

Figure F47. Plots of gamma ray attenuation (GRA) density, magnetic susceptibility, *P*-wave velocity, noncontact electrical resistivity, and natural gamma radiation determined by MSCL-W data for Core 343-C0019E-1R.

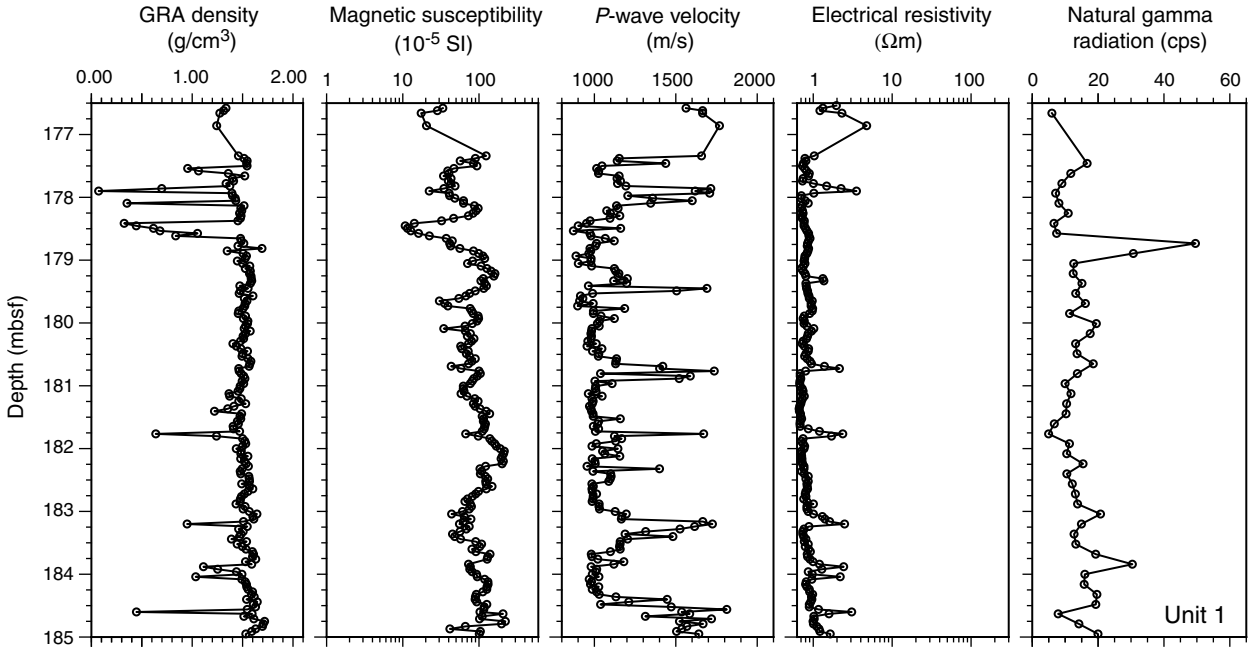

Figure F48. Plots of gamma ray attenuation (GRA) density, magnetic susceptibility, *P*-wave velocity, noncontact electrical resistivity, and natural gamma radiation determined by MSCL-W for Cores 343-C0019E-2R through 21R.

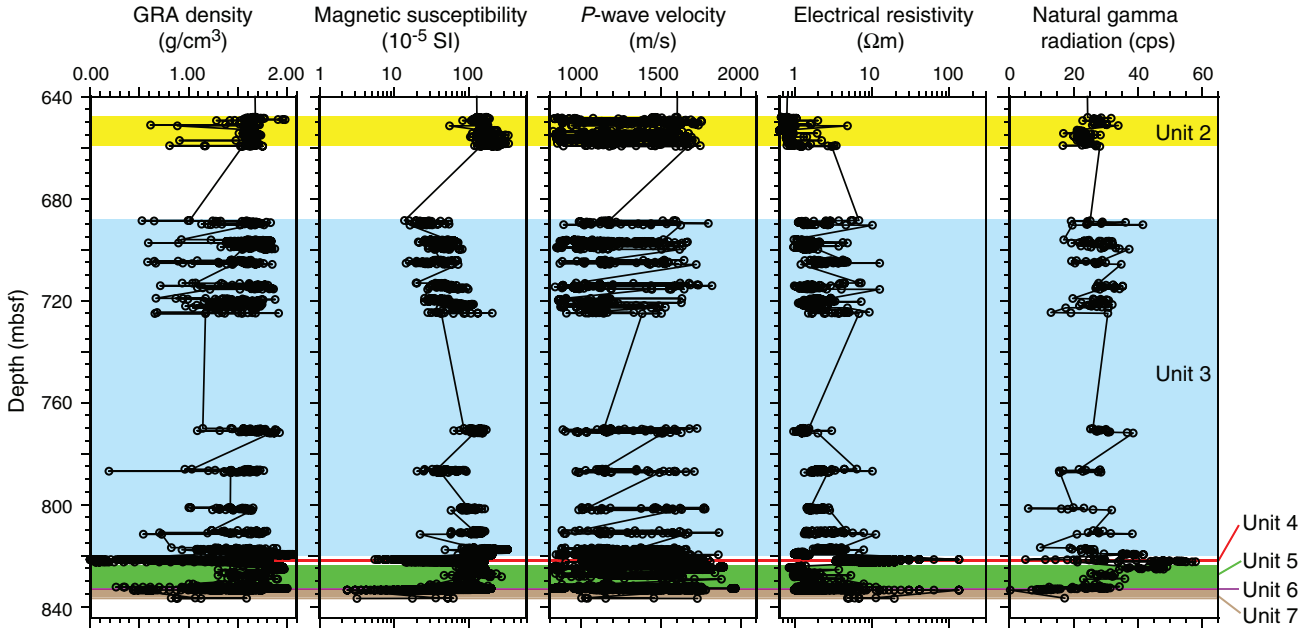

Figure F49. MSCL-W data for magnetic susceptibility, natural gamma radiation, gamma ray attenuation (GRA) density, and electrical resistivity for Core 343-C0019E-17R representing lithologic Unit 4 (plate boundary décollement zone). Shaded band = data considered most reliable based on GRA density measurements.

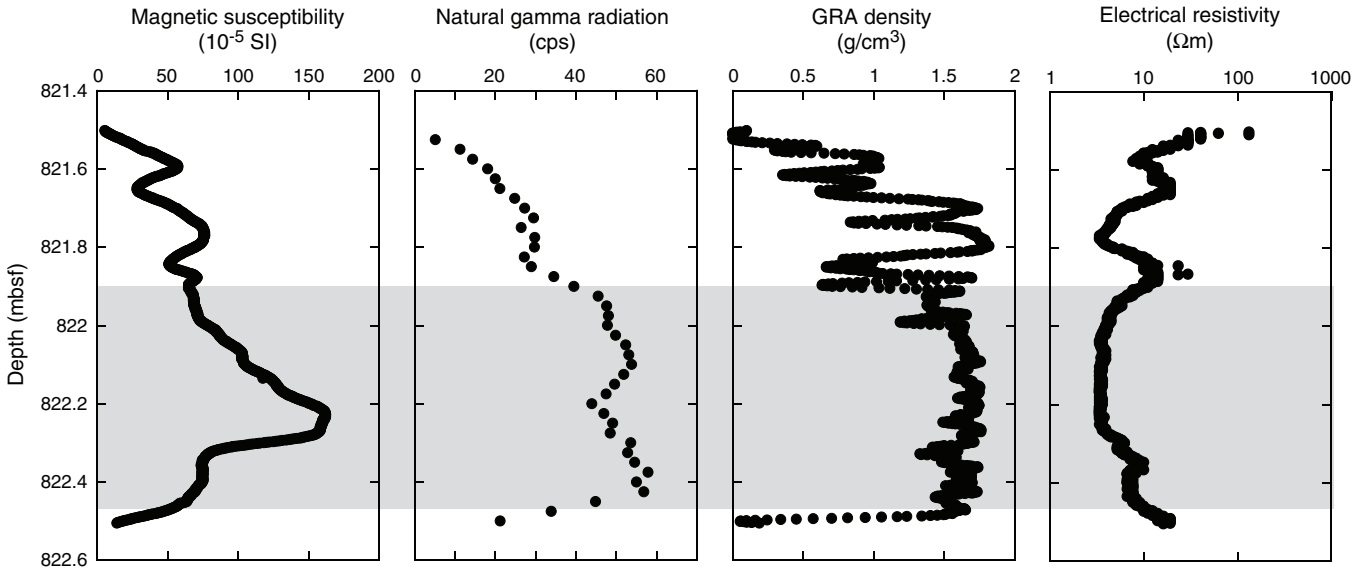

Figure F50. Plots of (**A**) bulk and grain density and (**B**) porosity on discrete samples, determined from MAD measurements, Hole C0019E. (**C**) *P*-wave velocity and (**D**) electrical resistivity measurements on discrete cube samples in *x*-, *y*-, and *z*-directions of the core reference frame. **E.** Thermal conductivity measurement results.

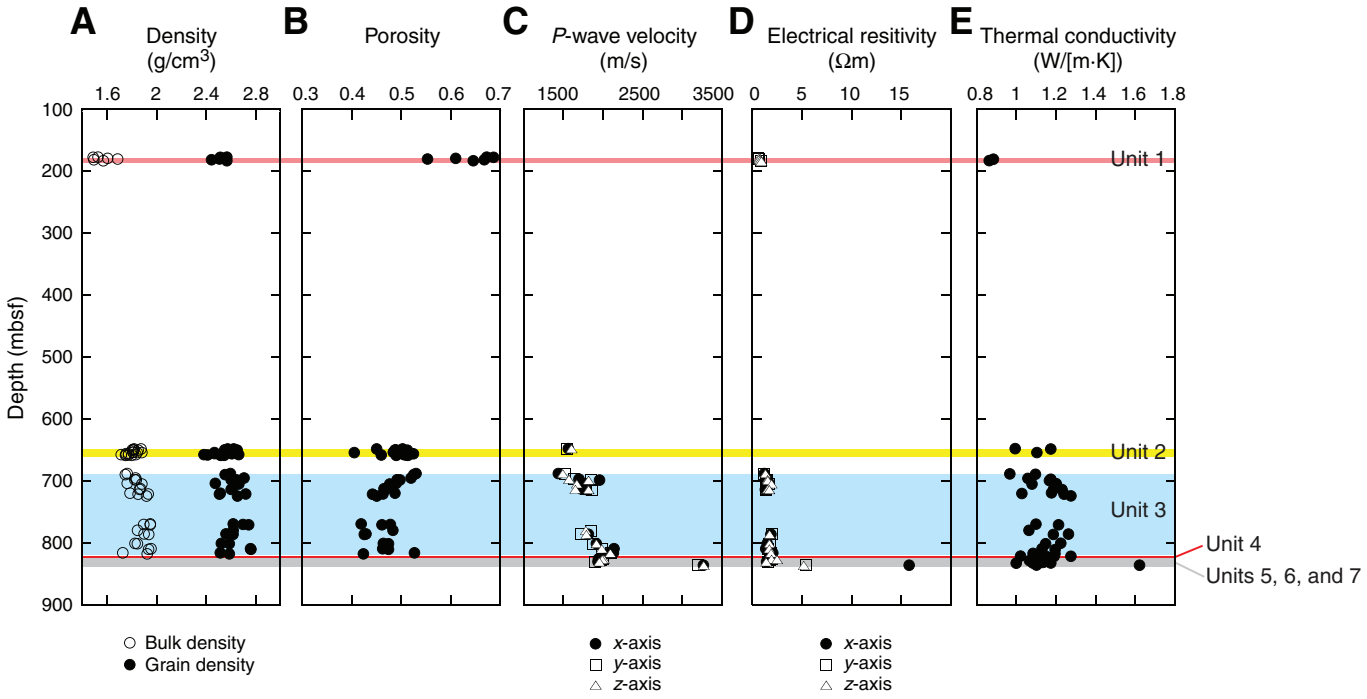

Figure F51. Plot of unconfined compressive strength (UCS) of discrete cylindrical samples, Hole C0019E. All values are corrected for sample geometry (see **"Physical properties"** in the "Methods" chapter [Expedition 343/343T Scientists, 2013]). Arrow on the lithologic Unit 7 sample indicates that this data point represents a lower bound on strength.

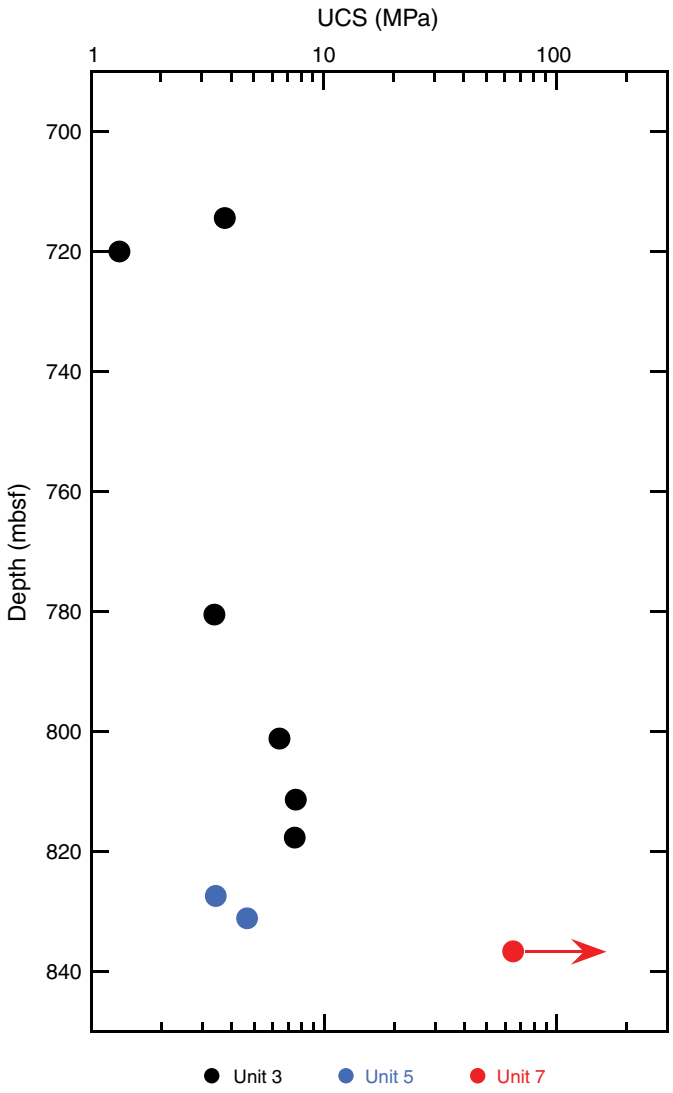

Figure F52. Plot of *P*-wave velocity as a function of porosity for discrete samples, Hole C0019E.

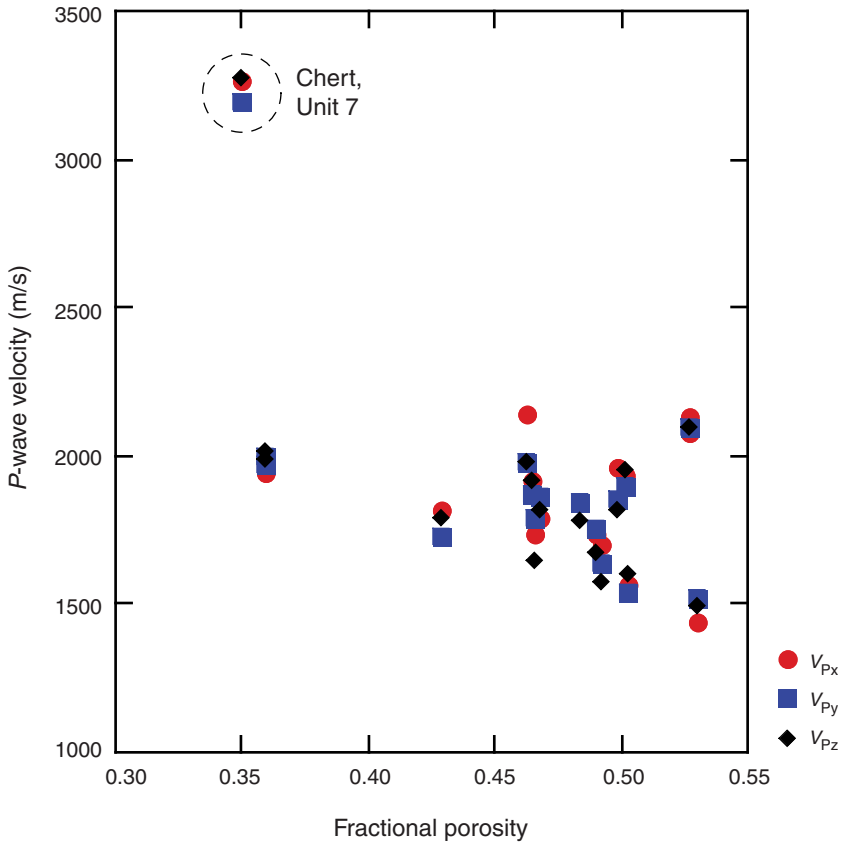

Figure F53. Plots of (**A**) vertical anisotropy of *P*-wave velocity for discrete samples and (**B**) vertical anisotropy of electrical resistivity for discrete samples, Hole C0019E.

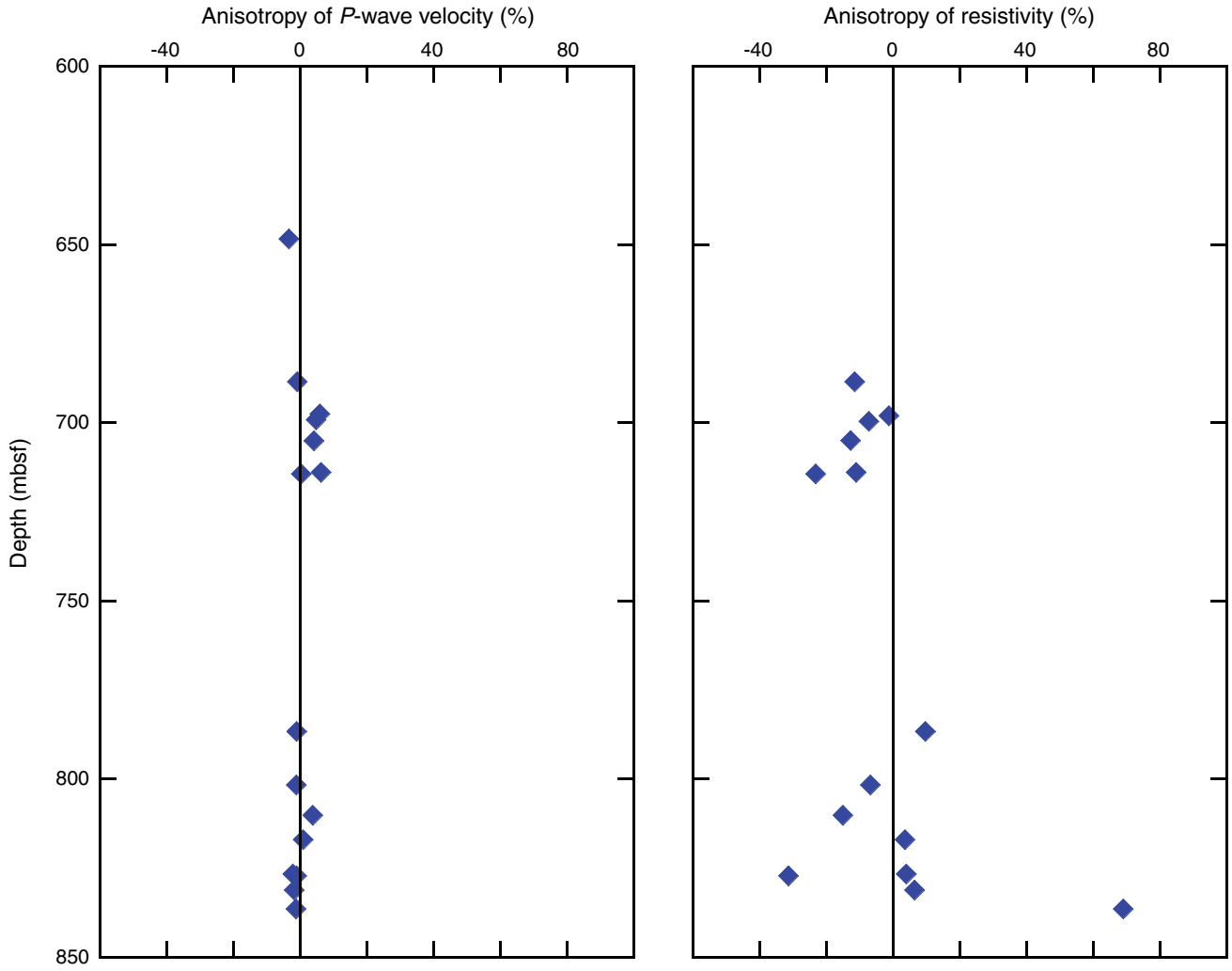

Figure F54. Plots of elastic wave velocity under high pressure for Sections (**A**) 343-C0019E-4R-1, (**B**) 5R-2, (**C**) 7R-1, (**D**) 19R-1, and (**E**) 21R-1. For each sample, nine measurements were attempted at every step in confining pressure. Large symbols = measured during pressurizing, small symbols = measured during depressurizing. We measured *S*-wave velocity considering polarization anisotropy along an axis. For example, SXz is the *S*-wave velocity propagating along the *x*-axis and polarized in the *xz* plane and SXy is the *S*-wave velocity propagating in the *x*-axis and polarized in the *xy* plane.

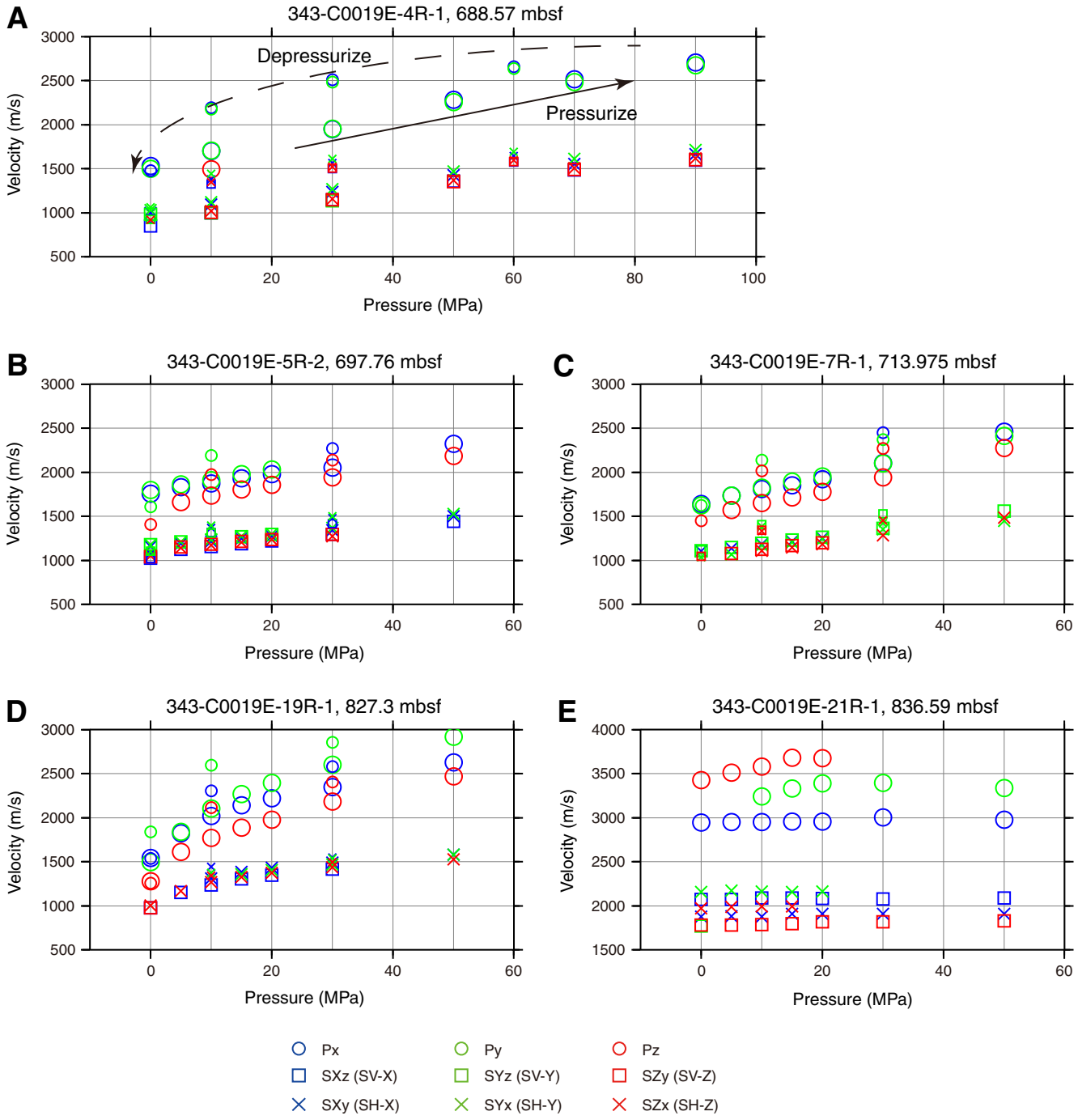

Figure F55. Plot of electrical resistivity as a function of porosity for discrete samples, Hole C0019E.

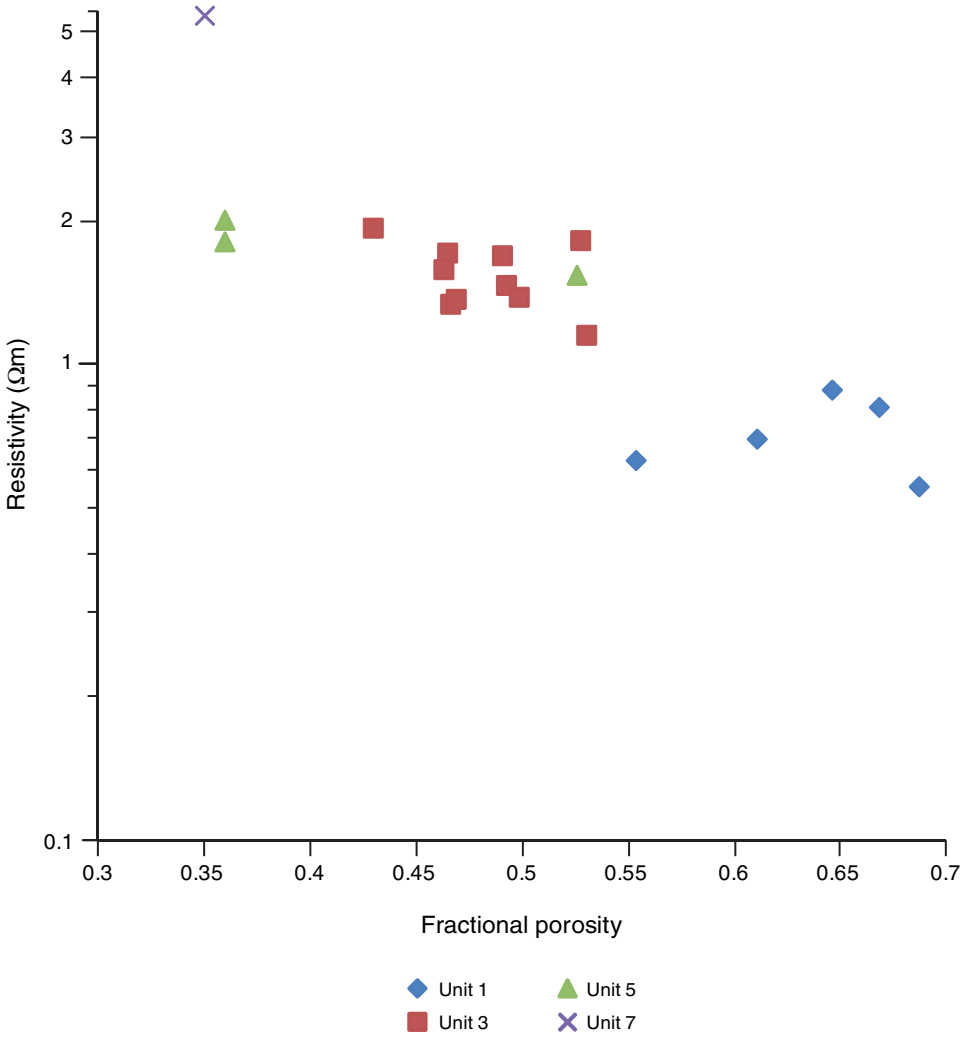

Figure F56. Plot of particle size analysis results of discrete samples, Core 343-C0019E-1R.

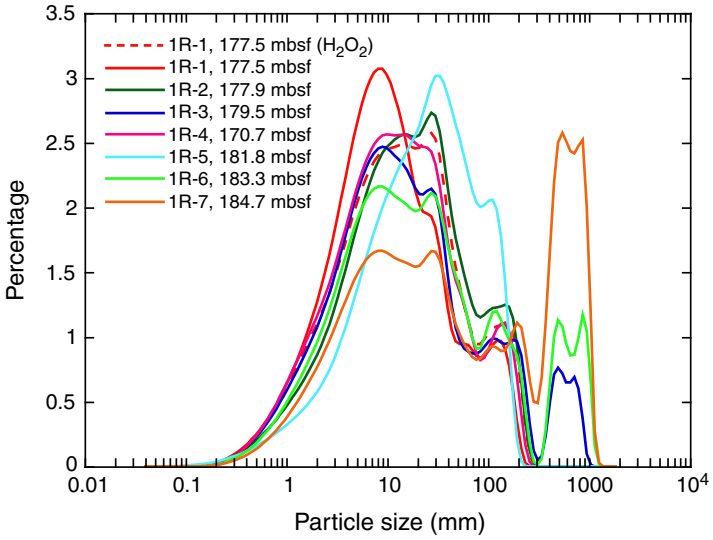

Figure F57. Color spectrometry parameters L*, a*, and b*, Hole C0019E.

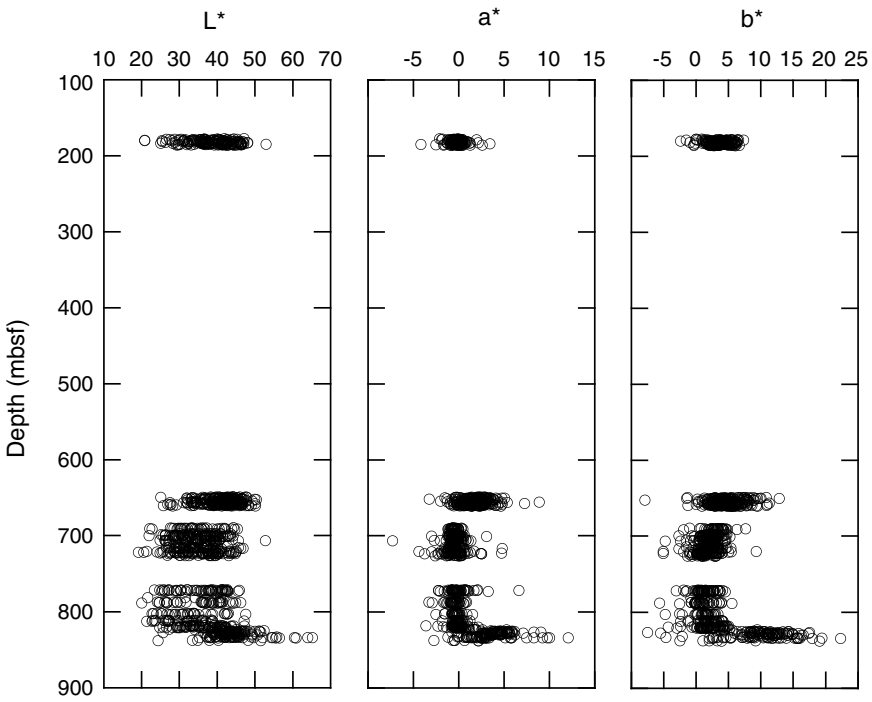

Figure F58. Plots of depth profiles of sulfate, alkalinity, pH, phosphate, ammonium, salinity, chlorinity, and bromide. Plots represent data summarized in Table T10. Arrows = seawater value.

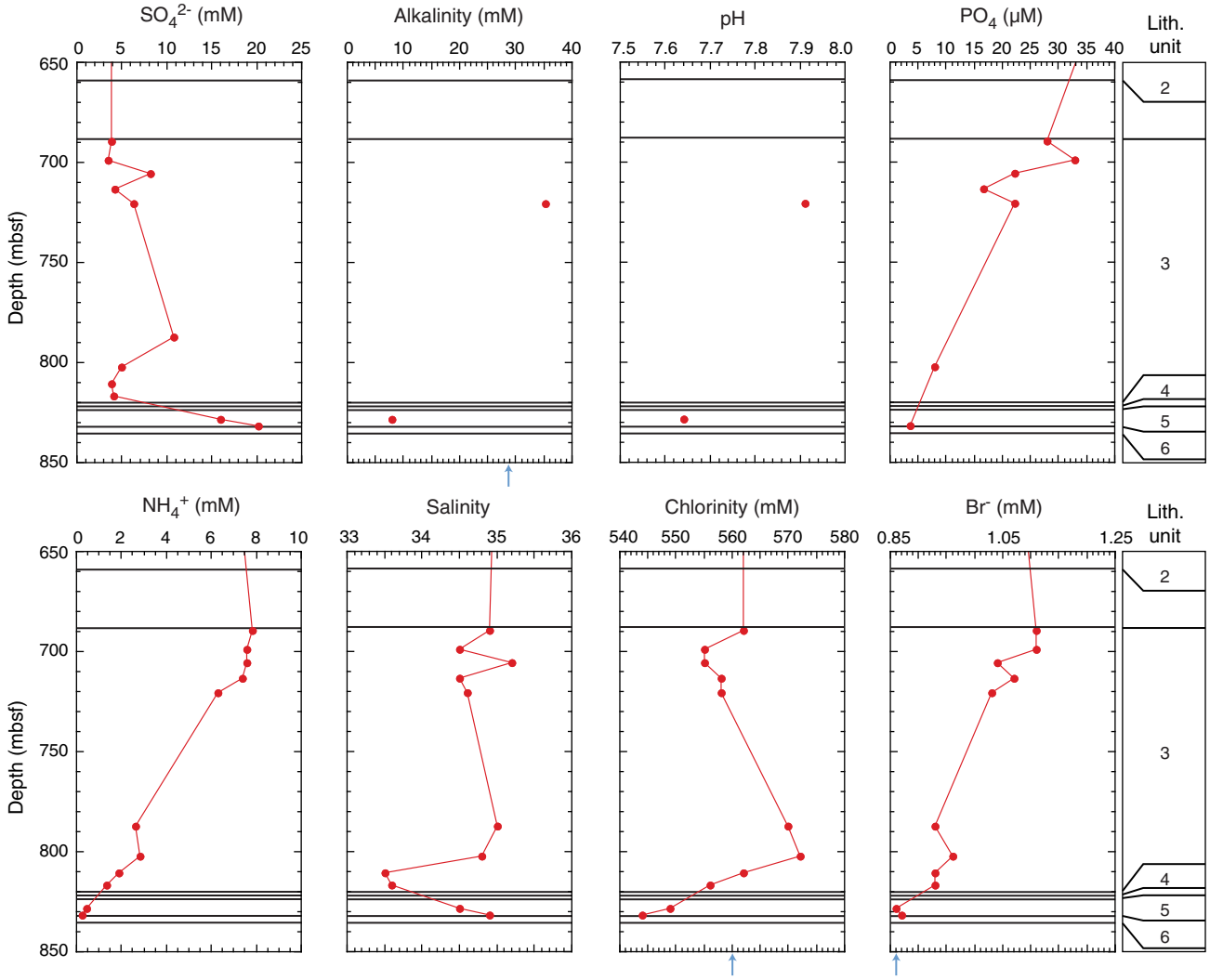

Figure F59. Cross-plots of selected elements, Site C0019. Circles = deepest five samples, squares = shallowest seven samples, open diamonds = seawater concentrations, closed diamonds = compositions of high-viscosity drilling mud.

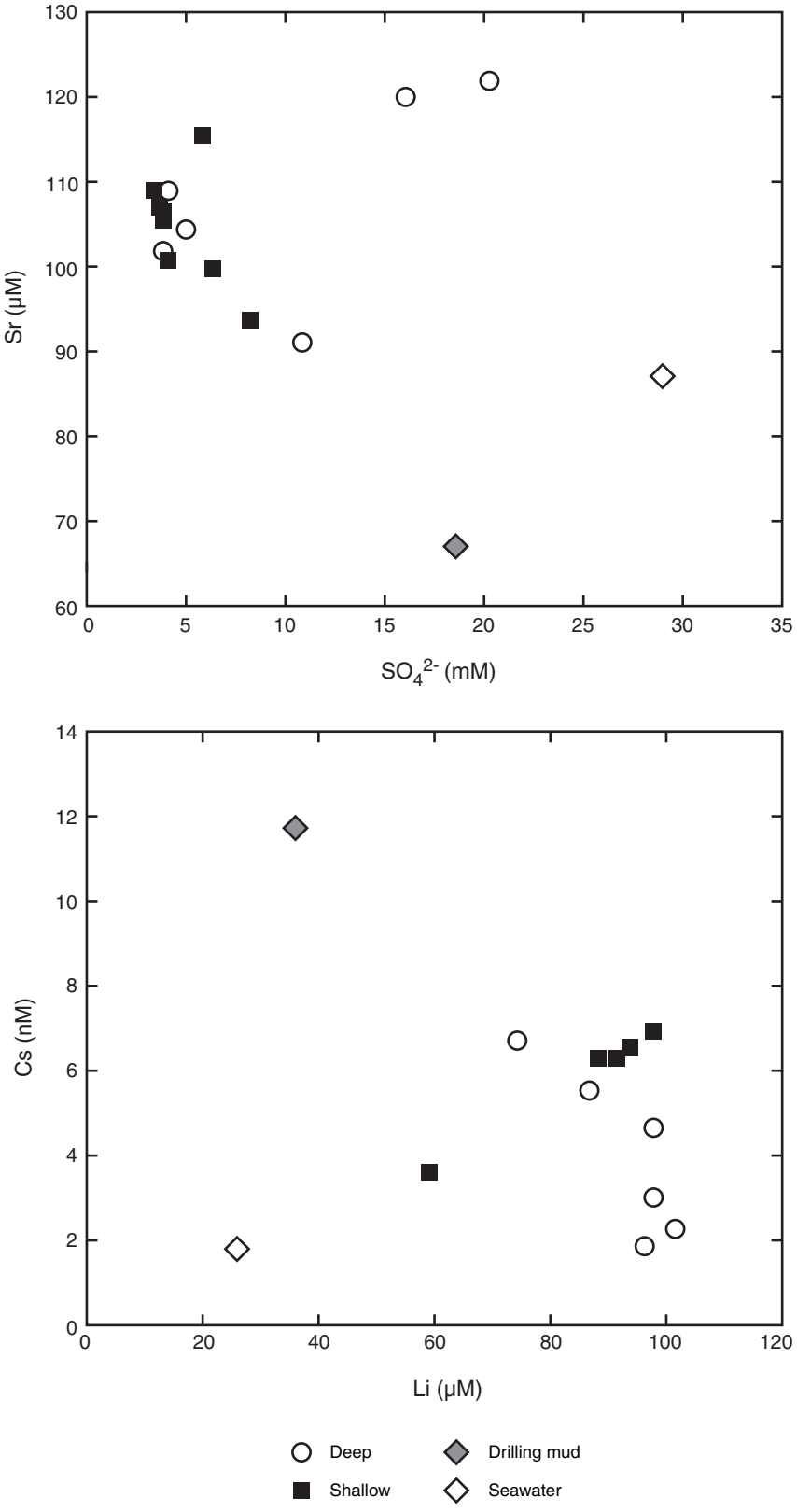

Figure F60. Plots of depth profiles of sodium, potassium, calcium, magnesium, barium, iron, silica, boron, lithium, and manganese, Site C0019. Plots represent data summarized in Table T10. Arrows = seawater value.

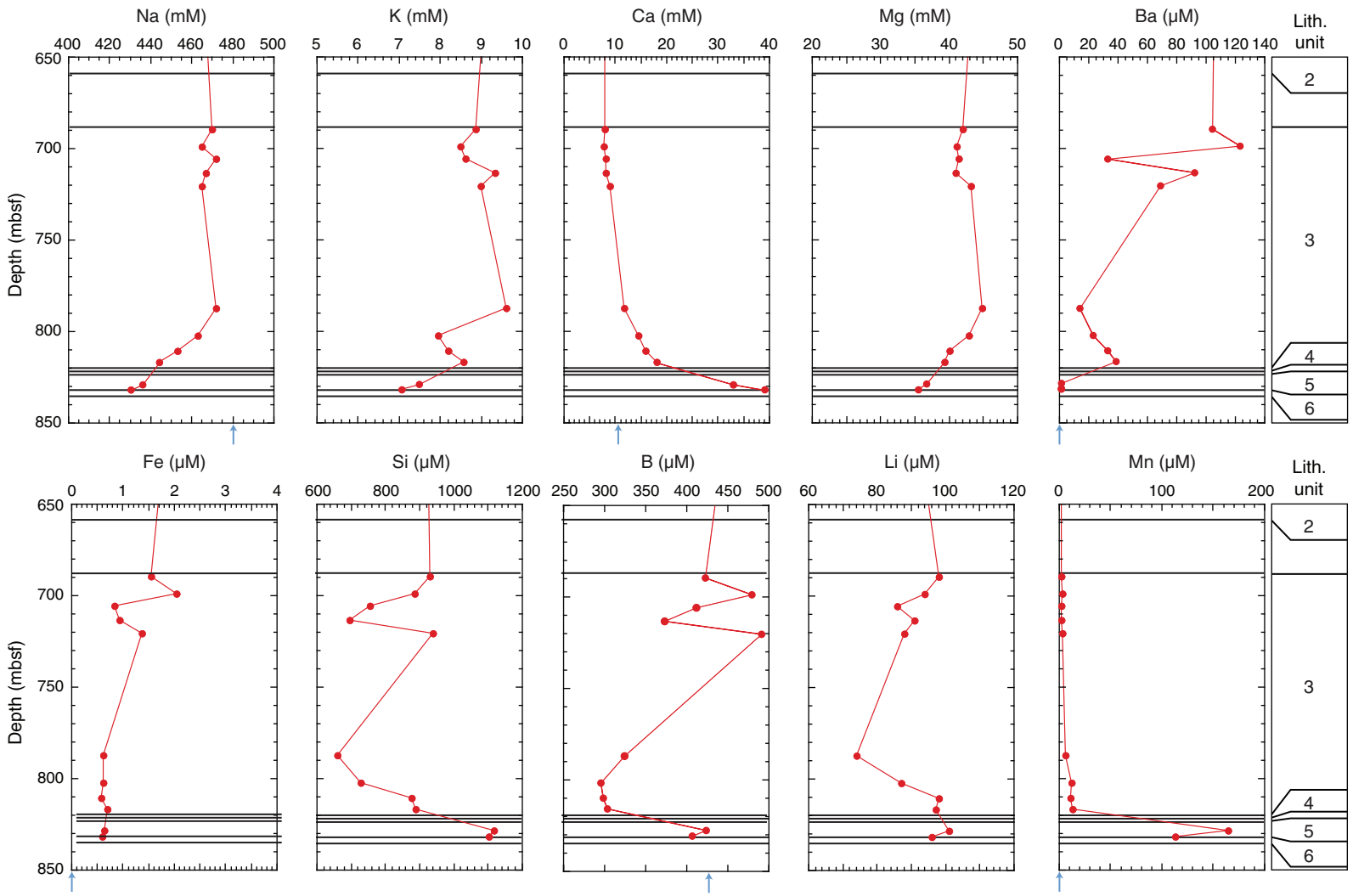

Figure F61. Plots of depth profiles of vanadium, zinc, strontium, rubidium, molybdenum, cesium, lead, uranium, and copper, Site C0019. Plots represent data summarized in Table T10.

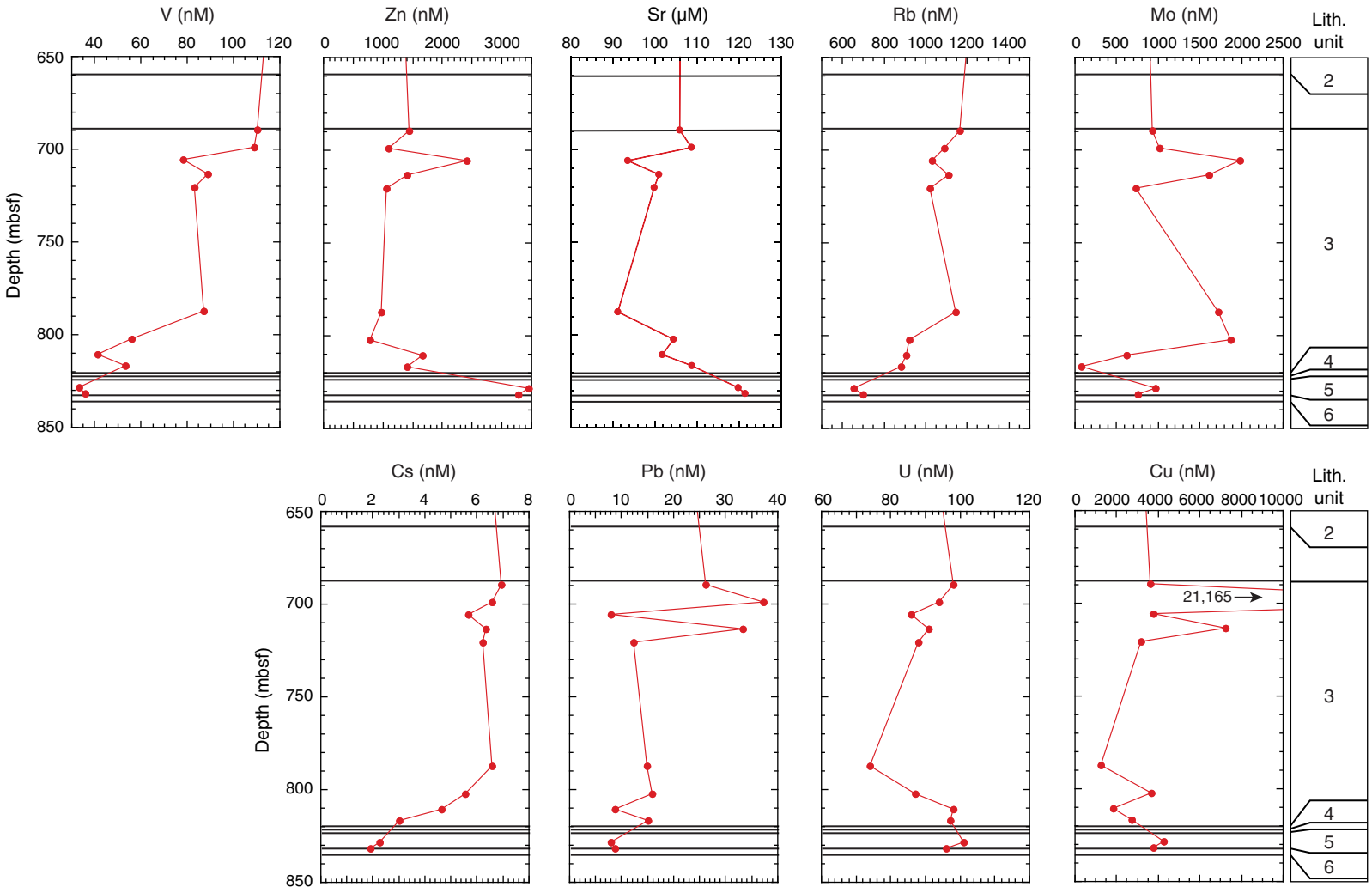

Figure F62. Plots of depth profiles of total carbon (TC), inorganic carbon (IC), calcium carbonate ($CaCO_3$), total organic carbon (TOC), total nitrogen (TN), total sulfur (TS), TOC/TN ratio, and TOC/TS ratio, Site C0019. Depth intervals of lithologic Units 2–6 are shown on the right.

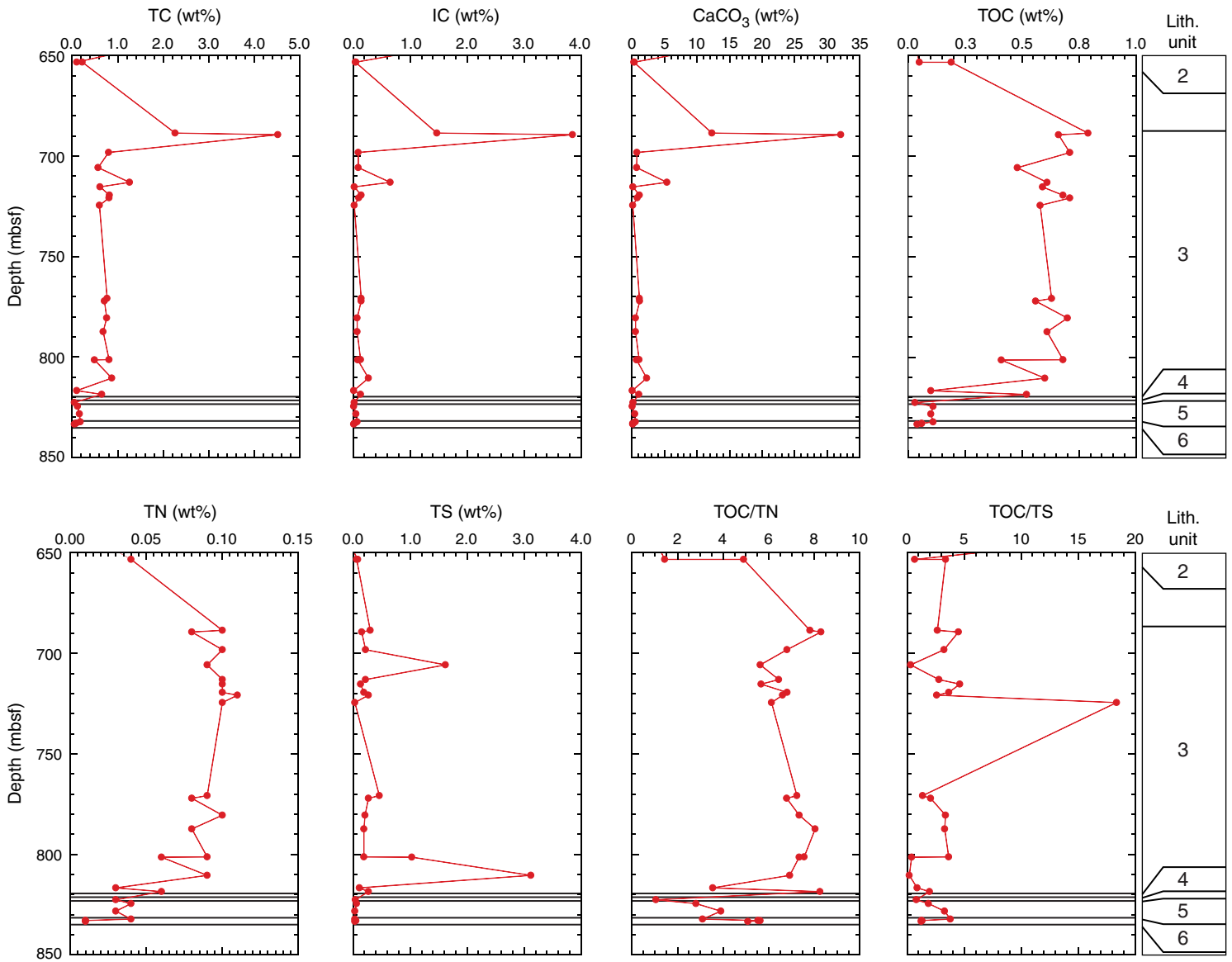

Figure F63. Plots of depth profiles of H_2, CO, methane, ethane, methane/ethane ratio, and H_2/methane ratio, Hole C0019E. Blue line = horizon of potential earthquake-induced fault slip, green line = depth range of great methane depletion.

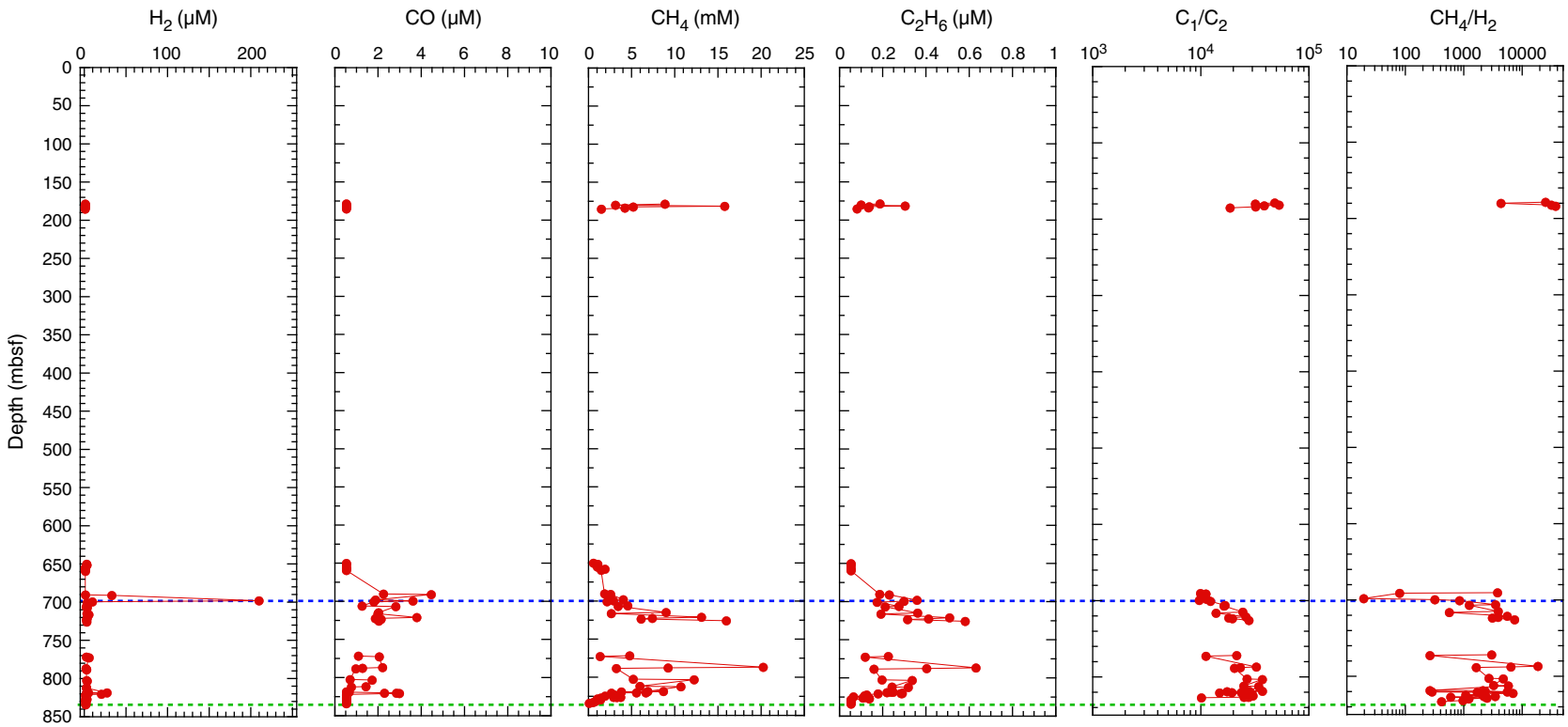

Figure F64. Plots of recorded temperatures and depths (converted internally from pressure data) as a function of time during free-fall MTL Run 1, Hole C0019E. JST = Japan Standard Time.

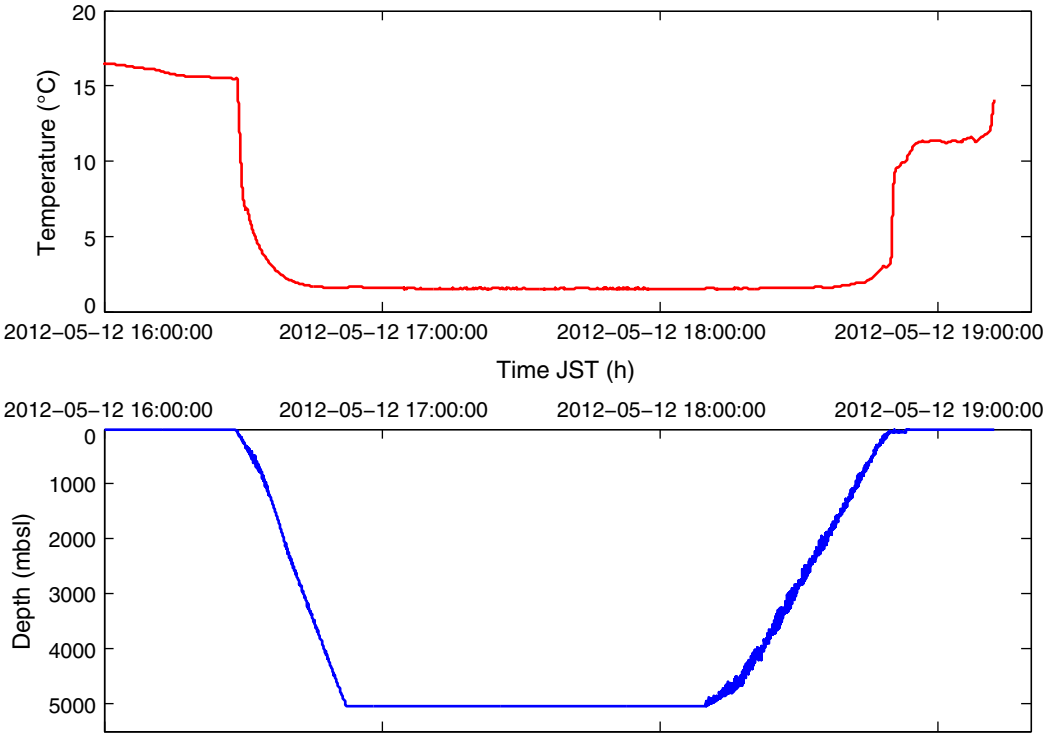

Figure F65. Plot of recorded temperature data as a function of depth during Run 1, Hole C0019E.

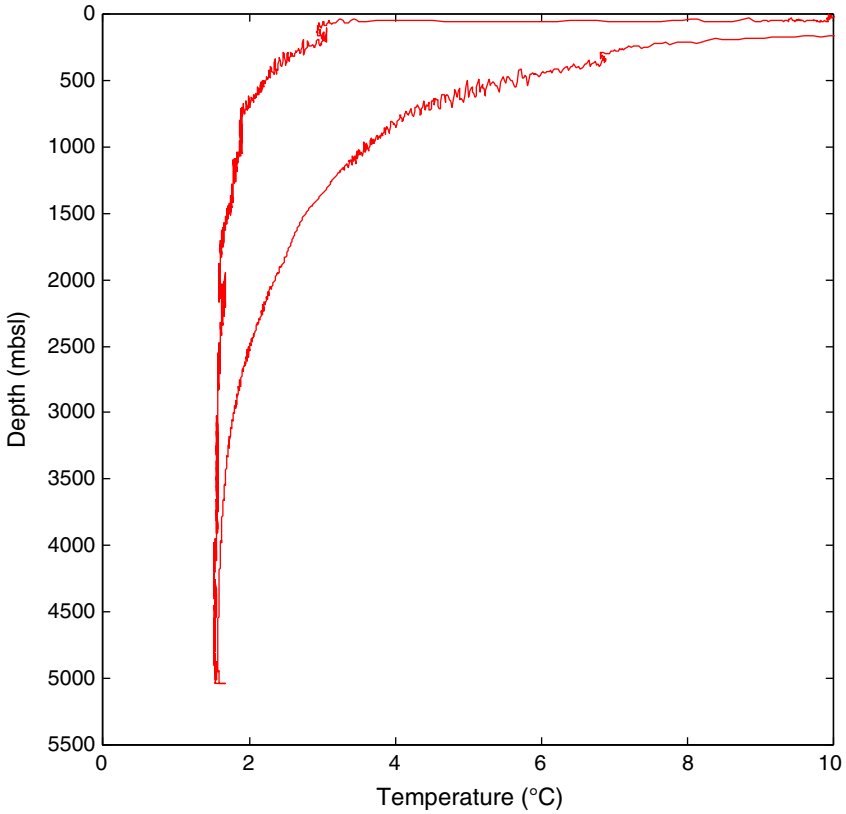

Figure F66. Plots of recorded temperatures and depths as a function of time during free-fall MTL Run 2, Hole C0019E. JST = Japan Standard Time.

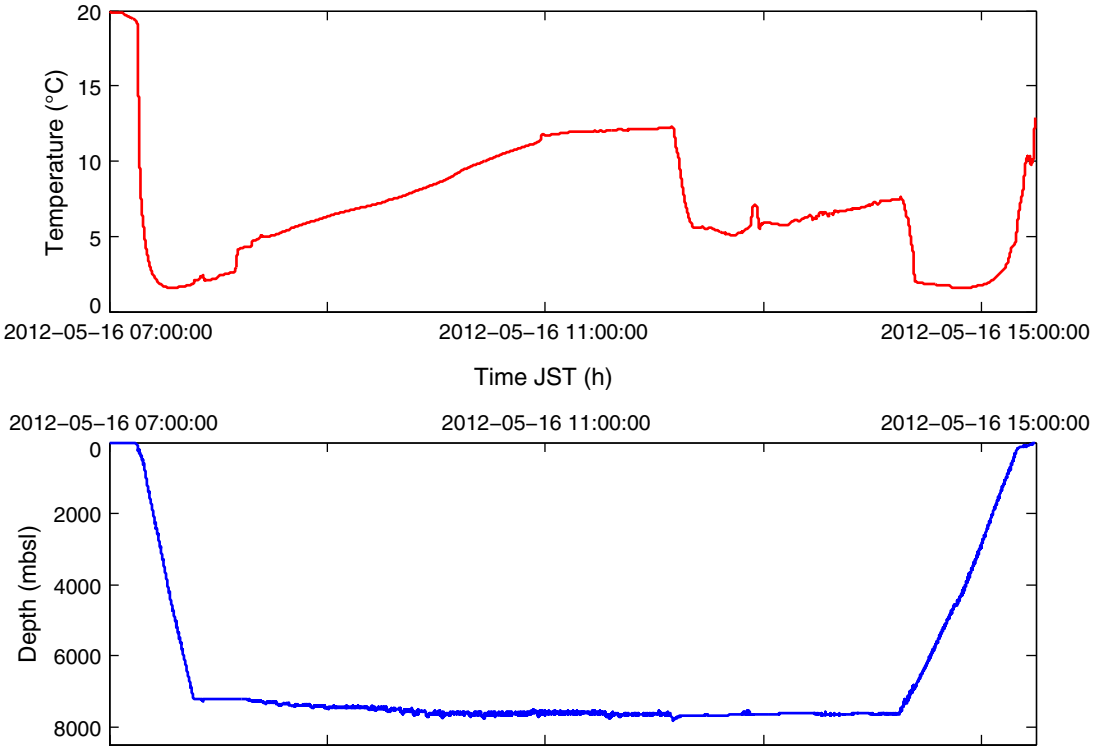

Figure F67. Plots of recorded temperature data as a function of depth during free-fall MTL Run 2, Hole C0019E. **A.** Data recorded in both the water column and subseafloor. **B.** Zoomed in version of A highlighting the temperature data as a function of depth during free-fall MTL Run 2 when the instrument was below seafloor. The figure is annotated to show how temperature changes correspond to other operations listed numerically in order of occurrence.

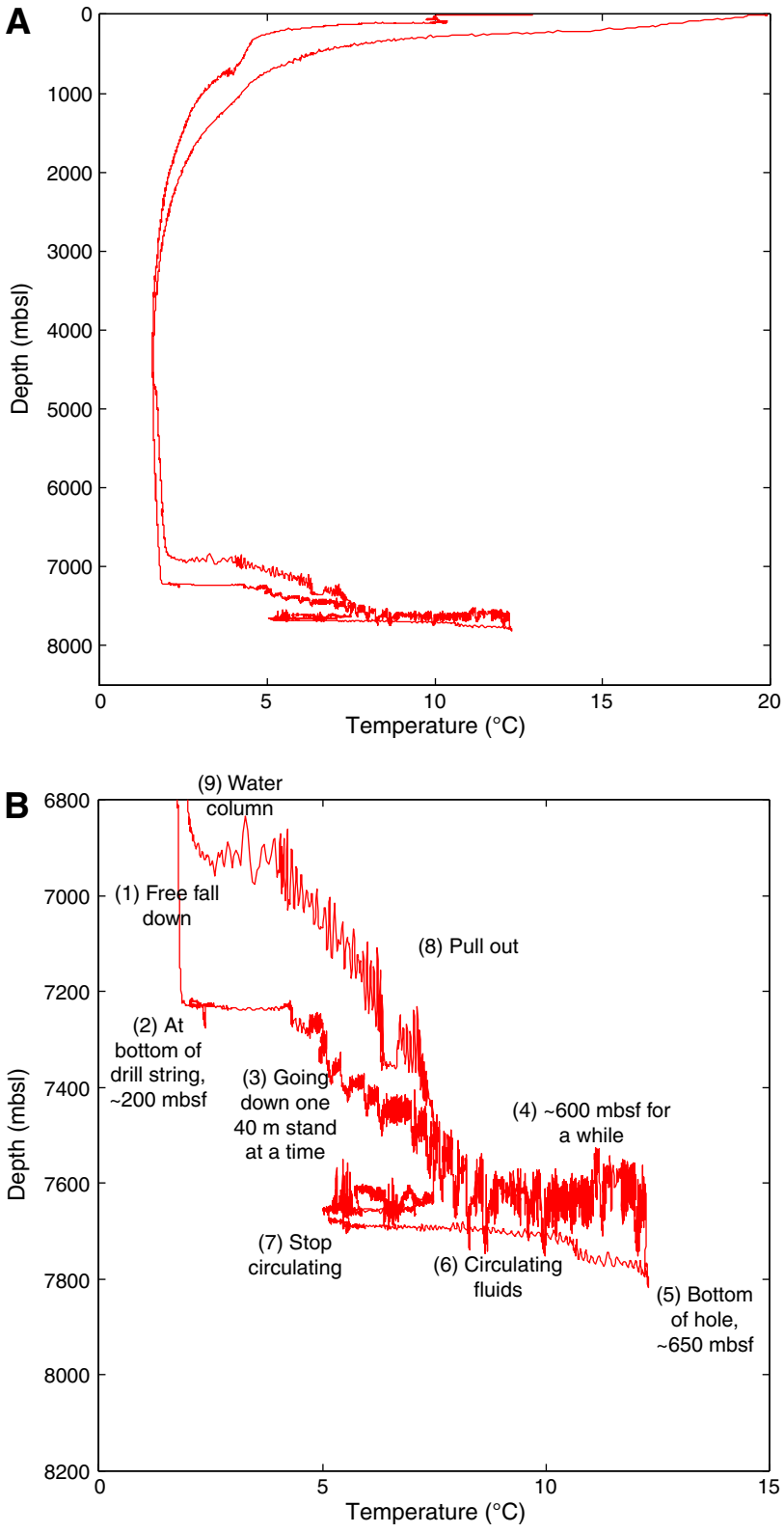

Figure F68. Plots of recorded temperatures and depths as a function of time during free-fall MTL Run 3, Hole C0019E. JST = Japan Standard Time.

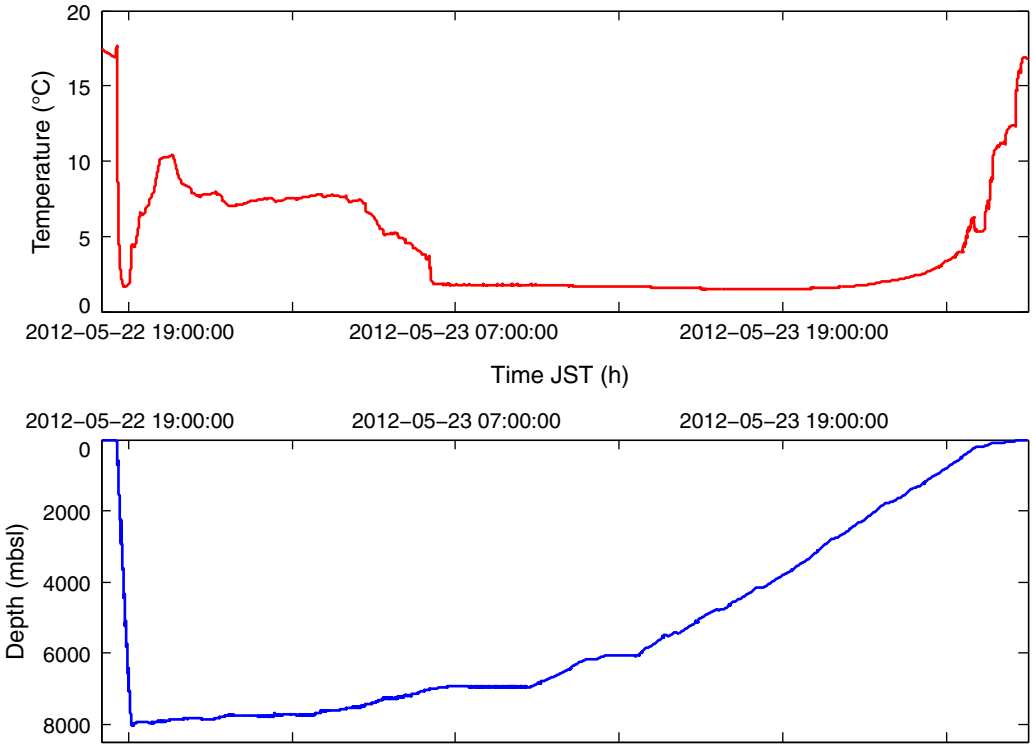

Figure F69. Plots of recorded temperature data as a function of depth during free-fall MTL Run 3, Hole C0019E. **A.** Data recorded in both the water column and subseafloor. **B.** Zoomed in version of A highlighting the temperature data as a function of depth during free-fall MTL Run 3 when the instrument was below seafloor.

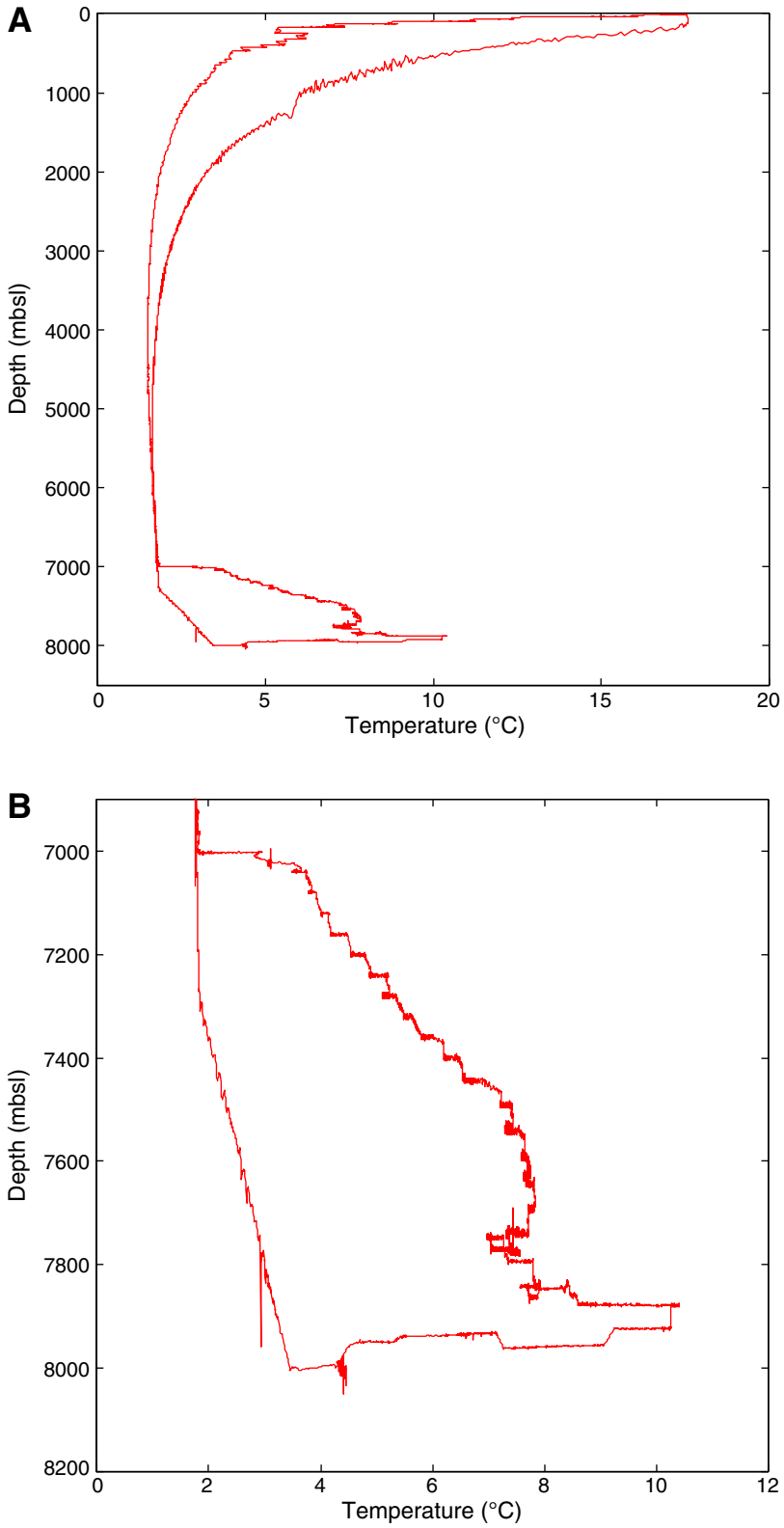

Figure F70. Log curves and synthetic seismogram on Line HD33B, Hole C0019B. The seismic section is in time and log data are overlain using the log-based time-depth curve. The synthetic seismic trace (black) is shown along the wellbore path with gamma ray (GR) (green) and button resistivity (RES) (royal blue = deep, light blue = medium, light green = shallow). VE = vertical exaggeration.

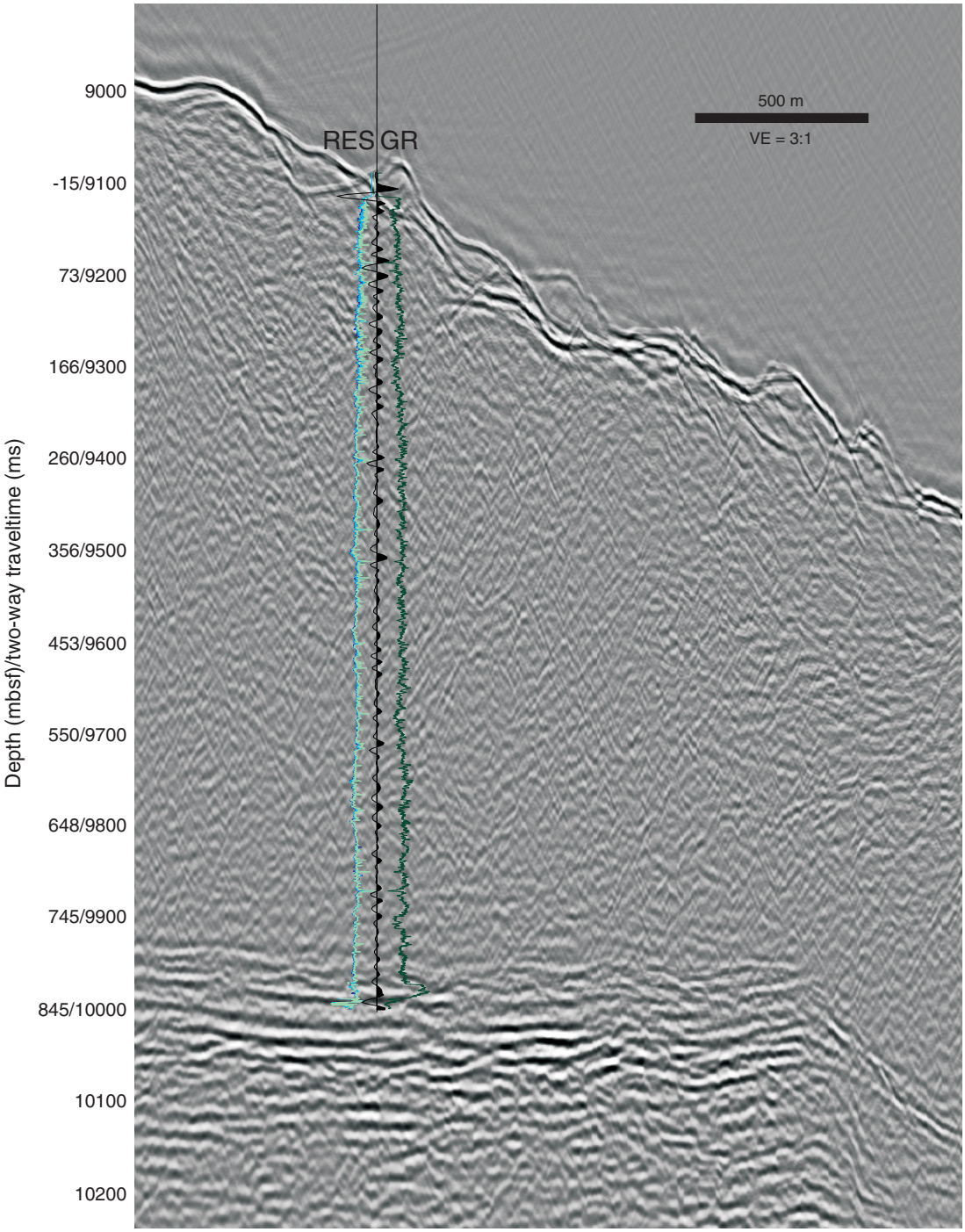

Figure F71. Log units on Line HD33B, Site C0019. The seismic section is in time and log units are overlain using the log-based time-depth curve. Blue = log Unit I, yellow = log Subunit IIa, orange = log Subunit IIb, green = log Unit III, red = log Unit IV. Interpreted seismic units are shown with transparent colors: brown = seismic Unit A, yellow = seismic Unit B, green = seismic Unit C. VE = vertical exaggeration.

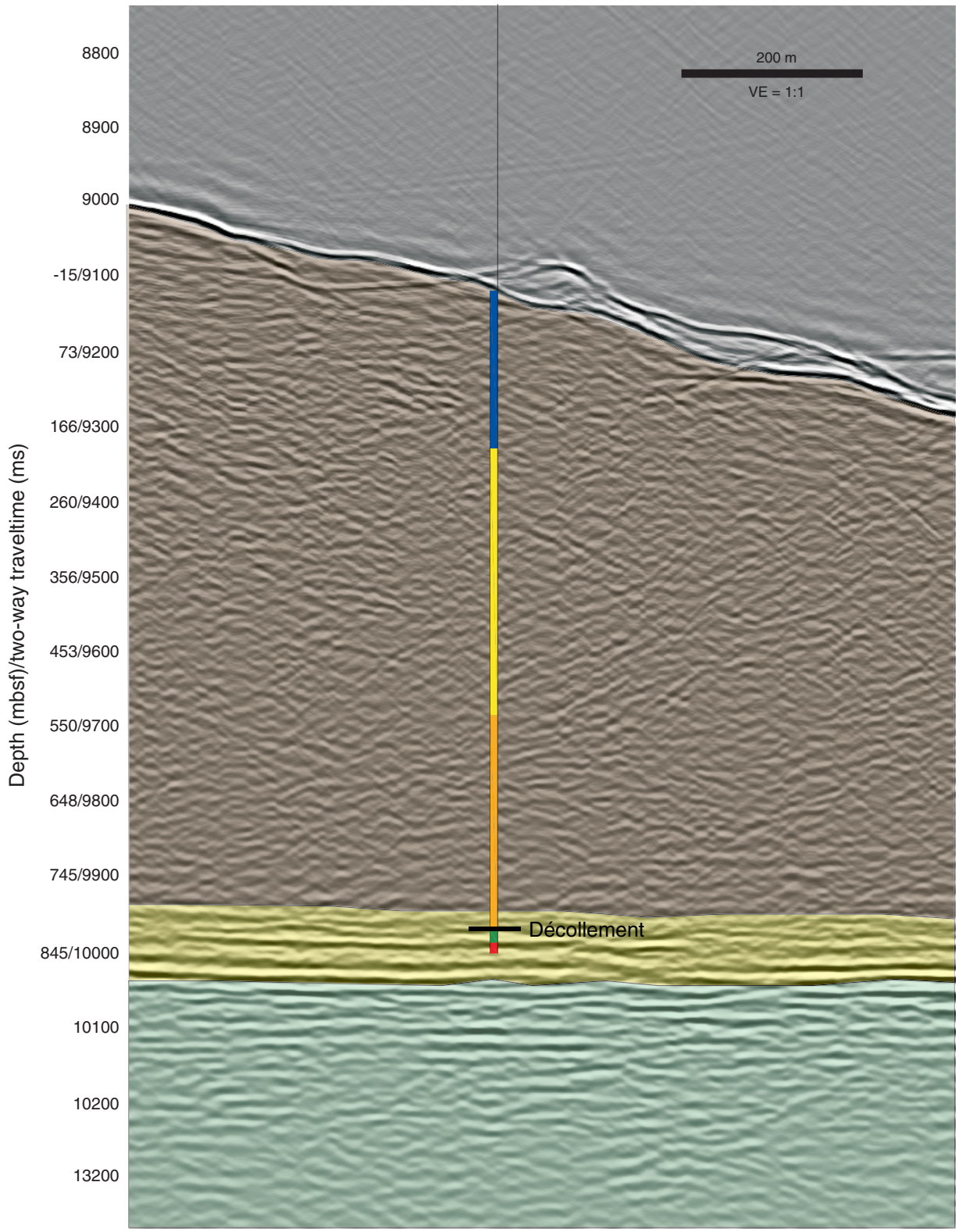

Figure F72. Core-Log-Seismic data structural summary diagram, Site C0019. Core recovery is shown in black for each core length. Log units are defined using LWD data. Gamma ray: green = LWD gamma ray. Resistivity: dark blue = deep button, turquoise = medium button, light green = shallow button LWD data. Lithologic units are defined from visual core description. X-ray fluorescence (XRF) analysis: K_2O, Al_2O, and MnO equate to potassium, aluminum, and manganese content in core samples, respectively. Structural domains are defined by LWD sinusoid picks on electrical images: f = fracture zone. Azimuth: bedding (red circles) and fracture (blue circles) orientations picked on LWD resistivity at bit images. Bedding dip: open circles = LWD data, filled circles = measured on core; fractures dip: open circles = LWD data, filled circles = measured on core. Orange transparent overlay boxes show fault zones (720 fault and 820 fault) as defined from visual core description. RAB = resistivity at the bit.

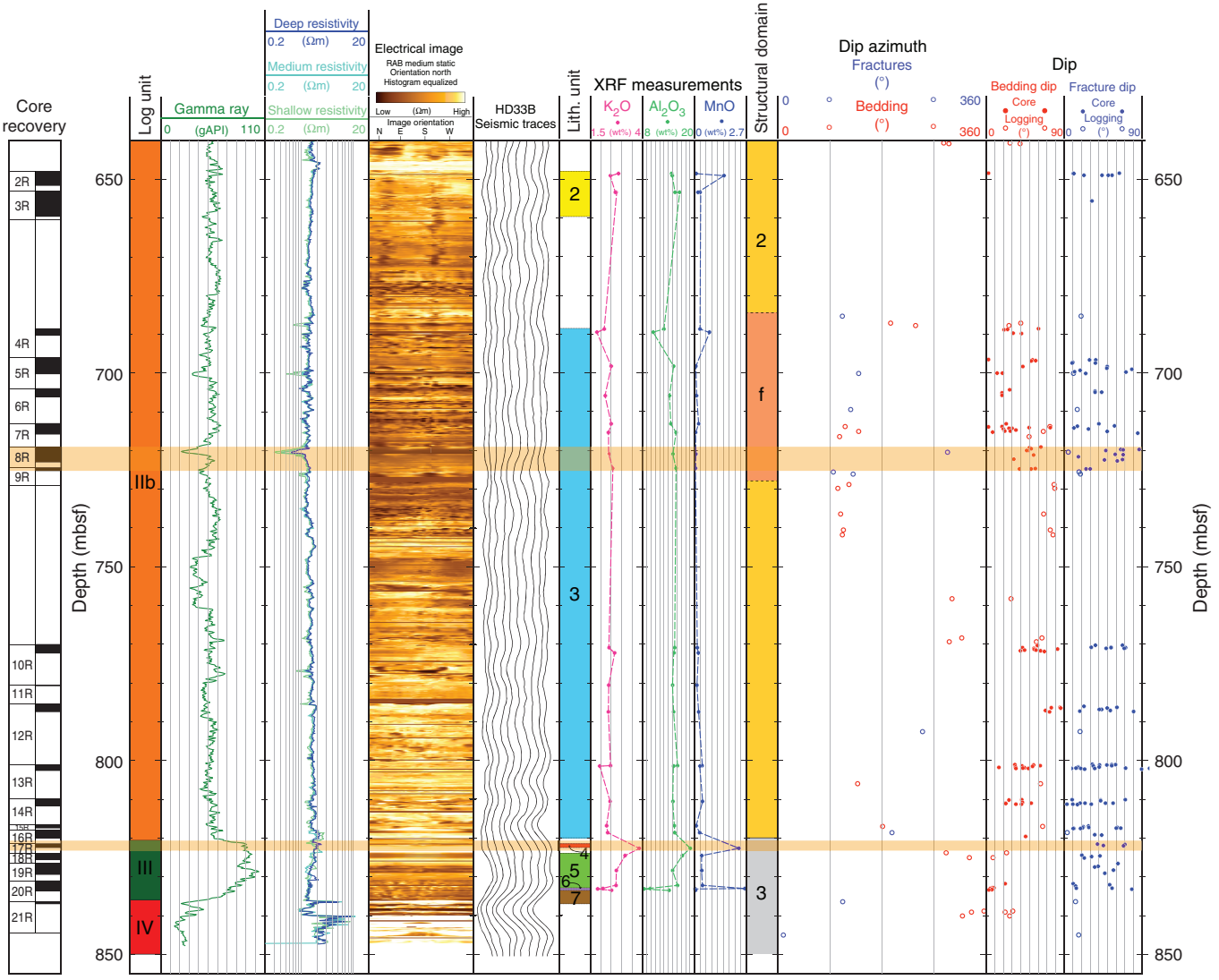

Table T1. Expedition 343/343T coring summary.

Hole	Latitude	Longitude	Water depth (mbsl)	Cores (*N*)	Interval cored (m)	Core recovered (m)	Recovery (%)	Drilled interval (m)	Total penetration (m)	Time on site (days)
343-										
C0019E	37°56.3343′N	143°54.8084′E	6889.5	21	137	53.31	43	844.5	844.5	9
C0019A	37°56.3367′N	143°54.8100′E	6883.5	0	NA	NA	NA	28	28	3
C0019B	37°56.3367′N	143°54.8100′E	6889.5	0	LWD/MWD	LWD/MWD	LWD/MWD	850	850.5	21
C0019C	37°56.3033′N	143°54.7875′E	6900.0	0	NA	NA	NA	120	121.5	3
C0019D	37°56.3224′N	143°54.8004′E	6897.5	0	NA	NA	NA	27.5	27.5	3
		Expedition 343 totals:		21	137	53.31	43	1870	1872	39
343T-										
C0019D	37°56.3224′N	143°54.8004′E	6897.5	0	NA	NA	NA	854.8	854.8	10
		Expedition 343T totals:		0	NA	NA	NA	854.8	854.8	10
		Site C0019 totals:		21	137	53.31	43	2724.8	2726.8	49

NA = not applicable. LWD = logging while drilling, MWD = measurement while drilling.

Table T2. Summary of lithologic units, Hole C0019E.

Lith. unit	Core, section, interval (cm)		Depth (mbsf)		Thickness (m)	Stratigraphic age	Lithologic description
	Top	Bottom	Top	Bottom			
	343-C0019E-	343-C0019E-					
1	1R-1, 0	1R-CC, 25	176.5	185.2	>8.7	Undetermined	Olive-gray siliceous mudstone
2	2R-1, 0	3R-CC, 0.05	648.0	659.7	>11.7	Undetermined	Interbedded bluish gray and brown ashy mudstones
3	4R-1, 0	16R-CC, 0.3	688.5	820.1	>131.6	Undetermined	Interbedded dark gray to black mudstone, ashy mudstone, and clayey mudstone
4	17R-1, 0	17R-1, 1	821.5	822.5	>1	Undetermined	Sheared clay
5	18R-1, 0	20R-2, 53	824	832.9	>8.9	Undetermined	Brown mudstone grading from silty at base to clayey at top; contains ash layers and pumice clasts
6	20R-2, 53	20R-2, 115	832.9	833.5	0.6	Undetermined	Bedded claystone
7	20R-2, 115	21R-CC, 18	833.5	836.8	>3.3	Undetermined (possible Cretaceous)	Chert

Table T3. List of samples used for biostratigraphic analyses, Expedition 343.

Core, section, interval (cm)	Sample volume (cm^3)	Top depth (mbsf)	Bottom depth (mbsf)
343-C0019E-			
1R-CCWR, 1.0–6.0	10	184.995	185.045
2R-CCWR, 9.0–14.0	10	651.57	651.62
3R-CCWR, 3.0–5.5	10	659.625	659.65
4R-CCWR, 10.5–15.5	10	690.54	690.59
5R-CCWR, 21.0–26.0	10	700.195	700.245
6R-CCWR, 15.5–20.5	10	706.305	706.355
7R-CCW, 10.0–15.0	10	715.7	715.75
8R-CCWR, 3.0–5.5	10	722.905	722.93
9R-CCWR, 0.0–5.0	10	725.115	725.165
10R-CCW, 18.0–21.0	10	772.175	772.205
11R-CCW, 10.0–13.0	10	780.6	780.63
12R-CCWR, 8.0–13.0	10	787.82	787.87
13R-CCWR, 25.5–30.5	10	802.845	802.895
14R-CCWR, 11.0–16.0	10	811.75	811.8
15R-CCWR, 18.5–21.5	10	817.895	817.925
16R-CCW, 27.0–30.5	10	819.975	820.01
17R-1WR, 48.0–50.0	3	821.98	822
17R-1WR, 103.0–104.0	3	822.53	822.54
18R-CCWR, 13.0–18.0	10	825.625	825.675
19R-CCWR, 21.0–24.0	10	829.445	829.475
20R-2W, 51.0–53.0	10	832.83	832.85
20R-2W, 53.0–56.0	10	832.85	832.88
20R-CCWR, 0.0–1.5	10	833.5	833.515
21R-CCWR, 17.0–18.0	10	836.98	836.99

Table T4. Results of MAD measurements on discrete samples, Hole C0019E.

Core, section, interval (cm)	Depth (mbsf)	Porosity	Void ratio	Bulk density (g/cm^3)	Grain density (g/cm^3)
343-C0019E-					
1R-1, 101.5	177.52	0.67	2.06	1.53	2.57
1R-2, 0.0	177.90	0.69	2.19	1.49	2.52
1R-3, 15.0	179.46	0.61	1.57	1.61	2.52
1R-4, 0.0	180.72	0.55	1.24	1.69	2.51
1R-5, 0.0	181.79	0.67	2.01	1.50	2.45
1R-6, 13.0	183.33	0.65	1.82	1.57	2.57
2R-1, 90.0	648.90	0.50	1.01	1.82	2.63
2R-1, 90.0	648.90	0.45	0.82	1.88	2.58
2R-2, 90.0	650.31	0.49	0.96	1.81	2.55
2R-2, 90.0	650.31	0.50	1.01	1.82	2.62
2R-3, 5.0	650.87	0.49	0.95	1.86	2.65
2R-3, 5.0	650.87	0.51	1.05	1.82	2.66
3R-1, 132.0	654.32	0.48	0.94	1.81	2.55
3R-1, 132.0	654.32	0.49	0.95	1.81	2.56
3R-2, 53.0	654.93	0.41	0.68	1.88	2.47
3R-2, 54.0	654.94	0.49	0.97	1.85	2.64
3R-3, 75.0	656.56	0.49	0.98	1.76	2.47
3R-3, 76.0	656.57	0.53	1.11	1.78	2.61
3R-4, 78.0	658.01	0.49	0.96	1.72	2.39
3R-4, 79.0	658.02	0.51	1.02	1.84	2.67
3R-5, 10.0	658.74	0.46	0.85	1.78	2.41
3R-5, 11.0	658.75	0.51	1.04	1.75	2.52
3R-6, 10.0	659.36	0.49	0.96	1.80	2.55
3R-6, 11.0	659.37	0.51	1.06	1.75	2.52
4R-1, 9.0	688.59	0.53	1.13	1.76	2.60
4R-2, 63.0	690.34	0.53	1.11	1.75	2.56
5R-1, 7.0	696.07	0.52	1.08	1.83	2.71
5R-2, 127.0	698.67	0.49	0.97	1.83	2.60
5R-3, 14.0	698.83	0.50	1.00	1.84	2.65
6R-1, 53.0	704.53	0.49	0.96	1.76	2.48
6R-2, 17.0	705.49	0.48	0.91	1.88	2.67
7R-1, 14.0	713.14	0.47	0.87	1.87	2.61
7R-2, 1.0	714.15	0.47	0.88	1.86	2.60
8R-1, 122.0	720.22	0.49	0.95	1.79	2.52
8R-2, 136.0	721.78	0.46	0.86	1.94	2.72
8R-3, 24.0	722.06	0.44	0.79	1.85	2.51
9R-1, 57.0	725.07	0.45	0.82	1.92	2.66
10R-1, 13.0	770.13	0.42	0.72	1.95	2.62
10R-1, 98.0	770.98	0.48	0.92	1.90	2.70
10R-2, 61.0	771.62	0.46	0.86	1.95	2.75
11R-CC, 0.0	780.50	0.48	0.94	1.84	2.62
12R-1, 12.0	786.12	0.43	0.75	1.90	2.56
12R-2, 2.0	786.89	0.43	0.74	1.94	2.62
13R-1, 47.0	801.47	0.46	0.87	1.83	2.53
13R-2, 9.0	801.90	0.47	0.90	1.85	2.59
14R-1, 27.0	810.27	0.46	0.86	1.96	2.76
14R-2, 19.0	811.21	0.47	0.90	1.94	2.76
15R-1, 37.0	816.87	0.53	1.11	1.73	2.52
16R-1, 5.0	818.55	0.42	0.74	1.93	2.59
17R-1, 99.0	822.49	0.48	0.93	1.98	2.86
18R-1, 148.0	825.48	0.48	0.91	1.89	2.68
19R-1, 37.0	826.87	0.36	0.56	2.03	2.60
19R-2, 29.0	827.98	0.47	0.90	1.93	2.74
19R-3, 0.0	828.74	0.46	0.87	1.86	2.58
20R-1, 7.0	831.07	0.53	1.11	1.76	2.58
20R-2, 3.0	832.35	0.50	1.01	1.82	2.63
21R-1, 28.0	836.78	0.35	0.54	2.01	2.54

Table T5. Unconfined compressive strength (UCS), Hole C0019E.

Core, section, interval (cm)	Depth (mbsf)	Diameter (mm)	Length (mm)	Reading force (*N*)	Strength (MPa)	l/d	Length correction factor	UCS (MPa)
343-C0019E-								
7R-2, 35–37	714.49	19.8	20.50	1320.00	4.29	1.04	0.87	3.75
8R-1, 108–110	720.08	19.8	21.50	460.00	1.49	1.09	0.88	1.32
11R-CC, 8–10	780.55	19.8	23.00	1170.00	3.80	1.16	0.89	3.38
13R-1, 26–28	801.26	19.9	14.40	2410.00	7.75	0.72	0.83	6.44
14R-2, 10–12	811.40	19.8	13.80	2820.00	9.16	0.70	0.83	7.57
15R-CC, 3–5	817.74	19.8	14.70	2770.00	9.00	0.74	0.83	7.50
19R-1, 97–99	827.47	19.8	21.30	1200.00	3.90	1.08	0.88	3.43
20R-1, 18–20	831.18	19.8	22.00	1630.00	5.29	1.11	0.88	4.68
21R-1, 19–20	836.69	12.5	18.30	8690.00	70.81	1.46	0.92	65.27

l = length, d = diameter.

Table T6. *P*-wave velocity measurements on cubic discrete samples, Hole C0019E.

Core, section	Depth (mbsf)	Velocity (m/s)			Vertical anisotropy (%)
		x	*y*	*z*	
343-C0019E-					
2R-1	648.48	1565	1540	1604	–3.26
4R-1	688.57	1440	1522	1493	–0.81
5R-2	697.62	1700	1636	1572	5.93
5R-3	699.25	1961	1855	1818	4.83
6R-1	705.12	1734	1752	1671	4.22
7R-1	713.98	1734	1788	1652	6.39
7R-2	714.45	1791	1864	1819	0.47
11R-CC	780.57	—	1849	1784	—
12R-1	786.75	1818	1727	1790	–0.98
13R-1	801.75	1919	1874	1917	–1.08
14R-1	810.29	2142	1985	1985	3.88
15R-1	817.13	2134	2098	2095	1.00
15R-CC	817.75	2080	—	—	—
19R-1	826.74	1944	1997	2013	–2.13
19R-1	827.30	1972	1973	1992	–0.98
20R-1	831.26	1940	1902	1955	–1.75
21R-1	836.59	3271	3197	3272	–1.17

— = no measurement.

Table T7. Resistivity measurements on soft sediments using a four-pin 2 kHz Wenner array, Hole C0019E.

Core, section, interval (cm)	Depth (mbsf)	Resistivity (Ωm)		Conductivity (S/m)	
		y	*z*	*y*	*z*
343-C0019E-					
1R-2, 10–14	178.00	0.56	0.67	1.80	1.48
1R-3, 63.5–66	179.95	0.70	0.76	1.43	1.32
1R-4, 16–18.5	180.88	0.63	0.69	1.59	1.46
1R-5, 124–126.5	183.03	0.82	0.76	1.23	1.31
1R-6, 55–57.5	183.75	0.89	0.91	1.13	1.10

Table T8. Electrical resistivity measurements on cubic discrete samples, Hole C0019E.

Core, section, interval (cm)	Depth (mbsf)	Resistivity (Ωm)			Conductivity (S/m)			Vertical anisotropy (%)
		x	*y*	*z*	*x*	*y*	*z*	
343-C0019E-								
4R-1, 6–8	688.56	1.22	1.16	1.33	0.82	0.87	0.75	–11.4
5R-2, 21–23	698.11	1.56	1.47	1.54	0.64	0.68	0.65	–1.2
5R-3, 55–57	699.74	1.49	1.39	1.55	0.67	0.72	0.65	–7.2
6R-1, 111–113	705.11	1.69	1.70	1.92	0.59	0.59	0.52	–12.7
7R-1, 96.5–98.5	713.97	1.44	1.34	1.56	0.69	0.74	0.64	–11.0
7R-2, 30–32	714.44	1.33	1.38	1.71	0.75	0.73	0.59	–23.1
12R-1, 74–76	786.74	1.88	1.94	1.73	0.53	0.52	0.58	9.7
13R-1, 74–76	801.74	1.51	1.72	1.73	0.66	0.58	0.58	–6.8
14R-1, 28–30	810.28	1.36	1.59	1.71	0.74	0.63	0.58	–15.0
15R-1, 62–64	817.12	2.06	1.83	1.88	0.48	0.55	0.53	3.6
19R-1, 23–25	826.73	2.03	2.02	1.94	0.49	0.50	0.52	4.0
19R-1, 79–81	827.29	1.83	1.82	2.50	0.55	0.55	0.40	–31.3
20R-1, 25–27	831.25	1.44	1.55	1.40	0.69	0.65	0.71	6.5
21R-1, 8–10	836.58	15.85	5.43	5.18	0.06	0.18	0.19	69.0

Table T9. Grain size parameters of sediments, Hole C0019E.

Core, section, interval (cm)	Depth (mbsf)	Mean grain size (μm)	Standard deviation (μm)	Skewness	Kurtosis	Remarks
343-C0019E-						
1R-1, 103–104	177.5	24.60	37.80	2.67	7.20	
1R-1, 103–104	177.5	32.48	46.74	2.40	5.64	H_2O_2 treatment
1R-1, 1–2	177.9	36.00	48.54	2.21	4.65	
1R-2, 16–17	179.5	69.45	154.50	3.49	12.34	
1R-3, 1–2	180.7	29.87	43.55	2.47	6.07	
1R-4, 1–2	181.8	39.94	41.90	1.50	1.70	
1R-5, 14–11	183.3	108.85	226.61	2.78	7.01	
1R-6, 11–12	184.7	215.17	306.56	1.37	0.58	

Table T10. Interstitial water geochemistry, Hole C0019E.

Core, section, interval (cm)	Depth (mbsf)	pH	Alkalinity (mM)	Refractive index	Salinity	Cl (mM)	Na (mM)	NH_4 (mM)	H_4SiO_4 (μM)	Ca (mM)	Mg (mM)	Sr (μM)	Li (μM)	K (mM)	PO_4 (μM)	SO_4^{2-} (mM)
343-C0019E-																
1R-1, 39–70	178.89	7.940	49.33	1.33947	35.4	561	444	3.21	885	7.20	51.65	107	59	10.65	95.67	3.63
4R-1, 94–111	689.44			1.33937	34.9	562	470	7.84	930	8.00	42.02	106	98	8.87	27.96	3.84
5R-2, 83–98.5	698.23			1.33931	34.5	555	465	7.59	885	7.73	41.06	109	94	8.49	32.87	3.41
6R-2, 53–74	705.85			1.33943	35.2	555	472	7.56	756	8.05	41.41	94	86	8.62	22.24	8.21
7R-1, 31–62	713.31			1.33930	34.5	558	467	7.39	695	8.11	40.91	101	91	9.33	16.63	4.16
8R-1, 0–30	720.42	7.910	35.25	1.33933	34.6	558	465	6.30	940	8.92	43.13	100	88	8.98	22.11	6.35
12R-2, 59–79	787.46			1.33940	35.0	570	472	2.62	660	11.65	44.87	91	74	9.61		10.79
13R-2, 45–70	802.26			1.33937	34.8	572	463	2.83	729	14.53	42.84	104	87	7.95	7.91	4.97
14R-1, 52.5–77	810.53			1.33913	33.5	562	453	1.89	876	15.77	40.09	102	98	8.19		3.87
15R-1, 0–21	816.50			1.33914	33.6	556	444	1.34	887	17.94	39.29	109	97	8.56		4.15
19R-1, 66.5–105	828.36	7.640	7.94	1.33931	34.5	549	436	0.44	1,116	32.73	36.69	120	101	7.50		16.03
20R-1, 45–65	831.45			1.33938	34.9	544	430	0.23	1,101	38.94	35.38	121	96	7.06	3.56	20.24

Core, section, interval (cm)	Depth (mbsf)	Fraction seawater	Fraction interstitial water	Mn (μM)	Br (mM)	Br/Cl	Ba (μM)	B (μM)	Fe (μM)	V (nM)	Zn (μM)	Rb (nM)	Mo (nM)	Cs (nM)	Pb (nM)	U (nM)	Cu (nM)
343-C0019E-																	
1R-1, 39–70	178.89	0.126	0.874	2.95	0.93	0.0017	112.6	576	3.40	145	548	1,585	547	3.59	3.75	18.26	1,010
4R-1, 94–111	689.44	0.133	0.867	2.44	1.11	0.0020	104.3	425	1.55	110	1,432	1,164	929	6.94	26.14	15.88	3,630
5R-2, 83–98.5	698.23	0.118	0.882	2.59	1.11	0.0020	123.1	482	2.05	109	1,101	1,091	1,018	6.59	37.28	9.65	21,165
6R-2, 53–74	705.85	0.284	0.716	2.22	1.04	0.0019	32.9	414	0.83	78	2,404	1,030	1,986	5.66	7.90	23.30	3,762
7R-1, 31–62	713.31	0.144	0.856	1.70	1.07	0.0019	92.2	375	0.93	89	1,397	1,111	1,604	6.32	33.35	13.24	7,236
8R-1, 0–30	720.42	0.220	0.780	3.06	1.03	0.0019	68.9	494	1.37	83	1,050	1,019	735	6.21	12.36	10.51	3,186
12R-2, 59–79	787.46			5.96	0.93	0.0016	13.9	325	0.63	87	963	1,144	1,717	6.59	14.85	14.38	1,260
13R-2, 45–70	802.26			11.70	0.96	0.0017	22.9	297	0.61	56	778	920	1,870	5.56	15.94	9.39	3,676
14R-1, 52.5–77	810.53			11.28	0.93	0.0016	32.9	300	0.58	41	1,658	906	623	4.64	8.78	5.89	1,814
15R-1, 0–21	816.50			13.21	0.93	0.0017	38.6	305	0.71	53	1,407	882	80	3.02	15.12	5.94	2,720
19R-1, 66.5–105	828.36			164.32	0.86	0.0016	1.4	426	0.63	33	3,443	654	965	2.27	7.85	47.17	4,248
20R-1, 45–65	831.45			113.22	0.87	0.0016	1.3	410	0.60	36	3,267	700	759	1.90	8.74	30.33	3,775

Table T11. Chemistry of six mud batches used during drilling, Expedition 343.

	Chlorinity (mM)	Br^- (mM)	SO_4^{2-} (mM)	Na^+ (mM)	K^+ (mM)	Ca^{2+} (mM)	B (µM)	Ba (µM)	Fe (µM)	Li (µM)	Mn (µM)	Si (µM)	Sr (µM)	V (nM)	Cu (nM)
Mud batch	362	0.55	19.37	379	5.64	12.31	111	0.40	0.43	37.33	0.29	299	68.16	34.28	10.04
Mud batch	367	0.57	19.78	377	5.68	12.42	111	0.45	0.37	37.21	0.25	261	70.30	34.86	13.48
Mud batch	342	0.53	18.59	354	5.27	14.45	124	0.57	0.52	33.32	0.21	222	60.50	29.71	11.90
Mud batch	361	0.56	19.42	380	5.65	12.17	88	0.41	0.31	34.55	0.18	505	68.37	37.94	8.73
Mud batch	294	0.45	16.12	301	4.22	11.59	59	0.39	0.40	33.01	0.18	1271	63.42	66.76	15.27
Mud batch	332	0.50	18.16	337	5.02	14.50	144	0.85	0.40	37.03	0.26	201	68.95	38.74	5.43
Average concentration:	343	0.53	18.57	354	5.25	12.91	106	0.51	0.41	35.41	0.23	460	66.62	40.38	10.81

	Zn (nM)	Rb (nM)	Mo (nM)	Cs (nM)	Pb (nM)	U (nM)
Mud batch	50.00	771	445	12.37	0.99	ND
Mud batch	49.71	801	449	13.44	1.21	ND
Mud batch	36.26	719	453	10.64	0.82	ND
Mud batch	35.02	756	425	12.03	0.83	ND
Mud batch	27.17	619	448	9.66	0.97	ND
Mud batch	39.26	720	529	12.13	1.05	0.21
Average concentration:	39.57	731	458	11.71	0.98	0.21

ND = not determined.

Table T12. Carbon, nitrogen, and sulfur data, Hole C0019E.

Core, section, interval (cm)	Depth (mbsf) Top	Depth (mbsf) Bottom	IC (wt%)	$CaCO_3$ (wt%)	TN (wt%)	TC (wt%)	TS (wt%)	TOC (wt%)	TOC/TN	TOC/TS
343-C0019E-										
1R-1, 85–88	177.35	177.38	0.02	0.15	0.05	0.41	0.23	0.40	7.43	1.71
1R-6, 14–16	183.34	183.36	0.02	0.15	0.05	0.24	0.08	0.22	4.49	2.65
1R-6, 123–125	184.43	184.45	0.02	0.15	0.02	0.08	0.01	0.06	3.01	5.15
2R-1, 48.5–50.5	648.49	648.51	0.03	0.27	0.03	0.11	0.02	0.07	2.27	4.41
2R-1, 99.5–101.5	649.00	649.02	0.90	7.49	0.03	0.94	0.00	0.04	1.25	7.82
3R-1, 31–35	653.31	653.35	0.05	0.38	0.04	0.10	0.08	0.05	1.44	0.65
3R-1, 31–35	653.31	653.35	0.04	0.30	0.04	0.22	0.06	0.19	4.90	3.38
4R-1, 12–16	688.62	688.66	1.47	12.29	0.10	2.26	0.30	0.79	7.81	2.65
4R-1, 91–93	689.41	689.43	3.85	32.07	0.08	4.51	0.15	0.66	8.29	4.50
5R-2, 82–83	698.22	698.23	0.09	0.77	0.10	0.80	0.22	0.71	6.80	3.23
6R-2, 51–52	705.83	705.84	0.09	0.73	0.09	0.57	1.62	0.48	5.63	0.30
7R-1, 7–8.5	713.07	713.09	0.65	5.39	0.10	1.26	0.22	0.61	6.44	2.79
7R-2, 119–122	715.33	715.36	0.02	0.16	0.10	0.61	0.13	0.59	5.67	4.62
8R-1, 51–54	719.51	719.54	0.14	1.16	0.10	0.82	0.19	0.68	6.81	3.65
8R-2, 44–49	720.86	720.91	0.10	0.83	0.11	0.81	0.27	0.71	6.62	2.58
9R-1, 5–9	724.55	724.59	0.02	0.14	0.10	0.60	0.03	0.58	6.13	18.37
10R-1, 85–90	770.85	770.90	0.14	1.14	0.09	0.77	0.46	0.63	7.24	1.36
10R-CC, 18–20	772.18	772.20	0.14	1.19	0.08	0.71	0.27	0.56	6.79	2.05
11R-CC, 4–6	780.54	780.56	0.07	0.55	0.10	0.76	0.21	0.70	7.34	3.36
12R-2, 57–59	787.44	787.46	0.07	0.56	0.08	0.68	0.19	0.61	8.04	3.29
13R-1, 32–33	801.32	801.33	0.13	1.11	0.09	0.81	0.19	0.68	7.56	3.64
13R-1, 45.5–47	801.46	801.47	0.08	0.70	0.06	0.49	1.03	0.41	7.34	0.39
14R-1, 50–53	810.50	810.53	0.27	2.28	0.09	0.87	3.12	0.60	6.92	0.19
15R-1, 28–34	816.78	816.84	0.01	0.05	0.03	0.10	0.11	0.10	3.55	0.87
16R-1, 5–10	818.55	818.60	0.13	1.06	0.06	0.65	0.27	0.52	8.25	1.97
17R-1, 113–114	822.63	822.64	0.02	0.17	0.03	0.05	0.04	0.03	1.05	0.80
18R-1, 55–56	824.55	824.56	0.01	0.06	0.04	0.12	0.06	0.11	2.81	1.86
19R-2, 66–67	828.35	828.36	0.05	0.44	0.03	0.16	0.03	0.10	3.90	3.28
20R-1, 126–128	832.26	832.28	0.07	0.54	0.04	0.18	0.03	0.11	3.10	3.78
20R-2, 68–70	833.00	833.02	0.03	0.27	0.01	0.09	0.04	0.06	5.54	1.25
20R-2, 79–82	833.11	833.14	0.02	0.13	0.01	0.08	0.05	0.06	5.63	1.32
20R-2, 114.5–116.5	833.47	833.49	0.01	0.12	0.01	0.05	0.03	0.04	5.09	1.23

IC = inorganic carbon, TN = total nitrogen, TC = total carbon, TS = total sulfur, TOC = total organic carbon.

Table T13. Concentration of dissolved gas components in core samples, Hole C0019E.

Core, section, interval (cm)	Depth (mbsf)	H_2 (μM)	CO (μM)	CH_4 (mM)	C_2H_6 (μM)	Methane/ Ethane	Methane/ H_2
343-C0019E-							
1R-1, 140	177.87	0.359	<0.5	8.7800	0.184	47,581	24,422
1R-2, 141	179.30	0.725	<0.5	3.0600	0.097	31,501	4,212
1R-3, 140.5	180.70	0.113	<0.5	15.7000	0.300	52,237	138,938
1R-4, 107	181.77	0.166	<0.5	5.1100	0.134	38,073	30,783
1R-5, 141	183.18	0.113	<0.5	4.1400	0.131	31,629	36,637
1R-6, 140	184.56	0.113	<0.5	1.4200	0.078	18,411	12,566
2R-1, 140.5	649.38	1.910	<0.5	0.4930	<0.05	ND	ND
2R-2, 141	650.78	2.360	<0.5	1.0100	<0.05	ND	ND
3R-1, 140	654.37	0.152	<0.5	0.9340	<0.05	ND	ND
3R-2, 141	655.80	0.684	<0.5	ND	ND	ND	ND
3R-3, 141.5	657.22	0.224	<0.5	1.8400	<0.05	ND	ND
3R-4, 141.5	658.63	0.505	<0.5	1.3900	<0.05	ND	ND
4R-1, 121	689.68	0.490	2.220	1.7900	0.183	9,782	3,675
4R-CC, 15.5	690.58	32.100	4.430	2.4900	0.227	10,988	78
5R-1, 140	697.37	209.000	1.850	3.9600	0.355	11,138	19
5R-2, 129	698.68	8.920	3.580	2.8100	0.295	9,525	311
5R-3, 129.5	699.98	2.510	1.770	2.0700	0.171	12,086	822
6R-1, 132	705.29	1.310	1.230	4.4800	0.272	16,494	3,410
6R-2, 83	706.15	2.780	2.790	3.3500	0.208	16,140	1,206
7R-2, 1	714.14	2.360	1.990	8.9100	0.358	24,071	3,769
7R-2, 146	715.59	4.651	1.960	2.5620	0.188	13,612	551
8R-1, 141.5	720.38	2.417	3.759	13.0175	0.506	25,740	5,386
8R-2, 140	721.80	1.950	1.840	7.3114	0.409	17,885	3,750
8R-3, 106	722.86	2.009	2.108	6.0167	0.311	19,328	2,994
9R-1, 61.5	725.08	2.211	2.002	15.8917	0.578	27,500	7,186
10R-1, 101	770.98	1.614	1.057	4.7015	0.222	21,144	2,912
10R-2, 98.5	771.98	4.959	2.021	1.2734	0.116	11,001	257
11R-CC, 13.5	780.62	1.117	2.172	20.1600	0.628	32,108	18,055
12R-1, 87	786.84	1.471	1.249	9.1513	0.400	22,885	6,220
12R-2, 87	787.74	1.982	0.936	3.1530	0.156	20,186	1,591
13R-1, 81	801.80	1.951	0.673	5.1021	0.194	26,365	2,616
13R-2, 78	802.56	2.642	1.689	12.1594	0.333	36,484	4,603
14R-1, 102	810.99	1.874	1.402	5.8854	0.240	24,564	3,141
14R-2, 62	811.61	1.889	0.730	10.6236	0.315	33,742	5,624
15R-CC, 11.5	817.82	26.442	<0.5	6.7975	0.246	27,685	257
15R-CC, 21.5	817.89	4.172	<0.5	8.6107	0.235	36,606	2,064
16R-1, 1	818.50	1.652	0.627	3.7293	0.216	17,238	2,258
16R-1, 120.5	819.70	1.217	2.817	6.5657	0.282	23,317	5,394
16R-CC, 1	819.71	19.745	2.265	5.4806	0.287	19,114	278
16R-CC, 30.5	819.98	1.564	2.957	2.5772	0.175	14,716	1,648
17R-1, 1	821.50	0.535	<0.5	3.5992	0.123	29,347	6,732
17R-1, 100	822.47	1.491	<0.5	2.9543	0.113	26,220	1,982
18R-1, 1	824.00	1.747	<0.5	1.8346	0.061	29,925	1,050
18R-1, 149.5	825.48	1.087	<0.5	3.6507	0.133	27,379	3,360
18R-CC, 1	825.50	1.320	<0.5	2.8400	0.105	26,972	2,152
18R-CC, 18	825.66	1.396	<0.5	3.2047	0.130	24,716	2,295
19R-1, 1	826.50	2.312	<0.5	1.3437	0.135	9,979	581
19R-1, 119	827.66	0.389	<0.5	0.9462	<0.05	ND	2,430
19R-CC, 1	829.23	1.112	<0.5	1.3223	<0.05	ND	1,189
20R-1, 1	831.00	0.772	<0.5	0.7294	<0.05	ND	944
20R-1, 132	832.29	1.101	<0.5	0.4452	<0.05	ND	405
20R-2, 118	833.47	0.808	<0.5	0.0096	<0.05	ND	12

ND = no data.

Table T14. Concentrations of perfluorocarbon tracer (PFC) in drilling mud and microbiological samples collected during Expedition 343.

Sample ID	Depth (mbsf)	PFC concentration (μg/cm^3)			Remarks
		Drilling mud	Core interior	Core exterior	
343-C0019E-					
1R	177.25		0.0014	0.0002	Negative controls (background data)
Mud-5/17		1.77			
4R	689.66		ND	0.0094	Noncontaminated
5R	698.70		0.0036	0.0314	0.20% of drilling mud
Mud-5/18		1.88			
6R	706.11		0.0256	0.0626	1.4% of drilling mud
7R	713.66		0.0040	0.0104	0.21% of drilling mud
8R	720.76		0.0032	0.0094	0.17% of drilling mud
Mud-5/19–20		932			
12R	767.70		ND	0.0032	Noncontaminated
Mud-5/20		989			
13R	802.50		0.0320	0.0692	Noncontaminated (needs careful examination)
14R	810.81		0.0008	0.0094	Noncontaminated
15R	816.75		0.0024		Noncontaminated
Mud-5/21–22		1.65			
19R	828.90		ND	0.0048	Noncontaminated
20R	831.42		0.0018	0.0054	0.11% of drilling mud

ND = no data.